Nano-Photonic Structures for the Scale-up of III-V Semiconductor Based Quantum Optical Devices

A thesis presented for the degree of
Doctor of Philosophy

Luke Brunswick

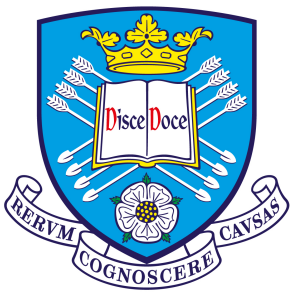

The University Of Sheffield.

Department of Physics and Astronomy
University of Sheffield
June 2022

This page intentionally left blank.

Abstract

This thesis describes the designs and measurements of three nano-photonic device schemes. The aim of which is to achieve the scale-up of III-V semiconductor based nano-photonic systems. Scale-up of the number of resonant quantum dots, and nano-structures on-chip is vital for the realisation of a quantum network using the III-V semiconductor quantum dot architecture.

The effect of varying the growth conditions of site-controlled quantum dots on their optical properties is investigated. This is combined with a study of a recently demonstrated *in-situ* local quantum dot strain tuning method. Optical waveguides are conformally coated in a dielectric material which when crystallised by a heating laser, induces a strain field in the quantum dots embedded in the waveguide.

An electro-mechanically tunable photonic crystal cavity design is proposed. The cavity and cantilever designs are optimised and tested for robustness against fabrication imperfections in simulation. The cavity design exhibits world-leading figures of merit for both the weak and strong coupling regimes. The cavity fabrication was optimised through several test sample iterations. The final design was fabricated, and a voltage-controllable cavity wavelength tuning range much larger than the standard deviation of the cavity mode wavelength distribution was measured.

A scheme which enables a quantum dot to exhibit both strong light-matter interaction enhancement, and strongly directional emission is presented. The design consists of a photonic crystal cavity coupled to two feeding photonic crystal waveguides. The operation of the design is verified through a theoretical model and simulations. A test device sample is measured to characterise various waveguide orientation designs and parameters. Strongly directional emission and a low Purcell enhancement are measured from a quantum dot embedded in a waveguide coupled cavity.

This page intentionally left blank.

Acknowledgements

I would like to extend my sincere and utmost gratitude to those who have made this work possible. I feel privileged to have been given the opportunity to study with the LDSD group at the University of Sheffield, and so would like to thank all of my colleagues, past and present.

In particular, I would like to thank my supervisor Luke Wilson, for not only his great wisdom, guidance and support, but also his excellent whit and humour, which have made working with him an absolute pleasure, Andrew Foster, for teaching me his meticulous approach to lab work and answering my many questions at a moments notice, Igor Itskevich, for his guidance in the lab early on in my studies, René Dost, for fabricating the samples measured in this work, and Chris Vickers, for supplying the Helium for the cryogenic measurements.

I would also like to especially thank: Sam Sheldon, Nicholas Martin, Catherine Phillips, Dominic Hallett, Alistair Brash, Chris O'Rourke and Mahmoud Mehrabad for making LDSD such an enjoyable place to work.

Outside of LDSD, I would also like to thank my family and friends for their unwavering support; especially Robert Russell, for his rigorous proof-reading skills and to whom I am incredibly grateful.

Finally, I would like thank my wife Emily, who's unconditional optimism, support, companionship and love, have truly made this work possible.

This page intentionally left blank.

Publications

L.A.F. Brunswick, A.P. Foster, R. Dost, M.S. Skolnick and L.R. Wilson, "An electro-mechanically tunable nanobeam photonic crystal cavity.", (*In preparation*)

C. Ovenden, A. Trapalis, **L.A.F. Brunswick**, D.J. Hallett, M.S. Skolnick, I. Farrer and J. Heffernan "Improving Site-Controlled Quantum Dot Yield via Growth Condition Control.", (*In preparation*)

L.A.F. Brunswick, A.P. Foster, R. Dost, M.S. Skolnick, L.R. Wilson, "Enabling Scale-up of on-chip Cavity-Cavity Interactions with an Electro-Mechanically Tunable GaAs Nanobeam Photonic Crystal Cavity." Poster Presentation, UK Semiconductors, Sheffield, UK, 2022

This page intentionally left blank.

This thesis is dedicated to my wife Emily.

This page intentionally left blank.

Contents

Abstract **ii**

Acknowledgements **iv**

Publications **vi**

1 Introduction **1**
1.1 Quantum information processing . . . 1
1.1.1 Creating a successful quantum network . . . 3
1.2 III-V integrated photonics as a platform for a quantum network . . . 4
1.3 Thesis outline . . . 6

2 Background **10**
2.1 Low dimensional III-V semiconductors . . . 10
2.1.1 Doping of semiconductors . . . 11
2.1.2 p-i-n diode . . . 11
2.1.3 Quantum confinement . . . 12
2.2 Semiconductor quantum dots . . . 13
2.2.1 Quantum dot growth . . . 14
2.2.2 Optical properties . . . 14
2.2.3 Site-controlled quantum dot growth . . . 16
2.3 Quantum dot emission energy tuning . . . 17
2.3.1 Quantum-confined Stark effect . . . 18
2.3.2 Zeeman splitting and magnetic field tuning . . . 20
2.3.3 Strain tuning . . . 20
2.3.4 Temperature tuning . . . 23
2.3.5 Quantum dot registration . . . 23
2.4 Nano-photonic structures . . . 25
2.4.1 Nanobeam waveguides . . . 26
2.4.2 Grating output couplers . . . 27
2.4.3 Photonic crystal waveguides . . . 28
2.4.4 Photonic crystal cavities . . . 30
2.5 Cavity quantum electrodynamics . . . 34
2.5.1 Weak coupling . . . 35
2.5.2 Strong coupling . . . 36
2.6 Photon statistics . . . 37
2.6.1 Coherent light . . . 37
2.6.2 Anti-bunched light . . . 38

2.6.3 Bunched light . . . 38
2.6.4 Degree of second order coherence . . . 39
2.7 Directionality of embedded emitters . . . 40

3 Methods 43
3.1 Introduction . . . 43
3.2 Wafer growth and nano-structure fabrication . . . 43
3.2.1 Semiconductor wafer growth . . . 43
3.2.2 Device fabrication . . . 45
3.2.3 Diode fabrication . . . 45
3.3 Experimental methods . . . 48
3.3.1 Excitation lasers . . . 48
3.3.2 Confocal microscopy . . . 49
3.3.3 Time-resolved measurements . . . 53
3.3.4 Spectroscopy . . . 54
3.3.5 Cryostats . . . 54
3.4 Computational methods . . . 56
3.4.1 Finite-Difference Time-Domain (FDTD) simulations . . . 56
3.4.2 MIT Photonic Bands (MPB) simulations . . . 60
3.4.3 Monte Carlo method simulations . . . 60

4 SCQDs and in-situ strain tuning of QDs 64
4.1 Introduction . . . 64
4.2 Site-controlled quantum dot background . . . 65
4.2.1 Site-controlled growth via etched nanoholes . . . 65
4.2.2 Nanohole etching techniques for site-controlled quantum dots . . . 66
4.2.3 Site-controlled quantum dot parameter considerations . . . 68
4.3 Site-controlled quantum dot sample results . . . 69
4.4 *In-situ* strain tuning background . . . 74
4.4.1 *In-situ* strain tuning via thin film crystallisation . . . 74
4.4.2 Tuning mechanism considerations . . . 76
4.5 Design of strain tuning sample . . . 76
4.6 Strain tuning results . . . 79
4.6.1 Experimental set-up for controllable laser exposures . . . 79
4.6.2 Laser power dependence . . . 79
4.6.3 Cumulative laser exposure time dependence . . . 82
4.6.4 Tuning ranges in nanobeam and photonic crystal waveguides . . . 84
4.6.5 Tuning two QDs into resonance over a short range . . . 87
4.6.6 Tuning two QDs into resonance over a long range . . . 89

4.7 Conclusions and outlook 90

5 Electro-mechanically tunable 1D photonic crystal cavities 93

5.1 Introduction 93
5.2 Theory 94
5.2.1 Cavity mode tuning 94
5.2.2 Electrostatic actuation of a free-standing cantilever 96
5.3 Optimisation of the 1D photonic crystal cavity design 99
5.3.1 Design overview 100
5.3.2 Initial nanobeam dimension selection 101
5.3.3 Variations of the number of air holes (n_m and n_t) 102
5.3.4 Variations of the uniform hole radius (r_0) and period (a_0) 106
5.3.5 Variations of the cavity width (w_c) and minimum taper period (a_{min}) 109
5.3.6 Variation of the nanobeam width w 113
5.3.7 Relative performance of optimised 1D photonic crystal cavities compared to 2D photonic crystal cavities 114
5.4 Optimisation of the perturbing photonic crystal membrane 116
5.4.1 Optimisation of in-plane separation of cavity and perturbing beams (d_0) . . . 117
5.4.2 Optimisation of perturbing beam photonic crystal period (a_p) and hole radii (r_p) 118
5.4.3 Optimisation of the length of the perturbing beam (n_b) 120
5.5 Fabrication error quantifying in simulation 121
5.5.1 Monte Carlo simulation approach for quantifying air hole radii error 121
5.5.2 Quantifying anisotropy of air hole etching in simulation 124
5.6 Experimental measurements of the 1D photonic crystal cavity designs 127
5.6.1 Initial 1D photonic crystal cavity test sample 127
5.6.2 Revised 1D photonic crystal cavity sample 130
5.7 Experimental measurements of cantilever devices 135
5.8 Conclusions 140

6 Waveguide coupled chiral H1 PhCC 143

6.1 Introduction 143
6.2 Theory 144
6.2.1 Origin of directionality in a waveguide coupled H1 photonic crystal cavity . . 144
6.2.2 Waveguide to waveguide transmission dynamics 147
6.3 Sample and device design 151
6.4 Results 154
6.4.1 Uncoupled H1 cavity results 154
6.4.2 Regular waveguide coupled H1 device results 157

6.4.3 Alternative waveguide orientation device results . . . 160
6.4.4 Transmission comparison between waveguide orientation designs . . . 163
6.4.5 Magnetic field dependence of QD in a waveguide coupled H1 cavity . . . 165
6.4.6 Lifetime measurements of QD in a waveguide coupled H1 cavity . . . 169
6.5 Conclusions and future work . . . 172

7 Summary and outlook **174**
7.1 Summary . . . 174
7.1.1 Chapter 4 . . . 174
7.1.2 Chapter 5 . . . 174
7.1.3 Chapter 6 . . . 175
7.2 Outlook . . . 175
7.2.1 Chapter 4 further work . . . 175
7.2.2 Chapter 5 further work . . . 177
7.2.3 Chapter 6 further work . . . 178

Acronyms **180**

References **183**

1 Introduction

The invention of the electronic computer was arguably the most important technological advancement of the 20th century. Since then, the technology that these computers rely on has been improving at an astounding rate. Computers powered the technological revolution of the late 90's and 2000's with the introduction of such notable technologies as the internet and smart phones, which have totally changed society. In 1965, Gordon Moore stated that the number of transistors on a microchip will double every two years (he later reduced this estimate to one year) [1]. This prediction has been extremely accurate and has come to be known as Moore's Law. However, this blinding pace has started to slow. Transistors are approaching a fundamental size limit on the order of a few atoms. If the power of our computing technology is to continue increasing, a new approach is required.

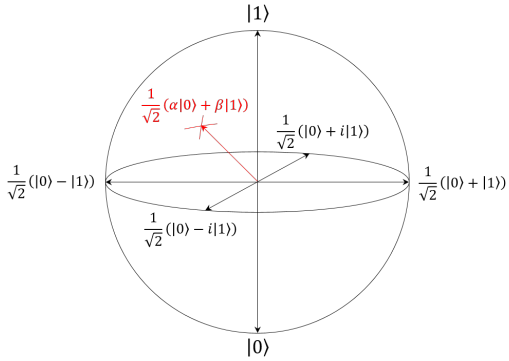

Figure 1: The Bloch sphere representation of the available states for a single qubit in a pure state. A qubit can take any value on the surface of the sphere ($\sqrt{|\alpha|^2 + |\beta|^2} = 1$) whereas a classical bit can only take a value of either 0 or 1.

1.1 Quantum information processing

The field of '*Quantum Information Processing*' (QIP) has gathered much interest in recent years owing to successful demonstrations of its potential for cryptography [2] and metrology [3] applications. Perhaps most importantly, as classical computers are fast approaching the fundamental limit, the applications of QIP for quantum computing has been an increasingly active area of research, with quantum supremecy over a classical system being recently demonstrated [4].

QIP utilises the linear superposition of a two-level system to perform complex tasks. These two-level systems are called qubits. Where a classical system is limited in that the bits can only take a binary value of 0 or 1, qubits can be in any linear superposition of 0 or 1; this is most easily

represented on a Bloch sphere (Figure 1). This representation shows that a qubit in a pure state can be represented in general by the wavefunction $|\psi\rangle = \alpha|0\rangle + \beta|1\rangle$ which denotes the qubit is in a superposition of the $|0\rangle$ and $|1\rangle$ states with probabilities of $|\alpha|^2$ and $|\beta|^2$ respectively. This allows for an ensemble of qubits to be in a superposition of all possible configurations at once, whereas a comparable ensemble of classical bits can only occupy one of these configurations (Figure 2). As the number of interacting qubits increases, so does the number of possible configurations and therefore so does the advantage of the quantum system over the classical counterpart. Moreover, quantum systems can utilise entanglement between qubits allowing for instantaneous interactions over an arbitrary distance between the entangled qubits. A system of entangled qubits is described by a mixed state; this means each qubit cannot be described individually, instead, the system is described as a superposition of the possible measurement outcomes. When the state of one qubit in the system is measured the superposition collapses and the state of the other qubits in the system is determined instantly. This however, does not allow the system break causality. Without the knowledge of the outcome of the initial measurement which collapsed the superposition, the measurement of any other qubit in the system is indistinguishable from a measurement of the mixed state. Therefore, to transfer any useful information, the result of the first measurement must be sent to the other qubits via a classical bit. Scale-up of the number of interacting qubits is therefore a key factor in the successful realisation of QIP systems as a serious competitor to classical approaches.

To facilitate this kind of scale up a '*quantum network*' must be created to interface a number of individual local quantum systems simultaneously. Kimble discusses the idea of a '*quantum internet*' [5] as an extension of the quantum network which enables interactions between an arbitrary number of quantum systems via the distribution of entanglement. The quantum internet would allow for large scale computation utilising many isolated quantum systems together as one. Moreover, quantum software could be distributed via the quantum internet allowing for further integration of quantum systems globally. A further advantage of quantum networks is that by linking multiple separate quantum systems they could overcome the fundamental size limitations of single quantum systems caused by size-scaling and error correlation [6].

These advantages allow for quantum systems to greatly excel over classical systems in specific scenarios. One such scenario is database searching (Grover's algorithm) [7]. In the quantum case, the time taken for an operation is reduced from $\mathcal{O}(N)$ to $\mathcal{O}(\sqrt{N})$ where N is the number of elements searched through. Another scenario where quantum computers excel over classical systems is prime number factorisation (Shor's algorithm) [8]. This quantum algorithm can solve for factors of any number N in a polynomial time, nearly exponentially faster than the best classical approach (number field sieve) [9]. Finally, quantum computers are far superior to classical systems when simulating quantum systems as they are able to directly simulate the probabilistic nature of quantum systems

whereas classical systems must take a deterministic approach. Moreover, quantum systems have access to a much larger state space compared to classical systems for a given number of (qu)bits [10].

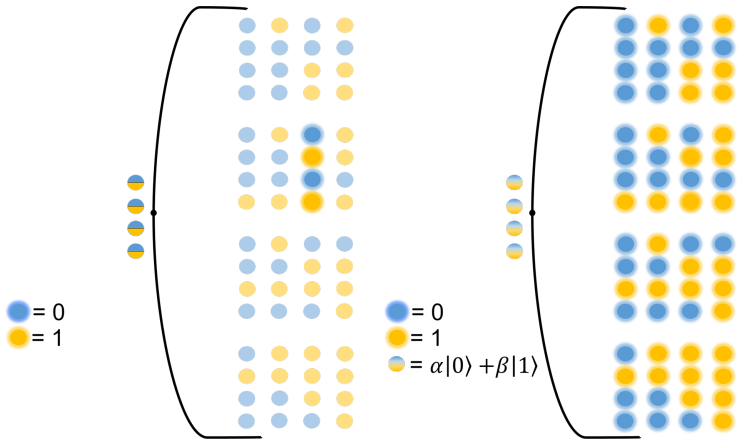

Figure 2: Visualisation of the increased state space available to quantum systems over a classical system with the same number of bits. Left: Four classical bits which can be in either the $|0\rangle$ or $|1\rangle$ states and all the possible arrangements of these bits. Only one of the possible arrangements can be accessed by classical bits at any given time. Right: Four qubits each in a linear superposition of the $|0\rangle$ and $|1\rangle$ states. The properties of the superposition allow the qubits to be in all possible configurations at once until they are measured and collapsed into a single outcome.

1.1.1 Creating a successful quantum network

In 2000, David DiVincenzo outlined a set of criteria [11] that a system should fulfil in order to be suitable for use as a quantum computing platform. By extension, a system being used to construct a quantum network must also fulfil these criteria, specifically the last two criteria as detailed below.

The ability to interconvert stationary and flying qubits

Qubits are split into two categories: stationary qubits, which have long coherence times useful for storing information, and flying qubits, with shorter coherence times but the ability to transfer information spatially. By converting between these two types of qubits, information can be transferred between stationary qubits and across a quantum network.

The ability to faithfully transmit flying qubits between specified locations

Following on from the criterion above, the flying qubits must transfer their information without

fault. In practical terms, the decoherence time of the flying qubit must be longer than the transfer time so that no information is lost during transfer.

Further to these points, Kimble outlines the two key research areas which are working towards the realisation of a quantum network. These research areas are: coherent control over light-matter interactions down at single photon levels and QIP with atomic ensembles [5]. Light-matter interaction is essential to the creation of a quantum network as, currently the only known flying qubits are photons. Therefore, it is key to the operation of quantum networks that, as per the DiVincenzo criteria above, the quantum information carried by these photons can be converted into a stationary quantum state. This will require strong and controllable light-matter interaction. QIP with atomic ensembles pertains more specifically to the computational side of the network and as such more closely to the first five DiVincenzo criteria. Multiple suitable systems for QIP have been demonstrated in recent years, as will be discussed in the next section.

1.2 III-V integrated photonics as a platform for a quantum network

Several candidate qubit systems are being pioneered in parallel with the goal of realising a scalable quantum computing network. Currently, the most successful single quantum systems are comprised of superconducting circuits which use Josephson junctions as qubits[12] where systems with over 100 qubits have been created. Other qubit candidates include: colour centres [13], trapped atoms/ions [14], photons [15], atomic assemblies via nuclear magnetic resonance techniques [16], and '*Quantum Dots*' (QDs) [17]. *This* thesis is concerned with III-V semiconductor systems, which use QDs and photons as stationary and flying qubits respectively. The III-V architecture provides a wealth of favourable features for the implementation of a quantum network. Highly controllable crystal growth techniques [18, 19] allow for the embedding of single photon emitters(e.g. QDs) [20] within the crystal and a high degree of control over the environment of these emitters. Moreover, a wide variety of fabrication techniques [21–23] have been demonstrated in III-V systems that can be used to create complex structures to further enhance the innate favourable properties of the III-V architecture, providing efficient photon routing [24], off-chip coupling [25], and enhancement of light-matter interaction [26].

If we examine how a III-V semiconductor based quantum network, utilising QDs and photons as qubits, performs with regards to the DiVincenzo criteria, we can see that such a system is an excellent candidate for the realisation of a quantum network. For both the QD and photon case, the system's energy levels and thus, Hamiltonians are well understood in multiple environments and scenarios, with many years of research underpinning them prior to their implementation in quantum networks. In principle, the scalability of III-V systems is excellent, as individual QDs can easily be addressed via resonant excitation of the desired qubit; such an excitation will produce a single photon qubit capable of transferring information through the network. However, the

difficulty in scaling up these systems comes from the random distribution of the QDs' dimensions and spatial positions, a result of the growth process, which makes each QDs energy levels slightly different. To form a network the QDs need to all have the same energy levels so that they may send and receive indistinguishable photons from each other. Moreover, intrinsic fabrication errors on the dimensions of nano-structures further complicate scale-up of these systems. Thus one of the main hurdles facing III-V based quantum networks is the ability to tune ensembles of QDs and nano-structures into resonance or selectively integrate resonant QDs into the network without compromising its effectiveness.

The initialisation of QDs into a fiducial state is easily achieved by optically addressing each QD with short pulses. Initialisation in this manner can be achieved in picosecond time-scales, faster than the coherence time of both single charge carriers and excitons in QDs. The coherence time (T_2) is determined by two dephasing mechanisms, longitudinal (T_1) depahsing, such as the radiative recombination and carrier tunnelling, and transverse or pure dephasing (T_2^*), such as coupling to acoustic phonons or charge fluctuation effects, where $\frac{1}{T_2} = \frac{1}{2T_1} + \frac{1}{T_2^*}$. Excitons in QDs typically exhibit coherence times of $\sim 1ns$ which are limited by the radiative recombination time of the exciton (T_1) [27]. Single charge carriers have coherence times which are typically longer than that of excitons, on the order of a few nanoseconds with fidelities of $\geq 99.5\%$ [28]. The coherence time of single charge carriers in QDs is limited by pure dephasing as the single charge carriers do not undergo radiative decay and as such T_2^* dominates. Schemes exist which allow the pure dephasing rate of single charge carriers in QDs to be greatly reduced allowing for much longer coherence times than that of an exciton in a QD (on the order of μs) [29]. Therefore, charge carrier spins are used as a quantum memory in QDs. By applying an electric field the QDs become charged with electrons. These electrons can be initialised into a long-lived spin state via optical pumping of the QD into a trion state while a magnetic field is applied to the QD. The magnetic field lifts the degeneracy of the electron spin ground states and depending on the orientation of the field, alters the optical selection rules. This allows for the qubit to be encoded in the ground state of the electron spin subspace [30, 31]. The initialised spin qubit can be manipulated via detuned laser pulses or an alternating magnetic field and spin read-out achieved on nanosecond time scales by addressing the QD with short optical pulses [32]. The energy of the read out photon indicates the spin state of the charge carrier [33]. Interactions between electron spins in multiple QDs can be facilitated through the use of entanglement between the electron spins. This can be achieved either through coupling via the coulomb interaction if the QDs are close together [34], or via the entanglement of photons which are themselves already entangled to an electron spin from each QD [35].

Coherence times of $\geq 1ns$ have been demonstrated for QD generated photons [36]. This far exceeds the necessary coherence time for photon based quantum gates such as a quantum relay [37] and allows for a coherence length on the order of centimetres, much further than is required for on-chip

photon routing. It has been shown that a universal set of quantum gates can be achieved by using just two types of gate: one single qubit gate and one two qubit gate [38]. Schemes for both single and multi-qubit quantum gates have been proposed for QD/photonic qubit systems, with some single qubit gates having been demonstrated experimentally, such as a CNOT gate [39]. Finally, readout from a III-V system is normally conducted via the measurement of a single photon emitted from a QD. Efficient photon routing via nanostructures and precise optical techniques provide a means to measure the output from individual qubits effectively and with high fidelity.

Turning our attention to Kimble's requirement for strong light-matter interaction, there have been numerous demonstrations of both weak and strong coupling between QDs and photons in III-V semiconductor architectures via integration with photonic nano-structures, such as optical cavities [40–44] and waveguides [45]. A recent review by P.Lodahl [32] discusses the requirements for a QD based quantum network and summarises the state-of-the-art QD based systems in this context. QD systems have shown excellent results of the basic functionalities required for a quantum network. QDs have been shown to perform extremely well as single photon sources, producing nearly perfectly indistinguishable photons [46] with exceptionally narrow linewidths [47] and ultra-high collection fidelity [48]. Photon-photon interactions are required to create a functioning quantum network. As single photons interact weakly in general, giant non-linearities are required to facilitate photon-photon interactions at the single photon level. QD systems have demonstrated such non-linearities in both cavity [49] and waveguide [50] geometries. Finally, experiments utilising QD based photonic architectures have been used to demonstrate techniques that have not yet been achieved in competing systems. Namely, deterministic entangled photon cluster states [51], resonance fluorescence squeezed light correlation detection [52] and photon boson sampling [53]. Recently, quantum advantage has been demonstrated for boson sampling in photonic systems giving further credibility to photons as a serious platform for a quantum network [54].

It is clear that III-V systems are an excellent choice for the realisation of a quantum network, as the DiVincenzo and Kimble criteria are met easily in principle, with promising experimental demonstrations of key basic operations for a quantum network and protocols only achieved in QD architectures, as outlined by Lodahl. Of course, the implementation of such schemes described above always prove to be extremely challenging and much effort has been expended in recent years towards the goal of a scalable III-V QD network.

1.3 Thesis outline

This thesis will present progress made towards the realisation of a III-V semiconductor based quantum network, with a focus on scale-up of resonant emitters and improving control over light-matter interactions. A brief introduction on the wider field (Chapter 1) will be followed by a more in-depth background of the operation of integrated photonic structures and III-V semiconductor QDs that

are used ubiquitously throughout the work in this thesis (Chapter 2).

The experimental and computational techniques employed in this work are detailed next including device fabrication and wafer growth techniques (Chapter 3). In Chapter 4, the effects of varying the nanohole array parameters and growth interrupt on the properties of site-controlled QDs is investigated. Moreover, multiple QDs are tuned into resonance in a nano-photonic waveguide. The tuning is achieved by altering the local strain field around each QD via the crystallisation of a thin layer of dielectric material that conformally coats the waveguide. A high power laser is used to heat the semiconductor membrane which in turn causes the dielectric membrane to be heated, inducing the crystallisation. The technique is performed '*in-situ*' whilst the sample is held at cryogenic temperatures. The behaviour of this technique is studied first, after this, the dependence of the tuning range and cumulative exposure time is investigated for increasing laser power and individual exposure window. The tuning range was compared for different dielectric deposition conditions to determine the optimal fabrication procedure and demonstrate the maximum tuning range observed. Multiple ensembles of QDs were tuned into resonance in photonic crystal waveguides over long and short tuning ranges.

The design of an electro-mechanically tunable nanobeam photonic crystal cavity is presented and optimised through simulation in Chapter 5. The wavelength of the cavity mode is tuned by the introduction of a perturbing beam in the evanescent field which alters the effective refractive index of the mode. This beam can be deflected out of the cavity mode field via a capacitive attraction between the membrane and substrate of the wafer. '*Finite Difference Time Domain*' (FDTD) simulations are used to conduct a comprehensive study of the cavity parameter space. The design is optimised through these simulations and the robustness of the design to fabrication imperfections is also tested using Monte Carlo simulations. The fabrication procedure is optimised through the creation of two cavity test samples. Finally, the first demonstration of an electro-mechanically tunable nanobeam photonic crystal cavity in Gallium Arsenide (GaAs) is demonstrated, exhibiting a tuning range larger than the standard deviation of mode wavelength distribution for like cavities.

Chapter 6 shows the design and experimental measurements of a photonic crystal waveguide coupled cavity demonstrating simultaneous strong light-matter interaction and directionality of photons. Strong light-matter interaction is an intrinsic property of all optical micro cavities. The directionality arises from interference from the two orthogonally polarised cavity modes causing asymmetric coupling of the modes to the photonic crystal waveguides. The design considerations are first discussed before results from a test sample of the cavity devices is presented. Lastly, results from a QD coupled to a cavity showing modest light-matter interaction enhancement and high directionality are presented and discussed.

Finally, Chapter 7 discusses the overall conclusions from the thesis and the direction of any further work.

This page intentionally left blank.

2 Background

2.1 Low dimensional III-V semiconductors

All the devices used in this thesis are fabricated from III-V semiconductor material. Before continuing onto more complex ideas, the properties and behaviours of the bulk semiconductor material should be discussed. As the name suggests, III-V semiconductors are alloys between elements in groups three and five of the periodic table. The term semiconductor refers to the conductivity of these alloys, falling between that of conductors such as metals and insulators such as dielectrics. In particular, this thesis will focus on Gallium Arsenide (GaAs) as the main semiconductor used. GaAs is a direct band gap semiconductor that forms a zincblende crystal structure [55] where each Ga atom has four As nearest neighbours and each As atom four Ga nearest neighbours as shown in Figure 3.

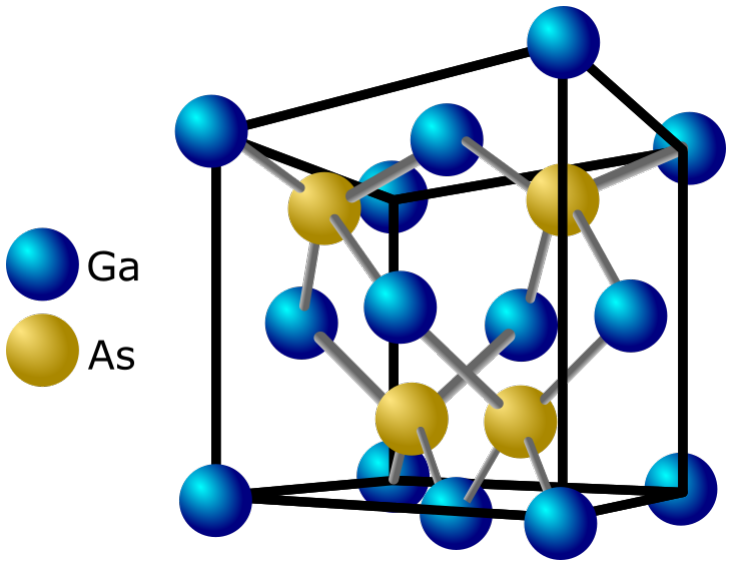

Figure 3: Image depicting the zincblende crystal structure of bulk GaAs semiconductor. Each Ga atom is covalently bonded to four As atoms in a tetrahedral arrangement. Likewise, each As atom is covalently bonded to four Ga atoms in the same tetrahedral arrangement.

An essential feature that must be considered when discussing any semiconductor is the band structure. The band structure of a semiconductor is a visualisation of the allowed energy levels available to charge carriers in the crystal. These bands arise due to the close proximity of neighbouring atoms in the crystal structure. The covalent bonds formed between the atoms are the cause of this close proximity. This causes the outer electron orbitals of the atoms to overlap, broadening the discrete atomic energy levels from that of a free atom into continuous bands. The electrons fill all available bands up to the Fermi energy which is defined by the electron density in the material. The band structure diagram contains two main features; the conduction and valence bands. The valence band

is the highest occupied band and the conduction band is the lowest unoccupied band. The amount of energy between these two bands is called the band gap, as seen in Figure 4. For semiconductors, the Fermi energy lies in the band gap leaving no states that electrons from the valance band can move to, save those across the band gap which are inaccessible as the energy of the band gap is much larger than the thermal energy available to charge carriers in the semiconductor.

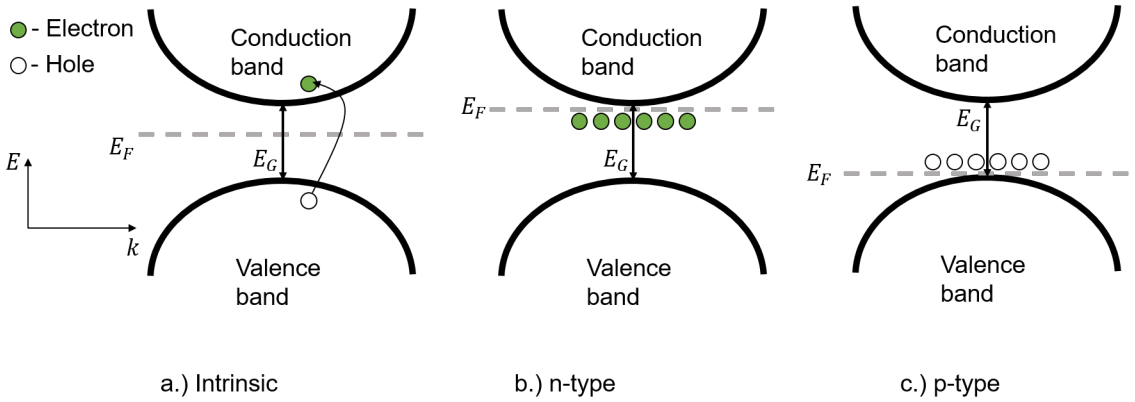

Figure 4: Simplified example of a semiconductor band structure showing the valence band, conduction band, band gap and Fermi energy for a.) Undoped(intrinsic) b.) n-type and c.) p-type semiconductor crystals. Electrons are shown in green and holes in white.

2.1.1 Doping of semiconductors

Pure GaAs has a band gap of $1.44eV$ at $297K$, this band gap can be altered by introducing impurities into the crystal with atoms from other elements. This procedure is called '*doping*'. Dopants fall into two categories: p-type and n-type dopants also called acceptors and donors. p-type dopants accept an electron from the bulk semiconductor introducing additional holes, whereas n-type dopants introduce additional electrons to the crystal; this allows for the creation of areas of semiconductor with higher concentrations of positive or negative charge carriers. The samples used in this work use Carbon atoms as p-type dopants and Silicon atoms as n-type dopants in GaAs. Doped semiconductors are essential for the creation of advanced semiconductor devices as they allow for the creation of electrically active devices via the formation of diodes.

2.1.2 p-i-n diode

The p-i-n diode is used extensively in this work to provide control over the electrical environment of embedded QDs in an optically active semiconductor by controlling the number of charge carriers that are injected into the intrinsic (un-doped) region. As the name suggests, the p-i-n diode consists of an intrinsic semiconductor region between p-type and n-type doped regions. Figure 5 shows the band structure of a p-i-n junction at both a zero external bias and in reverse bias (the magnitude of the applied external bias is negative). As the intrinsic region is highly resistive when compared

to the heavily doped p and n regions the external bias drops rapidly over the intrinsic region. This creates a depletion region across the intrinsic region of the diode, a region devoid of charge carriers [56]. From Figure 5 the Fermi energies of the p and n regions are equal, this equates to a voltage

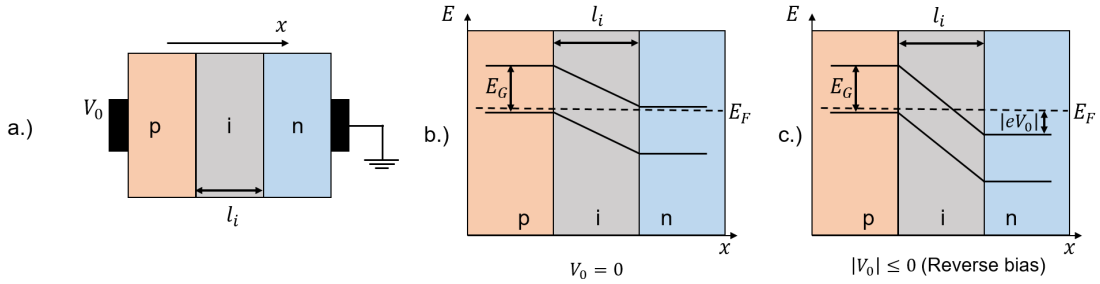

Figure 5: a.) Schematic of a p-i-n junction showing the distinct doped and intrinsic layers. b.) The band structure for a p-i-n junction at zero external bias. c.) The band structure for a p-i-n junction in reverse bias, showing the depletion region created by the highly resistive intrinsic region between the heavily doped p and n regions.

drop of E_G/e over the intrinsic region which is the built-in bias (V_{bi}) of the diode. When an external bias V_0 is applied to the diode the Fermi energies of the p and n regions are split by eV_0; as seen in Figure 5 in reverse bias such a splitting increases the bias across the intrinsic region of the device. The magnitude of the electric field across the intrinsic region is given by:

$$\mathcal{E} = \frac{V_{bi} - V_0}{l_i} \tag{1}$$

where l_i is the thickness of the intrinsic region in natural units.

If QDs are embedded in the intrinsic region of the p-i-n diode then a controllable electric field can be applied across them allowing for the tuning of the QDs' emission energy and the control of charge state emission (see Section 2.3.1).

2.1.3 Quantum confinement

In a bulk semiconductor system, the band structure and density of states are continuous. This allows for charge carriers to move freely around the material and access a continuum of energy states. These energies are given by the dispersion relation for a free particle:

$$E = \frac{\hbar^2 k^2}{2m} \tag{2}$$

Where k is the wavevector and m is the mass of the charge carriers in the semiconductor. As the physical dimensions of the semiconductor crystal are reduced, so is the number of available states for charge carriers to occupy. As the dimensions of the crystal becomes smaller than the De

Broglie wavelength of the charge carriers in a given dimension (x, y or z direction), the confinement of charge carriers becomes so strong that the density of states is altered and only specific energy states are able to be occupied by the charge carriers. This is known as quantum confinement. Depending on how many dimensions are strongly confined, the density of states and energy levels in the system are altered as shown in Figure 6. As expected, the density of states decreases with

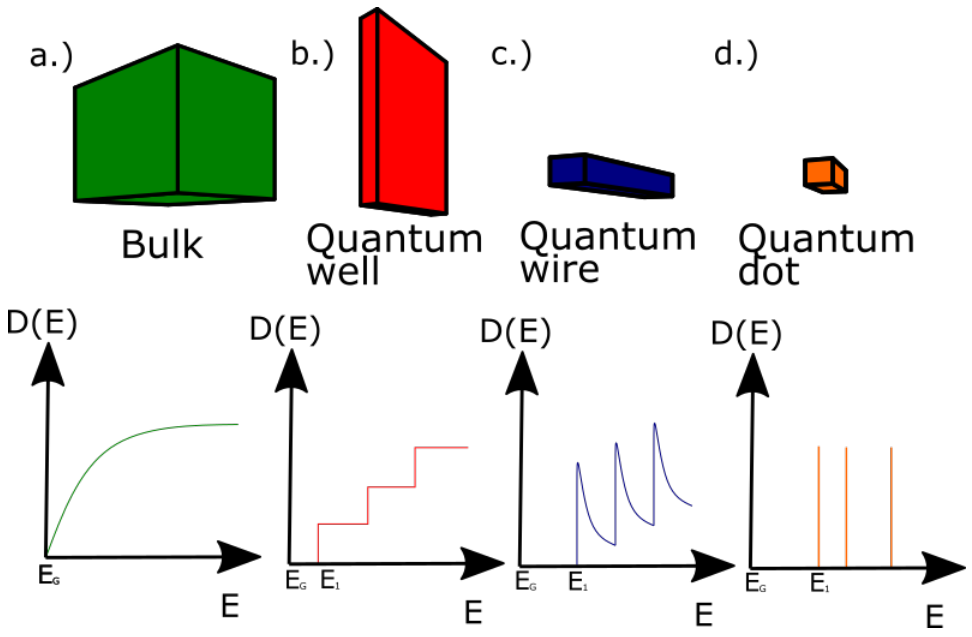

Figure 6: Comparison of the density of states and corresponding energy levels for a.) Bulk semiconductor b.) 1D confinement (quantum well) c.) 2D confinement (quantum wire) d.) 3D confinement (quantum dot).

increasing number of quantum confined dimensions. When all three dimensions are confined, the density of states reduces to a set of discrete delta functions, analogous to the energy levels in atomic shells. These 3D confined nano-crystals are called quantum dots (QDs) and will be discussed in detail during the next section.

2.2 Semiconductor quantum dots

Semiconductor QDs are nano-scale structures that provide three-dimensional quantum confinement of charge carriers into discrete energy levels, analogous to the behaviour of shells in atomic physics, while embedded in a bulk semiconductor. QDs have highly favourable properties which make them excellent candidates for qubits such as extremely pure single photon emission [57], easily addressable states leading to fast spin initialisation [28] and long coherence times [36].

2.2.1 Quantum dot growth

The QDs used in this thesis are self-assembled Indium Arsenide (InAs) QDs embedded in a GaAs bulk crystal. '*Molecular Beam Epitaxy*' (MBE) [18] was used to deposit the atomic layers used to form both the GaAs substrates and InAs QDs for this thesis. Atomic monolayers of InAs are deposited by thermal evaporation atop a GaAs substrate under an ultra-high vacuum. As the lattice constants of InAs and GaAs differ by 7%, each additional layer of InAs introduces more strain energy to the system. Eventually, a critical energy is reached (usually around two monolayers thick) and the strain is relaxed by the InAs nucleating into 3D islands (QDs) on top of the thin InAs layer deposited previously, this thin layer is known as the '*Wetting Layer*' (WL). More GaAs is then deposited on top of the QDs ('*overgrowth*') to prevent the islands from growing further thus creating the 3D confinement. The QDs grown via this strain relaxation process are known as '*Stranski-Krastanow*' (SK) QDs [58]. As the nucleation process by which the QDs self-assemble is random, a distribution of QD sizes (and therefore emission energies) are produced. This distribution is intrinsic to SKQDs. Moreover, the QDs are positioned randomly and non-uniformly across the substrate. These properties can be altered by changing the growth conditions such as the reactor temperature and rate of material deposition. However, it is currently still impossible to grow QDs of an exact desired energy and location via SK growth. This presents a major challenge in the scale-up of QD based QIP devices as multiple resonant QDs within nano-photonic structures are required to facilitate multiple qubit gates. There has been an increasing effort to control the spatial aspect of QD growth randomness via site-controlled growth. These methods are still under development and currently results for site-controlled QD growth compatible with free-standing waveguide architectures show larger linewidths than non-site controlled QDs with success rates up to 90% [59, 60]. While the success rate is high, the broad linewidths of the QDs are undesirable. The site-controlled growth of QDs is discussed in Section 2.2.3 and further in Section 4.2.

2.2.2 Optical properties

The energy levels in a SKQD can be approximated by a parabolic confinement potential in the growth direction [61]. This, coupled with the shape of SKQDs (much wider than they are tall) gives rise to circularly symmetric harmonic wavefunctions for in-plane orbitals [62]. This is analogous to the sub-shells in atomic physics and so can be labelled as such (s, p, d...). This work will focus on the lower energy levels only (s and p) as charge carriers in the higher energy levels quickly relax down to lower levels via phonon emission, as the available thermal energy is much smaller than the inter-band transition energy at cryogenic temperatures.

When an electron is excited across the band gap from the valence to the conduction band, the strong confinement of the charge carriers in the QD causes the electron and newly created hole to attract each other via the Coulomb interaction, forming a bound state called an '*exciton*'. As

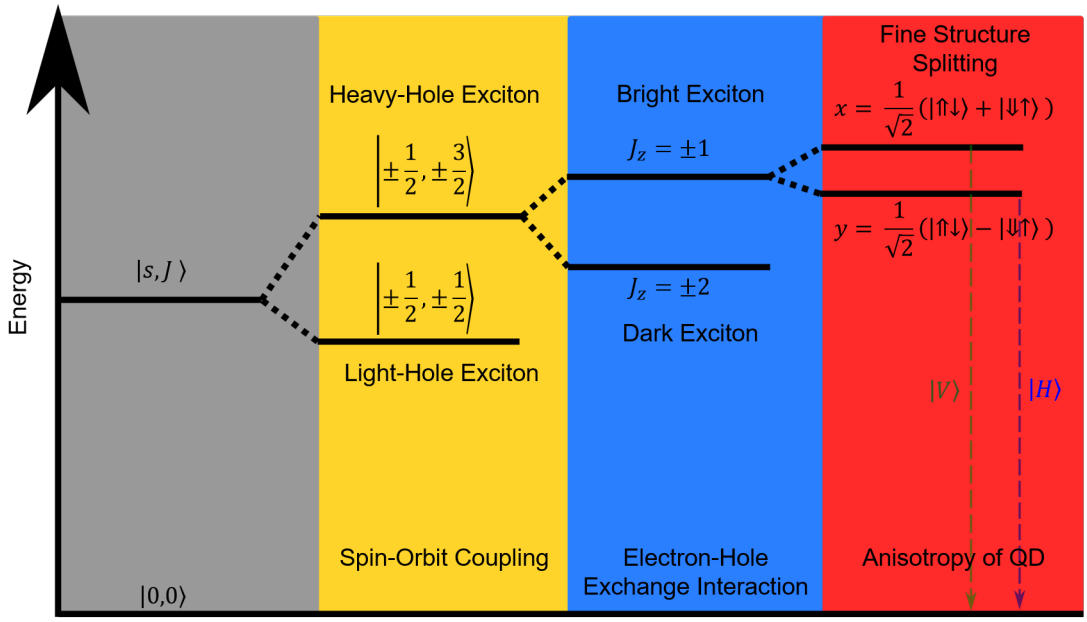

Figure 7: Graphic showing the neutral heavy hole exciton states in a QD. The fine-structure states emit orthogonally polarised photons to relax to the ground state. ($|H\rangle, |V\rangle$). The dark exciton states can be accessed via a spin flip transition from the bright states. The bright states can also decay to a single electron or hole state non-radiatively via phonon emission.

electrons and holes are fermions (spin $\frac{1}{2}$ particles) each discrete energy level can only be occupied by two charge carriers of opposing spin. The total angular momentum of charge carriers **J** is given by:

$$\mathbf{J} = \mathbf{L} + \mathbf{S} \tag{3}$$

where **L** is the orbital angular momentum and **S** is the spin angular momentum. The corresponding eigenvalues are $|l-s| \leq J \leq |l+s|$ [63]. When considering the conduction band, the lowest energy level has an s type wavefunction which equates to $\mathbf{L} = 0$, therefore, there are two allowed states with $|\mathbf{S}| = s_z = \pm\frac{1}{2}$. In the direction of growth (z direction) this gives values of total angular momentum of $J_z = \pm\frac{1}{2}$. The electron can exist in either a spin up or spin down state in the z direction leading to two available spin states $m_z = \pm\frac{1}{2}$.

The valence band has p type wavefunctions giving a value of $|\mathbf{L}| = l = 1$. This coupled with the inherent $s = \frac{1}{2}$ component splits the valence band into two states with $J = \pm\frac{1}{2}$ or $\pm\frac{3}{2}$. Looking at the z direction as before, the available angular momentum for holes in each of these states is $J_z = \pm\frac{1}{2}$ for $J = \pm\frac{1}{2}$ and $J_z = \pm\frac{1}{2}, \pm\frac{3}{2}$ for $J = \pm\frac{3}{2}$. These two states are separated by the spin-orbit splitting energy which for GaAs is $0.3eV$ [63]. These two bands are known as the heavy and light hole bands. These bands are ordinarily degenerate at $k = 0$ however, due to the strain present

in SK grown QDs, the degeneracy is lifted by a splitting on the order of 10's of meV [64]. For simplicity, only the heavy hole band is considered in this thesis. Figure 7 shows the states available for the most simple case, a neutral exciton. This allows for the approximation of the energy levels in a QD as a two level system between the heavy hole valence band and the conduction band.

The simplest exciton that can form in a QD is the neutral exciton (X_0) consisting of a single electron hole pair as mentioned above. The neutral exciton is split into four spin states, formed from the superposition of the individual heavy hole and electron spin states. These four states are themselves grouped into the bright states:

$$|Y_b\rangle = \frac{1}{\sqrt{2}}(|\Uparrow\downarrow\rangle + |\Downarrow\uparrow\rangle) \tag{4}$$

$$|X_b\rangle = \frac{1}{\sqrt{2}}(|\Uparrow\downarrow\rangle - |\Downarrow\uparrow\rangle) \tag{5}$$

and the dark states:

$$|Y_d\rangle = \frac{1}{\sqrt{2}}(|\Uparrow\uparrow\rangle + |\Downarrow\downarrow\rangle) \tag{6}$$

$$|X_d\rangle = \frac{1}{\sqrt{2}}(|\Uparrow\uparrow\rangle - |\Downarrow\downarrow\rangle) \tag{7}$$

The bright states have $J_z = \pm 1$ allowing them to relax to the ground state via the emission of a photon. Conversely, the dark states cannot relax to the ground state in this way as the transition is optically forbidden, this is due to the dark states having $J_z = \pm 2$; as a photon can only itself have a total angular momentum of ± 1, angular momentum cannot be preserved when transitioning from the dark states to the ground state which has $J_z = 0$ [65].

In a symmetrical QD the bright exciton eigenstates are degenerate, however, due to the asymmetric shape of SK grown QDs the degeneracy is lifted by the exchange interaction. This is known as '*fine-structure splitting*' (FSS). The magnitude of the FSS is usually 10-100 μeV for the bright states [66], the dark states are split by a much lower energy ($1\mu eV$) [67]. As discussed previously, there exist two bright exciton states with $J_z = \pm 1$; the charge carriers in these two states have opposing spins and so can exist together in the QD, this configuration is known as the '*biexciton*' state.

The optical behaviour of QDs as outlined here shows clearly that QDs produce highly anti-bunched light (see Section 2.6) and are therefore a source of pure single photons. This trait is exceptionally important for QIP applications and shall be explored further later in this chapter.

2.2.3 Site-controlled quantum dot growth

The random distribution in both position and emission energy of SKQDs is a side-effect of the growth process; this randomness makes it nearly impossible to consistently create like devices using QDs. Therefore, any amount of control over the spatial or spectral properties of QDs is

extremely desirable. As a result, there has been extensive research into techniques which could improve the spatial and spectral control over QD growth. One such technique is attempting to control where QDs nucleate on the substrate by manipulating the substrate surface prior to QD growth. QDs grown by this approach are called '*Site-Controlled Quantum Dots*' (SCQDs).

The SCQDs in this thesis were grown using a pre-patterned 2D array of nanoholes in which single QDs preferentially nucleate. This is due to the nanoholes having a lower chemical potential that the surrounding planar material, which increases indium flux towards the nanoholes. The shape of the holes also provides a surface on which QDs preferentially nucleate. Early attempts at this approach involved stacking multiple layers of optically inactive QDs above the nanoholes before growing the optically active QDs [59]. This was done to distance the QDs from the interface with the nanoholes to reduce the inhomogeneous broadening of the linewidth of the QDs whilst maintaining the definition of the site. However, the drawback of the large buffer and stacked QDs is the extremely limited control over the shape and nucleation of the QDs that this method exhibits. More recent progress in the technique removed the need to stack multiple layers of QDs. Instead, optically active QDs can be grown directly in the nanoholes while maintaining decent QD linewidths, reducing the overall thickness of the wafers [59]. This improvement in single layer SCQD growth was largely attributed to the ultra-clean regrowth process. This process greatly reduces the number of contaminants close to the growth surface that would cause performance degradation. The QDs used in this thesis were grown with a 30nm buffer layer between the nanoholes and the QDs (as shown in Figure 8), and exhibited linewidths as narrow as 27μeV with a single hole occupancy rate of 70%.

Naturally, these SCQDs do not show as narrow linewidths as SKQDs, which can show transform limited linewidths [47]. However, the high single occupancy success rate coupled with decent linewidths makes SCQD a promising avenue for scale-up of QD based devices. Currently, SCQD have only recently been demonstrated in free-standing membrane devices. As a result, the linewidths of these SCQDs are much broader than what is measured for SCQDs in bulk material. For SCQDs to be useful for QIP devices the narrow linewidth results shown thus far must be reproduced in free-standing membranes.

2.3 Quantum dot emission energy tuning

As mentioned in Section 2.2.1, the growth process of SKQDs is inherently random and produces a distribution of QD emission energies and spatial positions. This poses a challenge when attempting to interface multiple resonant QDs in the same nano-photonic structures. There is no way to ensure that if multiple QDs are in the correct spatial location that they have the same emission energy. Therefore, scalability of QD based QIP devices is a major roadblock to the success of such devices. However, much effort has been devoted to overcoming this issue and as a result, multiple viable methods exist that allow for either the controllable tuning of the emission energy of QDs or for

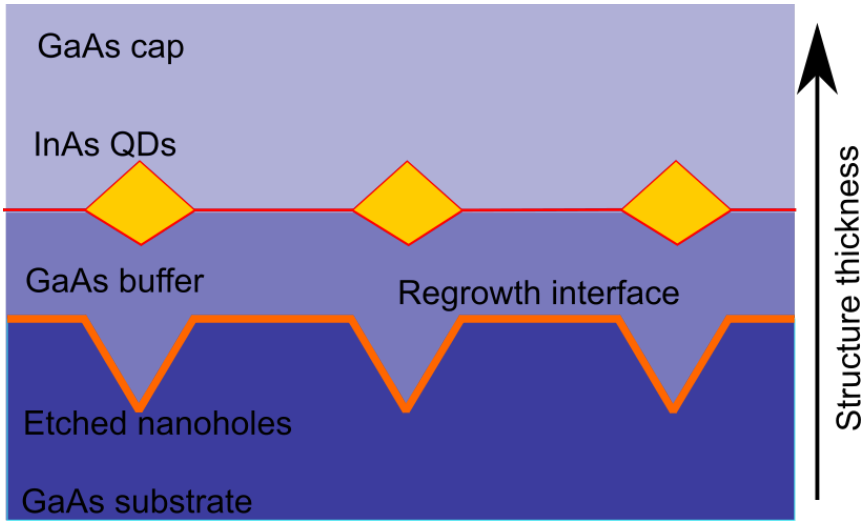

Figure 8: Cross-sectional schematic of a SCQD wafer showing the material layer structure and features. Nanoholes are etched into the GaAs substrate which is then cleaned thoroughly to remove any contaminants from the regrowth interface before a GaAs buffer layer is grown on top of the nanoholes. The QD layer is deposited directly above the buffer, QDs preferentially nucleate at sites above the etched holes. The sample is capped with another layer of GaAs to prevent oxidation of the QDs.

spatial control of the QDs. These methods shall be discussed here.

2.3.1 Quantum-confined Stark effect

Applying a DC electric field to an exciton in a semiconductor causes the electron and hole to be pushed away from each other as they have opposite electric charges. For a free exciton (in bulk material) if the applied field strength from Equation 1 '$\mathcal{E}$' exceeds the binding energy of the free exciton then the exciton will dissociate. This can be visualised by looking at the band structure diagram under an electric field such as in Figure 5. Under a non-zero electric field the bands are no longer flat, this causes charge carriers to travel along these sloping bands towards a lower energy state. As the electron and hole have opposite charges they will travel in opposite directions, thus dissociating. However, quantum confinement gives extra stability to excitons in QDs allowing for higher fields to be applied. This is visualised in Figure 9. The reduced band gap of the QD compared to the bulk semiconductor help to more strongly confine the electron and hole wavefunctions, allowing for larger electric fields to be applied. Therefore, the exciton energy can be shifted by a larger amount before the exciton dissociates. This energy shift by applying an eletric field is called the '*Quantum-Confined Stark Effect*' (QCSE). The magnitude of the QCSE energy shift is given by:

$$\Delta E = pF + \beta F^2 \tag{8}$$

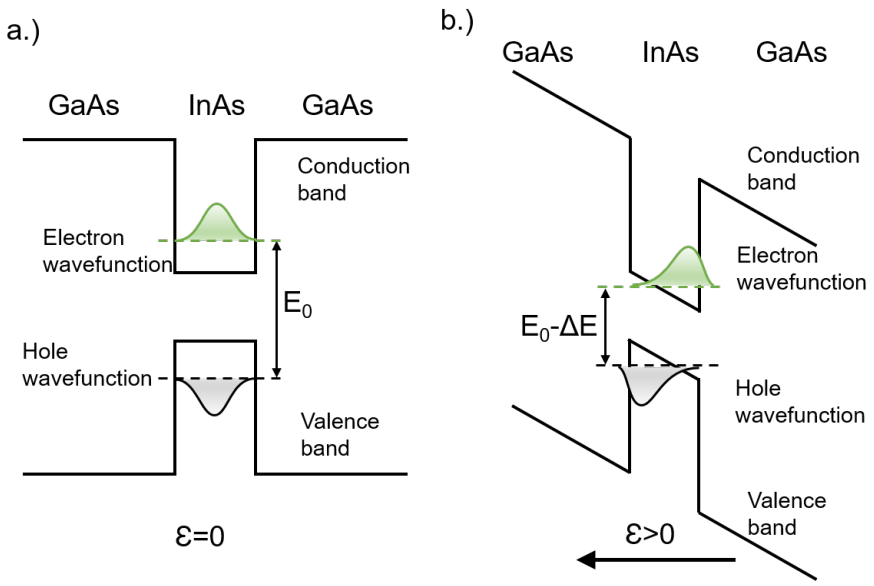

Figure 9: Visualisation of QCSE altering the emission energy of a QD. Applying an electric field across the QD causes the energy bands to slope, forcing the electron and hole wavefunctions closer together as the energy levels in the conduction and valence band are shifted to lower energies. This reduces the energy gap between the electron and hole thus reducing the QD's emission energy.

where p is the electric dipole moment of the QD, β is the polarisibility and F is the strength of the applied DC field. By carefully adjusting the applied field the energy of the QD can be precisely tuned. The maximum range observed for QCSE tuning of QDs is 25meV. To achieve this large range the QDs were grown inside quantum wells to further increase the exciton confinement [68]. The quantum wells were grown from Aluminium Gallium Arsenide (AlGaAs) which has a much larger band gap than GaAs, this raises the potential barrier between the InAs QDs and the bulk material. Without the extra confinement of the quantum wells the exciton would dissociate at the high magnitude electric fields required for such a tuning range due to the electron and hole tunnelling through the potential barrier and out of the QD. Quantum well layers used to increase the QCSE tuning range of QDs are referred to as '*barrier*' layers. For the structures and QDs studied in this thesis the observable tuning range was on the order of $0.10meV$ [69]. This largely reduced tuning range is due to the absence of large AlGaAs barriers in the wafers reducing the potential the charge carriers must overcome to tunnel from the QDs. Moreover, the QDs are situated in free-standing waveguide devices far from the electrical contacts. This increases the electrical resistance around the QD, reducing the effective voltage at the QD's location, therefore, reducing the tuning range. At larger fields the QD emission is also quenched by QCSE due to the large separation between the electron and hole wavefunctions [70]. The QCSE will tune all QDs that are in a p-i-n diode that has an applied bias. It has been shown that by etching an isolation trench through the p-layer of the diode, different bias' can be applied to different areas of the sample, allowing for independent

tuning of the QDs in these areas [71]. This increases the likelihood of being able to use the QCSE to tune multiple QDs into resonance in a device. The QCSE can also be used to tune/detune a QD from a laser line or cavity mode allowing for switching between resonant and off resonant excitation or cavity coupling.

2.3.2 Zeeman splitting and magnetic field tuning

Applying an external magnetic field across a QD increases the FSS between the energy levels, this is known as the '*Zeeman effect*'. The magnituide of the splitting is given by:

$$E_Z^i = g^i \mu_B B \tag{9}$$

where i is the (quasi)particle in question (e, h, or X for electron, hole or exciton respectively), g is the Landeé g-factor, μ is the Bohr magneton and B is the magnetic field strength. The magnitude of this splitting is around $1.2meV$ at a magnetic field strength of $B = 8T$, with the two states $0.6meV$ from the zero magnetic field case [72]. This energy shift is small even for large fields and individual QDs cannot be tuned independently of the ensemble. Therefore, magnetic field tuning is not a popular choice for pure tuning purposes.

Depending on the orientation of the magnetic field, either in plane (Voigt) or out of plane (Faraday) geometry, the optical selection rules and fine-structure are altered [73]. In Faraday geometry, the linearly polarised neutral exciton states (See Figure 7) become circularly polarised. The applications of this include high fidelity spin initialisation [74] and entangled photon pair production [72].

For Voigt geometry the bright and dark exciton states can become mixed and poorly defined, thus single carrier and trion states (an exciton and a single carrier) are more easily accessed. Voigt geometry has important uses in coherent control of spin states [75], a requirement for building a universal set of quantum gates.

2.3.3 Strain tuning

As discussed in Section 2.2.1, SKQD growth is a strain relaxation process, thus the QDs grown by this method have an intrinsic strain field across them. By altering this strain field, the strength of the Coulomb interaction between the electron and hole can be altered. More specifically, the confinement of the electron and hole wavefunctions is altered by the change in the strain field. This is due to the change in strain affecting the band gap of GaAs and InAs differently. Not only does this change the band gap of the QD but also the relative energy difference between the QD and its environment, thus changing the confinement of carriers in the QD [76]. Under compression the confinement of the electron wavefunction is increased and the confinement of the hole wavefunction decreases slightly; this results in an overall blue-shift of the exciton energy [77]. This effect is visualised with a band diagram in Figure 10. Depending on the orientation of the applied strain

field the FSS can also be affected. The FSS is caused mainly by the asymmetry of SKQDs, which are much wider than they are tall. By compressing the QDs perpendicular to the growth direction this asymmetry is reduced and thus the FSS is reduced also [78].

The magnitude of the emission energy tuning is dependent on the direction of the applied strain,

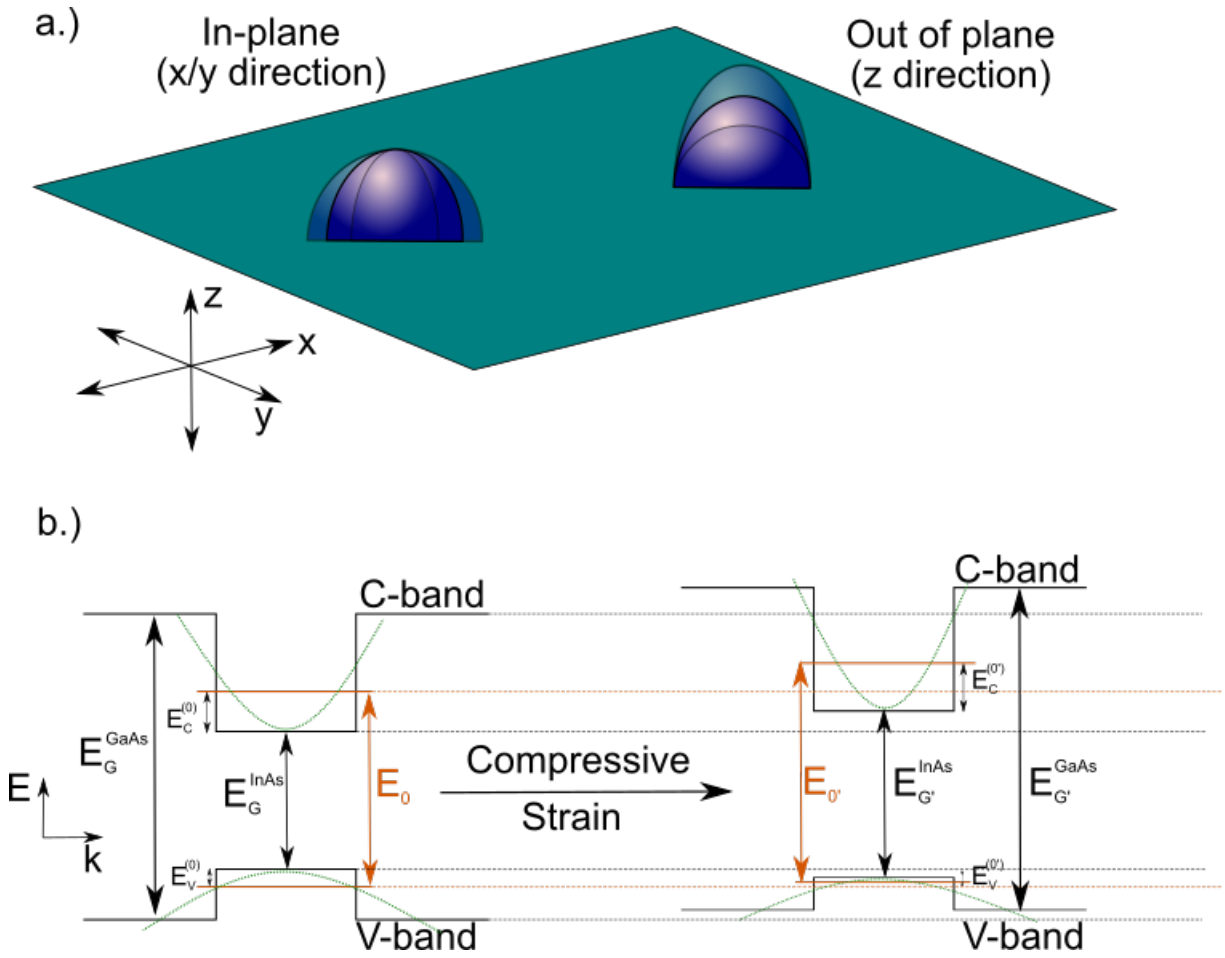

Figure 10: a.) Schematic of the two strain configurations available for strain tuning of QD emission energy. The left shows in-plane strain and the right shows out-of-plane strain. b.) The change in band structure caused by applying a compressive strain. The band gaps of both GaAs and InAs are both altered. The change in the InAs emission energy directly affects the binding energy of the exciton and therefore the emission energy; moreover, the change in band gap for GaAs and InAs is not equal, as such the potential barrier experienced by the exciton is altered. This change in potential changes the confinement of the exciton which leads to a shift in excitation energy. Additionally, for the in-plane case, the FSS between exciton spin states is altered due to the change in the QD asymmetry.

as explained above. The FSS is only altered when strain is applied perpendicular to the growth

direction (in-plane). In both cases, compressive strain blue-shifts the emission energy of the QD and tensile stress red-shifts the emission energy.

Strain tuning has been successfully implemented using several different approaches in the literature. A popular approach is to use piezo-electric actuation to controllably and reversibly deform the semiconductor wafer containing the QDs [77–80]. The advantages of this technique are the reversible nature of the tuning and the controllability of the tuning magnitude via adjusting the voltage across the piezo stack. Tuning ranges of up to $5.8meV$ have been demonstrated using this technique however, this was achieved using an unconventional '*flip-chip*' method where the devices are separated from the substrate [79]. For a more typical sample, tuning ranges of up to $2.5meV$ are observed [80] with incredibly fine control (on the order of pm per piezo step). This approach is popular due to its ease of implementation for a relatively large tuning range, high precision and ability to also tune cavity modes. However, the drawbacks of this method are that individual QDs cannot be tuned independently and the high strain fields exerted across high quality nano-structures may degrade their performance due to their sensitivity to feature dimension changes.

An alternative approach to the piezo actuation method is to use a high powered laser to create localised defects which alter the local strain of a desired area. This method has been demonstrated in micro-pillar cavities. A hole was burned into the top of the micro-pillar cavity by a tightly focused laser, causing the QD emission to red-shift [76]. This method yields a reduced tuning range of up to $0.5meV$ but can be localised to a desired area of the sample and does not degrade the performance of the cavities in which the QDs are situated. This technique has the obvious advantage of being able to tune multiple QDs independently, allowing for multiple QDs to be brought into resonance across the sample. This approach is limited as QDs within the same device cannot be tuned independently. This technique has only been demonstrated in micro-pillar cavities and not in free-standing waveguide structures, a requirement for building complex QIP circuits on-chip.

Recently, a modification of the laser heating approach to strain tuning has been demonstrated in free-standing waveguide structures [81]. In this approach the waveguide structures are conformally coated in a thin film Hafnium Oxide (HfO_2), a dielectric material. When a high power laser is incident on the waveguide the resulting heating causes the HfO_2 to crystallise which reduces its volume thus squeezing the waveguide and inducing compressive strain. Tuning ranges of up to $65meV$ have been demonstrated with a high degree of precision. This approach will be covered in more detail in Chapter 4. The main disadvantage of the laser based tuning methods are that they are not reversible and as such cannot be used for tuning QDs on and off resonance reversibly. This can be overcome by combining the strain tuning with an additional reversible tuning method such as QCSE or magnetic tuning.

2.3.4 Temperature tuning

All experiments performed on InAs QDs are performed at cryogenic temperatures (∼4K), as at higher temperatures the thermal energy of the carriers is greater than the confinement potential of the QDs, causing the carriers to escape. Moreover, the band gap of GaAs is reduced with increasing temperature. However, if the temperature of the sample is increased a small amount so that the thermal energy of the carriers is still much lower than the confinement energy, the confinement of the wavefunction and the band gap of the material are reduced and the emission energy of the QD red-shifts. Thermal tuning of QDs has been demonstrated using a high powered laser and dedicated heating pads on the sample to enable the temperature of the sample to be controlled via the laser power [82, 83]. This thermal tuning approach has a reported tuning range of up to $600\mu eV$. This range is limited by the degradation of the optical properties of the QDs with increasing temperature. The intensity of the QD emission is reduced and the linewidth broadened by high temperatures due to an increased phonon population. This method has been successfully used to tune two QDs into resonance in a waveguide [83].

2.3.5 Quantum dot registration

While all the previous approaches to realising resonant QDs involve tuning QDs found in pre-fabricated structures, one can also reverse this and locate suitable QDs first before fabricating devices around them. This approach is known as QD registration [84].

One of the key advantages of QD registration is that no specialist equipment or techniques are required, only a simple '*Micro-Photoluminescence*' (μPL) set-up is needed. On a bulk chip, etched markers are used to designate an area in which QDs will be registered. These markers also provide a positional reference for any QDs registered within the area. Typically the markers are either a series of crosses on each corner of the registration area or sets of lines along each face as shown in Figure 11. By scanning a laser across these macroscopic markers the registration can be calibrated to high precision in the two cardinal directions.

A PL map of the registration area is then acquired using an above band gap laser rasta-scanning across the area and the positions of QDs are recorded relative to the etched markers. The measured QDs can then be filtered for their desired features such as narrow linewidths and resonant wavelengths. When suitable QDs have been located roughly using the rasta scan the accuracy of the measurement is increased by repeated line scans over both the registration markers and candidate QD in both cardinal directions. This repeated measurement averages out any statistical fluctuations that may occur during any one scan.

Nano-photonic devices are then fabricated around the registered QDs. As the position of the

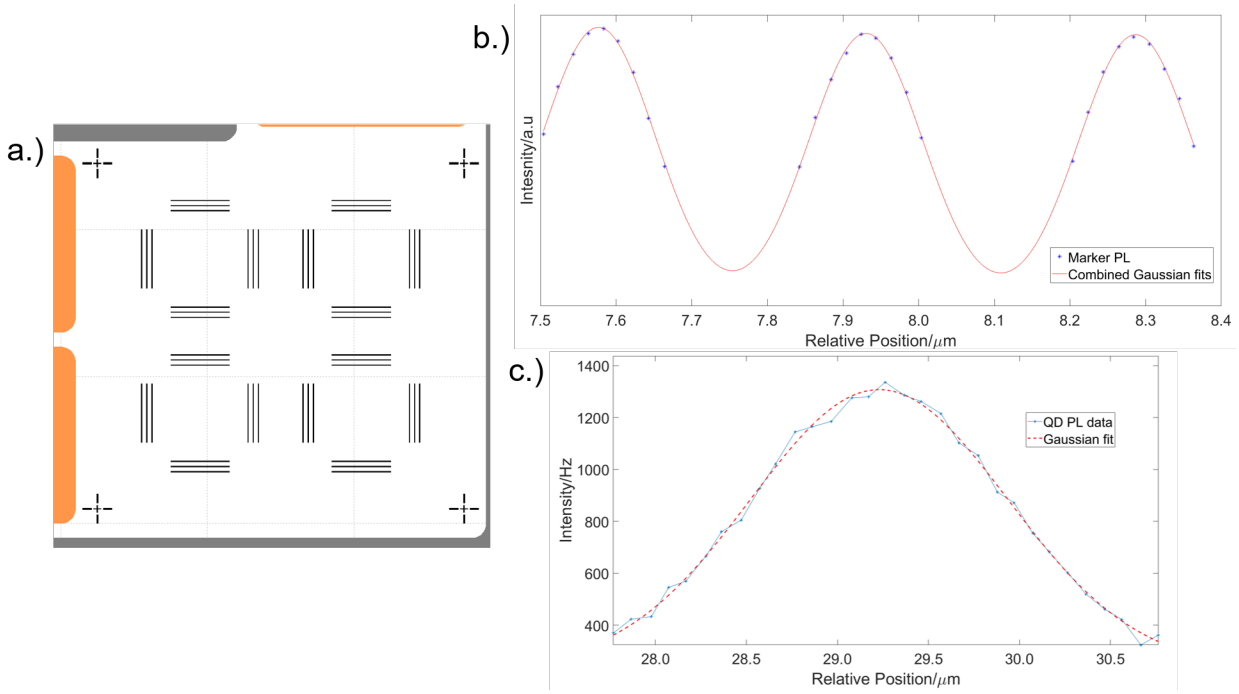

Figure 11: a.) Schematic showing four registration areas, each bounded by four sets of three parallel etched markers. Multiple lines are used on each face to increase the precision of the calibration and therefore the QD position registration. The crosses seen on the edges of the image are electron-beam lithography (EBL) alignment crosses for the etched markers themselves. b.) PL linescan over one set of markers used as a reference to align to when locating and fabricating around QDs. c.) Typical linescan over a single QD line, due to the spatial resolution of the laser the feature is very broad, however, the peak position is well defined.

QDs is known to a high precision, (the standard deviation on registered QD position can be as low as $\sigma = 5nm$ [85]) the devices can be carefully designed and positioned to incorporate the QDs at an exact spatial location in a device to maximise phenomena linked to the spatial position of QDs inside said structures such as the Purcell effect(see Section 2.5) or chiral contrast(see Section 2.7).

This technique has been used to position single QDs in photonic crystal cavities [40] and at chiral points in a nanobeam waveguide [85]. However, there have thus far been no successful demonstrations of multiple registered QDs resonant in a nano-photonic structure. Despite the high precision of the registration process the accuracy of the measurement is reduced by mechanical drift of the scanning stages during the long process of repeated linescans. Moreover, the imperfect accuracy of the device fabrication process further reduces the overall accuracy of the registration process. The process has a reported success rate of around 70% for positioning single dots [40].

Alternatively, recent developments have removed the need for rasta-scans improving the accuracy of

the registration. This is achieved by using a wide-field excitation via an above band '*Light-Emitting Diode*' (LED) to excite the whole registration region. A high-resolution CCD camera is then used to image the PL from all of the QDs in the area [86]. A tunable narrow bandpass filter is used to select a small window of PL so that individual QDs can be resolved on the camera. This method shows an improved positioning success rate of up to 96% [87].

One downside of QD registration comes from the fabrication of photonic structures around the registered QDs. Changes in the electrical and strain environment around the QDs occur after structures are etched around the QDs. This can cause the spectral properties of the QDs to change. Therefore, even if two QDs are resonant when registered, the fabrication of structures around the QDs can cause them to become off resonance. Because of this, QD registration is normally used alongside conventional tuning methods such as electrical or magnetic tuning in order to account for this unavoidable and unpredictable fabrication related shift.

2.4 Nano-photonic structures

To effectively take advantage of QDs as qubits for QIP light must couple efficiently to and from the QDs. Moreover, several advantageous behaviours exhibited between photons and QDs can only be seen when the QD resides in a specific photonic environment. Embedding QDs in nano-photonic structures allows for highly efficient coupling of light to and from QDs as well as off chip. Furthermore, due to the wealth of available fabrication techniques, precise control over these structures and therefore the environments of QDs is possible.

A broad range of photonic structures have been developed for use in quantum optical QIP including optical waveguides [24, 85, 88] and cavities [24, 26, 39], interferometers [89], phase shifters [90], resonators [91, 92], single photon sources [20, 57] and on/off chip light couplers [24, 25]. These structures are free-standing allowing for light to be confined far away from the semiconductor substrate.

In general, there are two main categories of nano-photonic structures depending on how light is confined within them: structures which use '*Total Internal Reflection*' (TIR) to confine and route light and structures that use both TIR and optical band gaps. Due to the high refractive index contrast between GaAs ($n \sim 3.4$ at 4K) and air ($n \sim 1$), which is used as the cladding for GaAs nano-photonic devices, the critical angle is low ($\sim 17°$). Therefore, the majority of the light emitted by an embedded emitter in the waveguide is confined by TIR making GaAs an intrinsically low loss medium for wavelengths of light $> 1000nm$. For longer wavelength photons, GaAs becomes transparent.

2.4.1 Nanobeam waveguides

The simplest nano-photonic structure that can be created is a narrow free-standing beam often called a bridge or '*Nanobeam Waveguide*' (NBW). The performance of optical waveguides can be

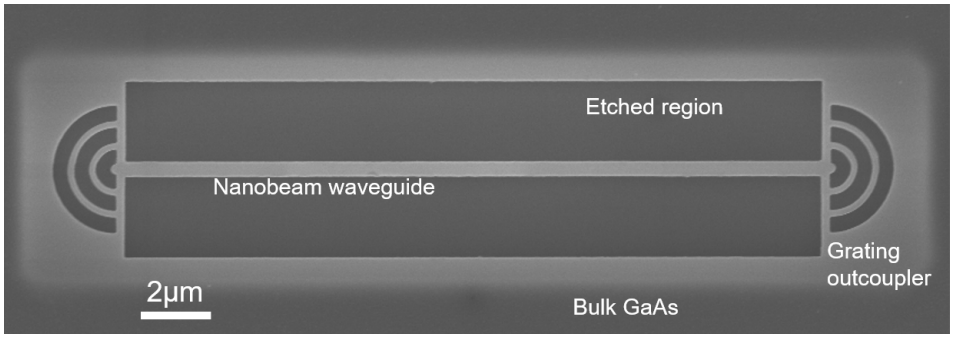

Figure 12: Top down scanning electron-microscope image of a suspended GaAs nanobeam waveguide between two $\lambda/2n$ grating outcouplers. The area either side of the beam has been etched away leaving a large air gap to separate the bulk material (seen at the top and bottom of the image) from the waveguide. Similarly, the material below (AlGaAs) has been etched away using hydrofluoric acid (HF) to create a free-standing waveguide.

quantified via the β factor, which describes the rate of light coupled from an embedded emitter into a single optical mode in the waveguide compared to the recombination rate by all possible decay processes [93].

$$\beta = \frac{\gamma_{wg}}{\gamma_{wg} + \gamma_{ng} + \gamma_{nrad}} \tag{10}$$

The β factor is given by Equation 10 where γ_{wg} is the rate of light coupled to the waveguide mode, γ_{ng} is the rate of light coupled to non-guided modes and γ_{nrad} is the rate of non-radiative recombination. For a nanobeam waveguide the β factor is fundamentally limited by the critical angle between GaAs and air but values as high as $\beta = 0.8$ have been demonstrated recently in a structure designed to maximise β [94]. For more typical nanobeam designs such as that shown in Figure 12 the β factor is lower, $\beta \sim 0.5$ [95]. Nanobeams are one of the most important nano-photonic structures due to their simplicity and versatility. Often they are used to route photons between more complex structures or into grating outcouplers so the light can be efficiently collected off chip.

The waveguides used in this thesis are 170nm thick GaAs waveguides. By adjusting the width of the waveguide the modes supported by the waveguide are altered. For most experiments in this thesis 280nm wide waveguides are used, this ensures only a single TE guided mode is allowed in the waveguide.

2.4.2 Grating output couplers

While many QIP protocols can be done on-chip, it is important to be able to efficiently extract the light off-chip as optical manipulation and detection of photons largely occurs off-chip. Most optical set-ups utilise top down excitation and collection of light. Therefore, a structure is needed that can route photons from the guided waveguide modes vertically towards the collection optics. A popular design for such a structure is the $\lambda/2n$ or semi-circular grating '*Output Coupler*' (OC) as seen at the ends of the nanobeam in Figure 12 [96]. These gratings consist of several concentric semi-circular rings (normally 3/4) radiating out from the end of a waveguide with a period of $\lambda/2n$. This choice of period provides maximal vertical scattering whilst minimising unwanted reflections back into the waveguide. The shape of the grating causes destructive interference in the plane of the structure causing the light to be scattered upwards. In this thesis the light is collected into a single mode optical fibre via a confocal microscopy set-up. This design is extremely popular due to the small spatial footprint of the device and the ability to fabricate the OCs in just one fabrication step. However, the efficiency of the design is fundamentally limited by the symmetry of the reflection directing half of the light down into the substrate. Even the highest predicted collection efficiencies are only ∼40% [48]. Moreover, strong back-reflections are seen from such OCs despite the design aiming to eliminate them [85].

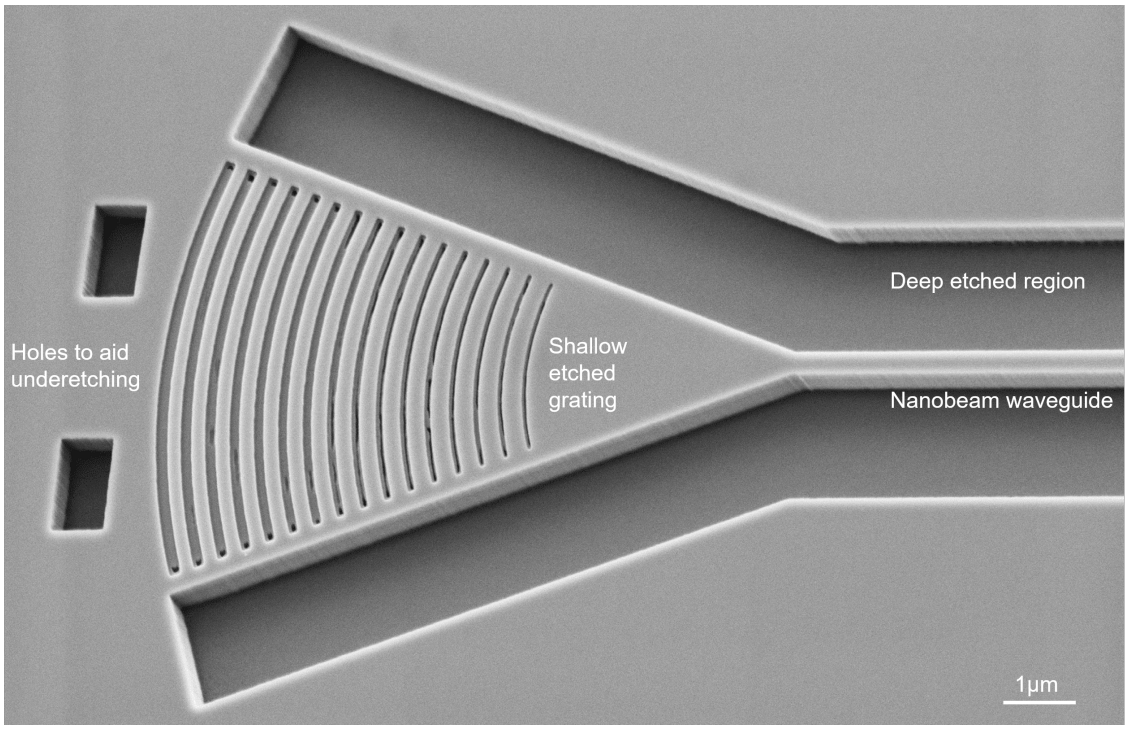

Figure 13: Scanning electron-microscope image of a shallow-etched grating outcoupler. (Image taken by Dr René Dost.)

Recently an alternative grating OC design has been developed which uses a '*Shallow-Etched Grating*' (SEG) as seen in Figure 13, to scatter light off chip with a remarkable improvement in efficiency over the $\lambda/2n$ OCs [25]. Whereas the $\lambda/2n$ OCs send the light directly upwards the SEG OCs reflect the light out at a small angle away from the vertical, this greatly reduces the amount of back-reflections seen into the waveguide. This can be explained by considering the Bragg condition for diffraction gratings.

$$\chi - k_x = m \cdot \frac{2\pi}{\Lambda} \tag{11}$$

Where $\chi = 2\pi\bar{n}_{eff}/\lambda_0$ is the propagation constant for the waveguide mode, $k_x = 2\pi/\lambda_0 \cdot \sin(\theta)$ is the wavevector component for the diffracted light in the propagation direction, m is the diffraction order, $\bar{n}_{eff}$ is the (average) effective index of the membrane and Λ is the period of the diffraction grating. As mentioned previously $\chi = \lambda/2n$ for the semi-circular OC design. From the Bragg condition in Equation 2.4.2 this leads to the first order diffraction ($m = 1$) to be scattered vertically. Crucially however, this condition leads to the second order ($m = 2$) diffraction to be scattered back into the waveguide. As $\bar{n}_{eff}$ is fixed, the pitch of the grating can be adjusted to engineer a small scattering angle, this causes the $m = 2$ diffraction order to no longer be scattered back into the waveguide, significantly reducing the back reflections from the OC. The efficiency of SEG OCs is also much greater than semi-circular OCs with measured efficiencies of 60% in experiment and up to 75% in simulation [25].

There are clear advantages to SEG OCs in both superior scattering efficiency and reduced back-reflections compared to semi-circular OCs, however, SEG OCs are several times larger and require multiple fabrication steps. Moreover, SEG OCs have a much narrower operation bandwidth and are less robust to fabrication imperfections.

2.4.3 Photonic crystal waveguides

As discussed briefly in Section 2.4, light can be confined in nano-photonic structures by both TIR and optical band gaps. The latter is present in '*Photonic Crystal*' (PhC) structures. PhCs are periodic lattices of materials of alternating refractive index such as air and semiconductor. Optical modes propagating through a PhC medium are separated into two bands, the air and dielectric bands, analogous to the conduction and valence bands in electronic band structures. If the refractive index contrast between the two media is sufficiently large, then due to destructive interference of light of certain wavelengths, an optical band gap arises between the air and dielectric modes. Light within this band gap cannot propagate through the PhC causing the PhC to act as a mirror at these wavelengths [97]. The energy of the band gap is related to the period a of the PhC by $a = \lambda/2n$, where n is the refractive index of the dielectric medium.

This allows light to be strongly confined and guided by PhCs. In this thesis only 1D and 2D PhCs are considered. The 1D PhCs are extremely simple in design, just a single row of air holes

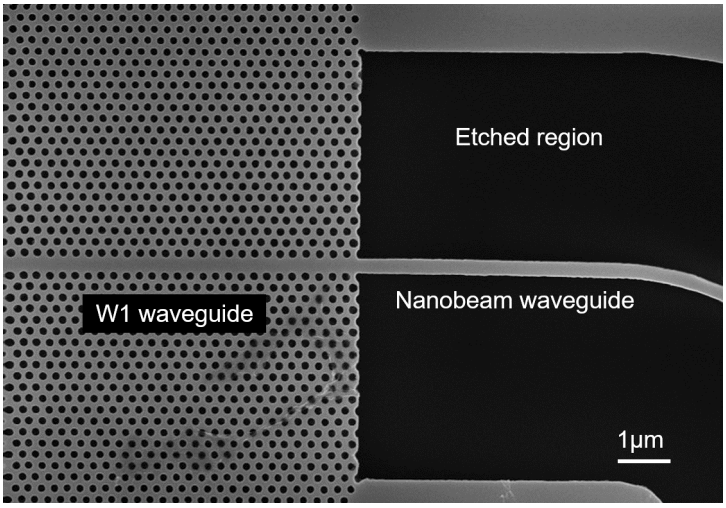

Figure 14: Scanning electron-microscope image of a W1 PhC waveguide coupled to a nanobeam waveguide. A single row of air holes has been removed from the 2D PhC to allow a single mode that is forbidden in the photonic band gap to propagate through the medium.

in a nanobeam waveguide. The 2D PhCs used in this thesis consist of a triangular lattice of air holes in a free-standing membrane. The simplest PhC waveguide is formed by removing a single row of holes from a 2D PhC as seen in Figure 14. This allows a forbidden mode to propagate along the dielectric region created by removing the air holes. This type of waveguide is known as a W1 waveguide and allows a single guided mode to propagate in the photonic band gap. The light is confined by the photonic band gap in the plane of the membrane and by TIR out of plane similarly to the nanobeam waveguide.

W1 waveguides exhibit a much higher β factor than nanobeam waveguides with reported values of up to 98% [48]. Additionally, due to coupling between the gap guided and index guided modes, the gap guided mode is highly dispersive near the band edge. Therefore, the group velocity of the light is incredibly sensitive to the wavelength of the light [98]. Near the band edge light is slowed down significantly, this phenomenon is called the '*slow-light*' effect. Light that is in the slow-light region (close to the band edge) experiences an increased light-matter interaction time due to the reduction in group velocity. This enhanced light-matter interaction is a highly desirable effect in quantum optics as it allows for the enhancement of the emission rate of QDs [45]. This enhancement can be quantified via the '*Purcell factor*', which is discussed in detail in Section 2.5.1. However, the slow-light effect can be detrimental to the propagation of light through the waveguide. The light can become trapped in the waveguide due to Anderson localisations. These localisations occur when the scattering induced by the slow-light effect and disorder in the PhC lattice is so pronounced that an effective cavity is formed in the waveguide. These localised modes are most common close to the band edge of the photonic band gap where the slow-light effect is strongest [99].

W1 waveguides provide much stronger confinement than NBW and the potential for strongly enhanced light-matter interaction within the waveguide making them an attractive choice for an optical waveguide. However, W1 waveguides struggle with guiding light around bends. Unmodified W1 waveguides experience losses of up to 40dB when guiding light through bends. Even after significant and precise modification to the PhC, the bandwidth of maximal bend transmission is very narrow ($\leq 9\%$ of the photonic band gap) and the loss rates remain high (up to 10dB) [100–102]. Moreover, the bend radius is fundamentally limited by the shape of the unit cell. Bending of a NBW is only limited by the critical angle of TIR ($\sim 17^\circ$ in GaAs) and so can take any arbitrary angle with minimal losses, assuming the bend radius is large enough ($\sim 1\mu m$) that the light confined does not exceed the critical angle.

Whilst normally PhC waveguides struggle to guide light around bends, certain PhC unit cell arrangements can form waveguides that have topologically protected guided modes. Modes with topological protection are robust to defects, robust to sharp changes of direction, and suppress back reflections, leading to broadband low loss transmission of the topologically protected mode. These waveguides are formed at the interface between two PhCs with unit cells which are mirrored at the interface [88, 91]. Whilst these waveguides do provide highly lossless transmission and exhibit strong directionality, the unit cells leave very little dielectric material for QDs to be embedded in the waveguide away from etched surfaces which can degrade the optical performance of QDs. Somewhat of a compromise between topological and W1 waveguides comes in the form of a '*Glide Plane Waveguide*' (GPW) [103]. A GPW is a modified W1 waveguide where the PhC on one side of the defect is shifted by half a lattice period in the waveguide direction. This breaks the reflection symmetry of the system which alters the electric field distribution of the waveguide mode, moving the maxima away from the centre of the waveguide. This allows circularly polarised modes to be present at the field maxima. Thus a GPW exhibits strong directionality whilst maintaining the space afforded to a W1 waveguide but does not have topological protection.

Overall, PhC waveguides are an incredibly versatile and diverse method of routing photons with major advantages over a NBW in terms of confinement strength, slow-light capabilities and strong directionality. However PhC waveguides are not suitable for all scenarios and struggle with wide bandwidth bend transmission. PhCs also require complex fabrication compared to NBWs which can introduce unwanted defects in the structure to which PhCs are more susceptible than NBWs.

2.4.4 Photonic crystal cavities

Thus far the purpose of the nano-photonic structures discussed has been to route light efficiently either on or off-chip. To supplement these highly effective photon routing devices, similarly effective devices are required which can trap light in a single spatial location. Such devices are called

optical cavities. The operation and underlying physics of these cavities are discussed in detail in Section 2.5, this section will focus on the overall performance and operation of specific cavity designs.

Whilst multiple optical cavity schemes exist in GaAs systems, such as open cavity [44], micro-disks [104] and micro-pillar [41] designs, '*Photonic Crystal Cavities*' (PhCCs) have been of particular interest in recent years. This is due to their low modal volumes and high quality-factors whilst being easy to integrate into existing nano-photonic circuits due to their planar geometry.

Like PhC waveguides, PhCCs use photonic band gap confinement to trap light within a small defect, this provides extremely strong confinement as propagation of the defect mode is forbidden in the surrounding crystal. PhCCs can be broadly split into two categories: 1D and 2D cavities. 1D PhCCs consist of a single row of a PhC in a NBW with a defect at the cavity centre; a schematic of the most simple 1D PhCC can be seen in Figure 15 which consists of a uniform PhC with a single air hole omitted to create a defect. This forms a Fabry Pérot cavity of length L in which a forbidden mode can propagate between the two mirrors.

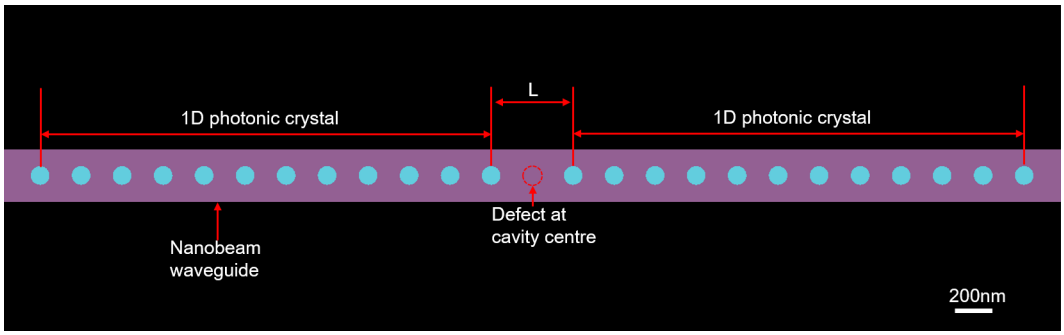

Figure 15: Schematic of the most simple 1D PhCC in which a single air hole is omitted from the PhC, creating a defect in which a forbidden mode can exist. The 1D PhCs either side of the defect act as mirrors in the waveguide direction confining the mode to the cavity centre via the photonic band gap; the mode is confined in the two remaining dimensions by TIR.

The wavelength of the cavity resonance is given by:

$$\lambda = 2n_{eff}L \tag{12}$$

where n_{eff} is the effective refractive index of the cavity and L is the cavity length. This cavity design is extremely simplistic, making it easy to fabricate. However, the performance of such a device is heavily limited by the large scattering losses from the cavity/mirror interface due to the

mismatch between the cavity and PhC modes [105]. By tapering the position and radii of several of the holes closest to the cavity centre, the mismatch between cavity and PhC modes can be smoothed, reducing the amount of light scattered out of plane at the interface and thus increasing the confinement of the cavity whilst keeping the mode volume constant [106, 107]. Figure 16 shows

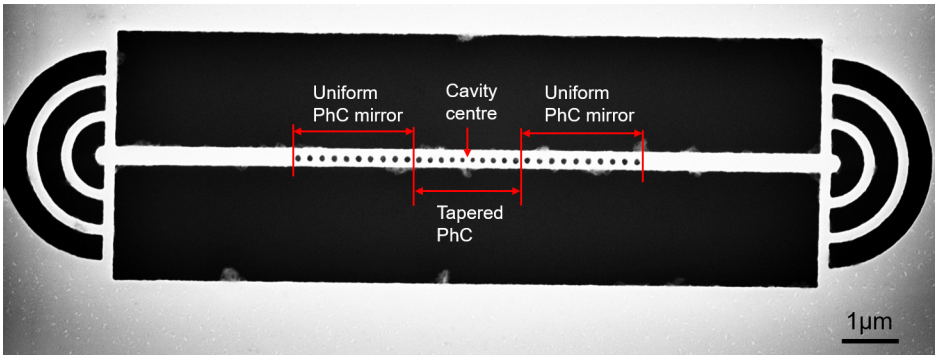

Figure 16: Scanning electron-microscopy image of a 1D PhCC with a tapered PhC section of 5 air holes either side of the cavity centre. The radius and position of the holes are tapered linearly down to a set minimum whilst keeping the ratio of radius to period constant from the uniform mirror section.

an example of a cavity formed using the mode matching taper. Due to the reduction in hole radius and spacing at the cavity centre the need to omit a single hole from the PhC is removed allowing for extremely small mode volumes to be realised in 1D PhCCs with some novel designs exhibiting mode volumes close to the theoretical limit $V_m = (\frac{\lambda}{2n})^3$ [108]. These low mode volumes combined with the strong confinement of 1D PhCCs has allowed strong coupling between a QD and 1D PhCC to be demonstrated [42]. Moreover, demonstrations of: lasing [109, 110], frequency conversion [111], spectral filtering [112], tunable cavities [113], and simultaneous temperature and complex refractive index sensing [114] show both the enormous versatility and potential applications of 1D PhCCs.

Expanding into two dimensional PhCs allows for more complex and differing cavity designs. The most common 2D PhCC designs are the H1 and L3 cavities as seen in Figure 17. H1 cavities are created by removing a single air hole from a 2D PhC, this missing hole acts as a defect, trapping light. As seen in Figure 17, the air holes surrounding the defect are modified slightly from the uniform PhC; this increases the confinement of the cavity significantly in the same fashion as for the 1D PhCC by improving the mode matching between the defect and mirror modes [105, 115]. L3 cavities are formed by removing a row of 3 holes from a 2D PhC, this creates a line defect. Similarly to the H1, the air holes at either end of the cavity are modified to improve the mode matching and reduce the scattering losses from the cavity [116]. This thesis will focus on H1 cavities rather than L3 cavities.

The mode profiles of the fundamental modes of an H1 cavity are shown in Figure 18. Two degener-

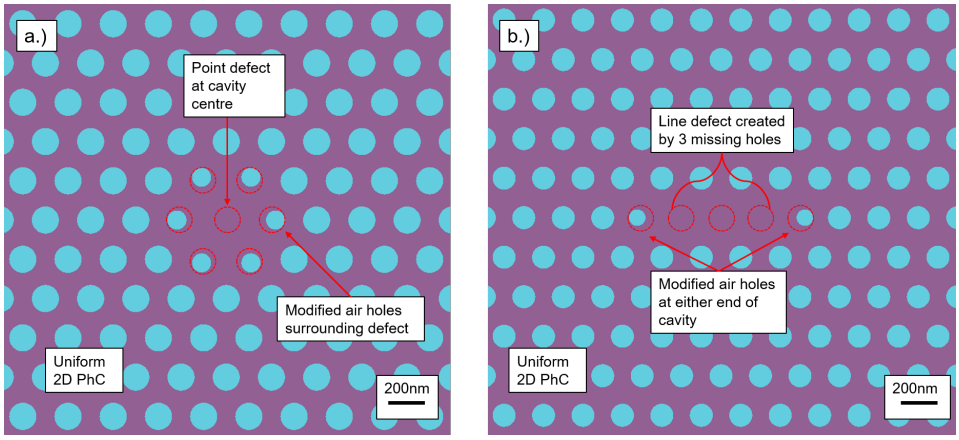

Figure 17: Schematic of a.) H1 and b.) L3 PhCCs. Both cavities are formed by removing air hole(s) from the PhC to create a defect. The air holes closest to the cavity are altered to improve the mode matching between the cavity and PhC modes, this increases the confinement.

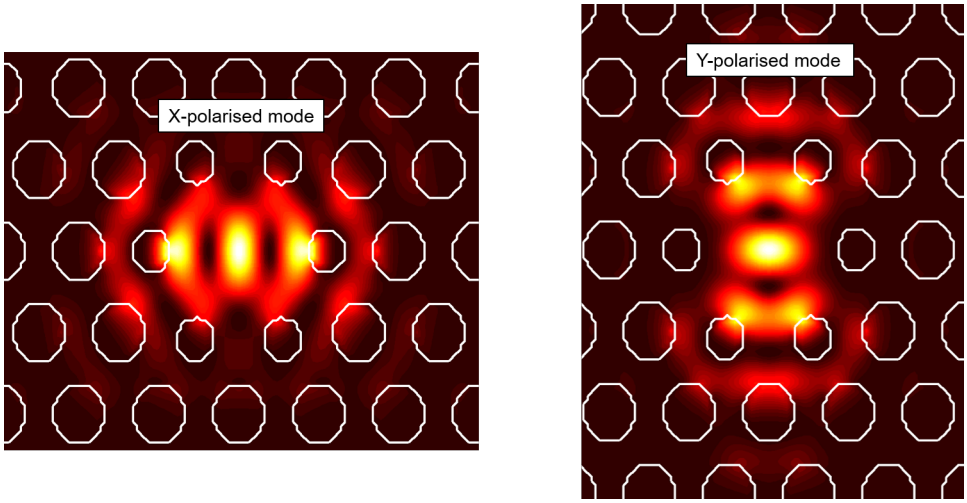

Figure 18: FDTD simulations of the electric field profiles of the two degenerate fundamental modes of an H1 cavity, the modes are spectrally degenerate but have orthogonal linear polarisations.

ate modes are present in an H1 cavity; these modes are the fundamental modes of the cavity and are linearly polarised with orthogonal polarisation to each other. Despite having differing spatial distributions the modes are truly degenerate. By altering the photonic crystal period in one direction the degeneracy of the modes can be lifted, although experimentally due to fabrication imperfections the mode degeneracy is already lifted. In this case the detuning of the modes can be adjusted by altering the PhC period in one dimension or by applying uniaxial strain to the PhC [117, 118]. Strong coupling has also been measured in H1 cavities [119]. Moreover, demonstrations of highly efficient single photon emission from an H1 cavity show the potential for the use of H1 cavities for QIP [43]. Whilst H1 cavities do not exhibit as low mode volumes or as strong confinement as 1D

PhCCs, their large dielectric areas at maximum E-field intensity, the existence of two fundamental modes and their ease of integration with PhC waveguides give them unique advantages over 1D PhCCs despite lower cavity performance.

When considering the viability of PhCs for scalable QIP devices, the repeatability and reliability of the device fabrication must be discussed. To interface multiple PhC structures for QIP processes, the modes in the PhC structures must be resonant. The properties of the modes in PhC structures are determined by the dimensions of the etched features. Therefore, the ability to reliably create resonant structures is highly dependant on the repeatability and reliability fabrication process. This is especially true for devices designed to operate in the near infra-red range (the range in which InAs QDs emit), where feature sizes in PhC structures can be on the order of tens of nanometres. State-of-the-art fabrication equipment and techniques can fabricate PhC structures where the standard deviation of the variation in feature size is as low as $0.4nm$; this results in a standard deviation of $1.34nm$ for the distribution of the centre of the PhC modes [120]. For waveguide devices, which typically exhibit modes with bandwidths on the order of hundreds of nanometres, the variation in the central frequency of the mode will not significantly effect the overlap of the modes between multiple PhC waveguides. However, for high quality PhCCs with mode bandwidths $\ll 1nm$, this variation poses a significant challenge when attempting to interface multiple resonant PhCCs. To combat the impact of fabrication imperfections on the repeatability of PhCC fabrication, methods by which the wavelength of the cavity mode can be tuned post fabrication have been developed. These methods allow for the impact of fabrication imperfections to be mitigated as the tuning range of the cavity mode is larger than the standard deviation of the cavity mode wavelength distribution. These methods are discussed in further detail in Chapter 5.

With the current state-of-the-art fabrication, PhC waveguide devices are highly scalable due to their bandwidths being much larger than the uncertainty in the central wavelength of the mode. For PhCC devices, if a combination of state-of-the-art fabrication and cavity tuning techniques are considered, PhCC systems can realistically be scaled up to a system of two resonant cavities. A system of three resonant cavities, while certainly achievable with current techniques, would be challenging to realise. Ultimately, the scalability of PhCC devices will continue to improve in tandem with improvements to both PhC fabrication and cavity tuning techniques as well as the development of surface passivation procedures. Surface passivation has been shown to reduce the variation in cavity mode wavelength whilst simultaneously increasing the average quality-factor of groups of nominally identical PhCCs.

2.5 Cavity quantum electrodynamics

The physics that describes the phenomena exhibited by light confined to an optical micro-cavity is known as '*Cavity Quantum Electrodynamics*' (cQED) and shall be discussed in this section. Firstly,

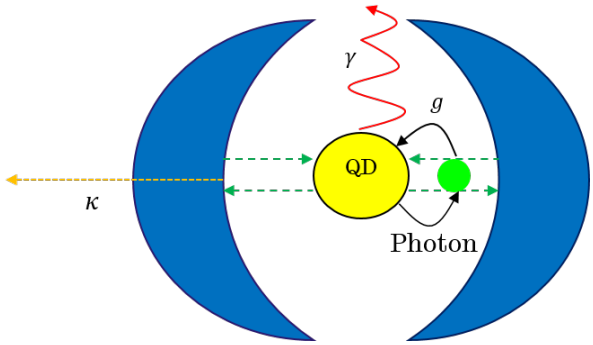

Figure 19: Diagram of the Jaynes-Cummings model description of a QD coupled to a photon in a micro-cavity κ is the cavity leakage rate, γ is the decay and dephasing rate and g is the coupling rate between the photon and the QD.

a relevant model of the system must be defined. A two-level system (in this case a QD) coupled to a photon trapped in a micro-cavity is described mathematically by the Jaynes-Cummings model [121].

When considering the performance of optical micro-cavities there are two main parameters to discuss. First is the '*mode volume*'. The mode volume describes the spatial confinement of the mode and is given by:

$$V_m = \frac{\int d^3r\epsilon(r) \mid E(r) \mid^2}{max(\epsilon(r) \mid E(r) \mid^2)} \tag{13}$$

where ϵ is the relative permittivity of the material and E is the electric field strength of the cavity mode. Second is the '*Quality-Factor*' (Q-factor). The Q-factor describes the confinement strength of the cavity and is given by:

$$Q = \frac{\omega_0}{\Delta\omega} \tag{14}$$

ω_0 is the resonance frequency of the mode and $\Delta\omega$ is the linewidth of the resonance peak. The cavity leakage rate κ is related to the Q-factor by:

$$\Delta\omega = 2\kappa \tag{15}$$

therefore, a larger Q-factor indicates a longer confinement time. Finally, the coupling rate between the QD and photon is given by:

$$g = \frac{1}{\hbar}\sqrt{\frac{\hbar\omega}{2V_m}}\mu \tag{16}$$

where μ is the dipole moment of the QD under the assumption that the QD is placed at the point of maximum E-field intensity. Figure 19 shows these parameters in relationship to each other pictorially. Depending on the values of each of these parameters relative to each other, different physical phenomena are observed. There are two main regimes that shall be explored; weak and strong coupling.

2.5.1 Weak coupling

In the weak coupling regime the loss rates from the cavity dominate the photon QD coupling to the point where photons emitted from the QD cannot be reabsorbed i.e. $g \ll \kappa, \gamma$. In this scenario the

emission rate of the QD is increased when on resonance with the cavity, this phenomenon is called the '*Purcell effect*' [122]. The emission enhancement follows from Fermi's golden rule as the local density of final photon states is greater in the cavity than in free space. The degree of emission rate enhancement is given by the Purcell factor:

$$F_P = \frac{3}{4\pi^2}\left(\frac{\lambda_c}{n}\right)^3\left(\frac{Q}{V_m}\right) \tag{17}$$

where λ_c is the resonance wavelength of the cavity and n is the refractive index of the cavity. From this it is clear that to obtain the highest Purcell factor for a specific cavity wavelength, the ratio of $\frac{Q}{V_m}$ must be maximised. Thus, cavities with low mode volumes and high Q-factors are ideal. The ratio of $\frac{Q}{V_m}$ is often taken as a figure of merit for weak coupling systems. Experimentally, the emission rate enhancement is characterised by a reduction in emitter lifetime, leading to an increased emission peak intensity and emitter linewidth. The weak coupling regime has been demonstrated comprehensively for QD systems [43–45, 110] and as such is an important phenomenon for the realisation of many QD based QIP systems.

2.5.2 Strong coupling

If the converse of the weak coupling conditions are considered, the QD-photon coupling dominates over the leakage rates $g \gg \kappa, \gamma$. This is know as the strong coupling regime. In the strong coupling regime, the photons confined to the cavity are reabsorbed and emitted many times by the QD before escaping the cavity, due to the low cavity loss rates compared to the QD-photon coupling rate. This causes the photons to oscillate between the cavity and QD fields. This behaviour is known as '*vacuum Rabi oscillations*' and causes a polaritonic state to form (a hybrid light-matter quasi-particle). This state produces characteristic spectral peaks with a splitting of $\Omega_R = 2g$ called the '*Rabi frequency*'. Experimentally these peaks can be observed to anti cross when the QD and cavity lines are tuned through resonance.

For small cavity lengths (e.g. those of micro-cavities) the cavity leakage rate is much higher than the losses associated with dephasing e.g. $\kappa \gg \gamma$. Therefore, the figure of merit for strong coupling can be defined as being $\propto \frac{g}{\kappa}$. From Equation 15 and Equation 16 it can be seen that:

$$\frac{g}{\kappa} = \sqrt{\frac{2}{\hbar\omega}}\left(\frac{Q}{\sqrt{V_m}}\right)\mu \tag{18}$$

therefore, the figure of merit for strong coupling is proportional to $\frac{Q}{\sqrt{V_m}}$. As mentioned in Section 2.4 strong coupling has been demonstrated in multiple different QD systems [40–42, 119].

It is worth mentioning that a third regime exists, known as ultra-strong coupling, when the Rabi frequency approaches or exceeds the cavity resonance frequency. Such a regime has not been reached in QD systems however, and so will not be discussed here.

2.6 Photon statistics

One of the fundamental aspects of the quantum description of light is the wave-particle duality. In classical physics light is described purely as a wave and behaves as such in all situations. In quantum mechanics, light is described as a stream of particles (photons) and as such different physics is expected [123]. The statistical nature of these photon streams can be categorised into three schemes and is an important attribute of quantum light in the context of QIP.

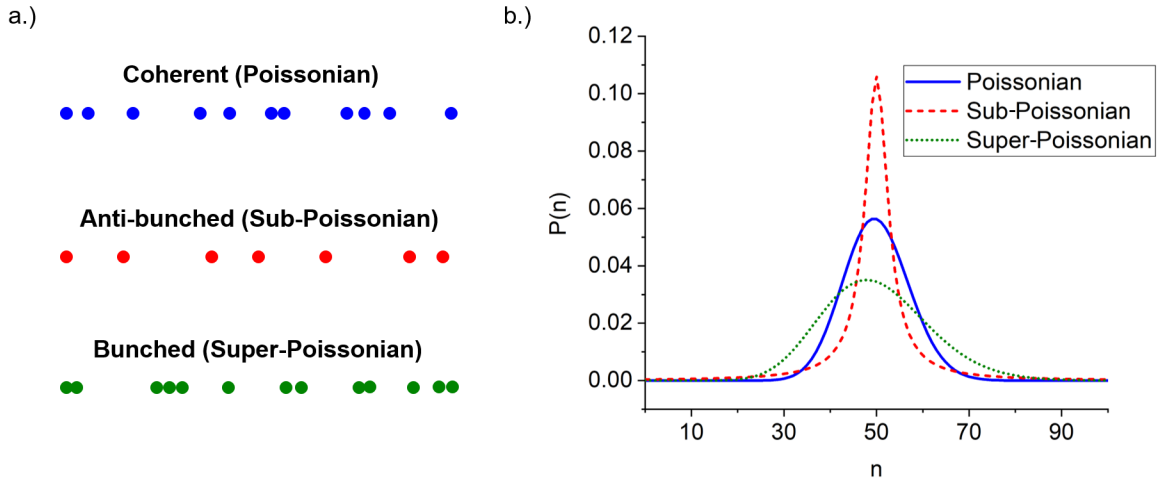

Figure 20: a.) Visual representation of the three schemes of photon statistics showing the time intervals between the photons for: coherent (Poissonian) light where there is no correlation in the time gap between photons, anti-bunched (Sub-Poissonian) light where individual photons are separated by some minimum time interval and bunched (Super-Poissonian) light where photons are likely in groups of two or more. b). Graph showing the probability distributions against the number of photons detected in an arbitrary time window for the three regimes of light depicted in a.), Poissonian, Sub-Poissonian and Super-Poissonian. The mean expected number of photons $\bar{n} = 50$ for all three distributions.

2.6.1 Coherent light

The first case is '*coherent light*'. In this scheme the photons are spaced randomly in time so that there is no correlation between photon number and arrival time at a detector. Most classical light sources are described by this scheme including lasers. In terms of a statistical representation, a coherent light source that is stationary (i.e. photon flux does not change with time) follows a Poisson distribution. A Poisson distribution describes the probability of a given number of events occurring in a discrete time window when the events are completely independent of each other given a known mean rate [124]. Figure 20 gives a visualisation of the photon streams and shows the probability density functions for all three photon schemes. For coherent light following the

Poissonian distribution the mean number of photons is equal to the variance.

$$\bar{n} = \Delta n^2 \tag{19}$$

Therefore, the standard deviation of the photon number distribution is given by:

$$\Delta n = \sqrt{\bar{n}} \tag{20}$$

2.6.2 Anti-bunched light

Secondly, and most importantly for QIP applications, is '*anti-bunched light*'. This scheme occurs when there is some minimum time gap between the individual photons. This leads to a stream of photons where it is highly unlikely that two or more photons will be grouped together, as such, the stream is made mostly of single photons. Anti-bunching is a purely quantum effect with no classical description and is described statistically by a Sub-Poissonian distribution. Comparing the distributions in Figure 20 b.) it can be seen that the fluctuation about the mean for the Sub-Poissonian distribution is narrower than the Poissonian distribution. This agrees intuitively with the idea of anti-bunching as one would expect the minimum time intervals between the photons to reduce the randomness in photon number per time interval. Furthermore, if the ideal case of an exact regular time gap between photons is considered, then the fluctuations in photon number will be eliminated entirely. Therefore, for Sub-Poissonian light, the standard deviation is lower than the mean value:

$$\Delta n_{sub} < \sqrt{\bar{n}} \tag{21}$$

Single photon sources such as QDs [20, 24, 43, 44, 47, 57] single atoms [14, 125–127] and colour centres [13, 128–130] produce anti-bunched light.

2.6.3 Bunched light

Finally, the last case is for light where the standard deviation of the distribution of photon numbers detected is larger than the mean:

$$\Delta n_{super} > \bar{n} \tag{22}$$

this scheme is called '*bunched light*' and is described by Super-Poissonian statistics. In bunched light photons are likely grouped into bunches of 2 or more photons. Sources of bunched light include classical sources with time varying intensity (also called '*chaotic light*') and thermal sources such as black-body radiation. The intensity fluctuations of chaotic light will undoubtedly lead to greater fluctuations in the number of photons detected compared to a coherent light source, thus leading to an increased standard deviation. In the case of thermal light, the number of photons detected follows a Bose-Einstein distribution where $P(n)$ is greatest at $n = 0$ and decreases exponentially. The variance of the Bose-Einstein distribution is always larger than that of the Poissonian distribution when considering a single mode of thermal light. When considering a large number of modes,

the variance approaches the result of a Poissonian distribution. However, if energy fluctuations from a black-body emitter are considered, it can be seen that the variance remains larger than the Poissonian case even for a large number of modes [123]. It is important to note that while a change in intensity fluctuations will alter the photon statistics, a change in the overall intensity (the mean number of expected photon detections $\bar{n}$) of the source will not occur.

2.6.4 Degree of second order coherence

Having discussed the three statistical schemes of light, a way of quantifying them is required so that a stream of photons may be measured and the photon statistics determined. This can be achieved by measuring the '*degree of second-order coherence*' or $g^{(2)}(\tau)$ of the light source. The degree of second-order coherence describes the correlation in intensity between the two outputs A and B of a light source incident on a beam splitter:

$$g^{(2)}_{A,B}(\tau) = \frac{\langle I_A\,(t+\tau)\, I_B\,(t)\rangle}{\langle I_A\,(t+\tau)\rangle\langle I_B\,(t)\rangle} \tag{23}$$

where τ is the time delay between the detections at A and B, and I_A and I_B are the intensities at the detectors. For a source where the intensity does not vary with time, the angled brackets can be interpreted as an ensemble average rather than a time average over a large range of t [131]. The most important case for QIP is the case when $\tau = 0$, which describes the correlation in intensities for simultaneous detections at A and B. It is useful to rewrite Equation 23 in terms of detection probabilities, this is known as the semi-classical $g^{(2)}$. The probability of detecting a single photon within a small time Δt on detector A is defined as:

$$P_A = \eta_A \langle I_A\,(t)\rangle \Delta t \tag{24}$$

where η_A is the efficiency of detector A. The probability of detecting a photon at B in a small time window Δt, τ seconds after detecting a photon at A also in a small time window Δt is given by:

$$P_{A,B}(\tau) = \eta_A \eta_B \langle I_A\,(t+\tau)\, I_B\,(t)\rangle \tag{25}$$

By combining Equation 24 and Equation 25 with Equation 23:

$$g^{(2)}(\tau) = \frac{P_{A,B}\,(\tau)}{P_A P_B} \tag{26}$$

As stated earlier the most important case is for $\tau = 0$:

$$g^{(2)}(0) = \frac{P_{A,B}\,(0)}{P_A P_B} \tag{27}$$

here $P_{A,B}(0)$ is the probability of a coincidence count in time window Δt between detectors A and B. For coherent light, there is no correlation between photon arrival times and as such no correlation between detections at A or B. Therefore, the coincidence probability is just equal to

the product of the two detector probabilities. As such, the value of $g^{(2)}(0) = 1$ for a coherent source.

For bunched light, the photons are more likely to arrive at the beam splitter in groups of 2 or more than as individuals. This increases the likelihood of coincidences being detected, as multiple photons are striking the beam splitter in Δt. In this case, the coincidence probability is greater than the product of the two detectors probabilities and so $g^{(2)}(0) > 1$ for bunched light.

Finally, for anti-bunched light individual photons are separated by a minimum time gap from each other. It is highly unlikely that two photons will be incident on the beam splitter in Δt and so only a single detection will be made. The probability of detecting a coincidence between A and B is smaller that the product of the individual detector probabilities and so for anti-bunched light $g^{(2)}(0) < 1$. For a perfectly anti-bunched source where the photons are emitted with a regular time gap to each other, if Δt is smaller than this time gap then $P_{A,B}(0) \rightarrow 0$. Therefore the expected result for a perfectly anti-bunched light source is: $g^{(2)}(0) = 0$. One figure of merit for the performance of a single photon source is the single photon purity. This can be found by comparing the value of $g^{(2)}(0)$ obtained experimentally to the ideal value. Other figures of merit include the indistinguishability and fidelity of single photons from a source.

2.7 Directionality of embedded emitters

For the majority of the nano-photonic devices discussed in Section 2.4, the emission of light from the embedded emitters is assumed to be isotropic and the operation of the device invariant of the emission direction and polarisation of the light. However, one can imagine the advantages and potential applications of a nano-photonic device with embedded emitters that exhibit deterministic directionality such as deterministic quantum state transfer and unidirectional coupling between qubits [132, 133].

To understand how to achieve this directional emission using nano-photonic devices, the properties of the electric field in a single mode nano-photonic waveguide must be considered. Due to the transverse confinement of light in the waveguide, the first-order field component is longitudinal (E_x) [134]. This field component oscillates with respect to the transverse field component (E_y) with a phase of $\pm\frac{\pi}{2}$ causing the electric field to be elliptically polarised. The degree of ellipticity is dependant on the relative amplitudes of (E_x) and (E_y), for the case where $|E_x| = |E_y|$ the field is circularly polarised. The sign of the phase difference between the field components is dependant on propagation direction of the mode in the waveguide. This is known as '*spin-momentum locking*' and is a consequence of the time reversibility of Maxwells equations [135]. Different waveguide architectures give rise to different polarisation distributions of the optical mode. For example, in a nanobeam waveguide the fundamental mode is linearly polarised at the centre of the waveguide as $|E_x| \neq |E_y|$ & $|E_x| = 0$ at the centre of the waveguide. Conversely, at the waveguide-cladding

interface the mode is circularly polarised as $|E_x| = |E_y| \neq 0$ [85, 136].

If the case of a single emitter placed in a nano-photonic waveguide is considered, the coupling strength of the emitter to the waveguide modes is given by the β factor (Equation 10). The emission rate into the waveguide modes can be split into the two propagation directions $\gamma_{wg} \rightarrow \gamma_+, \gamma_-$. Due to spin-momentum locking in general $\gamma_+ \neq \gamma_-$ leading to some directionality of the β factor. In the case where the emitter is located at a point in the waveguide where the electric field is circularly polarised, the polarisations for opposite propagation directions will be orthogonal. If a circularly polarised photon is emitted into the waveguide from this location it will couple only to the correspondingly polarised propagation direction, thus the emission becomes unidirectional [137].

At points away from the perfect case the emission will be preferentially but not completely directional. The degree of directionality for any point in a waveguide can be obtained using the Stokes Parameters, a set of equations which make up the observables of a polarisation field [138].

$$S_0 = |E_x|^2 + |E_y|^2 \tag{28}$$

$$S_1 = |E_x|^2 - |E_y|^2 \tag{29}$$

$$S_2 = 2\mathbb{R}\left(E_x E_y^*\right) \tag{30}$$

$$S_3 = -2\mathbb{I}\left(E_x E_y^*\right) \tag{31}$$

The degree of directionality is found by calculating the degree of circular polarisation at the point of interest. This is given by:

$$C = \frac{S_3}{S_0} = \frac{-2\mathbb{I}\left(E_x E_y^*\right)}{|E_x|^2 + |E_y|^2} \tag{32}$$

The degree of directionality is often referred to as the '*chiral contrast*'. Experimentally, in nano-photonic waveguides the chiral contrast (C) of an emitter can be calculated by measuring the intensity of the emitter at each end of the waveguide (I_R and I_L). By calculating the difference between these intensities and normalising over the total intensity the directionality of the emitter is found:

$$C = \frac{I_R - I_L}{I_R + I_L} \tag{33}$$

If the emitter was at a point of circular polarisation then only one output of the waveguide would measure any photons and $C = 1$. Conversely, in the case where the emitter is in an area of linear polarisation: $\gamma_+ = \gamma_-$. Therefore, $I_R = I_L$ and thus $C = 0$.

For QDs in nano-photonic devices, directional emission has been demonstrated in nanobeam waveguide structures [85, 139, 140], with chiral contrasts of up to $C = 0.95 \pm 0.05$ measured [85]. Further demonstrations of directionality from QDs in nano-photonic structures include both W1 PhC waveguides ($C = 0.98 \pm 0.02$) [141] and GPWs ($C = 0.9 \pm 0.13$) [103] as well as topological PhC waveguides ($C = 0.75 \pm 0.02$) [91].

This page intentionally left blank.

3 Methods

3.1 Introduction

In this chapter, the different methods used throughout the work in this thesis will be described. Firstly, the process of growing semiconductor wafers will be described. This will be followed by a description of the process by which nano-photonic structures and electrical diodes are fabricated onto the wafers, to allow for the photonic and electrical environment of embedded QDs to be controlled.

The various experimental measurement procedures used to obtain the data in Chapters 4 - 6 will be described next. Details of the lasers used in this thesis will be included first, before descriptions of the experimental set-ups. Confocal microscopy PL, white light reflectivity and time-resolved measurement procedures will be detailed with inclusions of schematics of each experimental set-up. Next, the operation of the cryostats which house the samples at cryogenic temperatures will be discussed.

Lastly, the computational methods used in this thesis will be outlined. The main simulation method used throughout this thesis is a Finite-Difference Time-Domain (FDTD) method, this will be discussed in detail first. A brief description of MIT Photonic Bands (MPB) software will follow this before a more detailed discussion of the Monte Carlo simulation method.

3.2 Wafer growth and nano-structure fabrication

3.2.1 Semiconductor wafer growth

The samples measured in this thesis are made from GaAs heterostructure wafers with embedded InAs SKQDs. These heterostructure wafers are grown via MBE, allowing for precise control over the composition and thickness of each material layer. The process by which SKQDs and SCQDs are grown is explained in detail in Section 2.2.1 and Section 4.2, respectively and so will not be covered in detail here. The composition and growth of the wafer heterostructure will be discussed. MBE growth is conducted in an ultra-high vacuum environment where sublimed molecules are deposited onto a heated substrate through mechanically-controlled molecular beams. The thickness of the layers can be monitored throughout the growth process using '*Reflection High Energy Electron Diffraction*' (RHEED). By scattering high energy electrons off the sample surface at small incidence angles a diffraction pattern is obtained. By analysing this diffraction pattern the properties of the deposited layers can be determined [142].

Figure 21 shows the heterostructure of the waveguide compatible wafers used in this thesis. Atop a 1000nm thick GaAs substrate a 300nm n-doped GaAs layer is grown to enable a diode to be

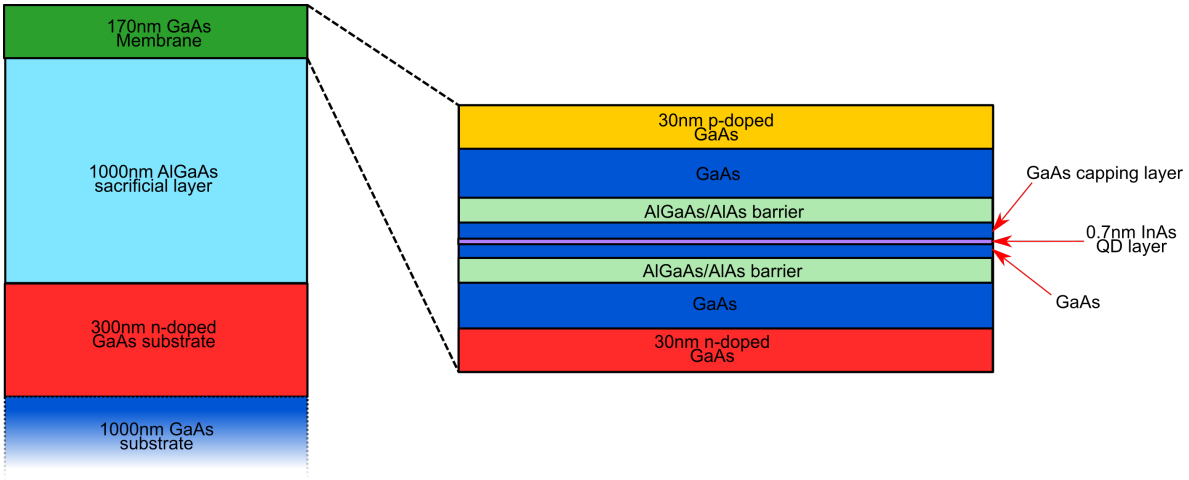

Figure 21: Schematic showing the general heterostructure of the wafers used to fabricate the samples in this thesis. The membrane is grown atop an AlGaAs sacrificial layer which is etched away in the device fabrication process to leave the membrane free-standing. The membrane contains both doped GaAs and AlGaAs/Aluminium Arsenide (AlAs) barrier layers to enable a p-i-n diode to be fabricated in the membrane and for the QCSE tuning range to be increased, respectively.

fabricated between the substrate and the membrane. The next layer deposited is a 1000nm thick AlGaAs layer. This layer is known as the '*sacrificial layer*', on top of which the GaAs membrane is grown which contains InAs QDs. Once nanophotonic devices have been fabricated in the membrane of the wafer, the sacrificial layer is removed via a hydrofluoric acid (HF) etch to leave the membrane free-standing around the structures. This enables the nano-photonic structures to be air-clad, leading to a high degree of confinement of light in the structures. The removal of the sacrificial layer is also essential to enable the operation of electromechanical devices such as the devices presented in Chapter 5. The 170nm thick membrane which is grown atop the sacrifical layer contains a complex layer structure to maximise the potential applications of the wafer. At the top and bottom of the membrane, p-doped and n-doped GaAs layers are grown to enable a p-i-n diode to be created across the membrane. This allows for the QD emission energy to be tuned via the QCSE and for the charge states of the QDs to be controlled. To increase the range of the QSCE tuning, AlGaAs or AlAs barrier layers are grown either side of the QD layer. The QD layer is grown atop a GaAs layer to create the lattice mismatch (7%) required for the QD growth. The QDs are then capped by a second GaAs layer before the top barrier layer is grown. By varying the thickness of the barrier layers, the QCSE tuning range can be altered. The SCQD wafers in this thesis do not contain a sacrificial layer and as such are not compatible with waveguide devices. The waveguide wafers in this thesis were grown by Edmund Clarke at the EPSRC National Epitaxy Facility at the University of Sheffield. The SCQD wafers were grown by Charlotte Ovenden at the EPSRC National Epitaxy Facility at the University of Sheffield.

3.2.2 Device fabrication

High quality fabrication of nano-photonic structures is essential to the success of III-V semiconductor based quantum devices. The structures studied in this thesis were fabricated through a combination of '*Electron-Beam Lithography*' (EBL) patterning and wet and dry etching processes. Figure 22 shows a step-by-step schematic of the device fabrication process. The semiconductor wafer is first prepared by depositing an electron-sensitive resist layer on top of the membrane. This deposition is done via a spin-coating technique to ensure even coverage of the resist. This layer is then exposed in an EBL machine which patterns the devices into the resist. The resist is then developed in xylene which removes the areas of the resist which have been exposed to the electron beam as they have become soluble in xylene. Following this, the structure pattern is etched into the membrane via an ICP etch. The remaining resist which was not exposed to the electron beam protects the parts of the membrane which will not be etched. Where the resist is removed, the ICP is easily able to etch away the GaAs. The structures are etched through the entire membrane and into the top of the sacrificial layer to enable the sacrificial layer to be removed in the next step. After this, the resist is no longer required and so is removed. The devices are under-etched by placing the sample in HF. The HF etches the semiconductors which contain aluminium much faster than the other semiconductors on the sample. As the sacrificial layer is made from AlGaAs, this layer is attacked by the HF and etched away. This leaves the structures in the membrane free-standing. To remove the HF from the sample, the sample is rinsed in water and acetone before the final step is conducted. A critical point drying process is conducted at the end of the fabrication to ensure that the surface tension of the rinsing agents does not produce strain upon the suspended structures, as this could cause them to collapse.

After the critical point drying process, the structure fabrication process has been completed and high quality suspended nano-structures have been created. All the nano-structures measured in this thesis were fabricated by René Dost at the University of Sheffield.

3.2.3 Diode fabrication

To enable electrical control over the QDs and the operation of electro-mechanical structures, electrical diodes must be fabricated in the semiconductor wafer. To enable this, the wafer must be etched to uncover the doped semiconductor layers to be contacted to make the diode. To create a diode across the membrane, an etch down to the n-doped membrane layer is required. For a diode across the sacrificial layer, both an etch to the n-doped membrane layer and the n-doped layer at the top of the substrate, are required. This etching creates a mesa on which the top diode contact and devices are situated. By etching separate mesas, multiple diodes can be created on the wafer which can be individually addressed.

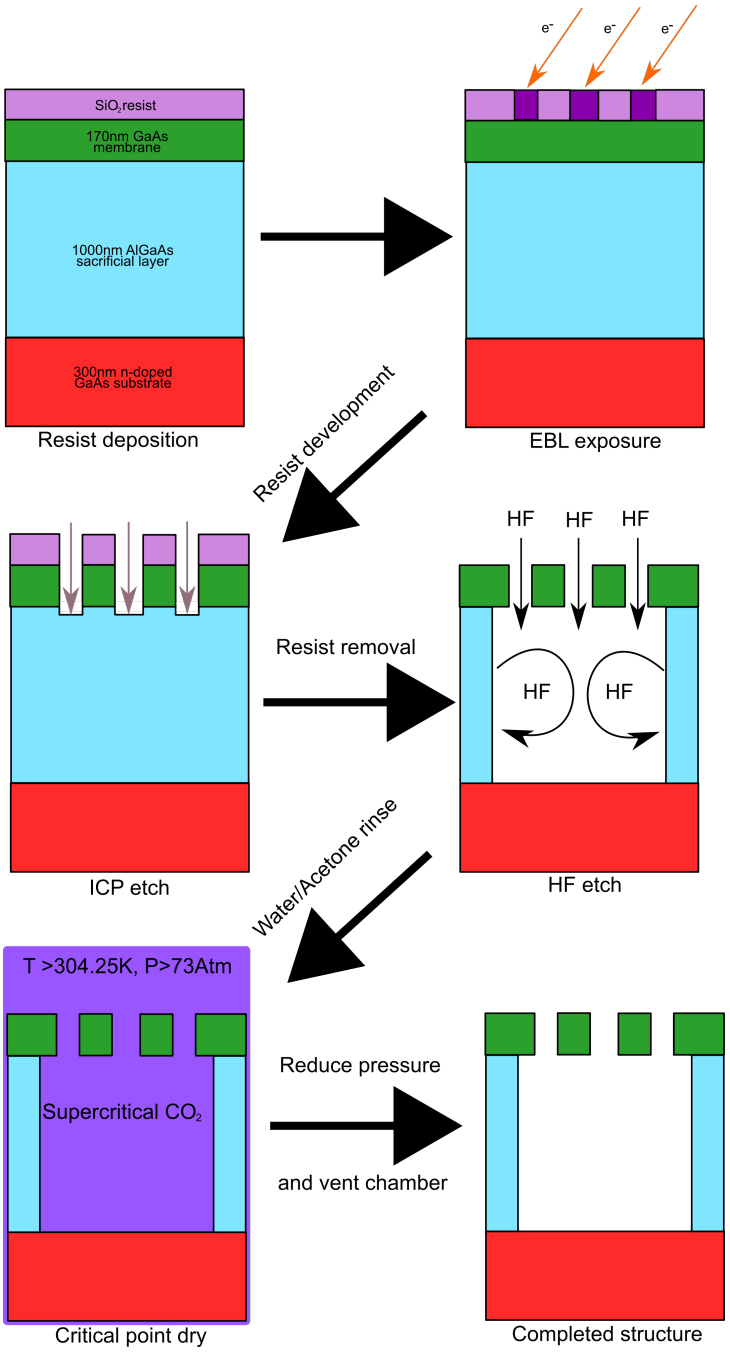

Figure 22: Schematic of the device fabrication process. An electron-sensitive resist is first deposited on the wafer before the structures are patterned into the resist via EBL. The structures, which have been designed in Computer-Aided Design (CAD) software, are then etched into the membrane by an '*Inductively-Coupled Plasma*' (ICP) etch. The resist is then removed before a HF wet etch is used to under-etch the membrane leaving the structures free-standing. Finally, after the sample is rinsed, a critical point dry is performed to reduce the surface tension on the devices.

The fabrication of the mesa is conducted in the same manner as the device fabrication steps depicted in Figure 22 but ending after the resist removal as no under-etching of the mesas is required.

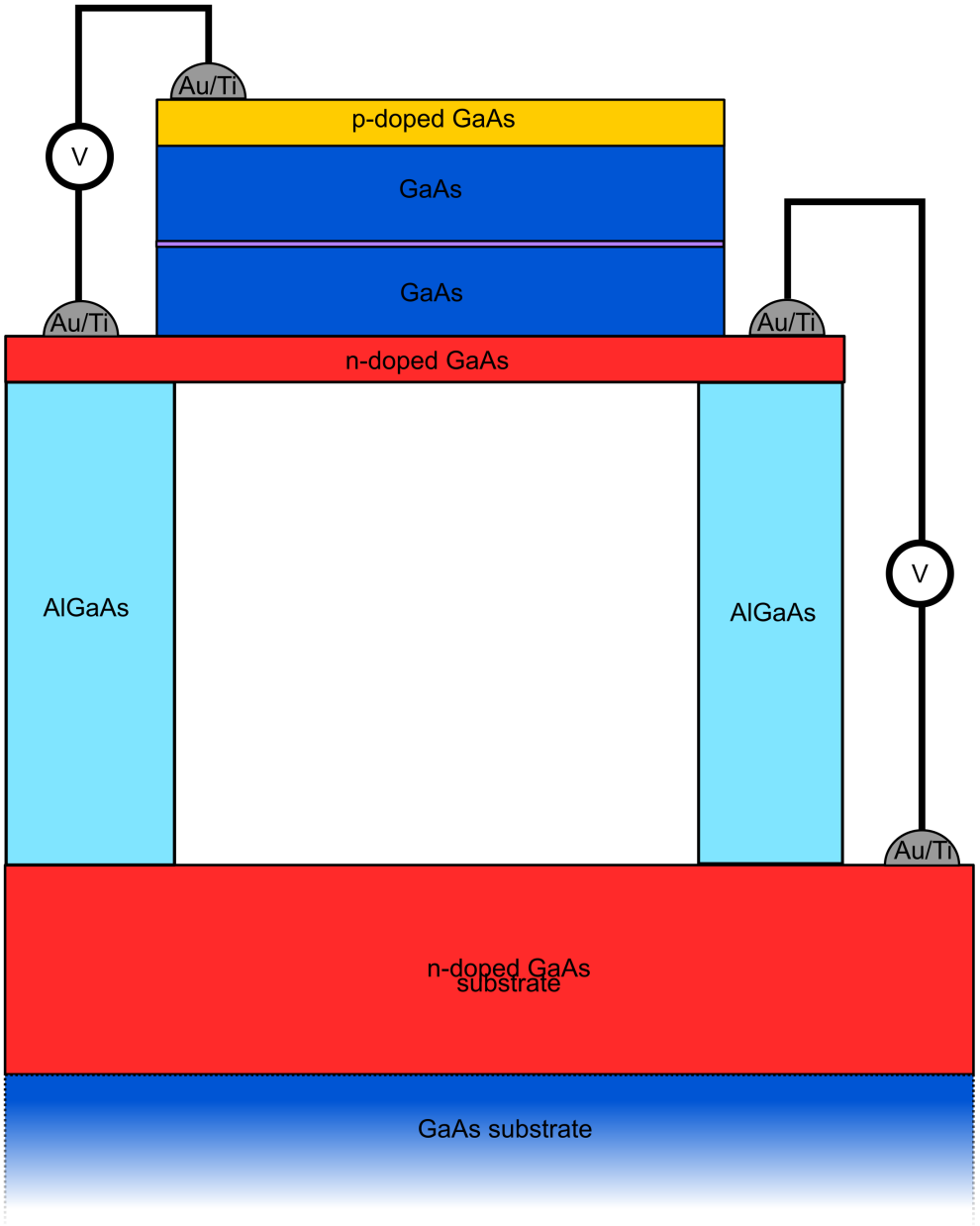

Figure 23: Schematic showing a cross-sectional view of free-standing photonic devices with two different diode schemes. On the left is a diode across the QD layer in the membrane. On the right is a diode across the sacrificial layer.

The depth of the ICP etch is controlled to ensure that the correct wafer layers are exposed for contacting. Figure 23 shows a schematic of the two diode schemes. After the etching of the mesa,

the metal contacts are deposited. Again, the same procedure of masking from Figure 22 is used to define the area for metallisation. Titanium-gold alloy is deposited onto the exposed areas to form the diode contacts. Titanium is included to reduce the amount of gold which diffuses into the doped semiconductor layers. Once the contacts are deposited, the wafer is ready to be transferred into a ceramic chip carrier, where the diodes on the wafer are bonded to the contacts on the chip carrier by a wire ball bonding method.

3.3 Experimental methods

This section will detail the various methods used to conduct experiments on the fabricated samples. Firstly, the lasers used to conduct the experiments will be detailed. Following this, descriptions and schematics of the spectroscopy and time-resolved measurements will be given before a discussion of the cryogenic systems used in this work.

3.3.1 Excitation lasers

The lasers used in this work will be listed in this section. Each laser was required for a different purpose which will also be listed.

Thorlabs L808 diode laser

The Thorlabs L808 diode laser is a continuous wave laser emitting at 808nm. The laser emits into free space but can be easily fibre-coupled to enable efficient arbitrary routing of the laser. The typical output power from the laser after being fibre-coupled is $\sim$100μW. This makes the laser ideal for low to mid power PL measurements as the emission wavelength of the laser allows above band-gap pumping of GaAs.

Helium-Neon (HeNe) gas laser

The Helium-Neon (HeNe) gas laser is a continuous wave laser operating at 633nm. This free space emitting laser has a typical output power of $\sim$500μW which makes it an ideal choice for high power PL measurements.

SLM-632.8-FS diode laser

The SLM-632.8-FS diode laser is a continuous wave laser operating at 632.8nm. This laser is much more powerful than both the L808 and HeNe lasers with a typical output power of $\sim$55mW. This laser is utilised in Chapter 4 as a heating laser. The power of the laser is controlled by a variable ND-filter.

M-Squared SolsTiS Titanium:Sapphire (Ti:S) laser

The M-Squared SolsTiS is a tunable Titanium:Sapphire (Ti:S) laser which emits single mode, continuous wave light. The SolsTiS laser is pumped by 532nm radiation from the M Squared Equinox frequency doubled Nd:YAG laser at a power of 10W. The tunable emission range of the Ti:S laser is 700-1000nm with a high precision of 0.001nm. The typical output power of the laser is 6.5W at 780nm. The laser wavelength is selected via a software interface and is controlled by an external wavemeter and reference cavity. This laser was used for quasi-resonant excitation of QDs in Chapter 6. The Ti:S laser is water-cooled to 20°C with de-ionised water.

Spectra Physics Tsunami laser

The Tsunami is a tunable pulsed laser source with a wavelength range of 750-950nm. The typical power output of the laser is 1.7W at 800nm. The Tsunami is pumped by 532nm radiation from the Millenia X frequency doubled Nd:YAG laser. The pulses produced by the laser have a duration of <100fs with a repetition rate of 80 MHz. The wavelength of the laser is adjusted manually via micrometer controls on the top of the laser body. Water-cooling with de-ionised water keeps the laser at 18°C to ensure optimal operation conditions. This laser was used to obtain lifetime measurements from QDs in Chapter 6.

NKT Photonics SuperK Compact

The SuperK Compact is a super-continuum pulsed laser source which emits collimated light. This laser is extremely broadband, emitting over a range of 450-2400nm with a total output power of 110mW over this range. The laser emits 2ns wide pulses with an adjustable repetition rate of 1-20kHz. As the laser is extremely broadband, the laser undergoes spectral filtering in a custom-built enclosure before the light is fibre-coupled for use in experiments. The spectral filtering is achieved by a combination of a 900nm long-pass and 1000nm short-pass filter. This laser was used in both Chapter 5 and Chapter 6 to characterise nano-photonic devices. Due to the broadband pulsed emission of the SuperK, the measurements with the laser often required a cross-polarised excitation and collection to remove the laser background.

3.3.2 Confocal microscopy

The techniques used to measure the devices in this thesis all utilise a confocal microscopy set-up. Confocal microscopy allows for light to be directed to, and collected from, a small area of the sample, reducing the amount of background light collected. This background reduction compared to a standard microscopy set-up is due to unfocused light being filtered out of the image by including a pinhole before the detector. This can be seen in Figure 24. In the set-ups used in this thesis the

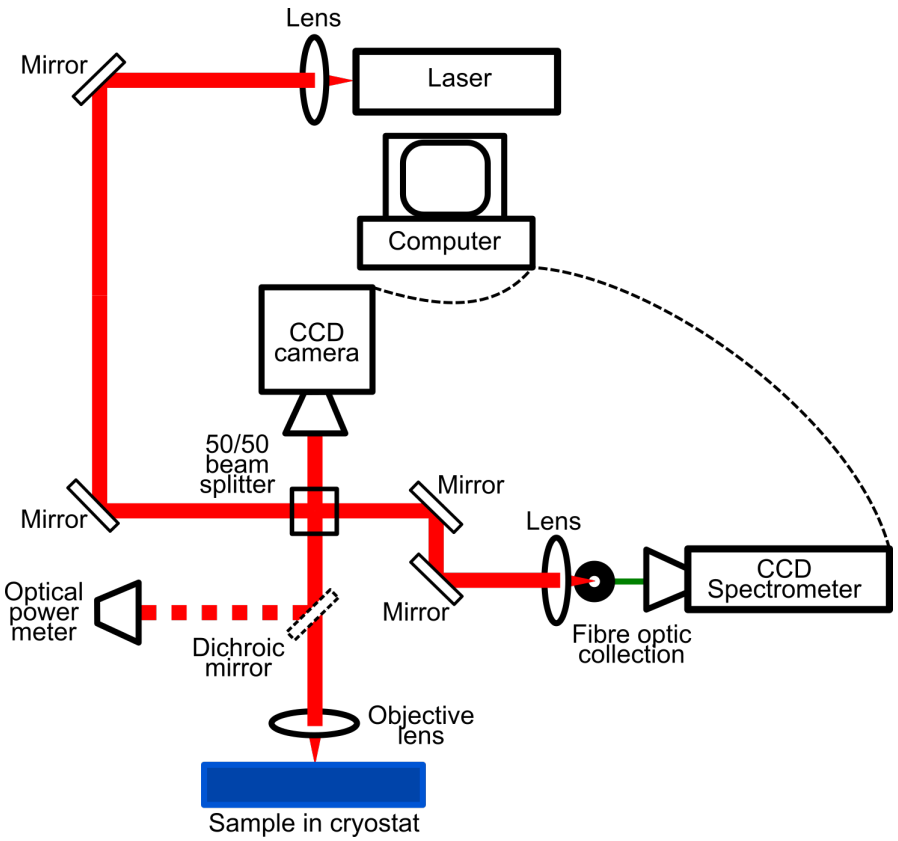

Figure 24: Schematic of a basic confocal microscopy set-up. The collection pinhole is defined by the radius of the single mode collection fibre. Pairs of mirrors in the excitation and collection paths allow for the beam direction and position to be adjusted. A camera aids in the alignment of the excitation and collection paths.

pinhole is defined by the core of a single mode optical fibre. The small radius of the fibre pinhole ($\sim 4.4\mu m$) allows for a near diffraction-limited laser spot to be incident on the sample. This allows for excitation of specific areas on the sample which is essential for measurements requiring a high degree of spatial precision. Additional optics can be included in the beam paths to facilitate more complex measurements. For example, '*Linear Polarisers*' (LPs) and '*Half-Wave Plates*' (HWPs) can be included in the excitation and collection paths to conduct polarisation-dependent measurements. The flexibility of confocal microscopy makes the technique highly popular for quantum optical experiments.

'*Micro-Photoluminescence*' (μPL) spectroscopy is one of the main confocal microscopy techniques used throughout this thesis. By using light from a laser or LED to create excitonic states in the QDs embedded in the semiconductor membrane, the emission from the QDs can be used to probe the systems as embedded emitters. The QDs can either be excited non-resonantly, quasi-resonantly or resonantly. In non-resonant excitation, the energy of the excitation photons is larger than the

band gap of the semiconductor. This creates excitons in the bulk semiconductor which emit energy non-radiatively and relax into one of the lower energy QD bound states where the electron and hole recombine to emit a photon at the energy of the QD transition. Quasi-resonant excitation uses a light source with a photon energy below the band gap of the bulk semiconductor but higher than the *s*-shell in the QD. This excites excitons in either the wetting layer or higher energy QD shells (*p*,*d*...). This scheme greatly reduces the amount of background light produced by the system. Quasi-resonant excitation can also be used to pump individual QDs via higher order state excitation. This reduces the relative brightness of other QDs with different higher order state energies to the target QD. Finally, in resonant excitation the energy of the excitation photons matches the energy of the QD emission exactly. This allows for only a single QD to be excited. Figure 25 shows

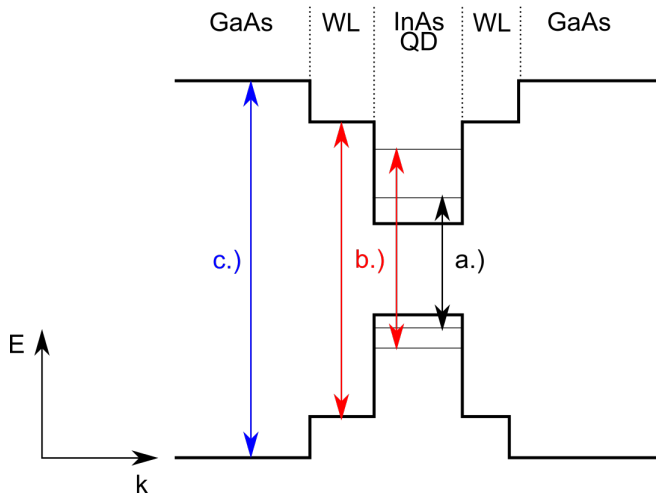

Figure 25: Simplified band structure diagram of an InAs SKQD embedded in a GaAs semiconductor, showing the three PL excitation schemes energetically. The band gap of GaAs is larger than that of the wetting layer (WL) which is larger than the energy of the QD transmissions. a.) Shows resonant excitation where the lowest energy QD transition is excited directly. b.) Shows quasi-resonant excitation where an exciton is created in either the WL or in a higher shell QD state. c.) Shows non-resonant excitation where an exciton is created in the bulk GaAs.

each of the three excitation schemes in a band structure diagram. Light emitted from the QDs is emitted directly into the optical modes of the nano-structures, allowing for the dynamics of these structures to be probed directly. The light can then be scattered off the sample and collected to be analysed using a spectrometer. The spectrometer displays the intensity of light collected as a function of wavelength. The operation of the spectrometer is discussed in more detail in Section 3.3.4. The small excitation and collection spot allow for single QDs or photonic structures to be selected and measured. If a low power light source is used, the emission of individual QDs can be seen. However, if a high power light source is used, the single QD emission features are indistinguishable from the broad QD ensemble background. High power measurements are ideal for probing photonic modes due to the broadband nature of the QD ensemble. Mirrors in the excitation and collection

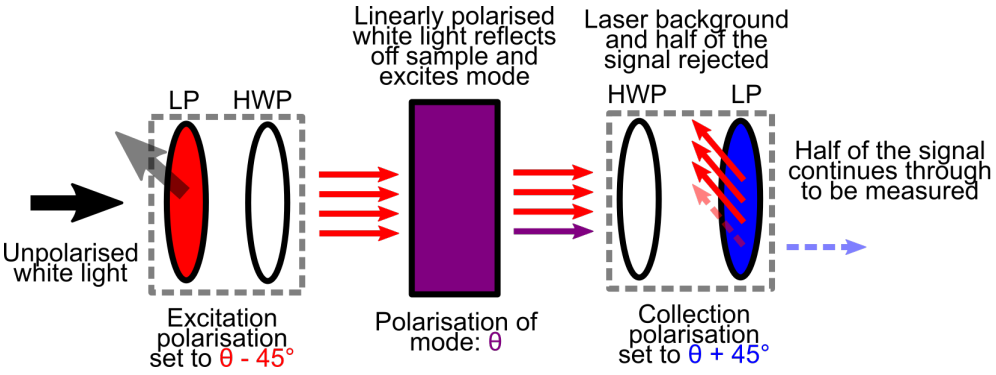

Figure 26: Schematic showing how a cross-polarised white light reflectivity measurement rejects laser background whilst obtaining a clear signal from an optical mode. The linear polarised input weakly excites the mode as it is 45° out of phase with the polarisation of the optical mode. The collection polarisation is orthogonal to the excitation laser polarisation and so rejects the laser background. The mode signal is partially transmitted through the collection optics as it is 45° out of phase with the collection polarisation. The remaining signal is extremely clear as the laser background has been strongly suppressed.

paths, as shown in Figure 24, allow for the spatial separation of the excitation and collection on the sample. This enables measurements of transmission through photonic structures.

In Chapter 5 and Chapter 6, white light reflectivity measurements are performed to measure the properties of photonic structures. White light reflectivity measurements allow for the photonic properties of structures to be measured without the need for embedded emitters. A super-continuum laser (see Section 3.3.1 - *SuperK*) is incident on the sample through a confocal microscopy set-up. The presence of photonic modes in the nano-structures will cause certain wavelengths of light to be scattered differently, creating features at these wavelengths on the spectrometer readout. To discern between background laser scatter and the measurement signal, use of a cross-polarisation set-up is often required. In this scheme, the polarisation of the excitation and collection paths in the confocal microscopy set-up are set to be orthogonal to each other. This is achieved by inserting a linear polariser and a half-wave plate into the beam path in both the excitation and collection paths. If the optical mode to be measured is strongly linearly polarised (e.g. PhCC modes), then if the excitation and collection polarisations are set at 45° to the mode polarisation (whilst orthogonal to each other), the mode can be measured whilst rejecting the maximal amount of laser background. This cross-polarisation method requires fine adjustments of the polarisation to obtain the clearest signal, therefore, an additional quarter-wave plate is often included to aid with fine adjustments to the polarisation. Figure 26 shows a schematic of the operation of a cross-polarised measurement.

3.3.3 Time-resolved measurements

Measurements which require information on the arrival time of photons are known as '*time-resolved measurements*'. Such measurements cannot be conducted using a '*Charge-Coupled Device*' (CCD) due to its slow time-resolution. Instead, time-resolving detectors such as '*Avalanche Photodiodes*' (APDs) or '*Superconducting Nanowire Detectors*' (SCNDs) are required. APDs turn single photons into measurable electrical pulses by exploiting the photoelectric effect. In an APD, a large reverse bias is applied across a semiconductor diode. An incident photon will create an electron hole pair which will dissociate quickly into free carriers due to the large electric field across the diode. These carriers will be greatly accelerated by the large electric field. When these high velocity charge carriers collide with the semiconductor lattice they will produce additional electron hole pairs due to their high kinetic energy. The process then repeats with the newly created charge carriers. Therefore, a single photon can create a large number of charge carriers. The APDs used in this thesis have a response time of $\sim$400ps. If two photons are incident on the APD within the response time they will not be resolved.

In SCNDs, semiconductor nanowires are held at cryogenic temperatures causing them to become superconducting. When a photon is incident on a nanowire and is absorbed, the temperature of the nanowire where the photon was absorbed is increased. This increase in temperature raises the temperature of the nanowire above the threshold temperature required for the nanowire to be super-conducting. This induces an increase in resistance of the nanowire. The increased resistance causes a voltage pulse from the system which is measured as the signal of a photon detection. Compared to APDs, the response time of SCNDs is much faster. The response time of the SCNDs used in this thesis was $\sim$15ps. Therefore, SCND are the preferred choice of equipment for measurements requiring an ultra-fast timing response and precision. However, APDs can operate at room temperature and therefore are easier, quicker and require fewer resources to use than SCNDs. Moreover, for most measurements the ultra-low response time of the SCNDs is superfluous.

The photons detected by either APDs or SCNDs must be sorted by arrival time. The detectors do not perform this task themselves and so additional equipment is required. In this thesis, a Stanford Research System SR400 photon counting unit is used to collate the signals sent from the single photon detectors into time-resolved bins. Each bin has a set width in time, the number of signal pulses detected in the width of the bin define the height of the bin on a histogram. This time-resolved information can be used to measure the lifetime of an excitonic state in a QD or the $g^2(0)$ of a single photon source.

3.3.4 Spectroscopy

To investigate the spectral properties of light collected from a sample, separation of the light by its spectral properties is required. This is achieved by using a grating spectrometer. Diffraction gratings are used to spatially separate light of different wavelengths. This light is then incident on a liquid nitrogen cooled CCD sensor, where the intensity at each spatially-separated wavelength is measured. The system is calibrated using a laser source with a well-defined wavelength so that the absolute wavelength of each spatially-separated photon stream is known. The spectrometer used in this thesis is a Princeton Instruments Acton SpectraPro SP750i. This system contains three different diffraction gratings with different spectra resolutions with a maximum resolution of 16μeV. The higher resolution gratings exhibit a much smaller operation bandwidth and lower intensity than gratings with lower resolution. The low resolution gratings are often used for initial characterisation before switching to the higher resolution gratings for more detailed studies. The central wavelength of the gratings can be adjusted to allow for spectrometry over a large range of wavelengths. As the CCD is silicon based, the detector efficiency is greatly reduced at energies close to the band-gap of silicon (>1000nm).

The spectrometer contains a narrow aperture side exit port which allows for one of the spatially-separated wavelengths to be directed out of the spectrometer and into an optical set-up. This allows the spectrometer to act as a tunable spectral filter. This operation of the spectrometer is essential for single photon level measurements as the signal background is greatly reduced by the spectral filtering.

3.3.5 Cryostats

All of the work carried out in this thesis required the samples to be at cryogenic temperatures. Therefore, the operation of the cryostats used to hold the samples at ultra-stable and low temperatures were essential to this work. Two types of cryostat were used in this thesis; a continuous flow cryostat and a bath cryostat.

In a continuous flow cryostat, the sample is placed on a copper cold finger in a small high-vacuum chamber. The chamber has a glass optical window above the sample to enable optical access to the sample. The copper cold finger is mounted in a heat exchanger through which liquid helium is pumped from a dewar. Upon touching the copper, the helium boils off and is pumped out of the cryostat. This process causes the copper to be cooled to cryogenic temperatures, typically between 4-8K. As the sample is mounted directly onto the copper in a high-vacuum chamber, strong thermal coupling exists between the sample and the copper. Therefore, the sample is also cooled to cryogenic temperatures. The gaseous helium which boils off is recycled using a helium re-liquefier. The cryostat itself is mounted on both manual translation stages for coarse alignment, and piezo-electric

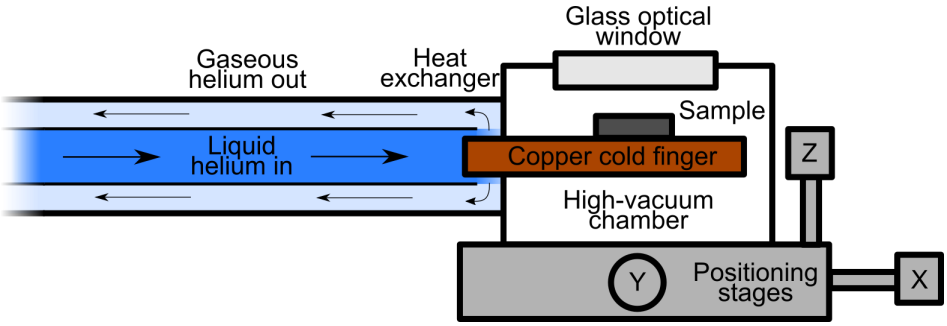

Figure 27: Diagram of a continuous flow cryostat.

nano-positioning stages for fine alignment. Due to vibrations from the helium pump, the alignment of the system drifts over time. This can reduce the accuracy of measurements which require a long acquisition time.

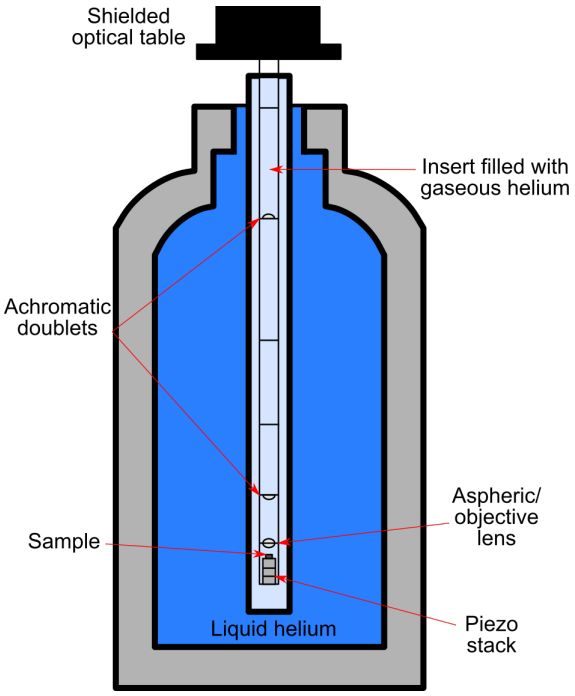

Figure 28: Diagram of a bath cryostat.

The other type of cryostat, the bath cryostat, is depicted in Figure 28. In this system, an insert tube containing the sample is placed directly in a dewar of liquid helium. The insert is pumped to a high-vacuum before being filled with a small amount of helium gas to facilitate thermal exchange with the liquid helium. All of the set-up components reside on an optical table which sits on top of the dewar. A glass window in the top of the dewar allows for light to be sent down to, and collected from, the sample. Inside the inset, a cage holds two achromatic doublets and a lens above

the sample which focus the light onto the sample. The sample is placed in a ceramic chip carrier on top of a stack of piezo-electric nano-stages. These stages and the chip carrier can be electrically controlled whilst in the dewar as the wiring is run up through the cage in the insert. The dewar can hold up to 90L of helium and can be refilled as the helium depletes. This allows for samples to be held at cryogenic temperatures indefinitely. The bath cryostat can also be surrounded by a superconducting electro-magnet which enables a magnetic field of up to $|B| = 5T$ to be applied across the sample. This magnetic field control is required to measure directionality of QD emission and provides a small QD emission energy tuning range. The measurements of the cantilever structures in Chapter 5 were conducted in a bath cryostat without magnetic field capabilities. In Chapter 6, all of the post-characterisation measurements were conducted in a superconducting magnet bath cryostat.

Bath cryostats exhibit superior temperature and mechanical stability over flow cryostats. The helium pump required to operate a flow cryostat introduces additional vibrations into the system, moreover, the helium flow rate is not constant and so the temperature of the system will fluctuate. Furthermore, the bath cryostat sits on an air-damped platform for extra stability. This makes bath cryostats the system of choice for samples that require high stability and long run-time measurements. Moreover, samples in a continuous flow cryostat are frequently thermally cycled as the helium pump is switched off between measurements to reduce helium usage and when changing the dewar to replenish the helium supply. Therefore, any samples which must be kept cold to prevent thermal cycle related degradation of the structures must be placed in a bath system. Continuous flow cryostats are much more suited to samples which require frequent switching in and out of the cryostat. Switching samples in a continuous flow cryostat is much faster and easier than in a bath cryostat. Moreover, continuous flow cryostat systems are significantly smaller and more flexible than bath systems. Furthermore, the optics are more accessible as they do not need to be placed on top of the dewar. This makes aligning and altering the experimental set-up much easier.

3.4 Computational methods

While the main focus of this thesis is the experimental study of photonic nano-structures, an essential part of the experimental process was the use of computational methods to design and test prototype structures. This section will present the simulation methods that were used throughout this thesis. The operation of the methods will be explained along with their uses.

3.4.1 Finite-Difference Time-Domain (FDTD) simulations

Simulations of how light interacts with the nano-photonic structures used in this thesis are essential to the design and optimisation of the experimental structures. The majority of the simulations conducted in this thesis used a '*Finite-Difference Time-Domain*' (FDTD) method to probe the time evolution of light propagating in photonic structures. Lumerical FDTD software was used to

run all FDTD simulations in this thesis. Lumerical FDTD is a commercial grade software package provided by Ansys.

The principle of operation of the FDTD method is time-iterative solving of Maxwell's equations in a 3D grid of cells. The form of Maxwell's equations used in the FDTD method are the differential, time-dependent versions given by:

$$\nabla \times \mathbf{E} = -\frac{\partial \mathbf{B}}{\partial t} \tag{34}$$

$$\nabla \times \mathbf{H} = \mathbf{J} - \frac{\partial \mathbf{D}}{\partial t} \tag{35}$$

and the two remaining time-independent Maxwell equations:

$$\nabla \cdot \mathbf{D} = \rho \tag{36}$$

$$\nabla \cdot \mathbf{B} = 0 \tag{37}$$

where $\mathbf{E}$ is the electric field, $\mathbf{H}$ is the magnetic field, $\mathbf{D}$ is the electrical displacement field, $\mathbf{B}$ is the magnetic induction field, $\mathbf{J}$ is the current density and ρ is the free electric charge. $\mathbf{D}$ and $\mathbf{B}$ can be written as:

$$\mathbf{D} = \epsilon_0 \epsilon_r \mathbf{E}$$

and:

$$\mathbf{B} = \mu_0 \mu_r \mathbf{H}$$

respectively. Here, ϵ_0 and ϵ_r are the free space and relative dielectric permittivity respectively, and μ_0 and μ_r are the free space and relative dielectric permeability respectively. The structure to be simulated is defined by a dielectric map ($\epsilon_r(r)$) which is created in '*Computer-Aided Design*' (CAD) software. When the simulation is run, this dielectric map is partitioned into small cells known as '*Yee Cells*' [143]. The dimensions of the Yee cells are defined by the user. By meshing the dielectric map $\epsilon_r(r)$ onto the grid of Yee cells, an approximation of the dielectric map is formed from the cells, $\epsilon_r(\Delta r)$ as shown in Figure 29 a.). This approximation, known as a '*Yee lattice*', defines the finite spatial areas in which Maxwell's equations will be solved. Figure 29 b.) shows how the electric and magnetic field components are calculated in each Yee cell. The electric field components are calculated along the edges of each cell whereas the magnetic field components are calculated at a normal to the faces of each cell.

Various light sources such as dipole emitters or mode sources can be embedded in the structures to inject light into the system. The spectral and spatial properties of these sources is fully customisable within the FDTD software interface. This enables a vast range of excitation schemes which can mimic any experimental situation, from narrow linewidth embedded emitters to super-continuum lasers. When the simulation is started, the light sources in the system emit for a length of time defined by the user. The FDTD algorithm calculates the results of Maxwell's equations for each

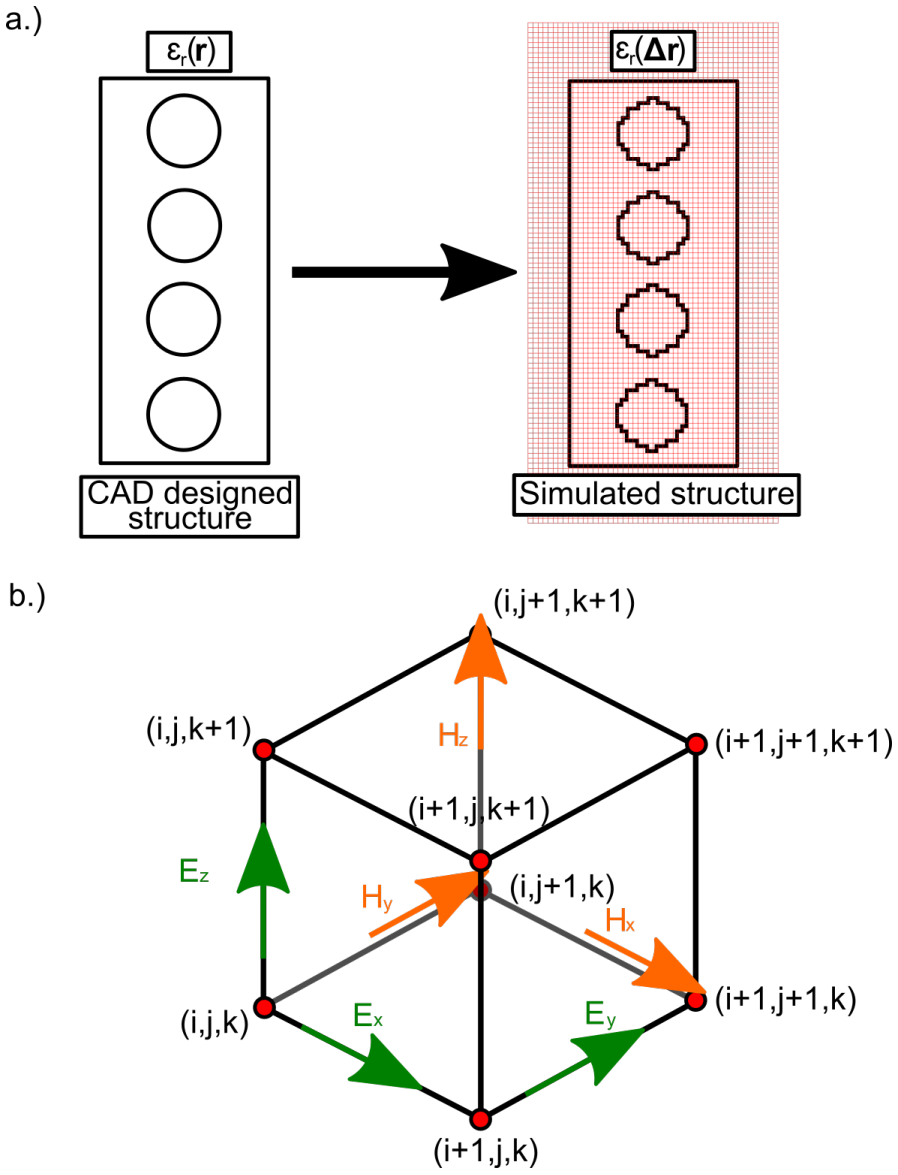

Figure 29: a.) Schematic showing the difference between designed and simulated structures after the structure has been meshed through the Yee cell grid. b.) Single Yee cell showing where the calculation of each field component is calculated in a cell. The electric field components are calculated along the edges of the cells whereas the magnetic field components are calculated at a normal to the Yee cell faces.

Yee cell, iterating over discrete time steps (Δt) which are also defined by the user. The algorithm proceeds as follows from the starting point $t = 0$:

1.) Calculate the electric fields in each cell at t from the results for the electric field at $t - \Delta t$ and the magnetic fields at $t - \frac{\Delta t}{2}$.

2.) Calculate the magnetic fields in each cell at $t + \frac{\Delta t}{2}$ from the results for the magnetic field at $t - \frac{\Delta t}{2}$ and the electric field at t.

This process is repeated for each iteration in time until the simulation is terminated. The termination of the simulation occurs either after the simulation reaches the user-defined end time T, or the energy remaining in the system drops below the set threshold [144].

To collate data from the simulation, monitors must be included in the simulation region. The monitors define both an area in which the data will be collected and what data will be recorded (e.g. the electric field intensity). The spectral bandwidth of these monitors is the same as the bandwidth of any light sources by default, however, the bandwidth can be set independently of the sources or other monitors if desired. Data analysis protocols can be programmed into custom monitors to collate and process data upon the completion of a simulation. For example, the Q-factor of an optical cavity can be calculated from the time-dependence of the electric field intensity in the cavity. Monitors record the dependence over the cavity area and at the end of the simulation the decay is fitted with an exponential decay lineshape to determine the Q-factor of the cavity mode.

One of the key considerations when configuring an FDTD simulation is the trade-off between simulation accuracy and runtime. As shown in Figure 29 a.) the Yee lattice can reduce the resolution of the structures, especially small or complex shaped features. To combat this, the size of the Yee cells can be reduced, this improves the resolution of the simulation, however, the simulation runtime will increase due to the increase in the number of cells. The FDTD software contains some features to reduce the overall runtime of the simulation without the need to reduce the resolution of the Yee lattice. Firstly, symmetric boundaries can be defined. These boundaries can be defined as either mirror or rotational symmetries and either symmetric or anti-symmetric. By defining the boundaries in this way, only part of the structure needs to be simulated. The other parts of the structure have their fields calculated via a transformation of the results from the reduced simulation region, according to the type of boundary symmetry present. This reduces the number of Yee cells required to simulate the full structure whilst the resolution remains the same. Symmetries can be applied in all three dimensions, as such, structures with many axes of symmetry can have their simulation runtime greatly reduced. Secondly, a non-uniform Yee lattice can be used. The size of the Yee cells can be altered across the structure to increase the resolution in complex regions whilst reducing the resolution in areas which do not require such a fine resolution, such as the air cladding of a NBW. Any increase to the resolution in these areas will not improve the accuracy of the simulation. This increases the accuracy of the simulation over the complex region whilst allowing for the overall runtime of the simulation to remain low due to the lower resolution areas. By combining symmetric boundaries with non-uniform Yee lattices, the runtime of high accuracy simulations can be greatly reduced.

FDTD simulations were used in Chapter 4 to calculate the photonic band edge of W1 PhC waveguides coated with various thicknesses of a dielectric material. FDTD simulations were also used extensively in Chapter 5 to perform parameter sweeps on a 1D PhCC to optimise the design and to conduct a Monte Carlo simulation to quantify fabrication error on the optimised design. Finally, in Chapter 6, FDTD simulations were conducted to probe the transmission properties of a waveguide coupled H1 PhCC.

3.4.2 MIT Photonic Bands (MPB) simulations

'*MIT Photonic Bands*' (MPB) is a free software package used to calculate the band structure of a photonic system [145]. While FDTD can be used to calculate band structures, the method MPB uses is much less computationally intensive and so results in much faster simulations. MPB uses a frequency-domain method to calculate the dispersion relationship, and therefore the band structure of a photonic system. The approach used is a finite matrix eigenproblem method, using linear algebra to find the eigenvectors and eigenvalues in a planewave basis.

MPB was used to calculate the NBW band structure in Chapter 5.

3.4.3 Monte Carlo method simulations

While individual simulations can offer an insight into a specific nano-structure, multiple simulations are required to gain insight into the effect of altering the structure parameters. Parameter sweeps are essential in the optimisation process when designing nano-structures. By simulating the entire parameter space, the response of the system to systematic changes of each parameter can be acquired. Due to fabrication imperfections, when nano-structures are fabricated, an error on the size of their features is present. This disorder is difficult to quantify in a regular simulation due to the random nature of the error. However, the robustness of nano-structures to fabrication imperfections is a key factor in the design process, therefore, it is important to know how the system will respond to different levels and sources of error.

The '*Monte Carlo*' method is a technique invented by John von Neumann and Stanislaw Ulam, which employs repeated random sampling of a distribution to obtain a numerical result [146]. The method can be used to solve deterministic problems using random sampling and the law of large numbers to achieve an accurate result. A classic example of the operation of the Monte Carlo method is the estimation of π. A circle of radius r is circumscribed by a square with sides of length $2r$ as shown in Figure 30 a.) and b.). The probability of any random point inside the square also being inside the circle is given by the ratios of the areas of the two shapes. The probability of a random point being in the circle is proportional to π, therefore the value of π can be estimated by counting the proportion of random points in the circle to those outside of it. For this experiment,

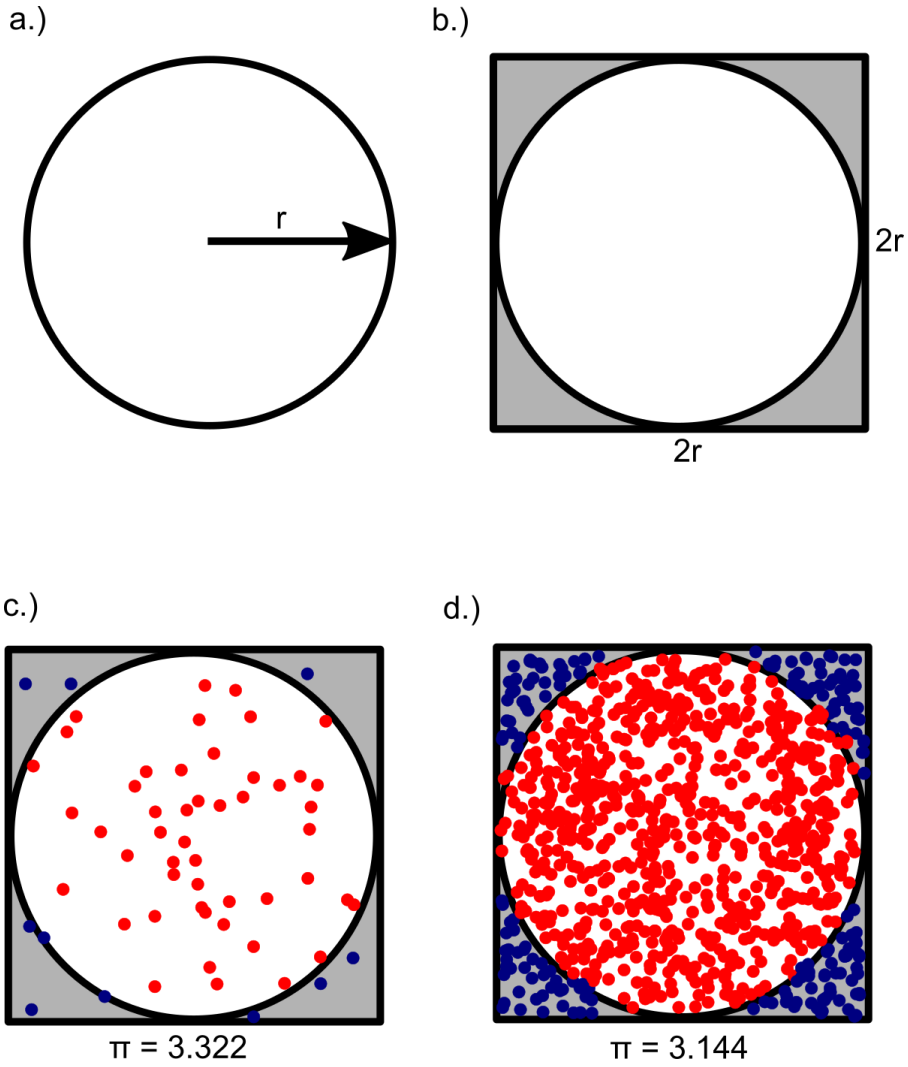

Figure 30: Diagram showing how the value of π can be estimated using a Monte Carlo simulation method. a.) A circle of radius r is defined and circumscribed by a square with sides of length $2r$ (b.)). Random points inside the square are chosen. The proportion of points in the circle is proportional to π allowing for a value of π to be estimated by calculating this proportion. c.) and d.) Show the effect of increasing the number of points chosen on the accuracy of the estimation. A larger number of points provides a more accurate estimate compared to a low number of points.

the value of $r = 1$ and the circle is positioned at point (0,0) in space. The Monte Carlo method will proceed as follows:

1.) Generate a random x and a random y value inside the square $(-1 < x, y < 1)$.

2.) Calculate $x^2 + y^2$, which will determine the radial location of the point. If this value is > 1 the point will be outside of the circle, if this value is < 1 the point will be inside the circle.

3.) Repeat steps 1.) & 2.) a set number of times.

4.) Calculate the proportion of points inside the circle and use this to calculate a value of π.

5.) Repeat steps 1.) - 4.) a set number of times and take the average of these results as the final value of π.

As can be seen in Figure 30 c.) and d.), by increasing the number of random points in each estimation, the accuracy of the result is increased. However, even for a relatively small number of events, the estimate is moderately accurate.

The generation of random numbers is required for the operation of the Monte Carlo method. However, computers cannot generate truly random numbers. Any method that computers use to generate apparently random numbers is deterministic. Despite this, computers can generate sequences of pseudo-random numbers which exhibit good random properties even for very long sequences. The most common pseudo-random number generation algorithm is a recursive technique known as the '*linear-congruential generator*'. In this algorithm, the sequence of pseudo-random numbers is given by:

$$x_{n+1} = (Ax_n + C) \bmod(m) \tag{38}$$

where A, C and m are large integers which can be adjusted to ensure a sequence of adequate length and randomness is produced.

In this work, the Monte Carlo method was used in Chapter 5 to simulate the effects of radii fluctuations in 1D PhCC air holes on the cavity mode wavelength and Q-factor. The radius of each air hole was considered independently and assigned a value from a uniform distribution about the hole radius. The range of the distribution was proportional to the radius of the hole, either 2, 5 or 10% of the hole radius. Lumerical FDTD contains a built-in Monte Carlo method tool which allows for the parameters, such as the number of runs and parameter variation distribution functions, to be customised. The built-in tool can be used to run and collate data from all the simulations. Alternatively, the tool can generate individual simulation files for each iteration in the Monte Carlo simulation. Each individual simulation will have a set of air holes with different radii. Running each simulation will provide a cavity mode wavelength and Q-factor for the specific hole radii variation in that simulation. These results are then plotted in histograms to be analysed. Due to the simulation volume and computational intensity of each FDTD simulation produced in the Monte Carlo method in Lumerical, each Monte Carlo simulation was iterated 50 times and the generated files were run separately using a high-performance computer.

This page intentionally left blank.

4 Site-controlled quantum dot growth and *in-situ* strain tuning of quantum dots for scale-up of nano-photonic systems

4.1 Introduction

Scale-up of nano-photonic systems is essential for the success of a III-V semiconductor based quantum network. The necessity of scale-up comes from both an intuitive and scientific requirement. Intuitively, the larger the number of qubits in a system, the faster it will be able to process and the more complicated tasks it can complete. Moreover, from the Di-Vincenzo criteria [11], a universal set of quantum gates is required to achieve a successful quantum computation system. It has been shown by Barenco et al. that a universal set of quantum gates can be realised by an arbitrary number of one-qubit, and a single two-qubit quantum gate [38]. Therefore, scale-up of the number of resonant QDs in a nano-photonic system is a key requirement for the realisation of QIP in III-V semiconductor systems.

The requirement for scale-up applies both to scale-up of the number of resonant integrated structures on a chip, such as optical cavities, and scale-up of the number of resonant QDs in these structures. While Chapter 5 is concerned with device scale-up, this chapter will focus on the scale-up of the number of resonant QDs in a nano-photonic system.

The most common method used, and the method used in this thesis, to grow QDs is Stranski-Krastanow growth (see Section 2.2.1). QDs grown via the SK method exhibit excellent optical properties, however, it is not possible to control where the QDs will grow and at what wavelength a specific QD will emit at once grown. This is due to the inherent randomness of the strain relaxation process by which SKQDs nucleate. This fact makes integrating multiple resonant QDs in a single nano-photonic structure extremely challenging. Currently, two methods for obtaining resonant QDs in a nano-photonic structure exist. The first is to fabricate the structure without prior knowledge of the QDs. By then characterising the QDs in the structure, a multitude of QD energy tuning regimes exist which allow for the emission energy of QDs to be altered, bringing QDs into resonance (see Section 2.3). One of the main drawbacks of this approach is the limitations of the QD tuning methods. Most tuning methods have a short range, fundamentally limiting their use. Moreover, many tuning schemes cannot tune individual QDs, instead the entire ensemble is tuned. Finally, the spatial location of the QDs is completely random. Some nano-photonic structures only exhibit desirable phenomena if a QD is situated in a precise location in the structure, by relying solely on QD emission energy tuning, no control is possible on the location of QDs. This makes attempting to observe such effect entirely non-deterministic and highly irreproducible. The other approach is quantum dot registration (see Section 2.3.5). In this approach, sets of resonant QDs are located pre-fabrication. This allows for the structures to be fabricated around known ensembles of high quality resonant QDs, therefore, QDs can be positioned in precise spatial locations

in a nano-photonic structure. While this offers a degree of control over the QD properties, QD registration has many drawbacks also. Due to uncertainty in both the registration and fabrication of devices, the spatial positioning of QDs is imperfect. Moreover, by fabricating structures around the registered QDs, changes to the charge and strain environment often cause the energy of the QDs to shift after the fabrication is completed. The registration process is also highly involved and requires valuable space on the sample be taken up by alignment markers. Finally, although the position of the QD in the structure can be controlled, the absolute position on the structure is still random. Ultimately, the best current approach is to combine QD registration with QD emission energy tuning methods.

An ideal solution would be for arbitrary control over both the QD emission energy or spatial position. While control over both the energy and position simultaneously is unrealistic currently, recent advances in SCQDs has made the concept of full control over the position of QDs possible (see Section 2.2.3). This high degree of spatial control over the QDs can be combined with QD energy tuning methods to facilitate scale-up. A recent paper by J.Grim et al. details a local strain tuning method which exhibits highly localised QD energy tuning over a large range with fine control over the tuning range [81]. Such a method, combined with SCQD would be the ideal pairing for facilitating scale-up of resonant QDs in nano-photonic devices.

In this chapter, the process of growing SCQD will be discussed along with how each growth consideration affects the properties of the resulting QDs. Results from a SCQD sample showing the effect of varying the growth parameters are presented and analysed. The local strain tuning method first presented in reference [81] is detailed next, as a tool to be used in tandem with SCQD to achieve scale-up. After discussing the operation and fabrication pertaining to the strain tuning scheme, results from tests of the method are presented. Various parameter-sets are compared to find the optimal set which maximises the QD tuning range. The maximum tuning range of the system is presented and discussed. Finally, the strain tuning method is used to tune individual QDs into resonance.

4.2 Site-controlled quantum dot background

Section 2.2.3 gives a basic overview of the mechanism by which SCQDs are grown, a more detailed account will be given here.

4.2.1 Site-controlled growth via etched nanoholes

InAs QDs grown on a GaAs substrate are inherently strained by the lattice mismatch between the compounds. In SKQD growth, the strain is allowed to relax naturally when a critical thickness of InAs is reached on a planar surface. This results in the QDs nucleating at random locations. In SCQD growth, the surface of the substrate is modified to create regions where QDs will nucleate

preferentially. This is done by etching nanoholes into the GaAs substrate before depositing the layers of InAs. The nanoholes on the surface of the GaAs have a lower chemical potential than the planar surface around them, this can be seen by considering the equation for chemical potential:

$$\mu(x) = \mu_0 + \gamma\Omega\kappa(x) + \Omega E_s \tag{39}$$

Where μ_0 is the chemical potential of a flat surface, γ is the surface free energy per unit area, Ω is the atomic volume, κ is the curvature of the surface and E_s is the local strain relaxation energy relative to a flat surface. This equation for the chemical potential shows that the chemical potential for a concave surface is lower than for a planar surface. Conversely, a convex surface has a higher chemical potential than a planar surface [147]. As the chemical potential of the nanoholes is lower than the rest of the surface, the deposited atoms migrate preferentially towards the holes. In addition to their concave shape, the nanoholes also possess many stepped edges as a result of the etching process. These reduce both the strain and free energies of QDs which nucleate on them, thus, these sites are preferential for QD nucleation [148]. This, coupled with the increased indium flux from the reduced chemical potential, provide a region with a higher QD growth rate than the surrounding surfaces. This can be seen from the equation for QD growth rate:

$$\frac{\partial h}{\partial t} = D\left(1 + |\nabla_s h|^2\right)^{\frac{1}{2}} \cdot \nabla_s^2 \mu \tag{40}$$

Where h is the height of the QD, t is the time, D is determined by the diffusivity, density and volume of the indium adatoms plus the surface temperature, ∇_s^2 is the Laplacian operator of the surface and μ is surface chemical potential from Equation 39 [149]. As the growth rate in the nanoholes is faster than for the planar surface, QDs will preferentially nucleate in the holes. Once nucleated, QDs will not grow in close proximity to the SCQDs as the surface energy is reduced by the nucleation of the QD in the nanohole. If the nanohole array parameters and growth conditions are optimised, this leads to pure single QD hole occupancy with no QDs growing off the array. An example of an array of nanoholes is shown in Figure 31.

4.2.2 Nanohole etching techniques for site-controlled quantum dots

The etching of the nanoholes is an essential step in the growth of SCQDs. The nanoholes need to be etched precisely and accurately with little variation between the holes. Two competing approaches exist for the etching of the nanoholes in the GaAs substrate: conventional EBL etching and '*Local Anodic Oxidation*' (LAO).

Firstly, the EBL nanohole etching will be discussed. Use of EBL to etch the nanoholes is by far the most popular approach used in SCQD samples. Using the EBL allows for rapid etching of many holes with extremely precise control over the parameters of the array and nanoholes. The nanoholes are etched in the same way that conventional structures are etched onto standard QD wafers, an EBL etch followed by a dry ICP etch [150], or a wet chemical etch [151]. While EBL

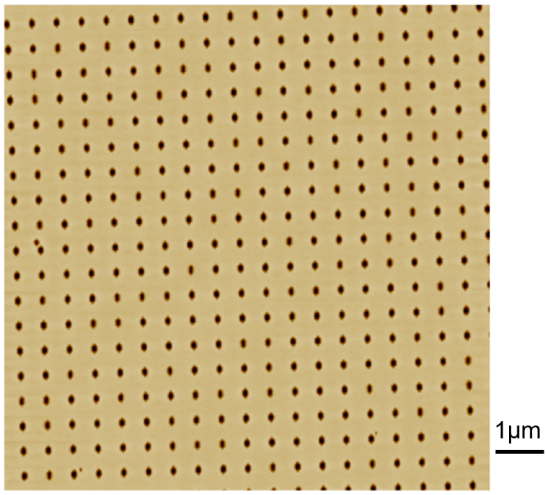

Figure 31: Atomic Force Microscopy (AFM) image of the surface of a SCQD sample showing an array of nanoholes etched to provide a surface where QDs will preferentially nucleate. (Image taken by Dr Charlotte Ovenden).

methods offer a high degree of fabrication precision a major drawback of the approach is the necessity to move the sample between growth and etch environments. This, coupled with the etch environment itself allows for contaminants to be incident on the surface of the wafer, either from processing chemicals or from etch debris. These contaminants degrade the optical properties of SCQD grown nearby by reducing their linewidths and increasing the probability of non-radiant decays occurring in the QD [152]. The detrimental effects of contaminants at the nanohole interface can be reduced by distancing the QD layer from the nanoholes by growing a buffer layer on top of the nanoholes. While the buffer improves the optical properties of the QDs, the definition of the nanoholes is reduced with increasing buffer thickness, as a result, the success rate of single QD occupancy is reduced. The effect of contaminants on the QDs can be reduced via a thorough cleaning of the nanohole etch interface post etch. This cleaning is shown to have a large effect on the quality of SCQD and removes the requirement for large buffer layers above the nanoholes [59].

The other, competing approach to EBL etching of the nanoholes is using LAO to create the nanoholes. Figure 32 shows a schematic of how the nanoholes are etched using LAO. A negatively charged '*Atomic Force Microscopy*' (AFM) tip is brought into close proximity with the surface of the semiconductor. Due to the presence of moisture in the surrounding air, a water bridge forms between the tip and the surface of the semiconductor substrate. The negatively charged tip causes negatively charged O^- and OH^- ions to form. These ions are accelerated towards the semiconductor surface by the electric field between the AFM tip and the substrate. Once the negatively charged ions reach the semiconductor, they react to form an oxide. The energy from the electric field provides the activation energy for the oxidation reaction, as this field penetrates

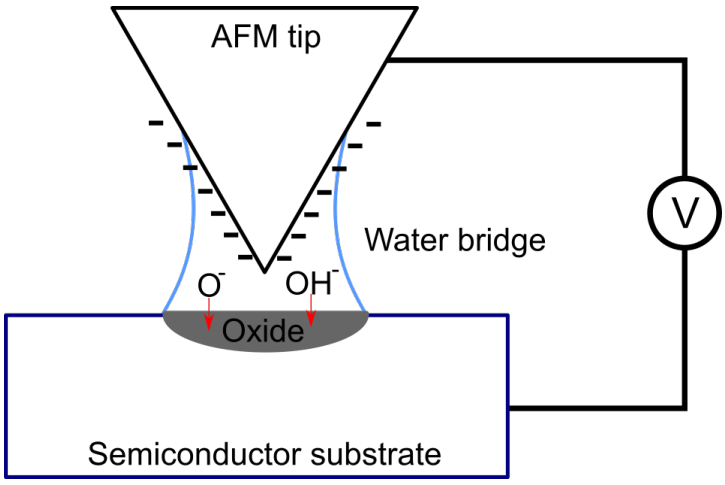

Figure 32: Schematic showing how LAO is used to etch the nanoholes for SCQD growth. The AFM tip is negatively charged and contacted to the semiconductor substrate.

into the semiconductor, the oxidation process continues beneath the surface of the substrate. At a certain distance from the tip, the field is no longer strong enough to provide the activation energy for the oxidation reaction. Therefore, the oxide will only penetrate into the substrate up to the point where electric field energy has reduced below the activation energy, allowing the depth of the nanoholes to be controlled by the strength of the applied bias. By holding the AFM tip over one area of the semiconductor substrate, a nanohole can be etched. Moreover, more complicated shapes can be etched by moving the tip whilst in close proximity to the surface [153]. After the LAO has been used to pattern the nanohole array, the oxide is removed from the substrate via a wet chemical etch or hydrogen cleaning, leaving an array of nanoholes [154]. The main advantages of LAO over EBL etching of the nanoholes are the removal of the fabrication interface, and the removal of organic masks required to etch with EBL, which are a prime source of contamination [154]. LAO etched samples can immediately be cleaned in an ultra-high vacuum environment after the oxidation process, limiting the time for contaminants to impinge on the surface. The main disadvantage of LAO is the shallowness of the holes. This limits the thickness of any buffer layer grown on the nanoholes, which can have a negative effect on the linewidths of the QDs [155].

The nanoholes on the sample measured in this chapter were etched using EBL and an ICP dry etch. This method was chosen for the speed and ease of the etching plus the superior depth of the nanoholes.

4.2.3 Site-controlled quantum dot parameter considerations

By altering the nanohole array parameters, the growth of SCQDs can be strongly influenced. The three alterable array parameter are the radius of the nanoholes, the depth of the nanoholes and the spacing between them, called the '*pitch*'. Due to the nature of nano-etching techniques, the radius

and depth of the holes are somewhat correlated. As the radius of the holes is increased so is the depth due to the additional etching in close proximity required. It has been seen that increasing the radius of the nanoholes increases the overall occupancy, whereas increasing the depth increases specifically the single QD occupancy [150]. Moreover, the height of the SCQDs increases with increasing nanohole radius. This leads to a red-shift in the emission energy of the QDs. Single hole occupancy is also seen to peak at a depth to area ratio of $d = 1.5A$ [156].

Alterations to the pitch of the nanohole array affect both the wavelength of the QDs and the occupancy of the nanoholes. When increasing the pitch of a nanohole array, it has been observed that the linewidths of the QDs decrease and the QD heights decrease [157]. Moreover, further studies of changing the pitch of the nanohole array have shown that there is a linear relationship between hole occupancy and array pitch [158].

Finally, altering the growth conditions of InAs on top of the nanoholes can affect the optical properties of SCQDs. It has been shown that increasing the temperature of the SCQD growth causes the QDs ensemble in the nanohole array to be more uniform in size [159]. It was observed that at lower temperatures, the QDs were larger than the nanoholes and so their size and dimensions were not well controlled. Whereas, at higher temperatures the QDs were the same size as the nanoholes. This caused the size of the QD to be controlled by the size of the nanohole. However, if the temperature is raised too high then no QDs will form due to indium re-evaporation [160]. Furthermore, after the In has been deposited and the QDs have formed, a step known as a '*growth interrupt*' can be initiated. By stopping the QD growth by shutting off the In supply and holding the growth chamber at a constant temperature for some time before capping the QDs, diffusion of the In is allowed to take place. In this diffusion process In migrates towards the low chemical potential nanoholes. By changing the length of time between shutting off the In supply and capping the QDs, the amount of diffusion can be controlled. The effect of changing the length of the growth interrupt on the SCQD properties is investigated in the next section.

4.3 Site-controlled quantum dot sample results

A series of SCQD samples were grown each with an identical set of parameter variations on the pitch, hole radius and EBL dosage of the nanoholes. The layout of the pitch and radius variations can be seen in Figure 33. The large parameter variations allow for the investigation of a wide range of potential combinations to ensure the entire parameter space is studied.

Each sample was grown with a different length growth interrupt (15, 30, 60 or 300s) to investigate the effect of the length of the growth interrupt on the optical properties of the SCQDs. For each different growth interrupt sample, the same measurements were conducted and compared. The sample was situated in a flow cryostat operating at 4K. An above band-gap (810nm) wide

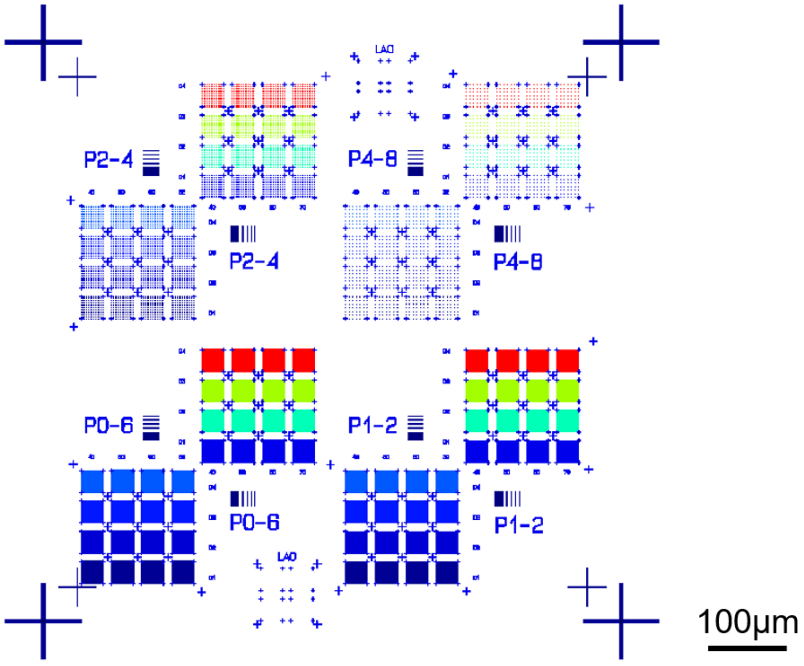

Figure 33: Schematic showing the layout of the different nanohole parameter variations on each SCQD sample. Four different array pitches ($a \in \{0.6\mu m, 1.2\mu m, 2.4\mu m, 4.8\mu m\}$) were fabricated with identical sets of nanohole radius variation grids. The radius of the nanoholes was drawn at $r \in \{32nm, 40nm, 50nm, 60nm\}$ and each array was fabricated at 8 different EBL dosages $D = 0.6 + 0.3n$, $n \in \mathbb{Z}$, $0 \leq n \leq 8$.

aperture LED source was used to excited PL in the QDs on the device. A high-resolution CCD camera was used to take wide field-of-view images of the PL emission from the samples. The field-of-view of the camera allowed each 4×4 grid to be imaged in a single exposure. Figure 34 shows a PL image from each pitch and growth interrupt combination apart from the $t_{int} = 60s$ which unfortunately exhibited no PL emission. These images were obtained from the higher dosage set of each pitch with a 900nm long-pass filter before the camera to remove the LED background. For all growth interrupts, a high amount of positioned QDs can be seen for $a = 0.6\mu m$ pitch. However, at this low pitch the single nanohole occupancy is difficult to discern over the background of QDs between the nanoholes. Increasing the pitch improves the single nanohole occupancy at all values of growth interrupt, this agrees with what has been seen previously in the literature [158].

Increasing the length of the growth interrupt appears to improve the single hole occupancy, most notably at larger pitches. This additional diffusion time allows for a large amount of In to collect in the nanoholes, improving the chances of a QD nucleating. The 300s growth interrupt shows

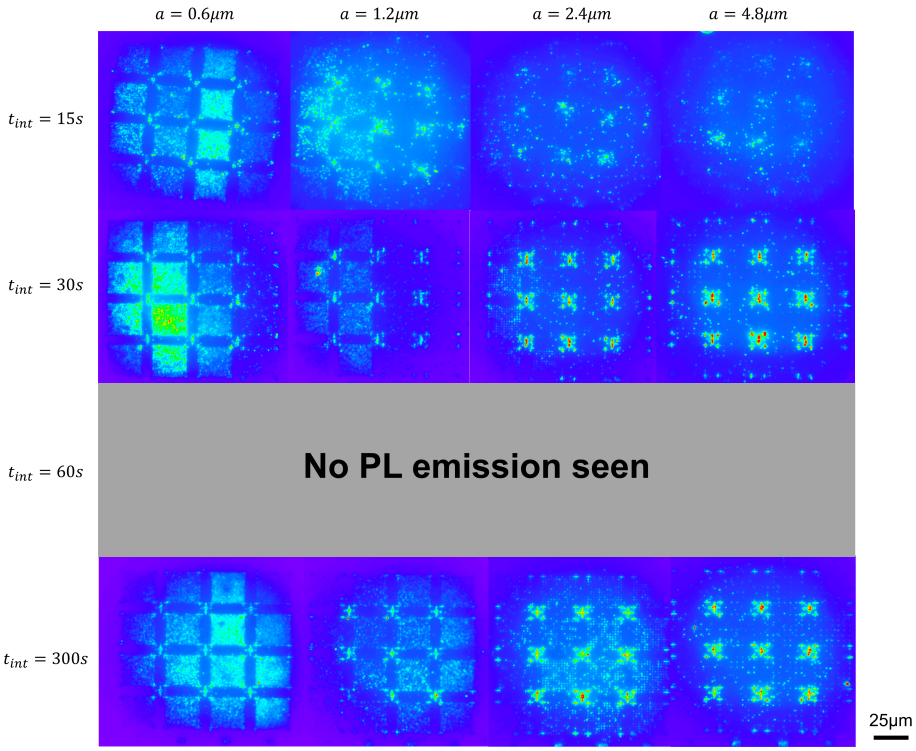

Figure 34: Wide aperture PL images of SCQD arrays with different nanohole array pitches a, from each of the four samples with different growth interrupt times t_{int}. In each 4×4 grid the drawn hole radius increases from left to right ($r = 32nm, 40nm, 50nm, 60nm$) and the EBL dosage increases from bottom to top ($D = 1.8, 2.1, 2.4, 2.7$). No PL emission was seen from the $t_{int} = 60s$ sample. Both the effect of changing the pitch and growth interrupt can be seen from the images. A high yield of area-controlled QDs is seen on all four samples at $a = 0.6\mu m$ Increasing the pitch reduces the number of QDs that nucleate outside of the nanoholes. Increasing the length of the growth interrupt increases the yield of positioned QDs especially at larger pitches. A pitch of $a = 2.4\mu m$ with a growth interrupt of $t_{int} = 300s$ appears optimal for yield and single hole occupancy.

excellent single nanohole occupancy at both $a = 2.4\mu m$ and $a = 4.8\mu m$ whilst maintaining a high yield of positioned QDs at lower values of the pitch. The highest yield seen in Figure 34 is for a growth interrupt of $t_{int} = 300s$ at a pitch of $a = 2.4\mu m$ in the larger nanoholes grids. For lower values of growth interrupt, the smaller nanoholes had a higher yield of single nanohole occupancy. This is likely due to these holes needing less In to fill up and a QD to nucleate. This would also suggest that shorter growth interrupts preferentially grow QDs at a shorter wavelength as the QDs will be smaller due to the lower amount of In diffused into the nanoholes. Figure 35 shows a comparison between two different growth interrupt samples' highest yield areas with a 900nm and 975nm long pass filter present before the imaging camera. By comparing the QD yield between the

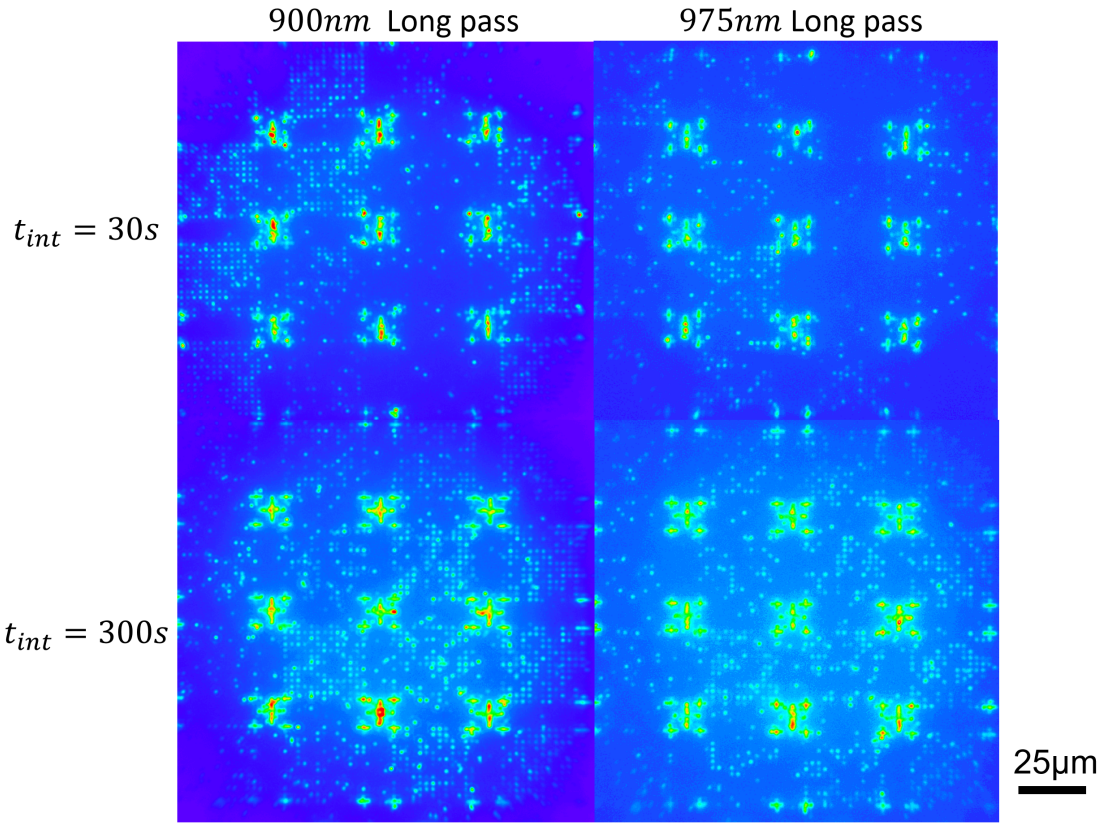

Figure 35: Comparison of the highest yield 4×4 areas from the $t_{int} = 30s$ and $t_{int} = 300s$ samples with a 900nm and 975nm long-pass filter placed before the imaging camera. At $t_{int} = 300s$, a higher proportion of QDs seen when the 900nm long pass filter is present remain visible when the 975nm filter is present, compared to on the $t_{int} = 30s$ sample. This suggests that the QD ensemble has a longer average wavelength for longer growth interrupts.

two different filter cases, the difference between the mean wavelengths of the two growth interrupt samples can be seen. For the $t_{int} = 30s$ sample, only $\approx 25\%$ of the QDs visible with the 900nm filter present are still visible with the 975nm filter. Whereas, on the $t_{int} = 300s$ sample $\approx 50\%$ of the QDs visible with the 900nm filter present remain visible with the 975nm filter present. This shows that the mean wavelength of the QD distribution must be at a longer wavelength for the longer growth interrupt case. This agrees with what is expected when considering the increased In diffusion facilitated by longer growth interrupts.

To supplement the high yield of single nanohole occupancy SCQDs seen on the $t_{int} = 300s$ SCQDs exhibiting narrow linewidths must be grown. A typical PL spectrum from a SCQD grown on a 30nm GaAs buffer above EBL patterned nanoholes is shown in Figure 36. The QD exhibits a

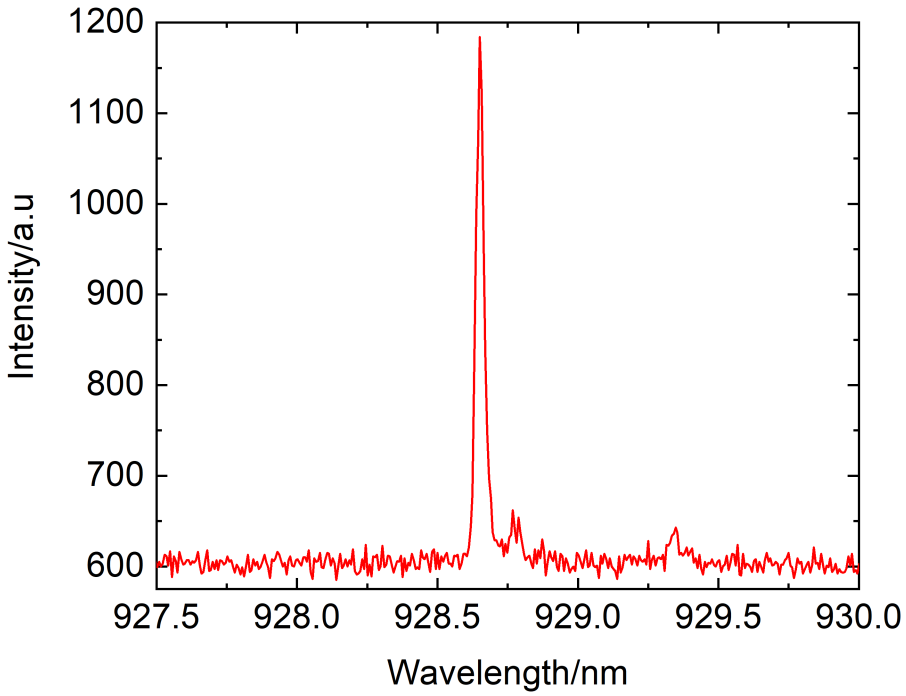

Figure 36: PL spectrum of a typical SCQD grown using EBL patterned nanoholes with a 30nm buffer layer betwen the nanoholes and the QD layer. The linewidth of the QD is $\Delta E = 40.5 \pm 1.4 \mu eV$

linewidth of $\Delta E = 40.5 \pm 1.4\mu eV$, a representative linewidth from the mode of the QD linewidth distribution. As mentioned in Section 2.2.3 the best linewidths seen from this type of growth are $\Delta E = 27\mu eV$. Both the mode and lowest linewidth results are still well above the resolution-limited linewidths exhibited by SKQDs. As such, further work is required to further improve the linewidths of SCQDs. Moreover, the wafer structure of the SCQDs wafers grown in this thesis do not allow for the QDs to be contained in a free-standing membrane. For SCQD to be integrated into waveguides further work is required to grow low linewidth, highly ordered SCQD in waveguide capable wafers.

4.4 *In-situ* strain tuning background

With good control over the spatial location of QDs exhibited through SCQDs, control of the spectral properties of the QDs must be addressed. As can be seen in Figure 35, a large wavelength distribution is observed for SCQDs in a nanohole array. To integrate multiple resonant SCQDs in a nano-photonic system the QDs must be tuned into resonance with each other. As discussed in Section 4.1, the most common QD energy tuning methods exhibit limitations such as non-localised tuning and low tuning ranges, which make them a poor choice for scale-up of nano-photonic QD systems. Recent work from J.Grim et al. [81] demonstrated a QD tuning method which exhibited long range (up to 65meV) and highly localised (spatial resolution $> 1\mu$m) *in-situ* tuning. They demonstrate the utility of this tuning method by tuning three QDs into resonance in a PhC waveguide which exhibit superradiance, an indication of quantum interactions between the QDs. Due to the promising results shown by J.Grim et al., this tuning method was chosen for investigation to address the suitability of the method for the realisation of scale-up of SCQD based systems.

4.4.1 *In-situ* strain tuning via thin film crystallisation

To enable the localised *in-situ* laser tuning, free standing GaAs waveguides with embedded InAs QDs are conformally coated in a thin layer of a dielectric material. In this experiment, Hafnium Oxide (HfO_2) is chosen as the dielectric. The HfO_2 is deposited onto the surfaces of the waveguides using '*Atomic Layer Deposition*' (ALD). By using ALD to deposit the film, the thickness of the film can be precisely controlled. Moreover, ALD allows for complex nano-photonic features to be coated conformally with layers of a controllable and uniform thickness, an essential requirement for this tuning technique [161]. The ALD coated sample is kept at cryogenic temperatures during the QD tuning process allowing for '*in-situ*' tuning of QDs. A high power, tightly focused short wavelength (632.8nm) laser is incident on an area of the waveguide which houses the QD chosen for emission energy tuning. As HfO_2 is transparent at the laser wavelength, the laser heats the suspended waveguide membrane. This heat dissipates from the waveguide into the HfO_2 film causing it to be heated. The crystallisation temperature of HfO_2 is $\approx$400°C, much lower than the melting point of GaAs ($\approx$ 800°C). By locally heating an area of the waveguide to a sufficiently high temperature using the laser, a localised area of the HfO_2 coating is crystallised. When HfO_2 undergoes a phase

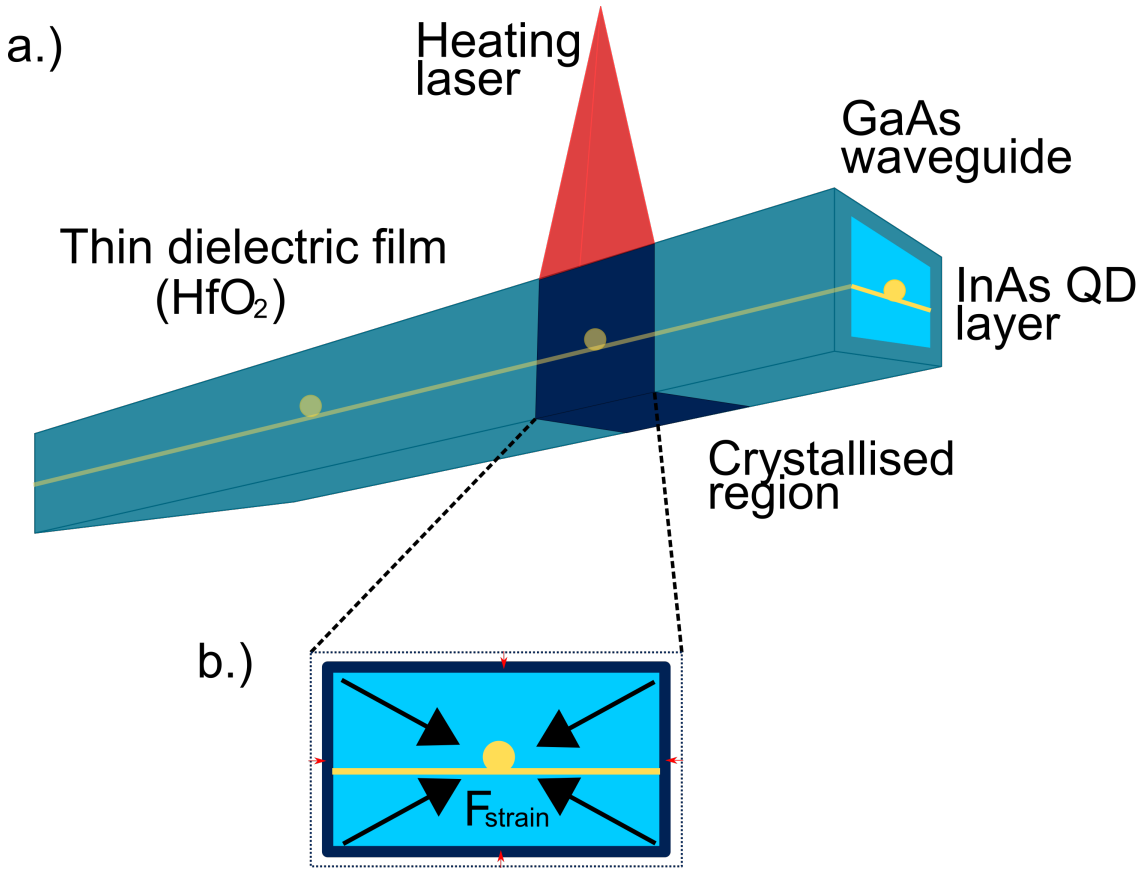

Figure 37: Schematic of the *in-situ* tuning mechanism. a.) A free standing GaAs waveguide with embedded InAs QDs is conformally coated in a thin layer of dielectric material. In this experiment, Hafnium Oxide (HfO_2) is used. The sample is held at cryogenic temperatures while a laser is used to heat the GaAs membrane. This heating causes the HfO_2 to crystallise where the laser spot is incident. This phase change reduces the volume of the dielectric by 3% which causes the coating to squeeze the waveguide, inducing a strain field as shown in b.). This strain blue-shifts the energy of any QDs in this area of the waveguide.

transition and crystallises, the material volume is reduced by ∼3% [162]. This volume reduction causes the waveguide membrane to be compressed, inducing a strain field in the waveguide. As the SKQDs used in this work are naturally strained through their formation, altering the strain environment of the QD induces an emission energy shift in the QD. As compressive strain is induced in the QD, the emission energy is blue-shifted (see Section 2.3.3 for a more detailed explanation of strain tuning of QD emission energies). Figure 37 shows a schematic of the tuning mechanism. Due to the small size of the laser spot incident on the sample and the cryogenic temperatures at which the sample is held limiting the heat dissipation, the laser heating is extremely localised. Therefore, individual QDs in the waveguide can be selected and tuned independently of each other. By controlling the power and length of the time the membrane is exposed to the laser, the degree of crystallinity of the HfO_2 film can be controlled. This allows for the amount of strain induced on the QDs and therefore, the QD tuning, to be precisely controlled.

4.4.2 Tuning mechanism considerations

To maximise the utility of the technique, each of the variables in the system must be considered with regards to their affect on the tuning mechanism. As this technique has only recently been demonstrated, the effect of altering the tuning parameters is not widely studied. J.Grim et al. indicate the three parameters which they observe to affect the tuning mechanism. Firstly, the surface morphology of the ALD deposition is observed to affect the tuning range of the technique. They observed that rougher films provided a larger tuning range due to an increase in the number of available nucleation sites for the crystallisation process [163]. In their study the roughness of the films was related to the deposition temperature, films deposited at higher temperatures exhibited rougher surfaces and therefore longer tuning ranges [81]. J.Grim et al. also show that changing the laser power and cumulative exposure time at a set power both affect the tuning of the QD energy. They show that very little tuning occurs until a '*turn-on*' laser power is reached, after which the tuning increases rapidly. By increasing the cumulative exposure time a large tuning is seen initially, before the trend plateaus sharply.

4.5 Design of strain tuning sample

To investigate this novel tuning technique, a sample was designed with H1 PhCC, nanobeam waveguide and W1 PhC waveguide structures. For the NBWs, an array of devices were fabricated with varied widths (100-1000nm) and lengths (10-30 μm) while the thickness was kept constant due to the wafer composition. A range of hole radii were included for the W1 and H1 PhC devices. As HfO_2 has a higher refractive index than air, coating a PhC membrane in the dielectric will shift the band edge of the PhC due to the higher refractive index material filling in the holes. Figure 38 shows the results from simulations of transmission through a W1 waveguide. a.) shows the shift in the short wavelength band edge for devices with different thicknesses of a conformal coating of HfO_2 with a constant nanohole radius $r = 76nm$. The simulations show that increasing the thickness

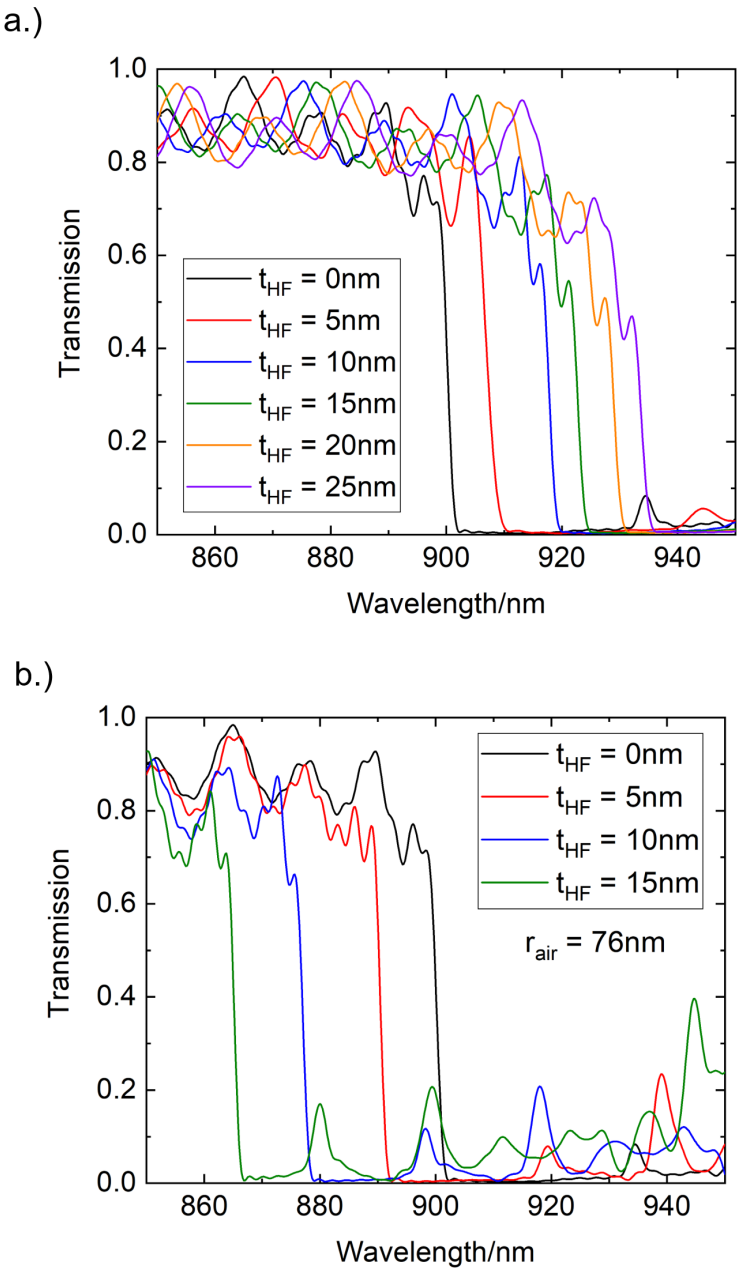

Figure 38: Results from FDTD simulations of a W1 PhC waveguide conformally coated with a thin layer of HfO_2 showing the effect of changing the thickness of the HfO_2 layer t_{HF} on the short wavelength photonic band edge of the PhC waveguide. In a.) the radius of the holes is kept constant at $r = 76nm$ and increasing t_{HF} reduces the volume of air in the holes. In b.) the volume of air in the holes is kept constant by maintaining an air hole of radius $r_{air} = 76nm$ in surrounded by the HfO_2.

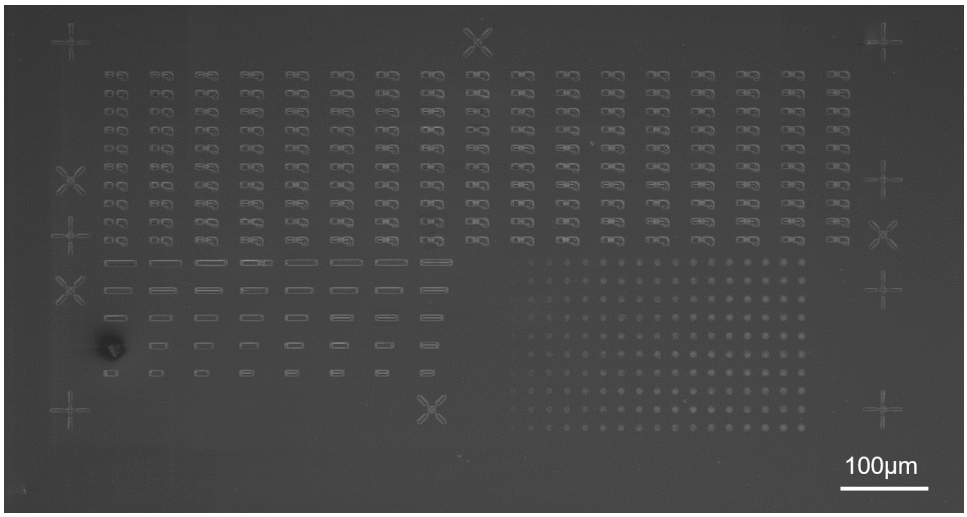

Figure 39: SEM image of the layout of devices on the sample designed to test the *in-situ* strain tuning technique. At the top of the sample are W1 PhC waveguides. At the bottom left are NBWs and at the bottom right are H1 cavities.

of the dielectric coating shifts the band edge to longer wavelengths. This occurs due to the HfO_2 having a refractive index of ~ 2, which is much larger than the air it has replaced. This causes the effective radius of the nanoholes to be reduced. Reducing the radius of the nanohole increases the effective index of the unit cell and shifts the band edge to longer wavelength as the wavelength of the band edge is directly proportional to the effective index of the unit cell ($\lambda = 2an_{eff}$). Figure 38 b.) shows the effect of increasing the thickness of the HfO_2 coating on the short wavelength band edge of a W1 PhC waveguide when the radius of the air portion of the nanohole is kept constant at $r_{air} = 76nm$. In this scheme, increasing the thickness of the nanoholes removes semiconductor material rather than air from the device. As expected, the opposite effect is seen to Figure 38 a.). Increasing the thickness of the HfO_2 coating while keeping the air hole radius constant increases the effective radius of the air holes and reduces the amount of high refractive index semiconductor. This reduces the effective index of the unit cell and shifts the band edge to shorter wavelengths.

Using the results from Figure 38, the design radius of the PhC airholes could be chosen to ensure that the band gap of the W1 waveguide would cover the entire QD emission energy distribution when conformally coated with HfO_2. A '*Scanning Electron-Microscope*' (SEM) image of the sample layout can be seen in Figure 39. Six copies of this layout were fabricated, one was left uncoated as a reference sample. The other five samples were conformally coated in HfO_2 using ALD. Between the samples, the thickness, growth method and deposition temperature of the film were altered. Two thicknesses of HfO_2 were used: 10 & 30nm, to investigate the difference in tuning range and repeatability between the two thicknesses. Two deposition temperatures and methods were used, 200 & 300°C and '*plasma*' or '*thermal*' respectively. In thermal ALD, H_2O molecules are used to

oxidise the surfactants whereas an O_2 plasma is used in plasma ALD. Varying these parameters will affect the morphology of the thin HfO_2 film and therefore should have an effect on the tuning capabilities seen.

4.6 Strain tuning results

4.6.1 Experimental set-up for controllable laser exposures

To ensure that a high degree of control over both the power and exposure time of the heating laser was possible, an automated software controllable laser exposure set-up was created. A schematic of the experimental set-up is shown in Figure 40.

The power of the laser was controlled by an adjustable ND filter mounted on a motorised stage. The stage was controlled through the computer to allow ultra-fine adjustments to the laser power and high precision when selecting a laser power to use. The flip-mounted mirror, which controlled the length of the heating laser exposure time, was also controlled via the computer. Custom-written software was developed which allowed for an arbitrary number of laser exposures of a chosen length to be automated, with PL spectra taken after each exposure. This was possible as an above band gap (808nm) laser was incident on the sample when the flip-mounted mirror was down. During a heating exposure, the flip mounted mirror was flipped up rapidly for a length of time chosen in the software before flipping back down rapidly to prevent over-exposure. While the mirror was flipped up the heating laser was reflected down onto the sample and the PL laser blocked. After the exposure, the PL laser was again incident on the sample. After a small time gap to allow the heat to fully dissipate and the mirror to have fully descended, a PL spectrum of the sample was taken and saved and the system initiated the next exposure. By automating the process in this way, not only was greater accuracy and precision of the laser exposure time and power achieved, but the process was greatly streamlined compared to manual adjustments.

After the structures were fabricated on the wafers in Sheffield, the samples were transported to the James Watt Nanofabrication Centre, where they were coated in HfO_2 using the range of different ALD deposition parameters discussed in Section 4.5. The samples were then transported back to Sheffield to be measured. Unfortunately, the H1 cavity structures on the sample were underexposed causing the air holes to be largely under-etched. Therefore, these devices were not measured as no cavity modes would have been present even before the HfO_2 deposition.

4.6.2 Laser power dependence

With the samples fabricated and conformally coated in HfO_2, the set-up was constructed as shown in Figure 40 and the samples were loaded into a flow cryostat, where they were kept at cryogenic temperatures ($\sim$4K). As this *in-situ* strain tuning technique has only recently been demonstrated

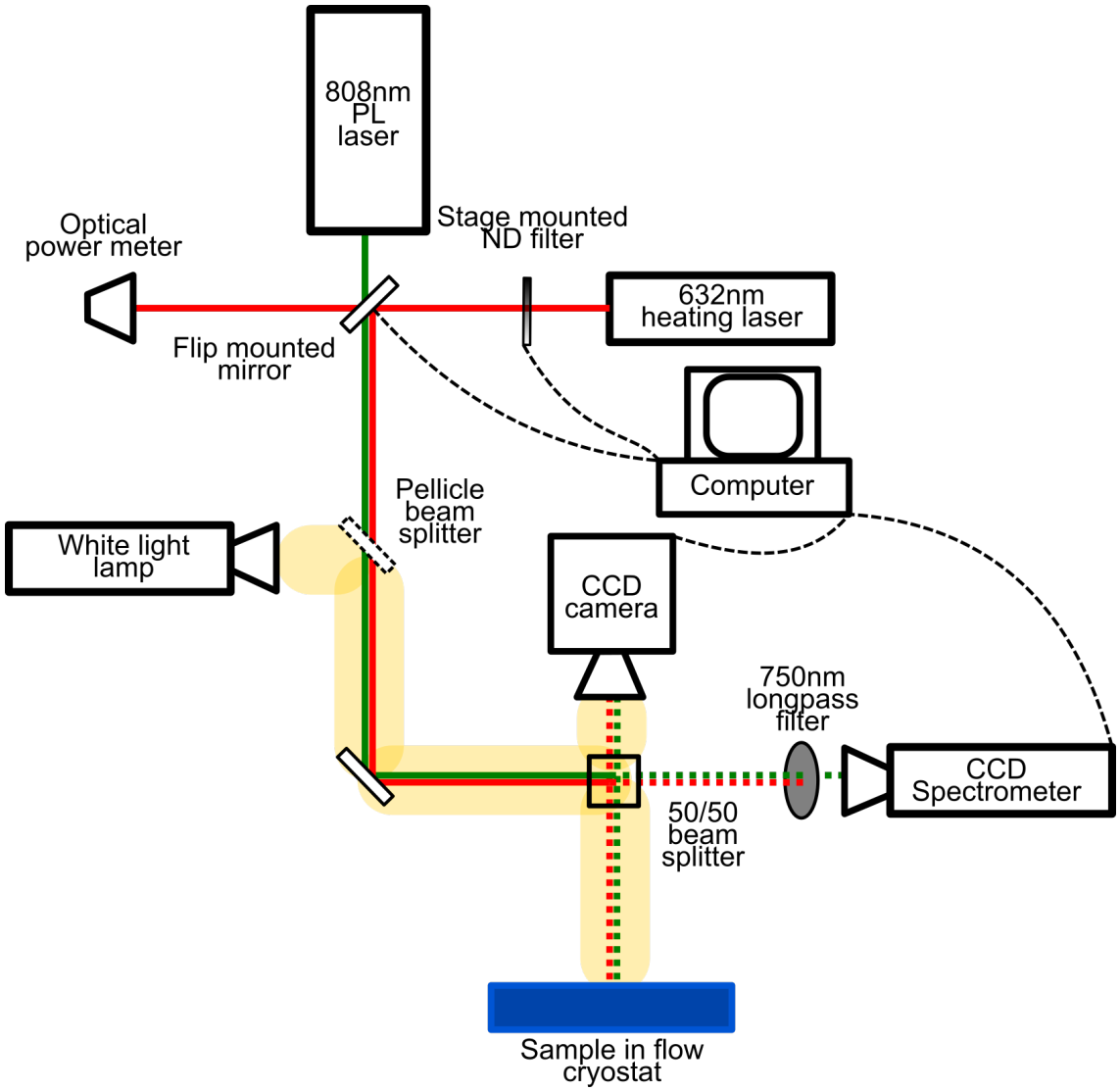

Figure 40: Schematic showing the automated laser exposure set-up used to control the power and exposure time of the heating laser. The set-up was modified from a standard μPL set-up by including computer-controlled components to automate the tuning process. The heating laser was incident on an adjustable '*Neutral-Density*' (ND) filter and flip-mounted mirror to control the power and exposure time of the laser. Both the filter and the mirror were controlled by custom-written software on a computer. When the flip mounted mirror was up, the sample was exposed to the heating laser; when the mirror was down, a low power 808nm laser was used to excite PL in the QDs to measure their wavelengths.

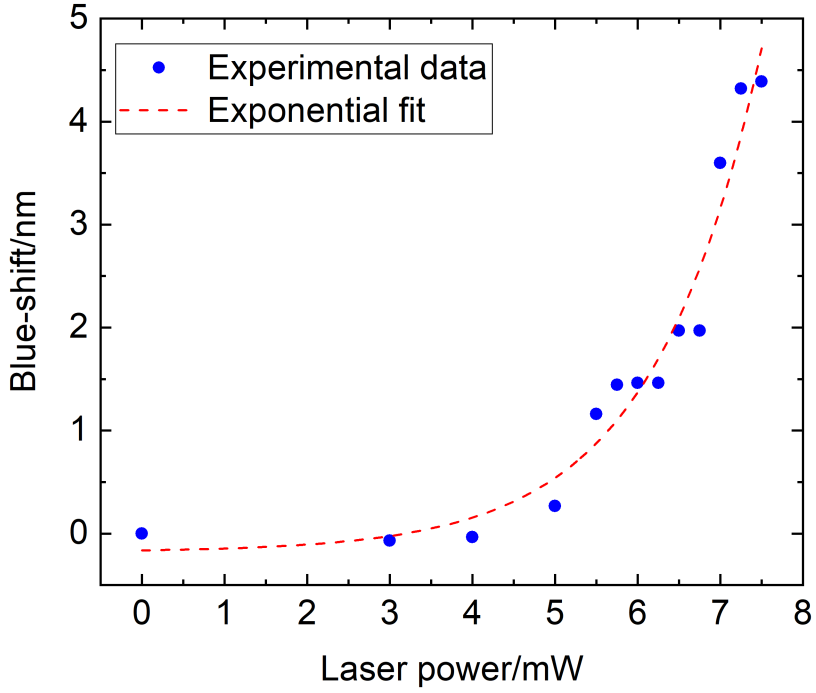

Figure 41: Graph showing the amount of blue-shift exhibited by a QD in a 0.5 × 30μm NBW after 30s cumulative exposure time at increasing laser powers. An exponential fit to the data is included to guide the eye.

for the first time, the tuning mechanism and procedure is not fully understood. Therefore, the first step in the measurement process was to gain an understanding of the operation of the system.

Firstly, the effect of increasing the laser power on the maximum achievable tuning range of a QD was investigated. The laser power was increased incrementally by adjusting the ND filter in the path of the heating laser. At each power increment, the sample was exposed to the laser for a total cumulative exposure time of 30s at each incremental laser power, to ensure that close to the maximum amount of tuning at each laser power was reached. The results shown in Figure 41 were obtained from tuning a QD embedded in a 0.5μm wide, 30μm long NBW. The power of the laser was measured as it entered the set up, the power down onto the sample will be lower due to the two beam splitters (90/10 pellicle and 50/50) in the laser path, between the power meter and the sample. The graph shows that at low powers, no blue-shift is observed. This is due to the laser power not being sufficiently high to heat the HfO_2 over its crystallisation temperature (∼400°C). The device measured in Figure 41 exhibits a threshold power of 5mW after which a roughly exponential trend is seen in the blue-shift with increasing laser power. This can be explained by considering the effect of the degree of crystallinity on the amount of tuning and the effect of the temperature

on the degree of crystallinity. At or just above the threshold power the temperature of the semiconductor membrane will only just surpass the crystallisation temperature of HfO_2. Therefore, as the heat dissipates, only a small fraction of the HfO_2 immediately surrounding the waveguide will reach a high enough temperature to undergo the phase transition and crystallise. As the amount of tuning is proportional to the degree of crystallinity, the amount of blue-shift observed will be small. Increasing the cumulative exposure time at this low power will not lead to more tuning as the small amount of HfO_2 which was able to crystallise will have already completed the phase transition. By increasing the laser power, not only will the maximum temperature of the semiconductor membrane be increased, but the area in which the crystallisation temperature of HfO_2 is surpassed will also be increased. This will lead to a larger achievable degree of crystallisation with increasing laser power. If the heating laser power is increased too high then the temperature of the GaAs membrane will approach the melting point of GaAs, at this point the waveguide will be damaged. An example of

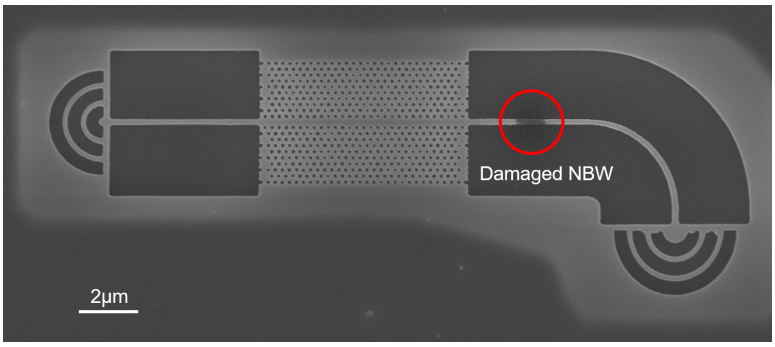

Figure 42: SEM image of a W1 PhC waveguide coupled to two NBWs and coated in HfO_2. The right hand NBW has been over-exposed by the heating laser which has caused damage to the waveguide as can be seen by the darker area.

such damage can be seen in the right hand NBW in Figure 42. When the sample is damaged in this way the QD PL emission is no longer visible, suggesting that the optical properties of the QDs have drastically changed.

The trend observed here agrees with a similar experiment conducted in [81]. If the laser power from the x-axis in Figure 41 is adjusted to account for the two beam splitters in the optical path before the sample to be comparable with the numbers from the J.Grim et al. experiment, the threshold power is found to be 2.25W. This is significantly lower than the power measured by J.Grim. This is likely due to the NBW being much thinner in this work, just 0.5μm wide, compared to 1.5μm wide in [81], and the wavelength of the laser being different.

4.6.3 Cumulative laser exposure time dependence

Next, the effect of increasing the cumulative exposure time at a fixed laser power on the tuning of the QD emission energy was studied. Figure 43 shows the results from a QD in a NBW being

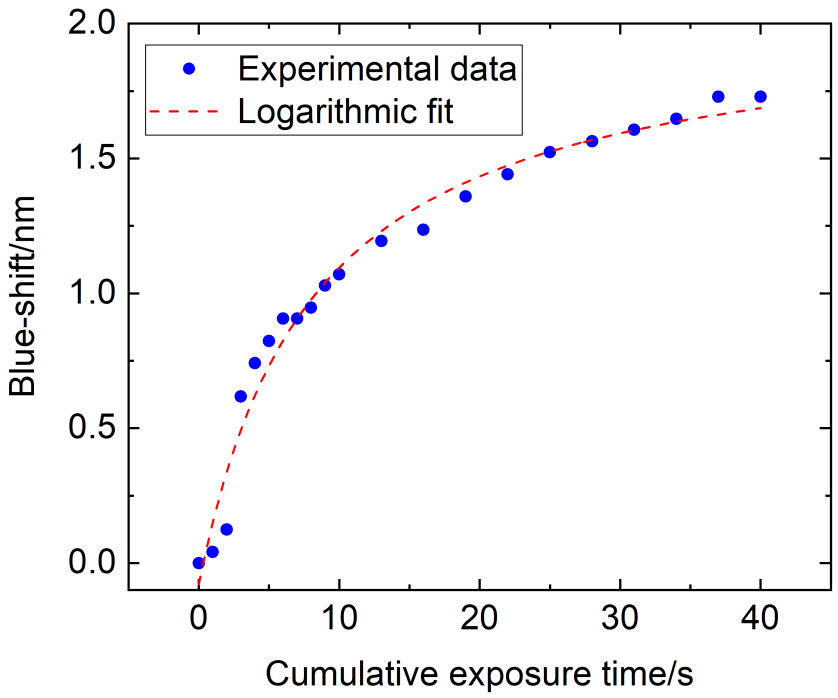

Figure 43: Graph showing the effect of increasing the cumulative heating laser exposure time at a fixed laser power above the threshold power, on the amount of blue-shift of a QD emission energy in a NBW. A logarithmic fit is included as a guide for the eye.

excited at a laser power above the tuning threshold power. The QD was excited in 1s intervals for the first 10s, followed by 5s intervals up to a cumulative exposure time of 40s, at a constant heating laser power. The graph shows that initially, at low cumulative exposure times, the blue-shift increases sharply. This is because, before exposing at a given power, the only HfO_2 that has already been crystallised is that which was able to be crystallised at a lower laser power. When the power is raised, more HfO_2 is able to be crystallised as a larger amount of heat energy is pumped into the system. As is seen in Section 4.6.2, this increases the tuning range compared to lower powers. At longer cumulative exposure times, the trend quickly flattens off with only a gradual tuning seen at cumulative exposure times above 20s. The longer that the HfO_2 is exposed to sufficient heat to crystallise, the higher the degree of crystallisation of the HfO_2 will be. Therefore, without increasing the laser power, after each exposure there will be less HfO_2 that can be crystallised at a given laser power. This causes the amount of tuning seen per second of heating laser exposure to drop off rapidly. Figure 43 shows that a roughly logarithmic trend is seen on the amount of blue-shift exhibited by a QD when increasing the cumulative heating laser exposure time. This trend is also seen in [81].

4.6.4 Tuning ranges in nanobeam and photonic crystal waveguides

With the tuning mechanism of the technique studied and the effects of changing the laser power and cumulative exposure time understood, the tuning range of the technique was studied next. Firstly, the tuning range in the NBW was studied. Figure 44 shows a heat map of consecutive

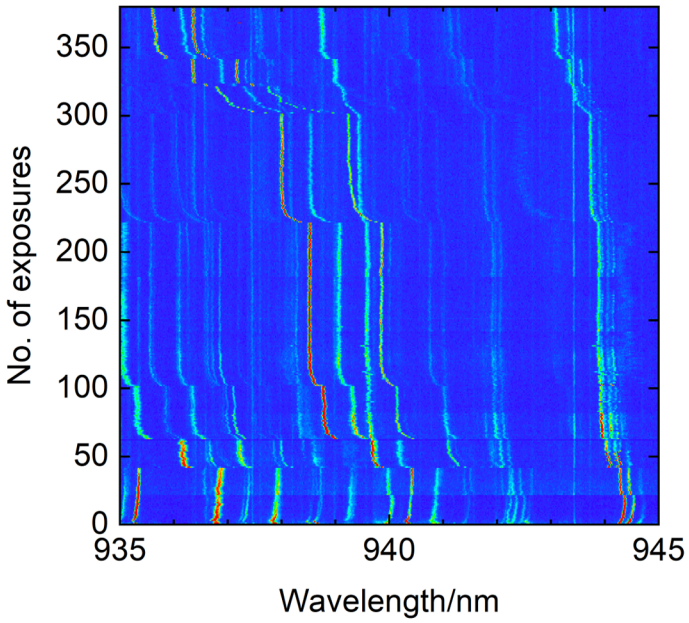

Figure 44: Heat map showing PL from QDs in a NBW after each heating laser exposure, showing the maximum tuning range achieved in this work for QDs in a NBW. A maximum blue-shift of $5.06nm$ was observed. The QD wavelength started at $\lambda = 941.42nm$ and finished at $\lambda = 936.36nm$

PL spectra from QDs in a NBW, taken between heating laser exposures. The maximum tuning observed from QDs in a NBW was $\Delta\lambda_{max} = 5.06nm$ with the QD energy starting at $\lambda = 941.42nm$ and finishing at $\lambda = 936.36nm$. Other QDs on the heat map in Figure 44 are observed to blue shift $> 4nm$ showing the repeatability of the tuning method. Some QDs tune only a small amount. These QDs are likely spatially located far from the heating laser spot and so are not strained to the same degree as QDs located directly under the heating laser spot. This maximum tuning was seen in a $0.5 \times 30\mu$m nanobeam with a 30nm thick HfO_2 film deposited at 200°C. Comparing the average tuning ranges observed for QDs in NBWs, thicker HfO_2 films deposited at lower temperatures showed larger tuning ranges. These finding do not agree fully with what was found by J.Grim et al.. Thicker films allow for a larger strain field to be created due to a larger amount of HfO_2 around the waveguide that can be crystallised. However, lower deposition temperatures should lead to a smoother surface morphology which reduces the tuning range due to the reduction in nucleation points for the crystallisation process. This work found that the opposite case was true in NBWs. Lower deposition temperatures provided more consistent and larger tuning range than films deposited at higher temperature. The largest tuning range observed for a 10nm thick film

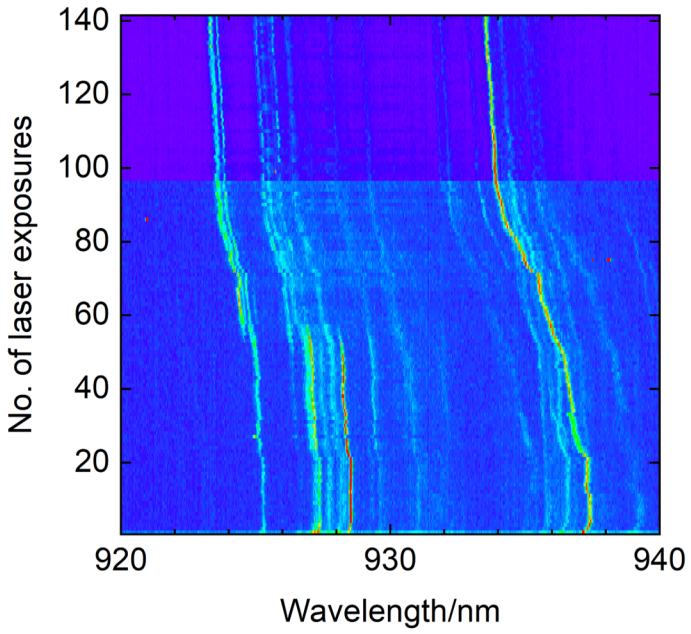

Figure 45: Heat map showing PL from QDs in a W1 PhC waveguide after each heating laser exposure, showing the maximum tuning range achieved in this work for QDs in a PhC waveguide. A maximum blue-shift of $3.59nm$ was observed. The QD wavelength started at $\lambda = 937.15nm$ and finished at $\lambda = 933.56nm$.

was $\sim 3.8nm$. This film was also deposited at 200°C. The films deposited at 300°C did not exhibit tuning ranges greater than 1nm in NBWs. As only one sample was coated in a film deposited by thermal ALD and this film was deposited at 300°C, any comparison between the two deposition methods would not be valid due to the clear under-performance of the 300°C deposited films.

Next, the tuning range of QDs in PhC waveguides on the samples was investigated. Compared to the NBWs, tuning QDs in the PhC waveguide required much higher heating laser powers. This is likely due to the increased thermal mass of the PhC waveguide, as compared to a NBW a PhC waveguide contains much more semiconductor. This causes the energy imparted by the laser to dissipate more quickly as the heat can dissipate along the waveguide and into the PhC cladding. This keeps the system temperature lower than for a NBW where the heat can only dissipate along the beam direction or into the HfO_2. Where the threshold laser heating power for NBW was $\sim 5mW$ in the PhC the threshold was $3\times$ higher at $\sim 15mW$. The heating laser was initially fibre-coupled onto the optical table, however, this did not provide enough power to tune QDs in the PhCs. Therefore, the laser was installed with a free space path to remove the coupling losses from the fibre. This enabled a high enough power to tune QDs in PhC waveguides to be reached.

The maximum tuning range for a QD in a PhC waveguide is shown in Figure 45. The maxi-

mum blue-shift observed for a QD in a PhC waveguide was 3.59nm. The QD wavelength started at $\lambda = 937.15nm$ and finished at $\lambda = 933.56nm$. The range seen is significantly lower than the longest tuning range seen in a NBW. However, the device measured in Figure 45 had only a 10nm thick film HfO_2 compared to the 30nm thick film for the NBW device in Figure 44. The maximum tuning range in a PhC waveguide coated with a 30nm thick HfO_2 film was 2.55nm, significantly lower than the best tuning range for a 10nm thick film. If the maximum tuning range in a PhC waveguide is compared to a NBW with the same film thickness then both exhibit a very similar tuning range ($3.59nm$ vs $3.8nm$). This shows that the type of waveguide does not fundamentally limit the tuning range of the strain tuning technique. The 10nm HfO_2 film deposited on this PhC waveguide was deposited at 300°C with plasma ALD. In the PhC devices, the tuning ranges on the 300°C deposited films were much larger than for films deposited at 200°C. In the PhC waveguides, thinner films deposited at higher temperature provide the superior tuning range. This is the opposite to what was observed in the NBWs where thicker films deposited at lower temperatures were superior. As the geometry of a PhC waveguide is much more complex than a nanobeam waveguide, the deposition morphology is likely to be affected by the many surfaces present due to the etched nanoholes. Thicker films may not strain around the waveguide as expected due to their relative thickness compared to the nanohole size, instead, they may strain around individual holes or the HfO_2 itself due to the complex geometry. With thinner films this is less likely to happen as the HfO_2 is in contact with less of itself in the nanoholes due to the reduced film thickness filling the nanoholes less. This reduces the likelihood of localised strain defects forming away from the waveguide. If the HfO_2 in a nanohole next to the W1 waveguide crystallises, the strain it produces would stretch the waveguide section of the device rather than compress it, leading to a red-shift of the QD. This would counteract any waveguide squeezing from crystallised HfO_2 surrounding the waveguide region of the device. As the PhC contains many surfaces for nucleation, there is no requirement for an increased density of nucleation points from the deposition morphology which is important to the NBW devices. An over-abundance of nucleation points would promote the formation of localised crystallisations away from the desired waveguide region, reducing the tuning range of the device. By comparing the maximum tuning ranges for different deposition temperatures in NBW and PhC waveguides, it is clear that the deposition temperature has much less of an impact on the tuning range of PhC (3.59nm at 300°C vs 2.18nm at 200°C) devices compared to NBWs (1.00nm at 300°C vs 5.06nm at 200°C).

Figure 46 shows PL heat maps for tuning attempts on an uncoated reference sample in both a NBW and PhC. No significant tuning is observed in either structure. This confirms that the HfO_2 film is the cause of the observed tuning in the devices.

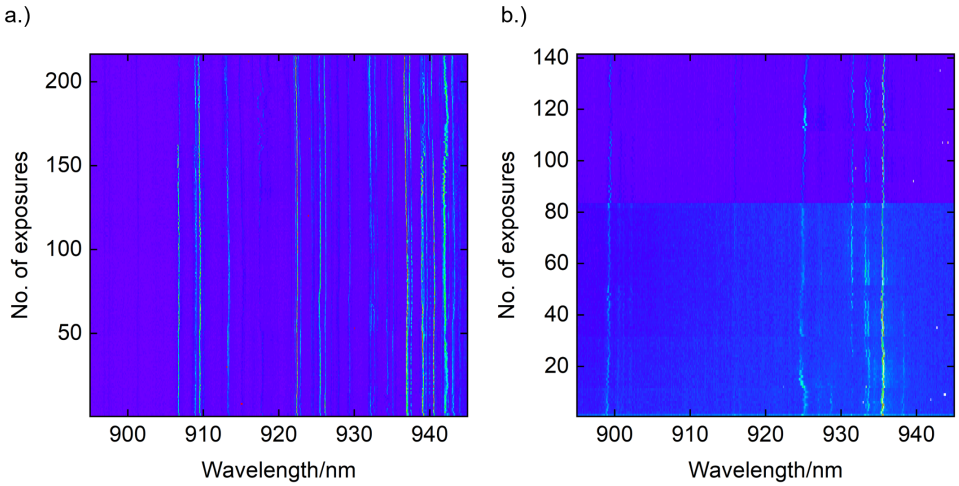

Figure 46: Heat maps of QD PL taken between heating laser exposures of an uncoated reference sample at increasing laser power. a.) Shows the results from a NBW whereas b.) Shows the results from a PhC waveguide.

4.6.5 Tuning two QDs into resonance over a short range

Having fully investigated each sample to determine which HfO_2 deposition temperature, method, and film thickness provided the largest and most repeatable tuning for both NBW and PhC waveguides, this knowledge was employed to tune multiple pairs of QDs into resonance. Firstly, the fine control of the method was demonstrated by tuning two QDs into resonance over a very short spectral range of just $\Delta\lambda = 0.14nm$. The PL spectra of the two QDs before and after tuning into resonance are shown in Figure 47 a.) and b.), respectively. The longer wavelength QD (QD 1) was located at the opposite end of a W1 PhC waveguide to QD 2, the device was coated with a 10nm thick film of HfO_2 deposited via plasma ALD at 200°C. The QDs were initially detuned by $\Delta\lambda = 0.14nm$. By crystallising the HfO_2 around QD 1, the QDs were brought into resonance at $\lambda = 918.64nm$. The final wavelength of the two QDs is met by both QDs shifting towards each other. The red-shift observed in QD 2 is likely due to the heating laser altering the charge environment of the waveguide and inducing a small stark shift in QD 2. From Figure 46 b.) a small red-shift can be seen in some of the QD emission energies when exposing an uncoated PhC waveguide to the heating laser, it is likely that this is the effect causing the red-shift seen in Figure 47. However, the red-shift could also be explained by considering the lineshape of the QDs before and after the tuning process. The lineshapes of both QDs change from doublets to singlets after the tuning process. These doublets could be caused either by the presence of the positivity charged trion state in addition to the exciton or the FSS of the exciton transition. The magnitude of the energy splitting between the peaks is on the order of μeV [66], this is typical of the fine-structure

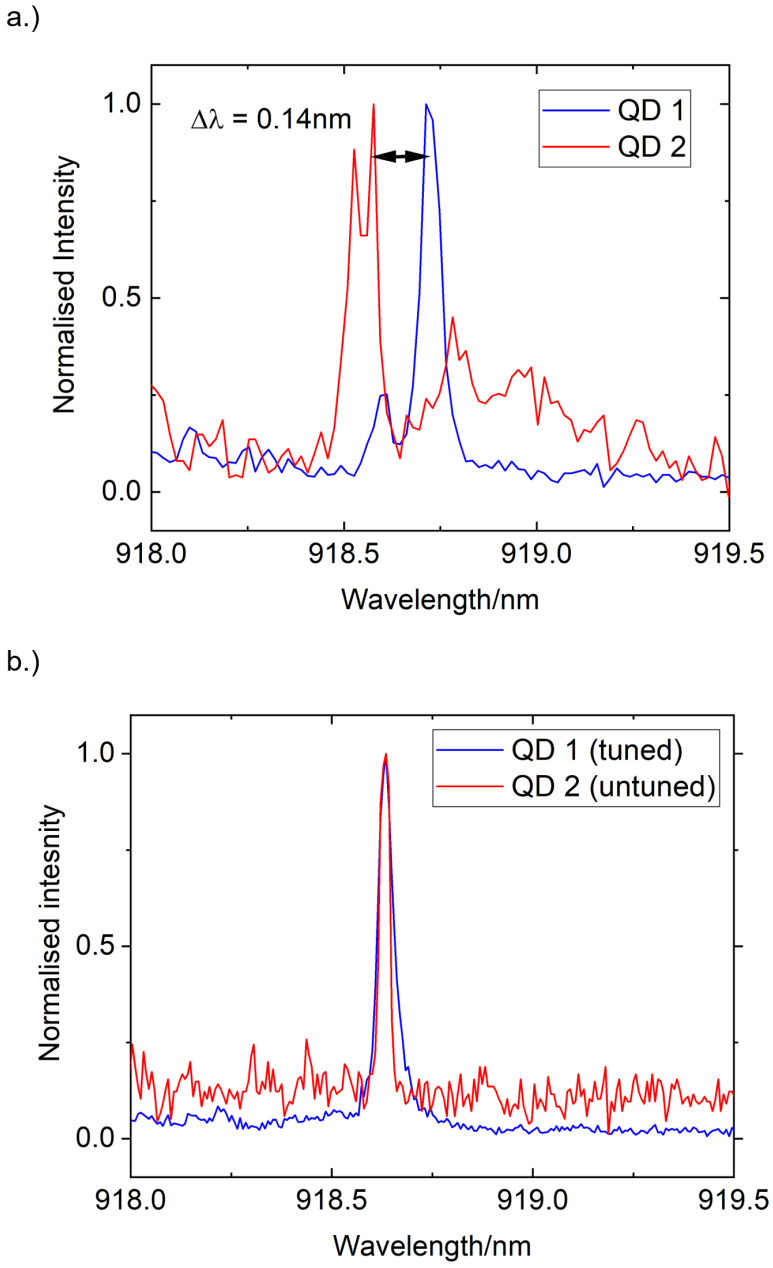

Figure 47: PL spectra from two QDs in a PhC waveguide a.) before and b.) after being tuned into resonance on a spectrometer using the *in-situ* strain tuning method described in this chapter. The QDs were tuned into resonance over a very small range ($\Delta\lambda = 0.14nm$).

splitting in QDs, whereas, the energy splitting between the exciton and positive trion state in a QD is typically on the order of meV [164]. As the magnitude of the FSS is related to the asymmetry of the QD, changes to the strain of the QD will alter the splitting (see Section 2.3.3). Therefore,

it is likely that the strain induced by the crystallisation of the HfO_2 film has significantly affected the FSS of the QDs in Figure 47.

The ability to tune QDs into resonance over such a short range demonstrates the utility and high level of control over QD energy tuning available with this tuning method.

4.6.6 Tuning two QDs into resonance over a long range

Having demonstrated very short range tuning, attempts to tune QDs into resonance over a larger spectral range were conducted. The longest range that two QDs in a PhC waveguide were tuned into resonance over was $\Delta\lambda = 0.72nm$. The PL spectra of the two QDs before and after tuning into resonance are shown in Figure 48 a.) and b.), respectively. As for the shorter tuning range seen in Section 4.6.5, despite the QDs being located at opposite ends of the PhC waveguide, a small red-shift was observed in QD 2 which was far from the heating laser location. In both cases, the magnitude of the red-shift is very small $> 0.1nm$ and so could easily be corrected for using electrical tuning of the QD energy. The waveguide was coated with a 10nm thick film of HfO_2 deposited via plasma ALD at 200°C, this HfO_2 deposition was chosen for both the short and long range tuning attempts as it exhibited both the longest range and most reproducible tuning in PhC waveguide structures. As can be seen between a.) and b.) in Figure 48, the shape of the QD peaks are changed by the tuning process. QD 1 appears to exhibit a narrower linewidth after the tuning process whereas QD 2 is broadened by the process. This may be caused by the changing charge environment of the waveguide altering the charge state of each QD. As this sample did not contain electrical diodes, control over the charge states of the QDs was not possible. Integrating electrical control on ALD coated samples is not trivial as conventional diode contacting pads are coated during the ALD process, rendering them unusable. As this sample was a test sample, diodes were not included in order to reduce the complexity of the sample fabrication. This broadening could also be caused by alterations to the FSS in the QD due to the strain induced by the HfO_2 crystallisation. The narrowing of the QD 1 lineshape could be due to a change in the magnitude of the FSS either separating or fully overlapping the two FSS states in the PL spectrum which were initially partially overlapped in the PL spectrum before the tuning process, causing the QD emission peak to appear broad. Similarly, the broadening of the QD 2 lineshape after the tuning process can be explained by an alteration to the FSS. The energy scale of the narrowing/broadening of the QD emission peaks in Figure 48 is consistent with that of FSS states in QDs ($\sim \mu eV$) and is lower than typical values for exciton-trion splitting ($\sim meV$). This suggests an alteration to the FSS in the QD is the most likely cause of the peak width change for the QDs before and after tuning.

This demonstration of long range tuning of QDs into resonance demonstrates the capabilities of this technique for use in a SCQD array where individual QDs can be tuned through large spectral ranges into resonance with high precision.

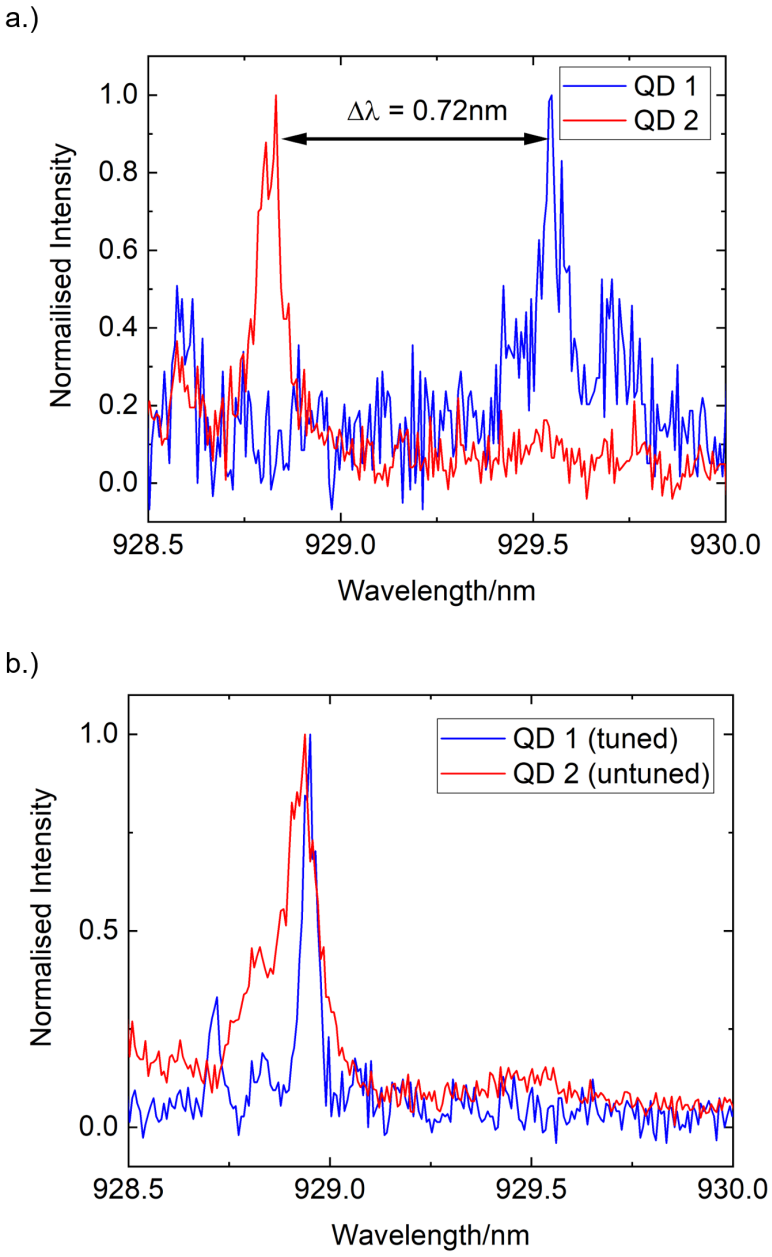

Figure 48: PL spectra from two QDs in a PhC waveguide a.) before and b.) after being tuned into resonance on a spectrometer using the *in-situ* strain tuning method described in this chapter. The QDs were tuned into resonance over a long range ($\Delta\lambda = 0.72nm$).

4.7 Conclusions and outlook

Advances in both SCQD and QD energy tuning techniques have been presented in this chapter towards the goal of the scale-up of QD based nano-photonic systems. Specifically, the combination

of the good spatial control offered by SCQD combined by the highly controllable and long range QD energy tuning provided by the *in-situ* strain tuning method described here, will significantly improve scalability of QD systems. The effect of altering the pitch and radius of nanohole arrays on the wavelength and nanohole occupancy of SCQD was investigated. Larger nanoholes at a pitch of 2.4μm giving the best results. Moreover, the effect of changing the growth interrupt on the wavelength and occupancy of SCQD was studied. It was found that longer growth interrupts improved the single QD nanohole occupancy rate and shifted the QD ensemble mean wavelength to longer wavelengths. An *in-situ* strain tuning method first demonstrated by J. Grim et al. was investigated for its suitability to be used in conjunction with SCQD to enable scale-up of the number of resonant QDs in nanophotonic structures. The tuning mechanism of the technique was studied; it was found that for NBWs, thicker films deposited at a higher temperature provided superior tuning performance whereas in PhC waveguides, the opposite was true. A maximum tuning range of 5.06nm and 3.59nm was observed for QDs in NBW and PhC waveguides, respectively. Two pairs of QDs were tuned into resonance over short (0.14nm) and long (0.72nm) tuning ranges. This shows the flexibility and precision of the tuning technique, confirming that such an approach would be suitable to be used with SCQDs, to enable scale-up of QD nanophotonic devices.

To build upon the work in this chapter two main avenues need to be explored. Firstly, for the SCQD work, a design for the nanohole-seeded growth which is compatible with free-standing waveguide devices is required. Without the waveguide structures, not only are most nanophotonic devices off-limits but the strain tuning mechanism will not be possible. The main challenge to growing SCQD in waveguide capable wafers is keeping the thickness of the waveguide membrane low. This could be overcome by improving the cleaning process further, allowing for a smaller buffer layer to be grown above the nanoholes. This would also allow the nanoholes to be shallower, further reducing the thickness requirement. For the strain tuning work, a new sample with electrical contacts would allow for control over the charge states of tuned QDs. Moreover, QCSE tuning could be used to supplement the strain tuning. To enable a measurement of QD-QD coupling via superradiance, the OC design on the sample will need to be adjusted to account for the HfO_2 coating. The OCs on the samples measured in this work were extremely inefficient and did not couple sufficient light in or out of the waveguides to perform such a measurement.

This page intentionally left blank.

5 Electro-mechanically tunable 1D photonic crystal cavities

5.1 Introduction

A key advantage of using QDs for linear optical QIP, is their ability to exhibit strong light-matter coupling in nano-photonic structures. This enhanced coupling provides an increased photon emission rate from the QD into the photonic medium, allowing for extremely rapid, deterministic data transfer via single photons and a highly non-linear response in the few photon limit. These attributes are essential to the realisation of quantum phase gates and efficient single photon sources. As discussed in Section 2.5, multiple approaches have been used to demonstrate strong light-matter enhancement of embedded QDs, including optical micro-cavities. Cavity systems have demonstrated the largest Purcell factors to date in single QD systems (43 ± 2) [43] and are much more compact than competing systems such as waveguide and ring resonator devices, leading to lower mode volumes. As such, PhCCs are the structure of choice for the realisation of strong light-matter interactions. Moreover, chains of resonant cavities have been shown to be capable of producing many-photon entangled states [165].

When considering the scale-up of coupled cavity systems, precise control over the wavelength of the cavity modes presents a significant challenge. Due to intrinsic fabrication imperfections, it is extremely unlikely that two cavities with the same design parameters will exhibit identical cavity mode wavelengths. Therefore, to achieve multiple resonant cavities on-chip, a controllable cavity mode wavelength tuning mechanism is required. Several competing approaches to PhCC mode control have been demonstrated in the literature. Tuning of cavity mode wavelength in an H1 PhCC has been demonstrated by using a piezoelectric mount to induce uniaxal strain in the system. This alters the PhC period in the direction of the applied strain, which tunes the cavity mode wavelength. This technique also alters the detuning between the two orthogonal cavity modes in the H1 PhCC [117, 118]. This method provides a high degree of control over the cavity wavelength shift, due to the fine control over the piezoelectric mount voltage. However, the method does not allow for cavities on the same sample to be tuned independently of each other. Moreover, the induced strain causes the QDs in the sample to be tuned along with the cavity modes. Electro-mechanical tuning of PhCCs has been demonstrated in two main schemes; horizontal (in-plane) and vertical (out-of-plane) displacement methods. Horizontal displacement methods commonly involve a cavity beam positioned between two perturbing PhC beams [113, 166], however, schemes with just two PhC beams [112] or a single dielectric probe exist [167]. In these schemes, the devices are tuned by altering the effective refractive index of the cavity mode. The perturbing elements are electrically actuated in close proximity to the cavity, allowing the effective index to be controlled. These devices can be tuned independently from each other and any embedded emitters. However, these schemes require high voltages and large device footprints, which limit their scalability. Vertical displacement methods operate on the same principal as the horizontal displacement methods. A

capacitive force between two parallel PhC membranes is used to alter the effective refractive index of the cavity mode. This method has been used to tune QD into resonance with an L3 PhCC [168].

In this chapter, a scheme is introduced for fine control over the cavity mode wavelength tuning in a 1D PhCC. This is achieved by altering the effective refractive index of the mode by using a photonic crystal membrane attached to a free-standing electromechanical cantilever, which can be actuated orthogonally to the cavity plane via a capacitive force. Whilst various demonstrations of electro-mechanically tunable 1D PhCCs exist in both GaAs [112] and silicon [113] systems, to date, none are capable of containing a QD at the electric field maximum of the cavity mode. The design is capable of including an embedded QD at the site of maximal electric field intensity in the cavity whilst exhibiting in-operando cavity mode tuning. This allows for the QD to be tuned on to resonance with the cavity mode thus exhibiting an enhancement in Purcell factor.

The first part of this chapter focuses on the design and optimisation of the 1D PhCC via FDTD simulations. The cavities were optimised for a high $\frac{Q}{V_m}$ ratio at $\lambda_{cav} \approx 910nm$. Extensive parameter optimisation sweeps are conducted across the entire parameter space to achieve this optimisation. The robustness of the optimised design to various fabrication imperfections is tested in simulation. By using a Monte Carlo simulation technique to simulate the random radii fluctuation of the air holes, the fabrication error can be quantified. Furthermore, the ellipticity of the holes is also studied in this section. Further simulation work is carried out to optimise the design of the perturbing PhC membrane. Parameter sweeps are carried out to reduce the cavity Q-factor degradation from the presence of the membrane whilst maintaining a large cavity mode tuning range. The optimised 1D PhCCs are studied experimentally and compared to the simulated devices. Finally, the full cavity perturbing membrane devices are fabricated and studied showing the first demonstration of an electro-mechanically actuated cantilever tunable cavity in GaAs.

5.2 Theory

5.2.1 Cavity mode tuning

As stated in Section 2.4.4 the wavelength of the fundamental mode of a 1D PhCC is given by Equation 12.

$$\lambda = 2n_{eff}L$$

Thus, to tune the wavelength of the cavity mode, either the length of the cavity L or the effective refractive index n_{eff} must be altered in a controllable manner. Once fabricated, changing the length of a PhCC is extremely challenging. Attempting to alter the length of a PhCC would likely lead to massive degradation of the cavity performance, unavoidable tuning of the embedded QD energies, and inability to independently tune multiple devices. As a result, tuning of the effective mode index is the clear choice for the realisation of cavity mode wavelength tuning. Multiple approaches

exist for the tuning of effective mode index through '*direct*' cavity tuning methods. These include: thermal tuning [169, 170], electro-optical tuning [90] and acoustic tuning [171]. However, these methods each have a critical flaw when considering QDs systems and scale-up potential. Thermal tuning often requires high laser powers to achieve a sufficient tuning range. Moreover, the heating effect can degrade the linewidths of embedded QDs. Acoustic and electro-optical tuning devices require a large device footprint, fundamentally limiting the scalability of such devices. An alternative '*indirect*' approach is to alter the effective index of the cavity mode by altering the environment of the evanescent cavity field. This is achieved by introducing some dielectric material, normally a nanobeam or cantilever tip, close to the cavity centre. This dielectric structure can be moved in and out of the evanescent field of the cavity mode, thus altering the effective index. This approach has seen successes in silicon based systems using in-plane displacement and in atomic force microscopy tip approaches [113, 167, 172].

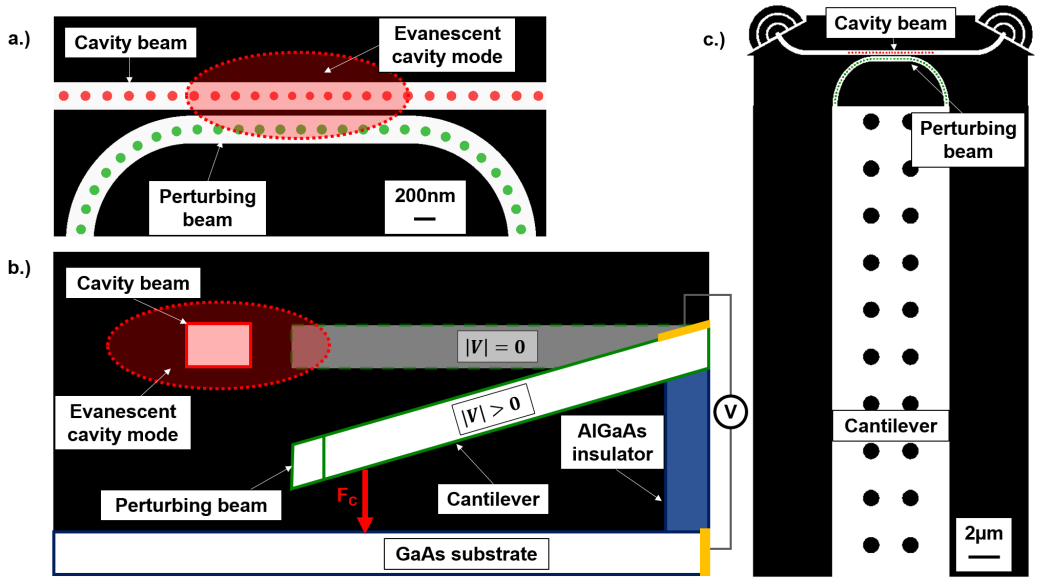

Figure 49: Schematic of an electro-mechanically tunable 1D PhCC. a.) Shows a top down view focused on the cavity region. The perturbing beam is fabricated extremely close to the cavity beam such that the evanescent field of the cavity mode extends into the perturbing beam. b.) Shows a cross-sectional view of the operation of the cantilever device. When a voltage is applied between the substrate and the cantilever membrane the resulting electric field produces a capacitive force (F_C) that acts on the cantilever. As the end of the cantilever is free-standing and far from the fulcrum point, the force is large enough to displace the perturbing beam, pulling it towards the substrate. If a large enough voltage is applied, the perturbing beam is displaced completely from the evanescent cavity field, leading to maximal mode tuning. c.) Shows a top-down view of the entire device. The air holes in the cantilever are present to aid the under-etching process.

In the system presented in this chapter, a perturbing PhC membrane is introduced in the evanescent field of the cavity mode. This membrane can be actuated out-of-plane with respect to the devices via an electrostatic force between the suspended device membrane and the substrate. A schematic of the device and its operation is shown in Figure 49. This out-of-plane approach has been used to realise optical switches using directional couplers [173, 174] and has the advantage of being much more compact in design than the in-plane designs. Moreover, indirect tuning methods are much less likely to damage the nanophotonic structures than direct tuning methods due to the high powers and stresses experienced by the devices as a result of direct cavity mode tuning methods.

When the cantilever is displaced from its resting point at zero bias, the perturbing beam is also displaced from the evanescent cavity mode, as shown in Figure 49 b.). As this method allows for very fine adjustment of the cantilever displacement, the amount of displacement of the perturbing beam can be precisely controlled. Therefore, the change of n_{eff} can also be precisely controlled as this is directly related to the proximity of the perturbing beam to the cavity. This allows for fine control of the cavity mode tuning over the entire tuning range of the device.

By adjusting the in-plane separation between the cavity and perturbing beams, the tuning range of the device can be altered as the magnitude of the n_{eff} modulation is changed. Adjusting the parameters of the PhC in the perturbing beam also affects the amount of n_{eff} modulation. However, the PhC parameters have a much smaller effect on the tuning range of the device than the separation of the beams. Optimisation of the PhC parameters is more important in reducing coupling and scattering losses from the cavity due to the presence of the perturbing beam, this will be discussed in detail in Section 5.4.

5.2.2 Electrostatic actuation of a free-standing cantilever

Figure 50 shows a detailed schematic of the electrostatic actuation of a free-standing cantilever device. When a voltage is applied between the device membrane and the substrate, a uniform electric field forms between them as they are separated by an insulator. This produces a capacitive force that acts on both the substrate and the membrane, attracting them towards each other. In reality, this manifests as an attractive force pulling the free-standing membrane towards the substrate as the substrate cannot deform as easily as the membrane. The electrostatic force F_C between two parallel plates seperated by distance d with an electric field E between them is given by:

$$F_C = \frac{1}{2}|\frac{\partial C}{\partial d}|V^2 = \frac{\epsilon A}{2d^2}V^2 = \frac{CV^2}{2d} \tag{41}$$

where C is the capacitance between the membrane and the substrate, ϵ is the permitivity of the material between the membrane and the substrate and $A = L \cdot w$ is the cantilever area. This attractive force pulls the cantilever toward the substrate causing the cantilever to bend away from

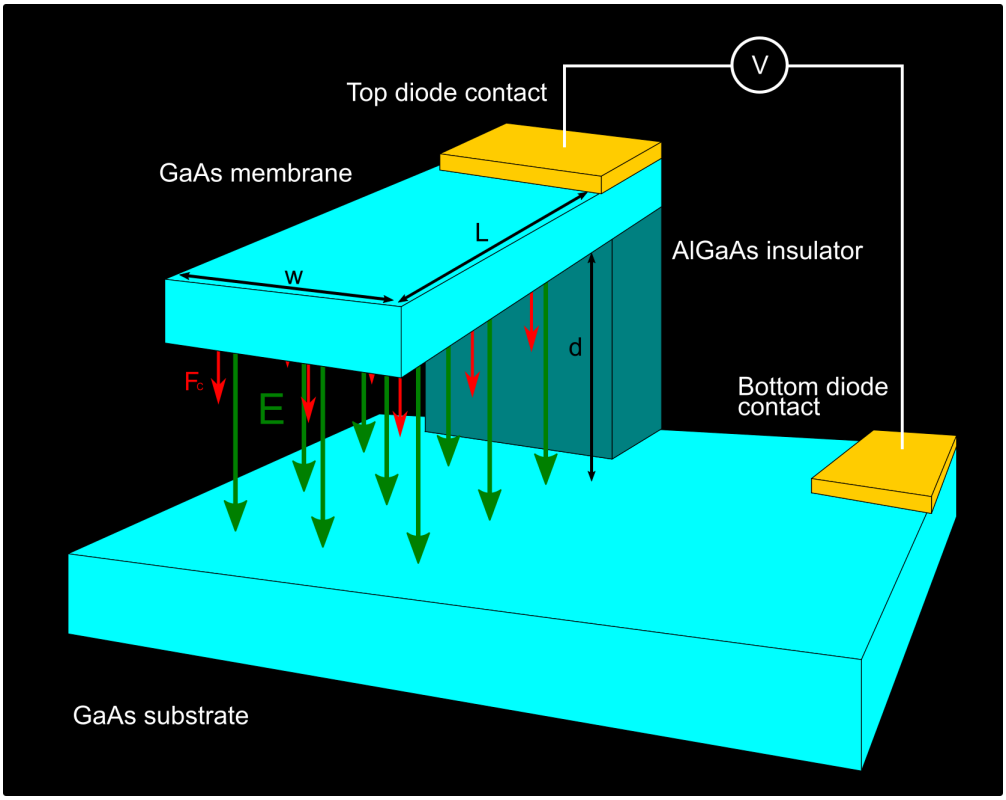

Figure 50: Diagram depicting a single free-standing cantilever device of length L width w and separated by some distance d from the substrate. When a non-zero voltage V is applied across the top and bottom contacts of the diode, a uniform electric field E is created between the cantilever and the substrate. This in turn produces a capacitive force F_C that acts to attract the cantilever and substrate to each other. This force causes a displacement of the free end of the cantilever towards the substrate which is governed by Hooke's law.

its equilibrium point. This induces stress in the cantilever which creates the restoring force F_R which acts against the electrostatic displacement to return the cantilever to its original location. When F_C and F_R are equal the cantilever will be at rest with some displacement s from its original location s_0. This force is given by Hooke's law:

$$F_R = K\left(s_0 - s\right) = \frac{\epsilon A}{2d^2}V^2 \tag{42}$$

Where K is the spring constant of the cantilever. An expression for the spring constant of the cantilever can be derived by considering a point load F incident on the tip of the cantilever of dimensions $L \times w \times t$. The internal moment M at any position x along the cantilever is given by:

$$M = -F\left(L - x\right) \tag{43}$$

and the equation for small angle displacements of a cantilever beam is:

$$\frac{d^2 s}{dx^2} = \frac{F}{\Sigma I}\left(L - x\right) \tag{44}$$

where s is the out-of-plane displacement of the cantilever, Σ is the Young's Modulus of the cantilever material and I is the moment of inertia of the cantilever. As this is a second order linear differential equation the solution is expected to have two boundary conditions, in this case these are:

$$s\left(0\right)=0;\frac{ds}{dx}|_{x=0}=0$$

As the right hand side of Equation 44 is linear with respect to x and is a second order derivative, it can be assumed that $s\left(x\right)$ is a third order polynomial and the following trial solution for Equation 44 can be introduced:

$$s=A+Bx+Cx^2+Dx^3 \tag{45}$$

From the boundary conditions: $A=B=0$. If the trial solution is now input into Equation 44 it shows

$$C=\frac{FL}{2\Sigma I};D=-\frac{F}{6EI}$$

giving the expression for the displacement as:

$$s=\frac{FL}{2\Sigma I}x^2\left(1-\frac{x}{3L}\right) \tag{46}$$

The spring constant of the cantilever is defined as the ratio of the maximum displacement to the point force. The maximum displacement occurs for $x=L$:

$$s_{max}=\frac{L^3}{3\Sigma I}F \tag{47}$$

Therefore, the spring constant is:

$$K=\frac{3\Sigma I}{L^3}=\frac{\Sigma wt^3}{4L^3} \tag{48}$$

where Σ is the Young's Modulus of the cantilever material, L,w,t are the length, width and thickness of the cantilever respectively and $I=\frac{1}{12}wt^3$ is the moment of inertia of the cantilever [175].

If Equation 48 is substituted into Equation 42, an expression for the out-of-plane displacement of the cantilever with respect to the bias between the substrate and membrane can be obtained:

$$(s_0-s)=\frac{2\epsilon L^4}{\Sigma d^2t^3}V^2 \tag{49}$$

As the distance between the two plates changes with displacement, it follows that: $d=s$. This allows a graph to be plotted showing the dependence of the cantilever displacement on the square of the applied bias (Figure 51).

The maximum displacement of the cantilever from the equilibrium point ($s=s_0$) possible is $s_0-s=\frac{1}{3}s_0$. The voltage at which this maximum displacement is achieved is called the pull in voltage (V_{PI}^2). At higher voltages the restoring force from the cantilever can no longer match the electrostatic force from the capacitance and the cantilever collapses onto the substrate below.

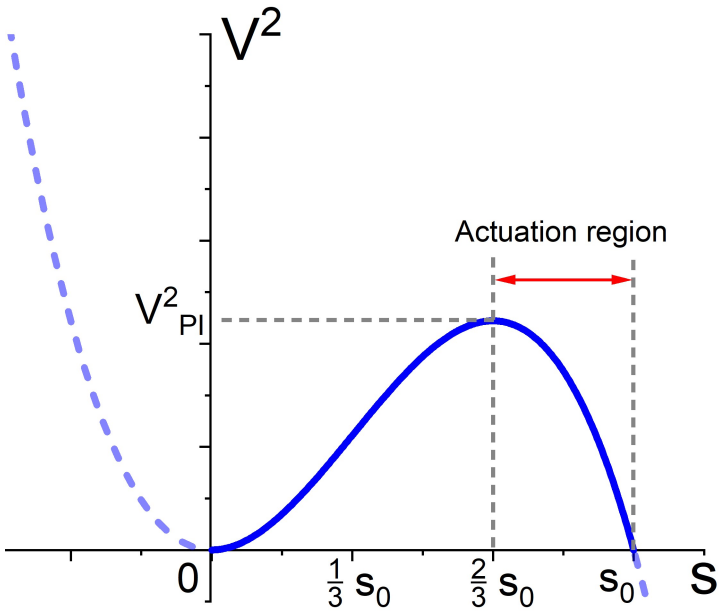

Figure 51: Graph showing the relationship between the distance between the cantilever and the substrate s and the square of the applied bias V^2. The maximum reversible displacement is $\frac{1}{3}s_0$ which is reached at the pull-in voltage V_{PI}^2. At higher voltages the electrostatic force overcomes the restoring force from the beam and the cantilever collapses down to the substrate. The region in which the actuation is controllable is marked on the graph

The cantilever can be released from the substrate if the restoring force is larger than the adhesive force between the cantilever and the substrate. For voltages below the V_{PI}^2 the displacement of the cantilever can be controlled precisely and rapidly, this allows for theoretically arbitrary control over the displacement.

For the devices proposed in this chapter, the maximum displacement is calculated from the thickness of the sacrificial AlGaAs layer between the membrane and the substrate. The thickness of this layer is approximately $1\mu m$ giving a maximum displacement of $(s_0 - s)_{max} \approx 333nm$. The theoretical pull in voltage can then be calculated from Equation 49. For a cantilever of dimensions $L = 30\mu m, t = 170nm$ at a displacement of $d = s = \frac{2}{3}s_0 = 666nm$ with the Young's modulus of GaAs taken as $\Sigma = 86GPa$ and vacuum permittivity $\epsilon = 8.85 \times 10^{-12}$, the pull in voltage is $V_{PI}^2 = 2.1V^2$. In reality, the applied voltage required to actuate the cantilevers is much higher due the resistance of the material and contacts [174].

5.3 Optimisation of the 1D photonic crystal cavity design

The first step in the designing of the tunable cavity devices was to develop a design for a 1D PhCC which exhibited a high Q-factor and low modal volume at a wavelength close to the centre of the InAs QD energy distribution (910nm was chosen). Moreover, the evanescent mode of the cavity

must extend far enough into the air cladding so that a perturbing beam can influence the effective index significantly without being too close to the cavity beam and risking the two beams adhering.

The design of the cavity is optimised using 3D-FDTD simulations. A single broadband dipole source is located in the cavity with a small displacement from the centre and used to directly excite the cavity mode. The source is displaced from the centre of the cavity and at a 45° angle to the nanobeam direction in order to excite modes of any polarisation and to excite modes that may have an electric field minimum at the cavity centre. A Q-factor monitor is positioned at the cavity centre which records both the wavelength and Q-factor of the cavity mode. This is achieved by fitting an exponential function to the cavity mode decay. A fine mesh override is positioned around the entire 1D PhCC as the differences in holes sizes for the tapered PhC can be extremely small and require high precision to be resolved. The simulation considers a sufficiently long time (10ns) so that most of the light has been dissipated from the cavity and the Q-factor measurement stabilises. Each cavity parameter is swept over a small range whilst the other parameters are kept constant. This allows for the effect of changing each individual variables to be investigated. The results are then analysed and an optimal design is presented.

5.3.1 Design overview

Figure 52 shows an overview of the 1D PhCC design that was chosen for optimisation for use in the tunable cavity system. The design features two photonic crystal areas: a uniform mirror section where the lattice period and hole radii are kept constant, and a tapered region where the period and hole radii reduce towards the cavity centre whilst maintaining the same period to radius ratio as the mirror (i.e. $\frac{r_0}{a_0} = \frac{r_{min}}{a_{min}}$) until a minimum period is reached. Due to the constraints of the fabrication process, the minimum hole radius cannot be smaller than 30nm as at radii below this, the holes cannot be reliably fabricated. Whilst different tapering schemes have been demonstrated to create effective cavities such as an increasing hole size taper [176] and tapering both the inner and outer holes [177], ultimately, an inner hole taper with a reduction in hole size was chosen. This scheme maximises the available dielectric space at the cavity centre that is far from any air interfaces whilst maintaining a high Q-factor and low mode volume. It has been estimated that within 40nm of an air/dielectric interface the optical properties of embedded QDs are degraded [178]. The smaller holes at the cavity centre increase the amount of dielectric material away from these interfaces compared to devices without a hole radii decreasing taper. Moreover, many cavity designs that use an increasing hole radii taper often create so called air mode cavities where the electric field maximum is in an air region of the device. This obviously does not allow for the cavity to facilitate embedded emitters at the field maximum. Therefore, such cavity designs are not suitable for our purposes.

In this section each of the cavity parameters will be studied in isolation to investigate the effect of each parameter on the cavity Q-factor and mode wavelength. The thickness of the nanobeam is

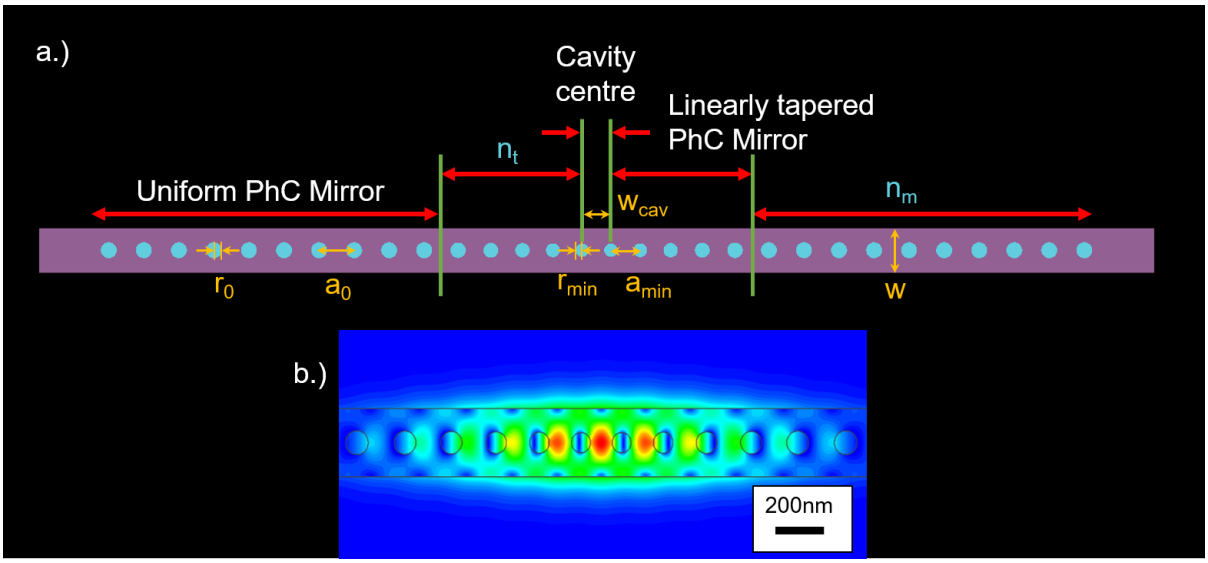

Figure 52: a.) Schematic of the 1D PhCC design that was optimised for use as a tunable cavity. The PhC contains uniform mirrors at either end of the device with air holes of radius r_0 separated by a period a_0. These mirrors surround an area where the radius and period of the air holes is tapered linearly by some factor to a minimum period and radius(a_{min} and r_{min}). This taper reduces the scattering losses from the cavity by reducing the mode mismatch between the cavity mode and the PhC mirror mode. b.) Shows the cavity mode electric field profile overlaying the cavity. The mode is strongly confined by the waveguide in the lateral direction and the tapered air holes in the waveguide direction.

fixed at 170nm by the GaAs wafer dimensions, as such the width is adjusted accordingly to support a single guided mode. This and the target mode wavelength of $\approx 910nm$ provides a set of fixed reference parameters from which the remaining cavity parameters can be optimised. The results of the optimisations will be presented graphically with the data points connected as a guide to the eye.

5.3.2 Initial nanobeam dimension selection

As mentioned in Section 5.3.1, the thickness of the nanobeam is determined by the semiconductor wafer dimensions and as such cannot be varied. Therefore, the other cavity parameters must be adjusted around this fixed thickness. Naturally, the first parameter to be considered is the width of the nanobeam as this is closely related to the thickness. By changing the ratio of the thickness of the nanobeam to the width of the nanobeam ,the band structure is changed. Therefore, the supported optical modes of the beam are also changed. The dispersion curve of a nanobeam features two bands which correspond to two orthogonal modes; '*Transverse-Electric*' (TE) and '*Transverse-Magnetic*' (TM), one for each cross-sectional axis. For a square cross-sectional nanobeam, where the width and thickness are equal, the two bands become degenerate. The further from the square beam case

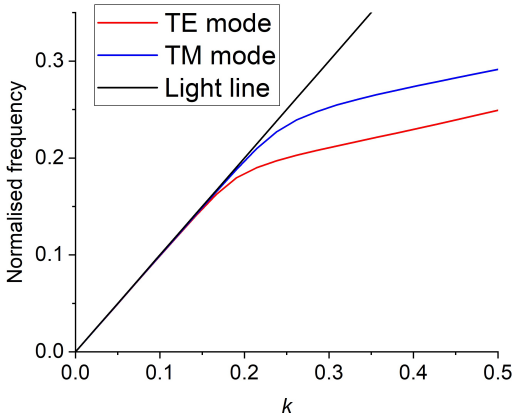

Figure 53: Graph showing the dispersion curve of the two orthogonal modes in a rectangular nanobeam waveguide with dimensions $t = 0.6w$. This roughly equates to a beam with dimensions $t = 170nm$, $w = 280nm$, the parameters used in the optimisation simulations. The dispersion curves were calculated using MPB.

the width to thickness ratio is, the further apart the two bands will be. The band structure of a nanobeam with the initial optimisation parameters is shown in Figure 53. A value of $w = 280nm$ was chosen as a starting point for the optimisation as for a beam of thickness $t = 170nm$ this gives a single TE mode which light can couple to at the target cavity mode wavelength. The effect of varying the beam width on the cavity performance is studied later in the chapter after the initial optimisation of the PhCC parameters for fixed beam dimensions.

5.3.3 Variations of the number of air holes (n_m and n_t)

The first parameter that will be discussed is the number of air holes either side of the cavity centre in both the tapered and uniform mirror PhC sections. The hole numbers are perhaps the most fundamental and obvious change that can be made to the cavity. It is intuitive to conclude that increasing the number of holes either side of the cavity will increase the strength of the photonic bandgap confinement, as the number of refractive index modulations is increased and therefore the number of reflective interfaces is also increased, leading to a stronger mirror. However, what is not obvious initially, is when or if this effect will saturate and how it will effect the cavity mode wavelength. Moreover, how the number of holes in the tapered PhC section affects the cavity performance is not trivial as the gradient of the taper is reduced when the number of holes is increased. It is vital to choose a number of holes that allow for a high Q-factor without making the devices too large as this would fundamentally limit the scalability of the devices. Figure 54 shows the results of the simulations of the 1D PhCCs with various numbers of uniform holes either side of the tapered PhC region at the cavity centre. From Figure 54 a.) it is clear that the Q-factor increases sharply between 8 and 12 uniform holes before saturating at 14 holes. The increase of the Q-factor is exponential up to 8 uniform holes as shown in Figure 54 c.), from 8 to 10 holes the Q-factor

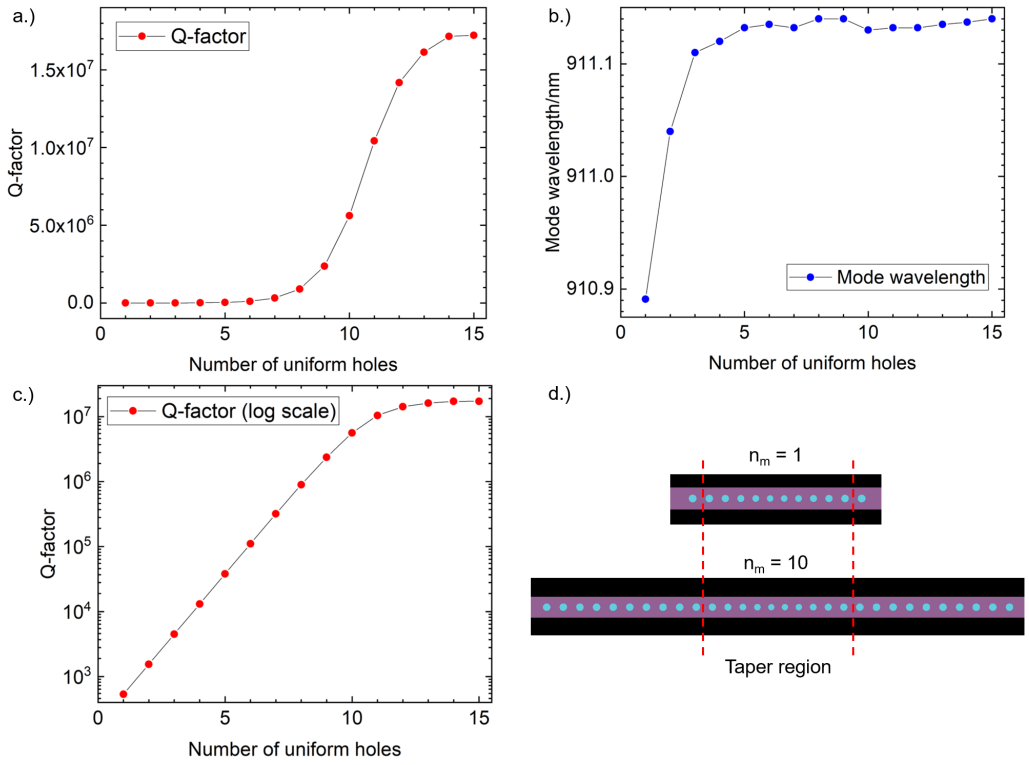

Figure 54: Graphs showing the effects of increasing the number of uniformly sized holes either side of the cavity centre on a.) The Q-factor and b.) The wavelength of the fundamental cavity mode of a tapered 1D PhCC. The other PhC variables are kept fixed at $n_t = 5, a_0 = 220nm, r_0 = 50nm, a_{min} = 184nm, w_c = 180nm$. The Q-factor increases sharply between 8 and 12 holes before saturating at 14 holes either side of the cavity. The wavelength of the cavity mode remains roughly constant for hole numbers above 2. c.) Shows the Q-factor dependence with a logarithmic scale to better represent the effect at smaller hole numbers. The trend is linear on the logarithmic scale up to 9 holes before falling off. d.) Shows a small schematic of the $n_m = 1$ and $n_m = 10$ cases to illustrate the difference between the simulated devices.

increase is only slightly slowed from the exponential case. For values above 10 the Q-factor growth drops off rapidly, however the magnitude of the Q-factor remains extremely high $> 10^7$. The effect of the number of uniform holes on the cavity mode wavelength is shown in Figure 54 b.). There is a very small wavelength shift of $\approx 200pm$ between 1 and 3 holes, past this the mode wavelength is stable.

These results confirm the intuitive thought that increasing the number of holes either side of the cavity will increase the Q-factor. This is true up until the saturation point at 14 holes. After this, the out-of-plane scattering losses from the cavity become dominant over the in-plane scattering losses. The extra confinement gained by adding more periods to the PhC only reduces in-plane

scattering losses and so the Q-factor saturates. What is extremely interesting is the exponential nature of the relationship between Q-factor and uniform hole number and the constant gradient of this trend over a large portion of the simulated hole numbers. This trend allows us to pick a number of holes to maximise the effective pay-off between Q-factor and device size by selecting a point at the end of the exponential trend as adding extra holes past this point gives less of a benefit in terms of Q-factor than the previous hole numbers. With this in mind, a value of 10 uniform mirror holes either side of the cavity is chosen to be optimal. Although 10 holes is off the truly exponential trend, the deviation is minor and so the value of the 9th and 10th holes is still significantly higher than any hole numbers > 10. As there is no significant effect on the mode wavelength for hole numbers > 3 it is safe to confirm 10 holes as the value to use for the tunable cavity devices.

Figure 55 shows the effect on the Q-factor and cavity mode wavelength when the number of holes in the tapered PhC region is altered. The way the taper region is designed means that the there will always be one hole with a radius of $r_{min} = a_{min}\frac{r_0}{a_0}$. Any other holes in the taper region will have a radius $r_i = r_{min} + \frac{i}{n_t} \cdot (r_0 - r_{min})$ where i is the number of holes between this hole and the cavity centre (e.g. for the holes immediately next to the cavity centre $i = 0$). This means that as the number of taper holes is increased, the difference in radius between neighbouring holes is reduced. This acts to smooth the interface between the cavity and uniform mirror modes, reducing scattering losses. From Figure 55 a.) it can be seen that at low numbers of taper holes the Q-factor is fairly low, this can be attributed to the interface between the cavity and mirror being too abrupt still and so the scattering losses remain high. The Q-factor increases exponentially up to 6 taper holes, here the maximum reduction in scattering losses is achieved, resulting in the highest Q-factor. At hole numbers > 7 the Q-factor drops off from the maximum value but remains high. It is possible that this drop off in Q-factor is due to the difference in diameter between adjacent holes in the taper being lower than the resolution of the simulations, thus not being resolved. The resolution of the simulations in Figure 55 was 2.5 x 2.5nm, for $n_t = 7$ the difference in diameter between adjacent holes is $d_{diff} = 2.34nm$, below the resolution of the simulation. For comparison, for $n_t = 6$, $d_{diff} = 2.73nm$ which is above the resolution of the simulation. Another explanation for this phenomenon could be that as the gradient reduces with the addition of more tapered holes, the radius difference reduces. Thus, adjacent holes approach uniformity with each other and therefore act as if they are part of a uniform mirror. This would cause an additional interface in the mode-matching between the cavity and mirror mode, introducing additional scattering and lowering the Q-factor.

If Figure 55 b.) is considered, the mode wavelength is seen to blue-shift with increasing taper hole number for a total of 23.8nm over the range of the simulations ($n_t = 1 - 10$). The amount of blue-shift seen when introducing additional taper holes is seen to reduce with each additional

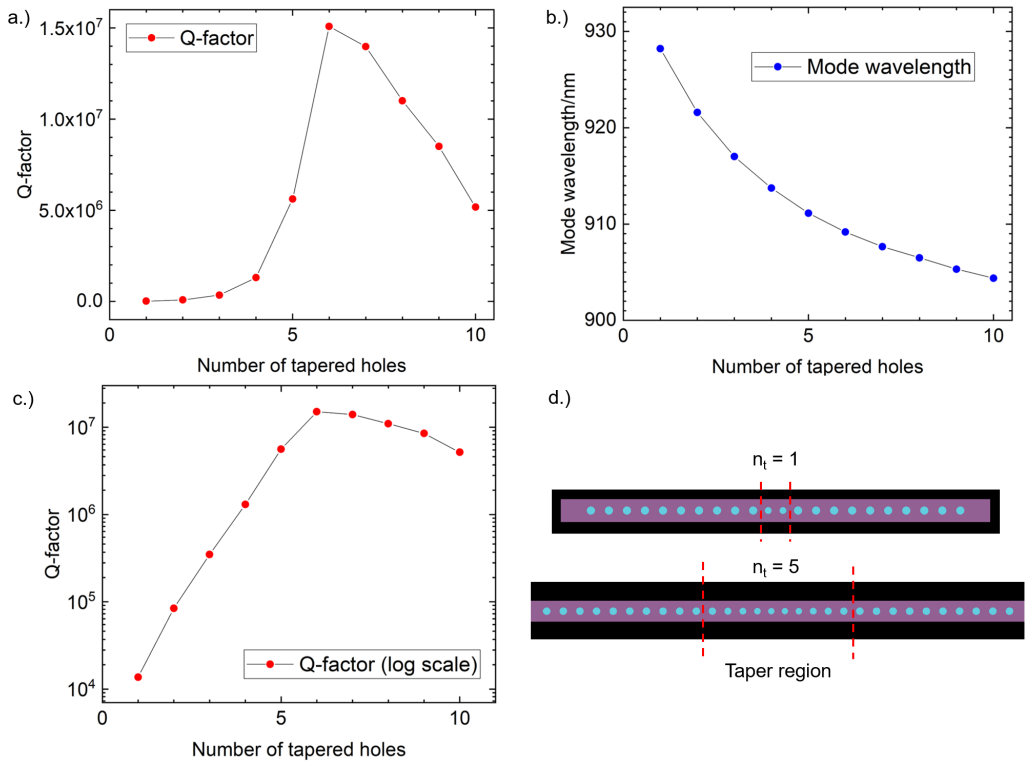

Figure 55: Graphs showing the effects of increasing the number of tapered holes either side of the cavity centre on a.) The Q-factor and b.) The wavelength of the fundamental cavity mode of a tapered 1D PhCC. The other PhC variables are kept fixed at $n_m = 10, a_0 = 220nm, r_0 = 50nm, a_{min} = 184nm, w_c = 180nm$. The Q-factor increases roughly exponentially up to 6 tapered holes after which the Q-factor drops off slowly whilst remaining high ($> 10^6$). The wavelength of the cavity mode blue-shifts gradually with increasing taper hole number. The magnitude of the blue-shift between taper hole numbers also reduces gradually with increasing total number of tapered holes. The total amount of blue-shift seen over the range of the simulations is 23.8nm. c.) Shows the Q-factor dependence on a logarithmic scale to better represent the trend for lower hole numbers. d.) Shows two schematics of the simulated devices for $n_t = 1$ and $n_t = 5$ to show the difference between simulated devices.

hole. By considering the taper gradient and radii differences between the adjacent holes, it is clear that at small taper hole numbers, where each additional hole reduces the taper gradient by a large amount, the resulting wavelength shift will be larger than for the case with a large number of taper holes, where any additional hole only change the gradient slightly.

For the devices the optimal number of taper holes was chosen to be $n_t = 5$. This value was chosen over $n_t = 6$ as an attempt to afford the device a degree of robustness against fabrication imperfections. A shallower taper is more susceptible to hole radii fluctuations due to the finer

difference between adjacent holes. By choosing a lower taper number that still exhibits a high Q-factor the effect of any radii fluctuations on the Q-factor of the cavity will be reduced.

Combining the results for both the n_m and n_t simulations, the optimal number of holes in each PhC region is $n_m = 10$ and $n_t = 5$ for a total of 15 holes either side of the cavity centre.

5.3.4 Variations of the uniform hole radius (r_0) and period (a_0)

Now the overall number of holes has been determined, the next logical step is to consider the dimensions of these holes and the spacing between them. Firstly, the uniform mirror PhC area is considered. The effect of changing the radius (r_0) of the air holes and the period of the PhC (a_0) on the cavity performance is investigated. Altering the mirror hole radius changes the '*fill factor*' (the ratio of hole area to unit cell size) of the PhC. Changing the fill factor of the PhC alters its '*mirror strength*', a measure of the reflectivity of each unit cell of the mirror. The mirror strength of the PhC mirror can be extracted from the evanescent field of the cavity mode in the PhC mirror. As the PhC mirror is a Bragg mirror, the evanescent field of the cavity mode is given by:

$$\sin\left(\beta_{Bragg}x\right)e^{-\kappa x} \tag{50}$$

Where κ and β_{Bragg} are the attenuation constant or mirror strength, and phase constant of the Bragg mirror respectively. For a given beam width, there will be a hole radius that gives a fill factor of maximum mirror strength. However, the effect that altering the hole size may have on the wavelength of the cavity mode must be considered. A parameter sweep on the uniform mirror hole radii over a range of 30nm was conducted.

The results of these simulations are presented in Figure 56. From Figure 56 a.) and c.) it can be seen that the Q-factor increases exponentially from 40nm up to its peak value at 57.5nm after which the Q-factor drops off as the hole radii increase further. This suggests that for the beam dimensions (280 × 170nm) a radius of 57.5nm is optimal for achieving maximal Q-factor. This peak in Q-factor, whilst indicative of a high mirror strength, may not reflect accurately the maximum mirror strength. When changing the uniform mirror radii, other aspects of the cavity are altered due to the fixed parameters. For example, as the minimum PhC period is fixed ($a_{min} = 184nm$) increasing r_0 will increase r_{min} due to the condition that the ratio between hole radius and period remains constant. This causes the size of the dielectric gap at the cavity centre to reduce as the spacing between the centres of the two central holes is fixed $w_c = 180nm$. Thus, the effective cavity width is reduced as the space available for the electric field is reduced. As will be shown later in Section 5.3.5, the cavity width is one of the most sensitive cavity parameters. Therefore, it is almost certain that there is a compound effect when increasing the uniform mirror hole radii. Both the mirror strength and the effective cavity width are simultaneously altered. The extent of this effect will be discussed later in Section 5.3.5.

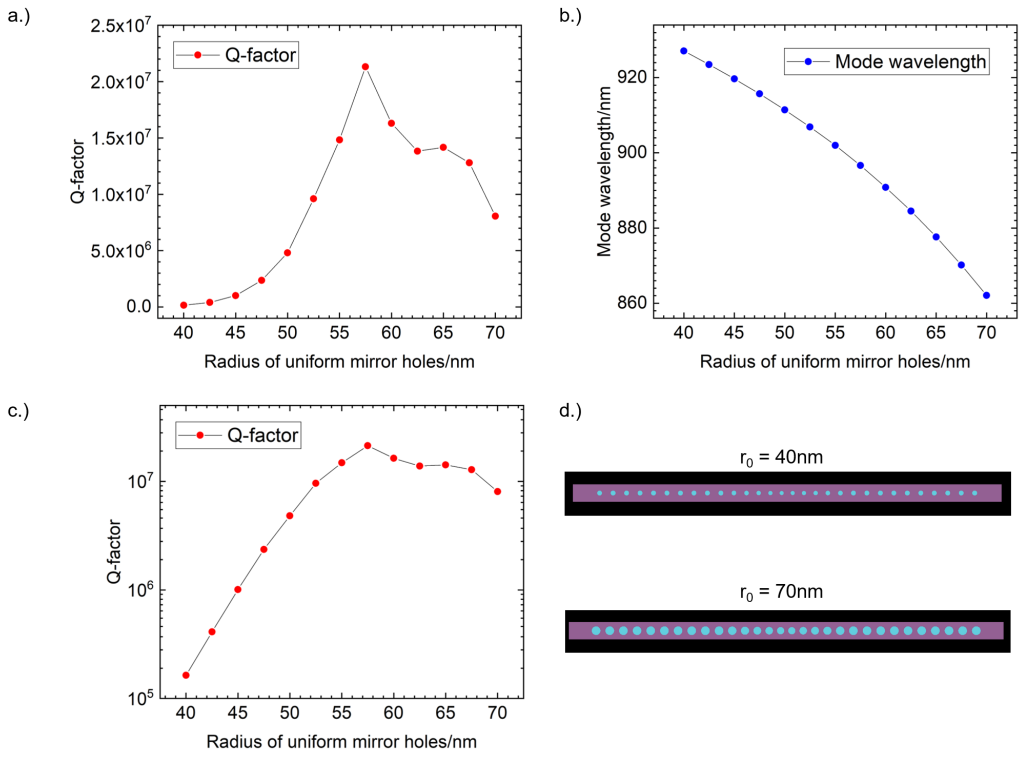

Figure 56: Graphs showing the results of parameter sweep simulations of the uniform mirror hole radii whilst keeping all other cavity parameters fixed at $n_t = 5, n_m = 10, a_0 = 220nm, a_{min} = 184nm, w_c = 180nm$. a.) The Q-factor of the cavity as a function of r_0, the Q-factor increases exponentially up to a radius of 57.5nm before dropping off sharply. b.) Shows the wavelength of the cavity mode blue-shifting steadily with increasing r_0. The rate of blue-shift increases slightly as the magnitude of the radius increases. c.) Shows the Q-factor relationship on a logarithmic scale to better represent the trend at lower radii. d.) Shows schematics of the smallest and largest radii simulated.

The wavelength of the cavity mode blue-shifts with increasing uniform mirror hole radii as seen in Figure 56 b.). The amount of blue-shift is roughly constant between each radius iteration with it gradually increasing as the hole radii increase. The rate of blue shift is approximately: $\frac{d\lambda}{dr} = -2.13 \pm 0.08$. The blue-shifting of the modes is a consequence of the band structure of the cavity changing with the increasing fill factor, causing the cavity mode to also shift. A 5nm shift ($\approx 10\%$) in hole radii equates to a roughly 10nm shift in the cavity mode resonance wavelength.

When deciding the optimal radius for the tunable cavity designs, the effects of fabrication imperfections on the features must be considered. If the design is over-etched, meaning the nano-holes are larger than designed and the width of the beams is narrower than expected, then there is a

large shift in the fill factor. This could easily lead to the cavity mode wavelength being heavily blue-shifted from the expected value. The radius of the smallest hole in the taper must also be considered. Current fabrication capabilities can only reliably fabricate holes with a minimum radius of 30nm. Therefore a value for r_0 should be chosen that gives a value of r_{min} that is greater than this limit. A value for the uniform mirror hole radius of 50nm was chosen, this gave some room for over etching of both the holes and nanobeam width whilst remaining in the high Q-factor region. The wavelength of the mode is close to the target of 910nm also.

The other variable in the uniform mirror PhC is the period a_0. The period of the PhC defines the regular spacing between the centres of the air holes. This, combined with the radius of the holes form the band structure of the PhC and therefore the photonic band gap. Therefore, optimising the period in tandem with the hole radii is essential to obtain a high Q-factor cavity mode at the correct wavelength.

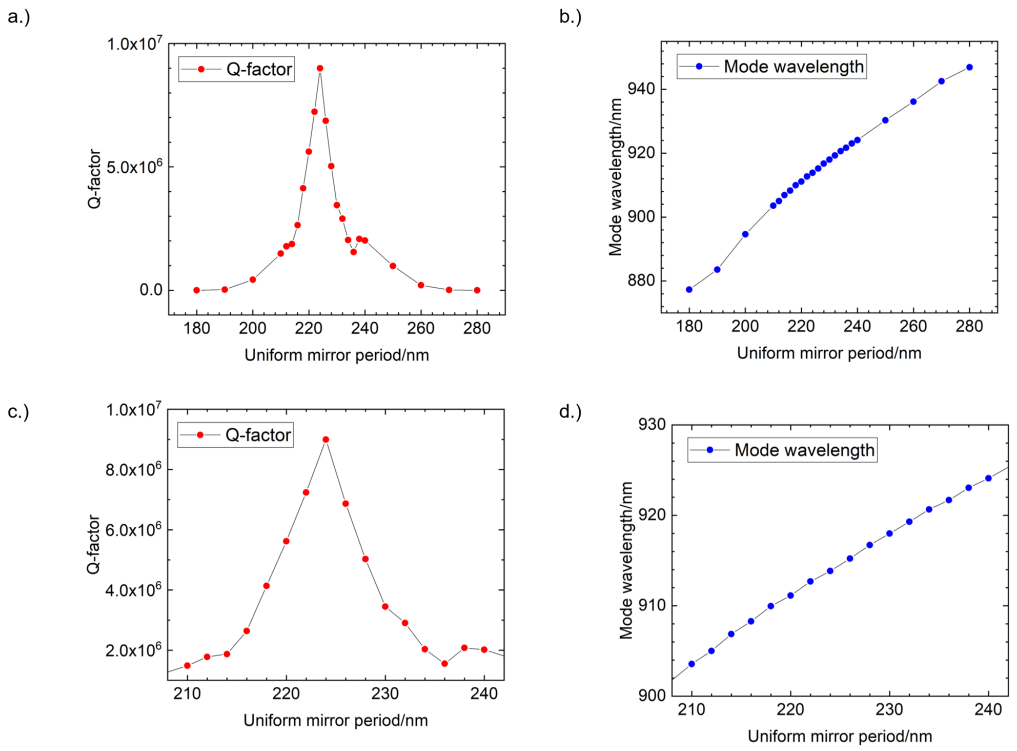

Figure 57: Graphs showing the effect of changing the uniform mirror air hole period on the cavity performance whilst keeping the other parameters fixed at $n_t = 5, n_m = 10, r_0 = 50nm, a_{min} = 184nm, w_c = 180nm$. a.) The Q-factor of the cavity peaks sharply at a period of 224nm in a resonance like manner. The width of the Q-factor peak is 9nm. b.) The cavity mode wavelength red-shifts linearly with increasing period at a rate of 0.68nm for every 1nm increase in period. This trend is consistent over the entire range of the simulations. c.) and d.) Show a zoomed in view of the Q-factor peak and corresponding cavity wavelengths respectively.

Figure 57 shows the effect of varying the uniform PhC period on the cavity mode Q-factor and wavelength. From Figure 57 a.) it can be seen that the Q-factor peaks sharply at a period of 224nm in a resonance like fashion. This sharp resonance behaviour likely derives from the large effect even a small change in period has on the overall cavity structure. Changing the PhC period of the uniform mirror whilst keeping the minimum period fixed causes the gradient of the taper to change. As discussed in Section 5.3.3 the correct gradient of the taper is essential to achieve a high Q-factor. Moreover, changing the spacing between the air holes alters the electric field profile of the mode. The optimal amount of space between the holes is required to naturally confine the electric field in the dielectric medium. If the holes are too close together there is not sufficient space for the anti-nodes of the electric field to exist purely in the dielectric. Therefore, the light is scattered by the air holes reducing the confinement of the cavity. Too much space and the same problem emerges; the holes are spaced so that some anti-nodes will end up in the air holes.

The wavelength of the cavity mode red-shifts linearly with increasing uniform PhC period as seen in Figure 57 b.). By fitting the trend with a linear fit, the rate of red-shift is extracted as 0.68nm per 1nm increase in period.

The fabrication error on nano-hole position is very low compared to the value of the period (roughly $\pm 5nm$) thus, it is not necessary to make any major concessions to reduce any fabrication-related imperfections. Therefore, a value of $a_0 = 220nm$ is taken for the devices. This is slightly off the highest Q-factor value, however, the drop in Q-factor is small and the wavelength of the mode is closer to the target 910nm. Moreover, this value is within the positioning error of the highest Q-factor value of $a_0 = 224nm$.

To conclude, the uniform mirror PhC parameters were chosen to be $r_0 = 50nm, a_0 = 220nm$.

5.3.5 Variations of the cavity width (w_c) and minimum taper period (a_{min})

The final two PhC parameters that need optimising are related to the cavity centre, where the maximum of the electric field lies. Naturally, this makes these parameters extremely important to optimise carefully, as they will have the largest direct impact on the cavity field profile. The first of these parameters is the minimum taper period a_{min}. This dictates the spacing between the last two holes in the taper before the cavity centre and therefore sets the taper gradient and minimum taper hole radius. As mentioned in Section 5.3.3 the taper gradient is the most important aspect for achieving ultra-high Q-factors in 1D PhCCs. Therefore, the value of the minimum taper period is arguably the most important parameter of the design.

Figure 58 shows the results for the parameter sweep simulations of the minimum taper period

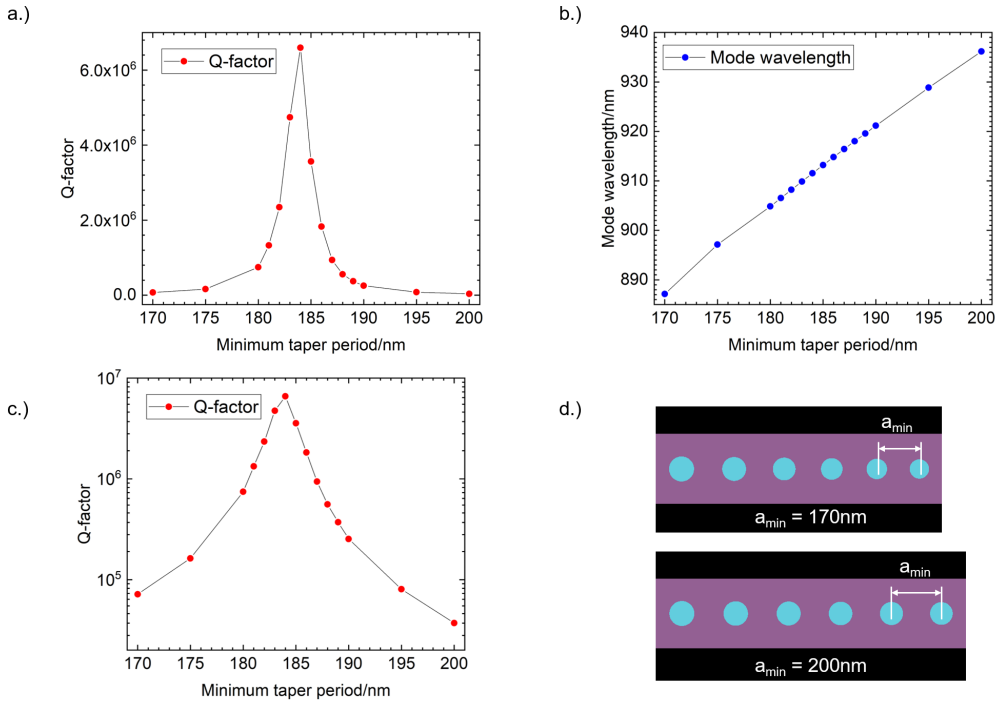

Figure 58: Graphs showing the effect on the cavity performance of altering the minimum taper period (a_{min}) whilst keeping all other cavity parameters constant at: $n_t = 5, n_m = 10, r_0 = 50nm, a_0 = 220nm, w_c = 180nm$. a.) Shows the effect of changing a_{min} on the Q-factor of the cavity mode. An extremely sharp resonance-like peak is observed at a value of $a_{min} = 184nm$. b.) Shows that the wavelength of the cavity mode red-shifts linearly with increasing a_{min}. The rate of red-shift is extracted from the gradient of the trend and is found to be $1.6nm$ of red-shift per $1nm$ increase in a_{min}. c.) Shows the Q-factor dependence from a.) on a logarithmic scale to better represent the lower values of the Q-factor. d.) Shows two schematics of the tapered PhC section demonstrating the lowest and highest a_{min} values that were simulated.

on the cavity performance. From Figure 58 a.) it can be seen that the Q-factor is incredibly sensitive to the value of minimum taper period, with a narrow peak in Q-factor at a value of $a_{min} = 184nm$. This narrow resonance-like peak shows the sensitivity of the cavity Q-factor to the minimum taper period which is further demonstrated in c.) where the peak remains sharp, even on a logarithmic scale. This is likely due to the compound nature of this variable. Changing a_{min} not only affects the taper gradient but also the minimum hole radius which in turn effects the effective cavity width. All of this has a combined effect on the Q-factor of the cavity. The peak in Q-factor is found at a value of $184nm$ for the fixed parameters. Comparing this to the value of a_0 the optimal value of a_{min} is found to be $0.84a_0$. This is consistent with the values used by Y. Zhang et al. [179] and D.Bracher et al. [180] for maximising the Q-factor of similar 1D PhCC designs.

Away from the peak value of a_{min} a roughly exponential decrease in the Q-factor is still observed as seen in Figure 58 c.). At these extreme values the taper gradient is either too steep, creating a large interface between the cavity and mirror modes, or too shallow, causing the same problem as the taper trends towards the uniform mirror dimensions, essentially eliminating the taper.

From Figure 58 b.) a linear red-shift of the cavity mode wavelength with increasing minimum taper period is seen at a rate of $1.6nm$ of red-shift per $1nm$ increase in a_{min}. This rate is more than double the rate of red-shift observed for changing the uniform mirror period by the same amount. This further demonstrates the sensitivity of the cavity parameters to the value of the minimum taper period.

Due to the high sensitivity of the cavity performance to the minimum taper period producing an extremely sharp resonance peak, this optimum value of $a_{min} = 184nm$ is chosen for the optimal cavity design. This value is chosen as any fabrication-related fluctuations to the hole radii will be about the peak and so guarantee the highest average Q-factor. Moreover, this value of $a_{min} = 0.84a_0$ is widely accepted as the standard in the literature and has shown success in multiple designs.

The last parameter to be optimised is the width of the cavity centre w_c. The results of the cavity centre width parameter sweep are shown in Figure 59. From Figure 59 a.) a sharp resonance-like peak in the Q-factor is seen at a value of $w_c = 180nm$. This peak is extremely similar to the peak seen in Figure 58 a.) for changes to the minimum taper period a_{min}. However, the w_c peak is slightly wider than the a_{min} peak. This confirms that as expected, the cavity performance is extremely sensitive to the cavity width given the large direct impact it has upon the electric field maximum. However, the sensitivity is lower than for the minimum taper period as is apparent from the difference in peak width. Inspecting the Q-factor peak more closely using the logarithmic scale of Figure 59 c.) it can be seen that the peak is slightly asymmetric about the maximum value. The Q-factor for wider cavity centres is higher than for the equivalent smaller cavity widths on the other side of the Q-factor peak. This asymmetry is more pronounced further from the peak value. The cause of this effect is not clear however, the difference is small compared to the Q-factors close to the peak value and so will not affect the choice of cavity width.

The effect of altering the cavity width on the cavity mode wavelength is shown in Figure 59 b.). A roughly linear relationship is seen between cavity width and mode wavelength, with the mode wavelength red-shifting with increasing cavity width. By applying a linear fit to values of the mode wavelength for cavity widths between 170 - 190nm the rate of red-shift of the cavity mode is found to be $0.68nm$ per $1nm$ increase in cavity width. This rate is the same as the rate calculated for changes in the uniform PhC mirror period. This implies that both parameters likely affect the cav-

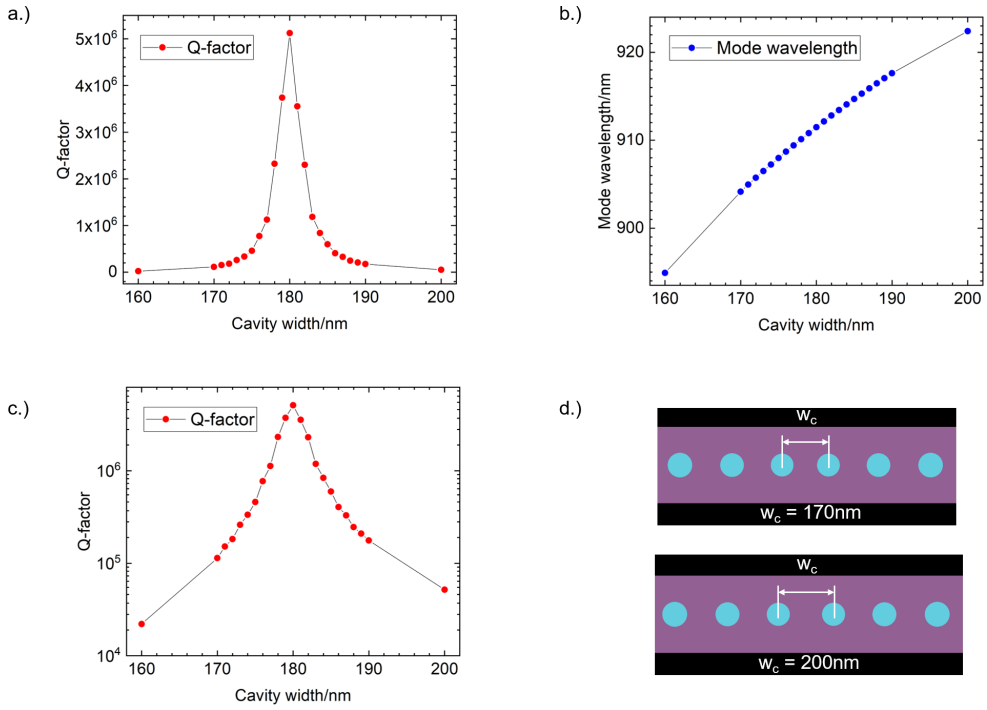

Figure 59: Graphs showing the effect on cavity performance of varying the cavity centre width w_c whilst keeping all other parameters fixed at: $n_t = 5, n_m = 10, r_0 = 50nm, a_0 = 220nm, a_{min} = 184nm$. a.) Shows that the Q-factor peaks sharply at a value of $w_c = 180nm$. b.) Shows the effect on the cavity mode wavelength of changing the cavity width. A roughly linear red-shift is observed for increasing cavity width. The rate of red-shift is calculated from a linear fit to the data and is found to be $0.68nm$ of red-shift per $1nm$ increase in cavity width. c.) Shows the Q-factor dependence on a logarithmic scale, this reveals the peak is slightly asymmetric about the maximum. d.) Shows two schematics of the cavity centre depicting lowest and highest cavity widths simulated.

ity mode wavelength via the same mechanism. When altering the uniform PhC period the distance between not only the holes in the mirror but also the holes in the taper is altered with the exception of the two holes either side of the cavity (governed by w_c) and the second hole either side of the cavity centre (governed by a_{min}). Changing the cavity width changes the spacing between the two central holes. This can be seen as changing the spacing between the two PhC mirrors that form the cavity. This is a similar operation to changing the uniform PhC period as all that is changed is the spacing between holes. Altering the cavity width only changes the spacing between two holes, however, this causes a systematic shift of all the holes symmetrically about the cavity centre. Thus, the position of all holes is indirectly affected. One can imagine that this shift is similar in nature to increasing the spacing between the uniform PhC holes, as both result in a positional shift of the holes. When compared to the Q-factor peak in Figure 57 a.) it is clear that the Q-factor is much

more sensitive to changes in the cavity width than it is to the same change in uniform PhC period.

A cavity width of 180nm was chosen to be optimal for the cavity design as it gave the largest Q-factor and was at the middle of the narrow Q-factor peak. By choosing the peak value, any fluctuation in cavity width should result in the maximum average Q-factor for a randomly distributed error around the starting value, as would be expected from any fabrication errors.

5.3.6 Variation of the nanobeam width w

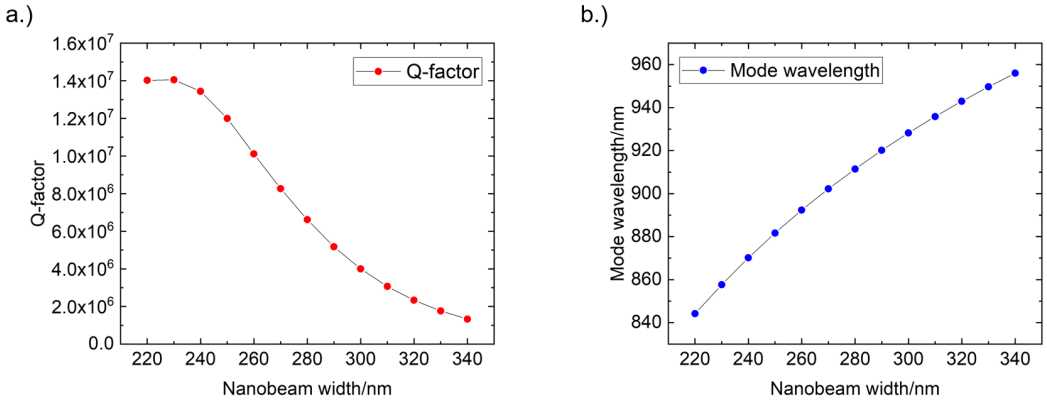

Figure 60: Graphs showing the effect of modifying the width of the cavity nanobeam on a.) The Q-factor and b.) The wavelength of the cavity mode.

Finally, with the PhC parameters optimised, the effect of altering the width of the nanobeam is investigated. Due to inaccuracies in the fabrication process, it is often challenging to reliably fabricate nanobeams of a desired width. Therefore, the width of the cavity beam will likely be variable in real structures. Figure 60 shows the results from the nanobeam width variation on an optimised 1D PhCC. The design was optimised for a beam width of $w = 280nm$ however, as can be seen in Figure 60 a.) this does not correspond to the nanobeam width which exhibited the highest Q-factor cavity mode for these parameters. The Q-factor increases with decreasing cavity width until a value of $w = 230nm$ where the Q-factor plateaus. Moreover, at $w > 280nm$ the Q-factor decreases gradually. This increase in Q-factor at low values of w is likely caused by an increase in the confinement of the light due to the increased relative size of the air holes. As the radius of the air holes is kept constant while the width of the nanobeam is reduced, the fill factor of the PhC is altered. This leads to an increase in the mirror strength of the PhC. Therefore, the confinement of the cavity is increased leading to an increase in the Q-factor. Figure 60 b.) shows that as the width of the nanobeam is reduced the cavity mode experiences a blue-shift. This is

expected as the available space in the cavity is reduced. Thus, the cavity can only support shorter wavelengths of light. Moreover, the band structure of the nanobeam is altered when changing the ratio of w to t leading to a change in the supported cavity mode. The choice of $w = 280nm$ remains a sensible choice to mitigate the effects of fabrication imperfections. If the beam width and other cavity parameters are over- or under-etched, then the intrinsic Q-factor remains high due to the intentional redundancy in the design.

5.3.7 Relative performance of optimised 1D photonic crystal cavities compared to 2D photonic crystal cavities

With the parameter sweep simulations completed, optimal values for each parameter for the tunable cavity design are obtained. The values chosen for each parameter were:

$$n_m = 10$$

$$n_t = 5$$

$$r_0 = 50nm$$

$$a_0 = 220nm$$

$$a_{min} = 184nm$$

$$w_c = 180nm$$

The resulting cavity has a Q-factor and mode wavelength of:

$$Q = 5.6 \times 10^6$$

$$\lambda = 911.1nm$$

These parameters give a high Q-factor cavity with considerations taken to mitigate any fabrication imperfections and keep the design compact, with the cavity mode very close to the target wavelength. If the cavity is designed purely to maximise the Q-factor then the cavity parameters are:

$$n_m = 15$$

$$n_t = 6$$

$$r_0 = 57.5nm$$

$$a_0 = 224nm$$

$$a_{min} = 0.84a_0 = 188nm$$

$$w_c = 185nm$$

which gives a cavity with a Q-factor and mode wavelength:

$$Q = 83.7 \times 10^6$$

$$\lambda = 908.3nm$$

As discussed in Section 2.5, the figure of merit for cavity performance in both the weak and strong coupling regimes depends on the Q-factor and the mode volume of the cavity mode. Whilst the Q-factor is calculated for each simulation in the parameter sweeps, the modal volume calculation is much more resource-intense and as such, it is not viable to calculate the mode volume for each simulation. Instead, the mode volume is calculated after the optimisation of the cavity parameters. The mode volume is calculated using Equation 2.5; the electric field intensity is obtained by using a field power monitor in the FDTD simulation which spans the entire simulation region at the cavity resonance wavelength. For the cavity parameters chosen for the tunable cavity, the mode volume is:

$$V_m = 0.488 \left(\frac{\lambda}{n}\right)^3$$

Using this value for the mode volume and the Q-factor calculated for the cavity, the figures of merit for both the weak and strong coupling regimes can be calculated.

$$\frac{Q}{V_m} = 11.5 \times 10^6$$

$$\frac{Q}{\sqrt{V_m}} = 8.0 \times 10^6$$

For the cavity optimised for maximal Q-factor the mode volume is slightly reduced.

$$V_m = 0.481 \left(\frac{\lambda}{n}\right)^3$$

Giving the figures of merit for weak and strong coupling as:

$$\frac{Q}{V_m} = 174.0 \times 10^6$$

$$\frac{Q}{\sqrt{V_m}} = 120.6 \times 10^6$$

These values obtained for the figures of merit from the 1D PhCC designs are compared to those found for 2D PhCCs in simulation [181] in Table 1. It is seen that the highest figures of merit for both strong and weak coupling are seen in the 1D PhCC design. It is clear from Table 1 that the advantage of the 1D PhCC design over 2D PhCCs is the ability to simultaneously support high Q-factor and low mode volume cavity modes. For the 2D PhCCs there is a strong trade-off between a low mode volume and high Q-factor except for a particular H0 design. However, this H0 design is extremely sensitive to fabrication imperfections. Minkov and Savona simulated a small Gaussian fluctuation to both air hole radius and position for each cavity design [181]. For a fluctuation

Table 1: Table comparing the values of Q-factor, mode volume and the figures of merit for weak and strong coupling ($\frac{Q}{V_m}$ and $\frac{Q}{\sqrt{V_m}}$ respectively) obtained via simulation for different types of PhCCs. It is clear that both the maximal Q-factor and tunable 1D cavity designs strongly outperform 2D PhCCs for both figures of merit due to exhibiting both a high Q-factor and low mode volume simultaneously. The 2D PhCCs either have a high Q-factor or low mode volume at the expense of the other with the exception of a very specific H0 design. Data for the 2D PhCCs was obtained from M. Minkov and V. Savona [181]

Cavity type	Q-Factor	Mode Volume	$\frac{Q}{V_m}$	$\frac{Q}{\sqrt{V_m}}$
H1	1.0×10^6	0.62	1.6×10^6	1.27×10^6
H0 low V_m	1.0×10^6	0.25	4.2×10^6	2.1×10^6
H0 high Q	8.9×10^6	0.64	14×10^6	11.1×10^6
L3	5.1×10^6	0.94	5.4×10^6	5.3×10^6
Tunable 1D	5.6×10^6	0.49	11.5×10^6	8.0×10^6
Max Q 1D	83.6×10^6	0.48	174.0×10^6	120.6×10^6

magnitude of $0.003a$ the average Q-factor for the high Q H0 design is reduced by over an order of magnitude to $Q_{ave} = 0.65 \times 10^6$. This reduction is the largest of all the 2D cavity designs considered and brings the Q-factor of the H0 to a value similar to the other cavity designs considered. To compare the robustness of the design to that of the 2D designs, similar error quantifying simulations must be performed. These simulations are outlined and completed in Section 5.5.1.

5.4 Optimisation of the perturbing photonic crystal membrane

Having optimised the cavity design, the next step is to optimise the perturbing beam structure to maximise the achievable tuning range and reduce any loss of Q-factor that may result from the presence of the beam in the evanescent cavity mode. The optimisation of the perturbing beam is conducted in a similar manner to that of the cavity. Figure 61 shows a typical cavity and perturbing beam simulation used to optimise the performance of the tunable cavity. The cavity parameters are kept constant at the values found in Section 5.3 for the tunable cavity design. The PhC parameters (hole radii, PhC period and length of perturbing beam) and the separation between the cavity and perturbing beams are studied via parameter sweeps to obtain the optimal dimensions for the device. In order to test the operation of the device, each parameter set is simulated over the full actuation range of the cantilever out-of-plane. This requirement for a large number of additional simulations for each parameter set makes the optimisation process much more resource-intense and time consuming. As a result, the range of the parameter sweeps are reduced.

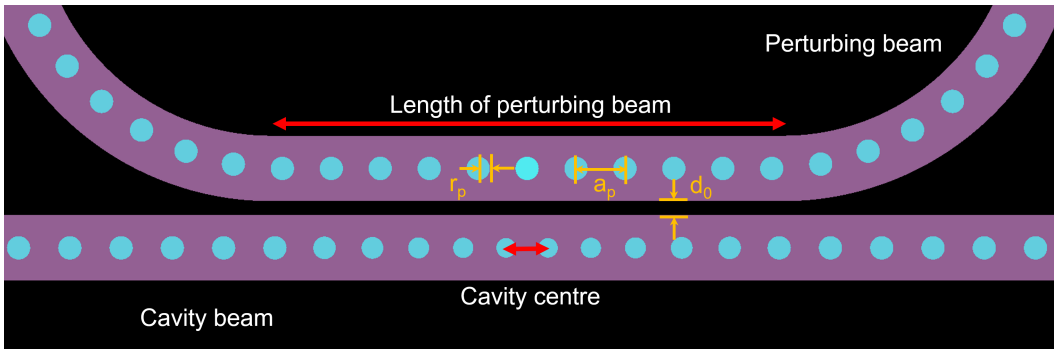

Figure 61: Schematic showing the relevant perturbing beam parameters that were optimised in simulation. r_p and a_p are the radius and period of the PhC in the perturbing beam. d_0 is the in-plane separation between the cavity and perturbing beams at zero out-of-plane displacement. The length of the perturbing beam was also altered by changing the number of PhC periods where the beams are parallel (n_b).

5.4.1 Optimisation of in-plane separation of cavity and perturbing beams (d_0)

The first parameter to be optimised is the in-plane separation between the two beams d_0. The in-plane separation defines the air gap between the extremities of the cavity and perturbing beams. This sets the overlap between the evanescent cavity mode and the perturbing beam at zero out-of-plane displacement. A larger overlap will lead to a larger change in effective index when the perturbing beam is actuated out of the evanescent mode, leading to a larger shift in cavity mode wavelength. However, the amount of scattering of light from the cavity due to the presence of the beam will be increased, leading to a reduction in Q-factor. Moreover, at very small separations, the fabrication of the device becomes extremely challenging. Not only could the beams be under-exposed and fail to be consistently separated in the fabrication, but subsequently, the closer the beams are together the higher the chance of them fusing via electrostatic effects once a bias is applied across the diode.

Figure 62 shows the results of the parameter sweep simulations for changing in-plane separation between the cavity and perturbing beams at zero out-of-plane separation. At large separation values, the cavity Q-factor and mode wavelength reach the unperturbed case as the perturbing beam does not intersect with the evanescent field of the cavity mode. Only at in-plane separations below $100nm$ is a perturbation of the cavity mode wavelength noticeable. As the in-plane separation decreases, the Q-factor of the cavity mode decreases and the cavity mode wavelength red-shifts exponentially. The decrease in Q-factor is due to scattering and coupling losses associated with the presence of the perturbing beam. Similarly, the introduction of the perturbing beam into the evanescent cavity field causes an increase in effective index which results in a red-shift of the cavity mode. Despite the exponential drop in Q-factor at small separations, the absolute Q-factor remains

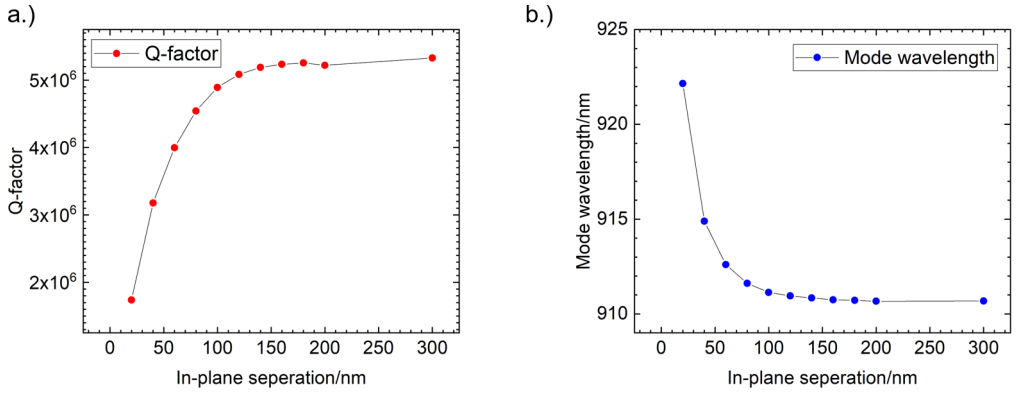

Figure 62: Graphs showing the effect of altering the in-plane separation between the optimised tunable cavity and an infinitely long perturbing beam at zero out-of-plane displacement on a.) The Q-factor and b.) The wavelength of the cavity mode. The Q-factor and mode wavelength exhibit similar but mirrored trends with a sharp trend initially that quickly plateaus around in-plane separation values greater than 100nm. The Q-factor increases with increasing separation due to the reduction in scattering and coupling losses from the perturbing beam. The mode wavelength blue-shifts with increasing separation due to the reduction in effective mode index.

above 10^6 and so the cavity performance is not greatly affected by the introduction of the perturbing beam. It is clear from Figure 62 b.) that to achieve a large tuning range the separation of the two beams must be minimised. However, as discussed earlier, if the separation is designed to be too small then the fabrication becomes extremely challenging and unreliable. It is estimated that the smallest separation which can be reliably achieved is $d_0 = 60nm$. This gives a maximum tuning range of $1.5nm$ whilst only reducing the Q-factor of the cavity by 25%. Therefore, an in-plane separation of $60nm$ is aimed for in the design. All simulations on the cavity and perturbing beam system going forward will use $d_0 = 60nm$.

5.4.2 Optimisation of perturbing beam photonic crystal period (a_p) and hole radii (r_p)

The perturbing beam PhC parameters are optimised next. The Q-factor of the cavity is reduced when the perturbing beam is introduced into the evanescent cavity field. This is due to light both scattering off the PhC and coupling into the guided modes of the perturbing beam. By adjusting the PhC parameters, the scattering and coupling losses can be minimised. By adjusting both the physical and momentum space overlap between the cavity and perturbing beam modes, it has been shown it is possible to maximise the coupling efficiency into a waveguide in the same geometry as the design [182]. Therefore, it is also possible to minimise the coupling in a similar fashion to remove any unwanted coupling losses from the system.

The starting point for the perturbing beam PhC parameters was that of the uniform cavity mirror($a_0 = 220nm$,$r_0 = 50nm$) as the cavity mode does not couple strongly to this PhC. From these initial parameters firstly, the period of the PhC a_p was altered. Figure 63 shows the effect of

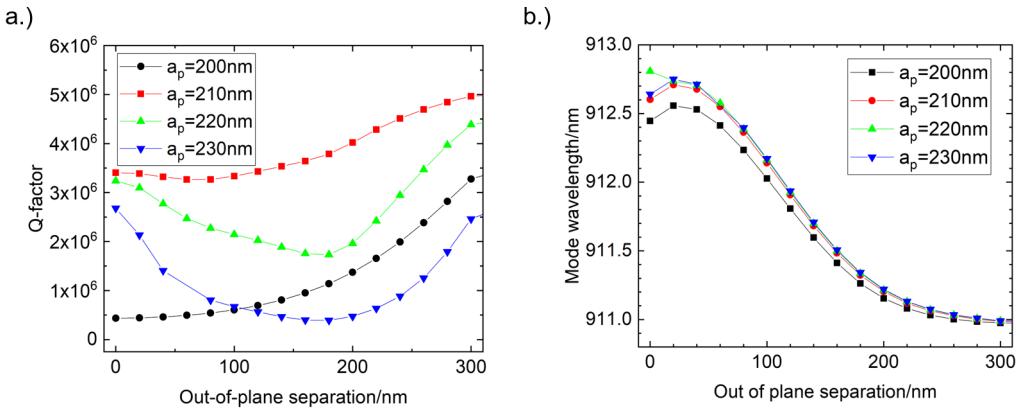

Figure 63: Graphs showing the effect of varying the out-of-plane separation between the cavity and perturbing beams on a.) The Q-factor and b.) The cavity mode wavelength for different perturbing beam PhC periods. The Q-factor reduction is minimised for a value of $a_p = 210nm$ with no noticeable reduction in the cavity tuning range.

changing the out-of-plane separation on the cavity Q-factor and mode wavelength for different values of the perturbing beam PhC period a_p. The period of the uniform cavity mirror is $a_0 = 220nm$. As can be seen from Figure 63 a.) this is not the optimal value for the perturbing beam PhC period as at this value the Q-factor experiences a dip between zero displacement and the maximum actuation range. Instead, a small reduction down to $a_p = 210nm$ is required to eliminate this Q-factor drop at intermediate displacements. The initial and final Q-factors are also maximised for $a_p = 210nm$. Moreover, there is no noticeable reduction in the maximum tuning range for this small reduction in PhC period. Therefore, the optimal value for the perturbing beam period is $a_p = 210nm$.

Having optimised the period, the perturbing beam PhC hole radii must now also be optimised. The results of the optimisation simulations can be seen in Figure 64. It is clear that over the scope of the simulations changing the hole radii only has a small impact on the Q-factor drop and tuning range of the device. Any deviation from the initial value of $r_p = 50nm$ either increases the Q-factor drop experienced by the cavity or reduces the recovery rate of the Q-factor at large out-of-plane separations. Therefore, the optimised value is equal to the uniform cavity mirror radius.

In reality, this optimisation of the perturbing beam is likely a local maximum in the parameter space due to the joint effect of PhC period and hole radii on the band structure and effective

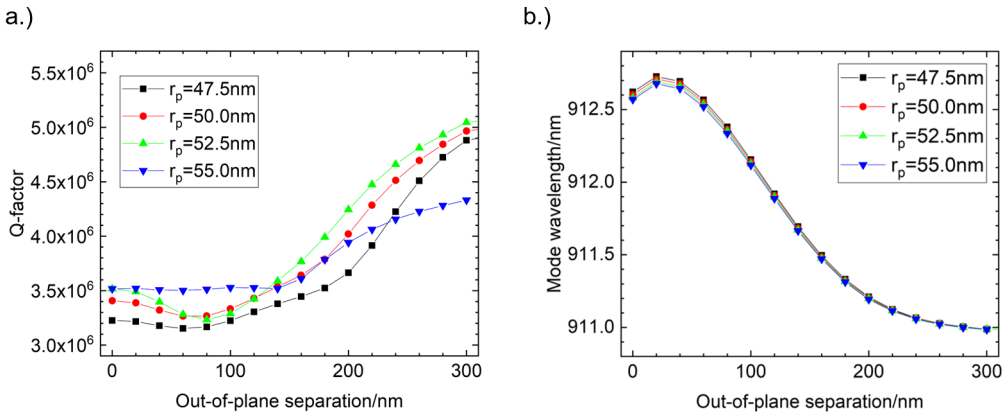

Figure 64: Graphs showing the effect of varying the out-of-plane separation between the cavity and perturbing beams on a.) The Q-factor and b.) The cavity mode wavelength for different perturbing beam PhC hole radii. The variation in Q-factor drop and tuning range is extremely small over the scope of the simulations.

index of the cavity mode. Due to the computational intensity of these types of simulations, it is infeasible to conduct a full investigation of the parameter space. Therefore, the results of the small scale optimisation are considered.

5.4.3 Optimisation of the length of the perturbing beam (n_b)

The final perturbing beam parameter to optimise is the length of the beam parallel to the cavity beam. All simulations up to this point assumed an infinitely long, straight beam parallel to the cavity beam. This is both unrealistic, for obvious reasons, and undesirable as the device footprint should be kept to a minimum. Furthermore, the longer the beams run parallel, the higher the chance of the beams fusing post fabrication. However, if the beam is too short then the effective index change will be reduced, thus reducing the tuning range of the device.

From Figure 65 it can be seen that increasing the length of the perturbing beam not only reduces the drop in Q-factor at low displacements, but also increases the wavelength tuning range of the device. The effect of increasing the beam length on the tuning range of the device saturates at $n_b = 5$ (a total of 11 holes parallel with the cavity beam, as depicted in Figure 61). At this value, the Q-factor at zero displacement is roughly half of that in the infinite perturbing beam case. Therefore, a value of $n_b = 5$ is chosen for the devices to maximise the tuning range whilst keeping the device dimensions as small as possible. The Q-factor still remains high at zero displacement ($> 10^6$) and so the drop from the ideal case is an acceptable trade-off for the reduced device size.

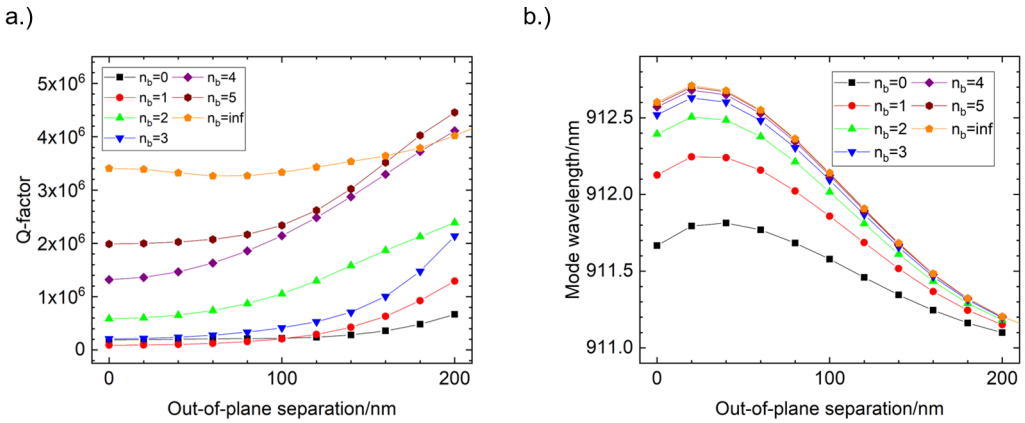

Figure 65: Graphs showing the effect of varying the out-of-pane separation between the cavity and perturbing beams on a.) The Q-factor and b.) The wavelength of the cavity mode. n_b is the number of PhC periods either side of the perturbing beam centre which are parallel to the cavity beam. Increasing n_b increases the length of the perturbing beam. As the length of the beam is increased, the available tuning range is also increased. The drop in Q-factor at low displacements is reduced with increasing beam length also.

5.5 Fabrication error quantifying in simulation

When fabricating any nano-photonic structures, especially devices with small and complex features such as the tunable 1D PhCCs, an intrinsic fabrication error exists on the size and uniformity of said features. When optimising the device parameters, this error is not considered in the simulations. However, it is important to test the robustness of the final design to this error. This will allow us to predict the effect that any fluctuations to the size and shape of the features will have on the performance of the devices. By both using a Monte Carlo simulation approach and altering the shape of the PhC air holes, the effects of the fabrication error on the structures are quantified.

5.5.1 Monte Carlo simulation approach for quantifying air hole radii error

A Monte Carlo simulation approach produces a set of individual simulations where specified parameters are varied according to a chosen probability distribution and range. Each individual simulation is unique, with the parameters chosen at random from the probability distribution. By producing and running many of such simulations, for a given parameter set, the effect of the random variation on a parameter can be seen. The more simulations that are produced over the range, the more accurate the result will be. However, even at a relatively low number of simulations the result is fairly accurate. In this case, a uniform percentage error on the radii of the air holes in the PhCs was introduced. A uniform distribution was chosen for simplicity. A total of 50 simulations for each distribution were conducted. This number was chosen as an appropriate trade-off between

computation time and accuracy, given the high intensity of each individual simulation. Firstly, just

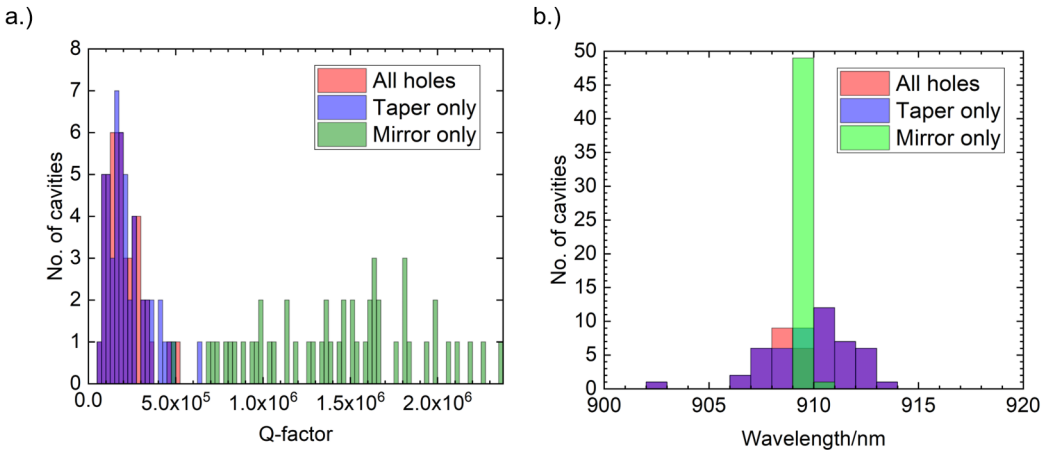

Figure 66: Graphs showing the results of a 50 iteration Monte Carlo simulation for a uniform 10% error on the air hole radii. The graphs compare the cases where all the holes, only the uniform mirror hole and only the taper holes are affected by the variation. a.) Shows the Q-factor distribution and b.) Shows the cavity mode wavelength distribution. It is clear from these graphs that the variation in the taper affects the performance of the cavity much more strongly than variations in the mirror.

the isolated cavity beam was considered. A worst-case scenario was simulated with a 10% uniform error on the radius of each air hole in the cavity. For each of the 50 iterations of the Monte Carlo simulation the cavity Q-factor and wavelength were acquired. The distributions from three different scenarios are plotted in Figure 66: the case where only the air holes in the taper are varied, the case where only the holes in the uniform mirror are varied and the case where all the air holes are varied. It is clear from the distributions for both the Q-factor and mode wavelength in Figure 66 that variations to the air holes in the taper have the largest effect on the cavity performance. The difference between the case where only the taper holes are varied and all the holes are varied is negligible. The median values for Q-factor and mode wavelength for the case where all holes are varied are

$$Q_{med} = 182,000, \lambda_{med} = 910.037nm$$

the standard deviations of the wavelength distributions (σ_λ) is:

$$\sigma_\lambda = 1.986nm$$

and the minimum value of the Q-factor is:

$$Q_{min} = 74,700$$

It can be seen that a 10% error on the hole radii reduces the expected Q-factor by over an order of magnitude from the ideal case ($Q_{ideal} = 5.6 \times 10^6$). While this is a dramatic reduction, even in the

Table 2: Table comparing the minimum Q-factor, median Q-factor and the standard deviation of the mode wavelength distribution for the three Monte Carlo simulation distributions depicted in Figure 67.

Percentage error	Q_{min}	Q_{med}	σ_λ
2%	1.26×10^6	2.20×10^6	$0.29nm$
5%	2.69×10^5	5.56×10^5	$0.74nm$
10%	7.47×10^4	1.82×10^5	$1.99nm$

case of the minimum Q-factor, the magnitude of the Q-factor is still $> 10^4$. The linewidth of the resonance at the minimum Q-factor is still well bellow the maximal tuning range of the device. If the standard deviation of the wavelength distribution is considered, it can be seen that it is slightly larger than the available tuning range for the chosen parameter set ($\Delta\lambda = 1.5nm$). Moreover, the mode volume of the cavity resonance is unaffected by the hole radii error, thus the $\frac{Q}{V}$ ratio of the system remains high.

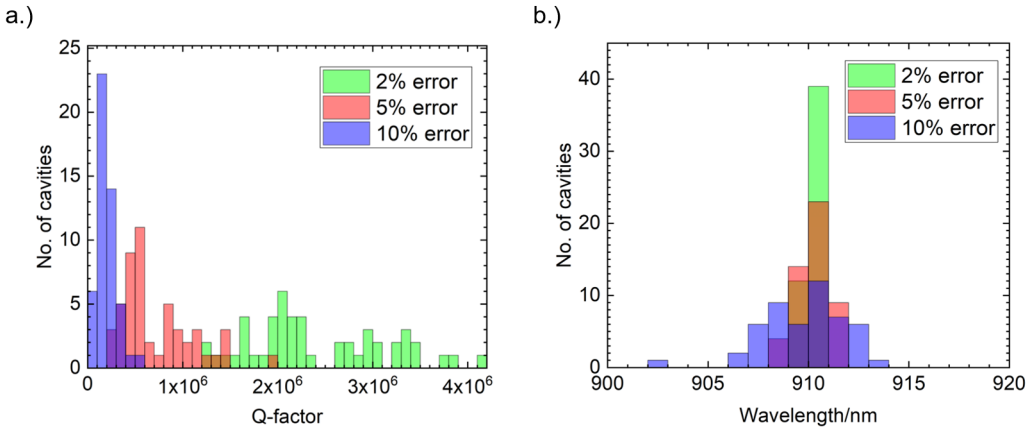

Figure 67: Graphs showing the results of a 50 iteration Monte Carlo simulation for different hole radii percentage errors. a.) Shows the Q-factor distribution and b.) Shows the cavity mode wavelength distribution for each percentage error.

Having looked at a worst-case scenario of 10% error of the hole radii, the effect of a lower percentage error on the Q-factor and mode wavelength distributions is considered in Figure 67. It is clear that a reduction in the percentage error results in a much higher mean Q-factor and a much narrower cavity mode wavelength distribution. The relevant parameters from each distribution in Figure 67 are summarised in Table 2. These results can be compared to the values discussed in Section 5.3.7 for the 2D PhCCs obtained from Minkov and Savona [181]. For the H0 cavity, 1000 iterations from a Gaussian distribution were used to simulate the disorder in both the hole radii and position.

Disorder was governed by altering the standard deviation of the Gaussian distribution (σ_{gauss}). Two values of disorder were considered: $\sigma_{gauss} = 0.003a = 0.012r$ and $\sigma_{gauss} = 0.0015a = 0.006r$. A direct comparison between the disorder simulations conducted by Minkov and Savona, and those conducted on the 1D PhCCs is difficult as the probability distributions used to create the disorder are different. The Gaussian distribution favours values close to the mean of the distribution, compared to a uniform distribution. If the width of the Gaussian distribution is assumed to be $\pm 3\sigma$ then the error on the hole radii becomes $\pm 0.036r$ and $\pm 0.018r$. A comparison can now be drawn between the two cavity types by assuming these $\pm 3\sigma$ width distributions are uniform distributions. For an error of 3.6% on the hole radius the median Q-factor of the H0 cavity falls from 8.9×10^6 to 6.5×10^5: $Q_{dis} = 0.07Q_0$. When this is compared to the 5% error case in the 1D PhCC a drop from 5.6×10^6 to 5.56×10^5: $Q_{dis} = 0.10Q_0$ is seen. Similarly if the 1.8% error case in the H0 is compared to the 2% error case for the 1D PhCCs a drop from 8.9×10^6 to 2.0×10^6: $Q_{dis} = 0.22Q_0$ for the H0 and from 5.6×10^6 to 2.20×10^6: $Q_{dis} = 0.39Q_0$ for the 1D PhCC is seen. Even when making generous assumptions in favour of the H0 cavity, for a comparable error in hole radii, the 1D PhCCs are more robust and experience a lower relative Q-factor drop.

In order to bring the standard deviation of the cavity mode wavelength distribution below the maximum tuning range of the device, the error on the hole radii must be below 10%. Extrapolating from the data in Table 2 a standard deviation of $1.5nm$ is obtained for a value of 8.4% error. The typical uniform percentage error seen in the radius of nanoholes is $\sim 2 - 5\%$ for high quality fabrication [120]. Therefore, achieving an error of below 10% is highly likely with high quality fabrication.

5.5.2 Quantifying anisotropy of air hole etching in simulation

Fluctuations in the radii of the air holes is not the only source of fabrication-related error that can be seen in PhC devices. Some etch processes used to fabricated the structures can preferentially etch along the crystal axis of the semiconductor membrane thus causing anisotropy in the etching of the air holes. The intentional inclusion of elliptical holes in a 1D PhCC has been attempted previously in silicon systems [180] where it was theoretically shown to obtain high Q-factor with a mode volume $V_m = 0.45\left(\frac{\lambda}{n}\right)^3$, slightly below what the tunable cavity design shows $\left(V_m = 0.45\left(\frac{\lambda}{n}\right)^3\right)$.

This anisotropy can be approximated in simulation by using elliptical holes. By changing the degree of ellipticity of the air holes, varying degrees of anisotropy simulated. The axes of the ellipse relative to the waveguide direction are defined as follows: r_x is the radius in the waveguide propagation direction and r_y is the radius perpendicular to the waveguide propagation direction. This is shown graphically in Figure 68. The results in Figure 69 show how increasing the ellipticity of the holes in both the 'x' and 'y' directions effects the cavity performance. It can be seen immediately that any anisotropy in the waveguide direction has a much larger effect on the cav-

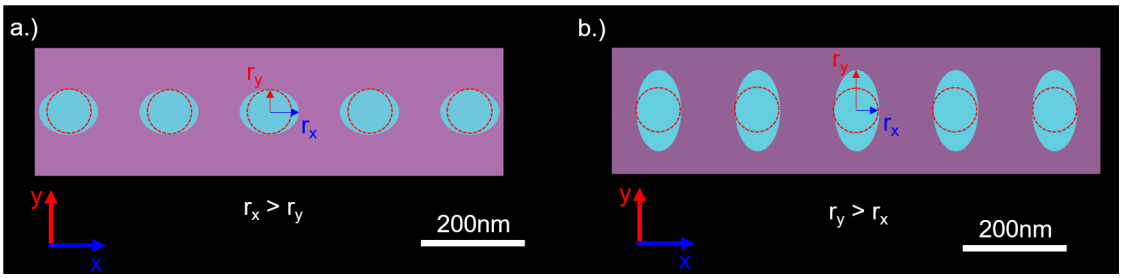

Figure 68: Schematic showing the parameter definitions used to estimate the effect of anisotropic etching of the air holes in the 1D PhCC design using elliptically shaped holes. a.) Is the case where the holes are etched more in the waveguide 'x' direction and b.) Is the case where the holes are etched more perpendicular to the waveguide in the 'y' direction.

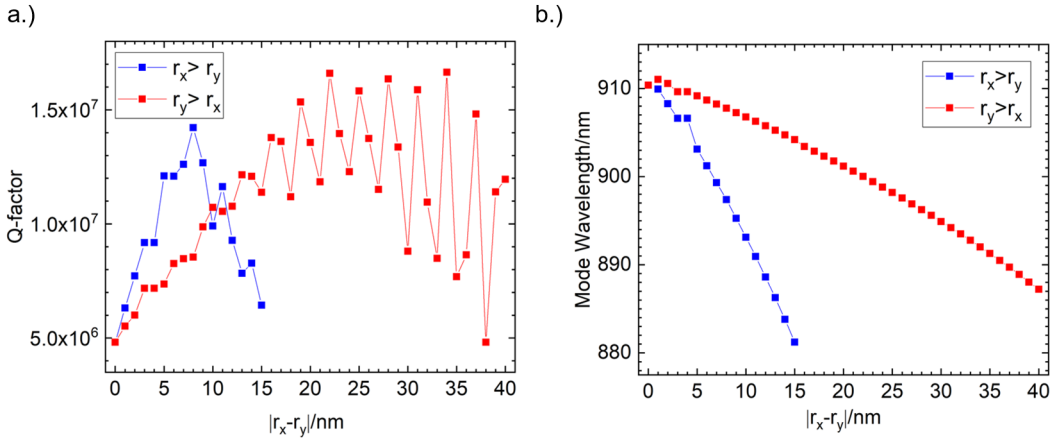

Figure 69: Graphs showing the effect of increasing the difference between the semi-major and semi-minor axes of elliptically shaped air holes both parallel and perpendicular to the waveguide direction on a.) The Q-factor and b.) The wavelength of the cavity mode. For both cases the semi-minor axis has a radius of $r_{minor} = 50nm$ and the semi-major axis increases accordingly.

ity performance when compared to the same radius difference in the perpendicular case. This is due to any anisotropy in the waveguide direction changing not only the hole shape but also the effective pitch of the PhC and the cavity width as the amount of material between each hole is reduced. Conversely, in the perpendicular case only the fill factor of each unit cell is altered with the effective pitch and cavity widths remaining constant. Thus a more gradual change in cavity performance is seen over the simulation range. In both cases a peak is seen in the Q-factor at a non-zero ellipticity value and a blue-shift in the cavity wavelength with increasing ellipticity. This increase in Q-factor at low ellipticity is attributed to an increase in the mirror strength of the PhC due to an increase in the fill factor. Moreover, the results from Figure 69 agree with what is seen in Figure 56 for an increase in uniform PhC mirror hole radius, where an increase in Q-factor at radii

slightly above $r_0 = 50nm$ and a blue-shift in mode wavelength for increasing hole radii is seen. The large oscillations in the Q-factor results at large ellipticity in the 'y' direction are likely caused by the simulation mesh parameters and are not a physical effect.

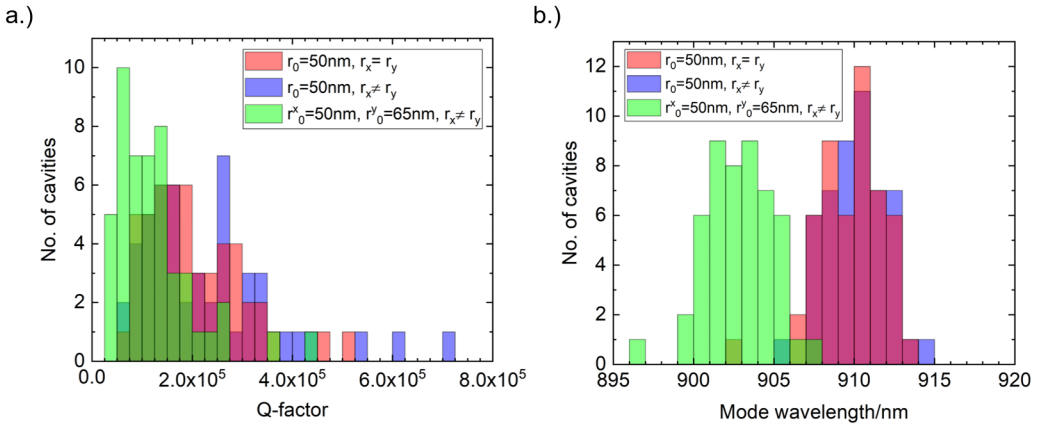

Figure 70: Graphs showing the distributions of a.) The Q-factor and b.) The cavity mode wavelength from a 50 iteration Monte Carlo simulation with a uniform 10% error on the hole radii. Three different parameter restrictions are plotted for comparison. Red: $r_0 = 50nm$ and the axes are varied together so the holes remain circular, Blue: $r_0 = 50nm$ and the axes are varied independently, Green: $r_0^x = 50nm, r_0^y = 65nm$ with axes varied independently.

Although an increase in the Q-factor is seen for slightly elliptical holes, the effect of introducing such an ellipse on the robustness of the cavity design must be investigated. This is investigated via a Monte Carlo simulation as outlined in Section 5.5.1. The Monte Carlo simulation is run from a starting parameter set of $r_x = 50nm$ & $r_y = 65nm$ which equates to the peak Q-factor for an ellipse in the 'y' direction. An ellipse in the 'y' direction is chosen over the 'x' direction as the performance of the cavity is much more stable over the simulation range for the 'y' direction case. Figure 70 shows the results of a 50 run Monte Carlo simulation for a uniform 10% error on the hole radii. Three cases are considered; the red bars are the control case with no initial ellipse and where the holes remain circular ($r_x = r_y$ always). The blue bars are for the case where there is no initial ellipse however, the two axes are varied independently by the Monte Carlo simulation producing non-circular holes ($r_x \neq r_y$). Finally, the green bars show the case where the initial state is an ellipse with $r_x = 50nm$ & $r_y = 65nm$ and the two axes are varied independently. It can be seen from Figure 70 a.) that introducing an intentional ellipse into the design results in a shift of the Q-factor distribution towards lower Q-factors. The key results from Figure 70 are summarised in Table 3. Both the minimum and median Q-factors of the distribution are reduced for the elliptical hole case when compared to both circular hole starting point cases. The standard deviation of the cavity mode wavelength distribution is only very slightly different between all three cases. The

Table 3: Table comparing the minimum Q-factor, median Q-factor and the standard deviation of the mode wavelength distribution for the three Monte Carlo simulation distributions displayed in Figure 70.

Parameter scheme	Q_{min}	Q_{med}	σ_λ
$r_0 = 50nm$ & $r_x = r_y$	7.47×10^4	1.82×10^5	$1.99nm$
$r_0 = 50nm$ & $r_x \neq r_y$	6.57×10^4	2.01×10^5	$1.82nm$
$r_0^x = 50nm, r_0^y = 65nm$ & $r_x \neq r_y$	2.45×10^4	7.98×10^4	$1.88nm$

reduction in the Q-factor even from a much higher initial Q-factor for the elliptical case cannot be attributed solely to the non-uniformity of the holes as only a very minor difference in performance is seen between the $r_0 = 50nm$ & $r_x = r_y$ and $r_0 = 50nm$ & $r_x \neq r_y$ cases. The reduction therefore, must be mainly due to the choice of parameters, namely the ellipticity of the holes. As the starting ellipticity is large, the fluctuations in the radii are likely to exaggerate this even further. This leads not only to the creation of extremely elliptical holes but also a to potentially large variation in the shape of neighbouring holes. Both these effects will increase the amount of scattering from the cavity and also reduce the overall reflectivity of the PhC mirror. It is clear that in order to create a robust cavity design, the air holes should be designed circularly despite elliptical holes promising potentially much higher Q-factors.

5.6 Experimental measurements of the 1D photonic crystal cavity designs

Having completed an extensive simulation study on the design considerations for both the 1D PhCC and cantilever structures, the next stage was to fabricate a test sample containing just cavity structures. This is done to optimise the fabrication processes of the small features in the 1D PhCC. Additionally, it allows a wide range of cavity parameters to be tested to see how the performance of these parameter sets compare between experiment and simulation.

5.6.1 Initial 1D photonic crystal cavity test sample

The first 1D PhCC test sample was designed to test as many parameter variations as possible on a single chip. Therefore, the sample contained an extremely high density of cavities. Many arrays of sets of three cavity beam devices were fabricated on the sample. Each array had a different combination of cavity parameters. The parameters varied on the sample were: n_m, n_t, r_0, a_{min}, w_c and w. The sample was fabricated as described in Section 3.2.2 without electrical contacting, to save space and with a larger EBL write-field than is normally used ($500\mu m^2$ rather than $200\mu m^2$), to speed up the fabrication process. The SEM images in Figure 71 a.) and b.) show the successful fabrication of the devices. However, the uniformity of the air holes is poor, as can be seen clearly in Figure 71 b.). In addition to this, the PhC taper which is essential to obtaining high Q-factors in 1D PhCCs is not present. These fabrication imperfections are attributed to two

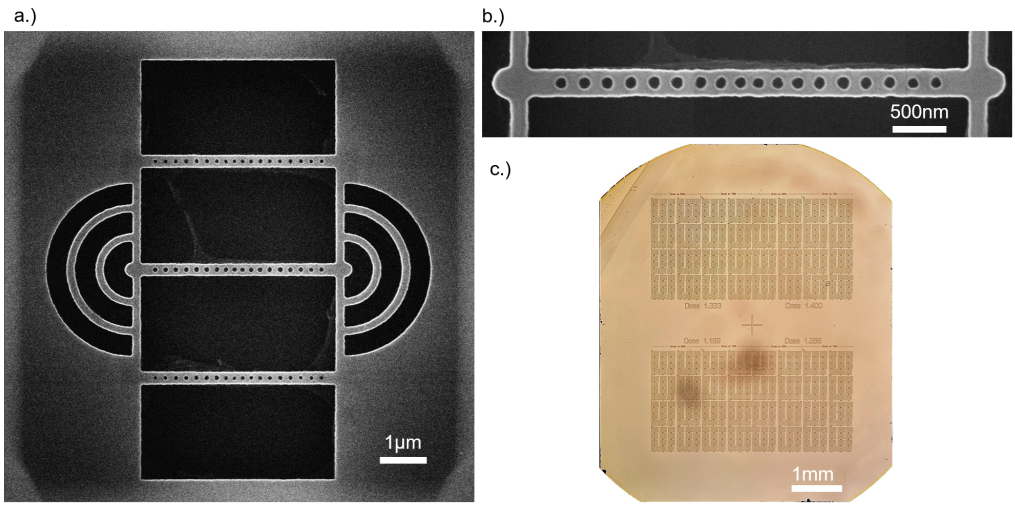

Figure 71: a.) SEM image of a typical triple cavity beam structure used to maximise the cavity density on the initial 1D PhCC test sample. Each cavity in a single device has the same design parameters to test the repeatability of the design. b.) Close-up SEM of a single cavity, the poor uniformity of the holes and lack of definition of the taper can be clearly seen. c.) Optical microscope image of the entire sample chip.

factors: too much etching in the immediate area surrounding the cavity beams, and the write-field being too large. The large etch areas either side of the cavity beams, coupled with the triple beam design and proximity of the OCs, all contribute to a large amount of etching in close proximity to the air holes, which will produce a large amount of electron backscatter. As the air holes are extremely small compared to the other features, any electron backscatter will have a much larger impact on the shape and size of the holes than on other features. Moreover, using a large write-field reduces the resolution of the EBL, further reducing the uniformity and accuracy of the hole etching.

To measure the cavity modes and characterise the devices, a high power (150μW) laser operating at 808nm (above the band gap of GaAs) was incident on the cavity centre. The diameter of the excitation spot on the sample was 1μm The semiconductor wafer chosen for the sample had a large distribution of QD wavelengths. When excited via the laser, PL from the QD ensemble produces light over the broad range of the ensemble. This PL in turn then excites the cavity mode, producing a strong signal at the cavity's resonance wavelength when light is collected from above the cavity. Additionally, by using an 810nm LED to excite a large area above the band gap of GaAs, multiple cavities can be imaged simultaneously using a high sensitivity and resolution CCD camera. A typical PL image from the CCD camera along with a μPL spectrum of a cavity mode from the image is shown in Figure 72 a.). The CCD image clearly shows PL emission from the OCs from each device but also some devices exhibit bright PL signals from the centres of the cavity beams, indicating the presence of bright cavity modes. In this case bright modes do not necessarily

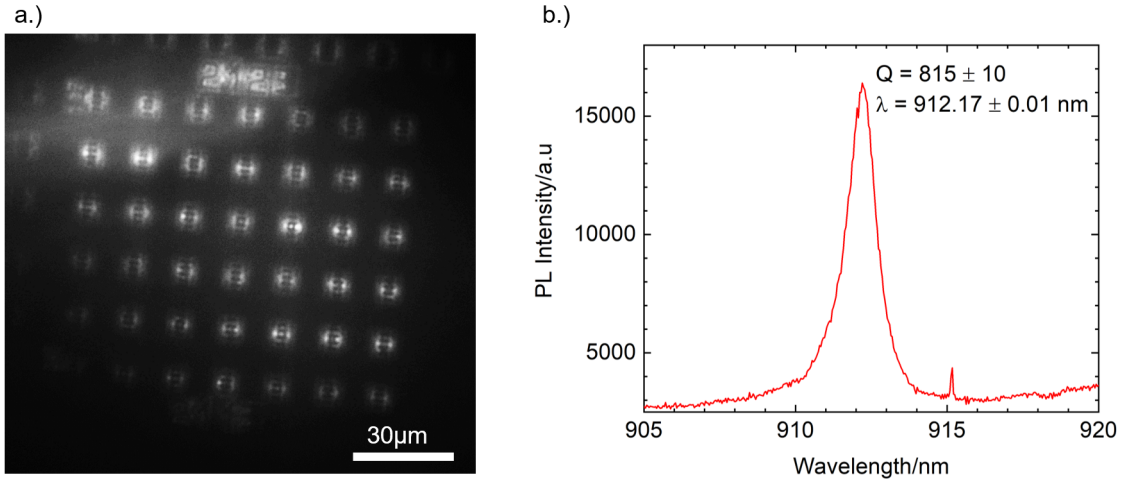

Figure 72: Results from the first 1D PhCC test sample with arrays of triple cavity devices. a.) Shows a high-resolution wide aperture PL image of one array of devices on the sample. An 810nm LED excites PL across a large part of the sample which is incident on the CCD camera. Evidence of cavity modes in multiple devices in the array is indicated by the bright PL spots in the middle of the devices. Also strongly visible are the output couplers on either edge of the devices. b.) Shows a PL spectrum of a typical cavity mode found on this sample. The cavity parameters are: $n_m = 6$, $n_t = 5$, $r_0 = 52nm$, $a_0 = 220nm$, $a_{min} = 192nm$, $w_c = 190nm$ and $w = 340nm$

indicate the modes have a high Q-factor as would typically be expected. Brightness on the CCD is related to integrated counts across all detectable wavelengths. Therefore it is more likely the bright modes on the CCD camera in fact have a low Q-factor as the integrated counts will be larger. Figure 72 b.) shows a typical PL spectrum from a single cavity mode that appears bright on the CCD camera. The mode indeed has a low Q-factor of just $Q = 815 \pm 10$.

Overall, the cavities on this sample exhibited low Q-factors or did not exhibit any cavity modes in the measurement range. This is likely due to the poor uniformity of the holes combined with the lack of taper definition and narrowing of the cavity centres. Analysis of SEM images from the initial sample show that the average circularity of the holes is $< 85\%$ and as low as 60% for some devices.

5.6.2 Revised 1D photonic crystal cavity sample

To improve upon the initial cavity sample, several design and fabrication revisions were made. Firstly, the write-field size was reduced from $500\mu m^2$ to $200\mu m^2$. Secondly, devices with a single cavity beam rather than three parallel beams were included to reduce the amount of etched areas surrounding the cavity. Finally, copies of both the single and triple beam designs where the air holes were patterned in a separate EBL step to the nanobeam and outcouplers were included. All these revisions were made to try to improve the uniformity of the holes and definition of the tapers by reducing any extra electron scatter.

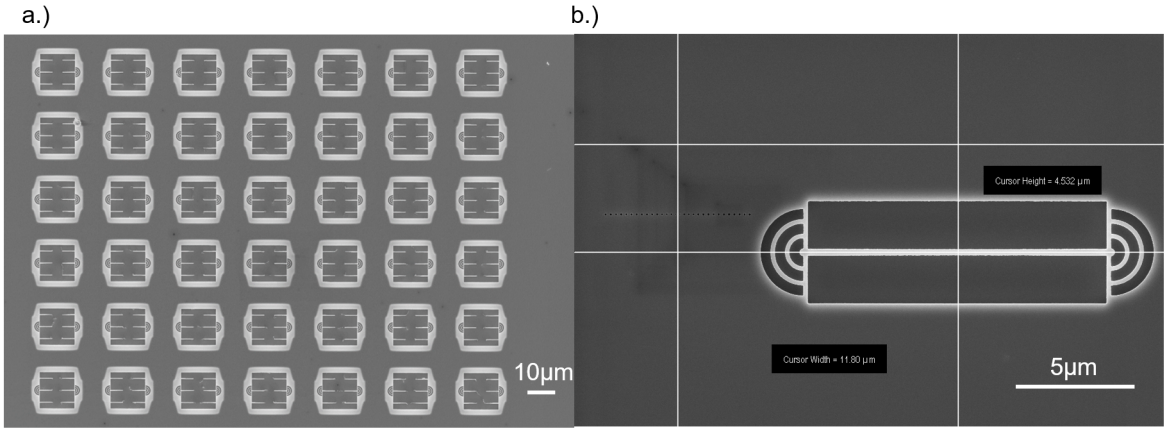

Figure 73: SEM images from the revised 1D PhCC test sample showing the major fabrication errors that the sample experienced. a.) Shows an array of triple beam cavities which have been massively over exposed. b.) Shows a single beam device where the air holes were fabricated separately to the rest of the device. An alignment error has caused the devices to be fabricated in the incorrect location relative to the air holes.

Unfortunately, as can be seen in Figure 73 two major fabrication errors occurred during the fabrication of the sample. All of the triple beam cavity devices became overexposed causing the beams to collapse. This is especially surprising as no changes were made to these devices when compared to the previous sample apart from the length of the nanobeams. Moreover, all the devices where the air holes were patterned separately to the nanobeams became misaligned between EBL steps due to an error. This caused the structures to be fabricated away from their corresponding holes as shown in Figure 73 b.). The only devices which were successfully fabricated were single cavity beam devices patterned in one EBL step. As can be seen in Figure 74, the devices that were

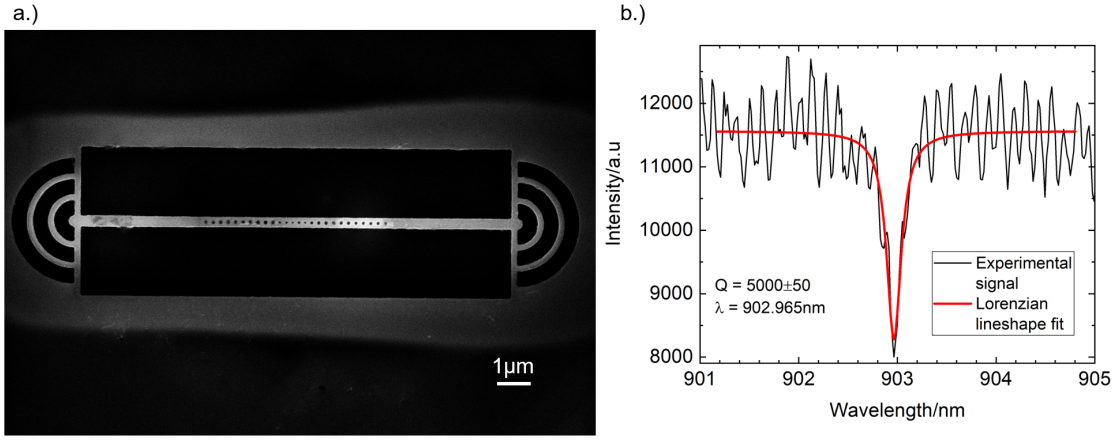

Figure 74: a.) SEM image of the highest Q-factor cavity measured on the revised sample. b.) Cross-polarised white light reflectivity measurement from above the cavity centre, showing the cavity mode resonance. The cavity exhibited a Q-factor of 5000 ± 50 and a resonance wavelength of $902.965nm$. Large fringes can be seen in the experimental data, these arise from etaloning between the top and bottom of the sample chip.

successfully fabricated were a vast improvement over the first sample. The uniformity of the holes was vastly improved with the mean and minimum circularity being improved to $> 95\%$ and 90% respectively. This improvement in hole uniformity and circularity meant that many more of the cavities exhibited cavity modes. Moreover, the cavity modes exhibited a higher Q-factor. The best Q-factor measured on the sample was $Q = 5000 \pm 50$, as shown in Figure 74 b.). This allowed for a more thorough investigation of the parameter space than the previous sample, in which only a handful of devices showed modes. Unfortunately, no PL emission from the QDs on the sample was seen. Therefore it was not possible to use PL to measure the cavities on the sample. Instead, a broadband white light laser source was used to excite the cavities. As the cavity modes are strongly linearly-polarised perpendicular to the beam, it is possible to use a cross-polarisation excitation scheme to reject most of the laser background when exciting and collecting from above the cavity.

The laser was filtered between 850-1000nm to reduce the overall power onto the sample. The cross-polarised excitation and collection were orientated at 45° to the cavity polarisation to maximise the collectable cavity signal. Despite the cross-polarised excitation scheme there was still a large amount of background visible in the spectra obtained using the white light. Namely both a large wavelength and polarisation-dependant background and extremely fine Fabry-Perot type fringes were present throughout all the measurements. The former was caused by the optics in the set-up not being perfectly achromatic, the latter by reflections between the top and bottom of the sample chip.

Table 4: Comparison between experimental measurements of 1D PhCCs with different values of a_{min}.

a_{min}	Q_{max}	Q_{min}	Q_{med}	σ_Q	λ_{max}	λ_{min}	λ_{med}	σ_λ
182nm	4000	2200	3000	650	899.9nm	892.9nm	894.8nm	2.6nm
184nm	2900	1150	2500	600	909.4nm	903.8nm	906.9nm	2.1nm
186nm	2750	1450	2050	500	890.3nm	885.0nm	888.7nm	2.0nm
188nm	2900	2550	2700	140	898.9nm	900.5nm	899.6nm	0.6nm

Table 5: Comparison between experimental measurements of 1D PhCCs with different values of n_t.

n_t	Q_{max}	Q_{min}	Q_{med}	σ_Q	λ_{max}	λ_{min}	λ_{med}	σ_λ
3	5000	900	3400	1300	921.5nm	887.1nm	904.5nm	10.8nm
5	2750	1450	2050	500	890.3nm	885.0nm	888.7nm	2.0nm

Table 6: Comparison between experimental measurements of 1D PhCCs with different values of w_b.

w_b	Q_{max}	Q_{min}	Q_{med}	σ_Q	λ_{max}	λ_{min}	λ_{med}	σ_λ
300nm	2900	1150	2500	600	909.4nm	903.8nm	906.9nm	2.1nm
320nm	3700	950	2350	850	889.0nm	880.3nm	885.5nm	3.0nm

Table 7: Comparison between experimental measurements of 1D PhCCs with different values of n_m.

n_m	Q_{max}	Q_{min}	Q_{med}	σ_Q	λ_{max}	λ_{min}	λ_{med}	σ_λ
6	3470	1030	2000	820	898.5nm	886.1nm	893.0nm	5.5nm
10	2750	1450	2050	500	890.3nm	885.0nm	888.7nm	2.0nm

The results of the parameter space investigation are presented in Table 4 - Table 7. In general, the results show that there is a trade-off between devices that exhibit the highest Q-factors and those which have the smallest mode wavelength distribution between like devices. This can be seen most clearly in Table 4 when comparing the $a_{min} = 182nm$ and $a_{min} = 188nm$ results. For the $a_{min} = 182nm$ set of devices, the maximum Q-factor achieved was 4000 and the median Q-factor was 3000, both of which are larger than for $a_{min} = 188nm$. However, the standard deviation of the mode wavelength spread for $a_{min} = 182nm$ is much larger than for $a_{min} = 188nm$ ($\sigma_\lambda = 2.6nm$ compared to $\sigma_\lambda = 0.6nm$). Overall, a trend can be seen where increasing the value of a_{min} reduces both the Q-factor and mode wavelength spread. When considering the number of taper holes in the design in contrast to the simulations, it is observed experimentally that designs with fewer taper holes exhibited much higher Q-factors than devices with more taper holes, at the expense of mode wavelength consistency, as shown in Table 5. This is likely due to the taper gradient being more pronounced in devices with few taper holes. As the difference in radius between adjacent holes is larger in steeper taper gradients, the taper is less susceptible to being washed-out, due to electron scatter broadening the air holes. It is seen in experiments from Table 6, that the narrower beam cavities showed both slightly higher median Q-factor and a smaller mode wavelength spread. The narrower beams which had a design width of 300nm were very close to the target width of 280nm after the fabrication. Therefore, as the rest of the cavity parameters were set according to the beam dimensions, it is expected that beams with widths close to the target width perform the best, as is seen experimentally. this agrees with the simulation results from Section 5.3.6. Finally, from Table 7 it can be seen that the Q-factor is largely unaffected when increasing the number if mirror holes in the PhC from 6 to 10. This indicates that the strength of the PhC mirror is not the limiting factor on the Q-factor. However, the mode wavelength spread is improved for devices with the larger number of mirror holes.

The spectra of the cavity modes which exhibited the lowest mode wavelength spread are presented in Figure 75. The standard deviation of the wavelength spread is $\sigma_\lambda = 0.6nm$ which is well below the theoretical tuning range of the tunable cavity devices. This design was the only parameter set to achieve a wavelength spread lower than the tuning range of the devices and as such is the optimal design to use going forward despite the lower Q-factors. Some of the cavity lineshapes in Figure 75 do not exhibit a Lorenzian shape, instead they exhibit a modified Lorenzian lineshape known as a Fano lineshape. The modification to the Lorenzian lineshape is caused by an interference effect between a resonator scattering process and a background scattering process. When measuring the cavity modes of the 1D PhCCs, this interference can occur between the cavity and the excitation laser fields when the polarisation of the cavity and laser excitation differ. Finally, the effect of increasing the design radius on the cavity mode wavelength is plotted in Figure 76. A blue-shift is seen with increasing design hole radius in agreement with the simulation. However, the rate of blue shift is slightly higher than that seen in simulation (-2.13 ± 0.08 over the full simulation range

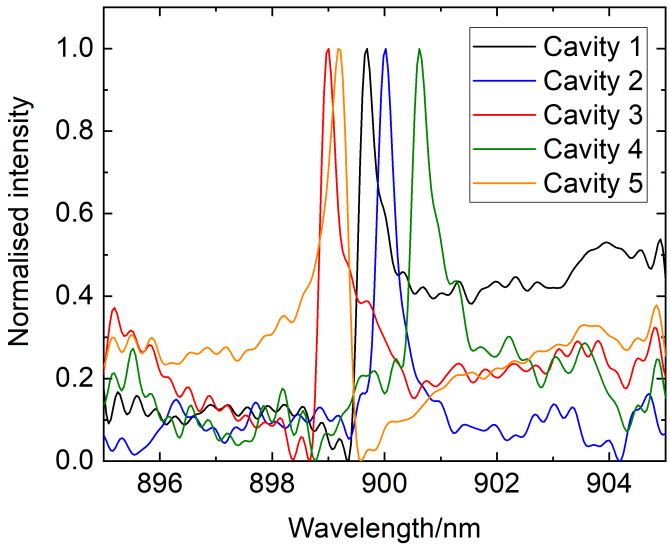

Figure 75: Graph showing the overlapping cavity mode spectra of the set of like cavities which exhibited the lowest standard deviation in their mode wavelength spread $\sigma_\lambda = 0.6nm$. The spectra have been filtered using a '*Fast-Fourier-Transform*' (FFT) method to remove the high frequency etaloning fringes, making the spectra more readable.

and -2.87 ± 0.27 over the experimental range). The rate measured experimentally is likely higher than in simulation due to the lack of control over other cavity parameters experimentally such as the radius of the taper holes and the exact beam width. Moreover, the relationship between the designed and actual hole sizes may not be linear. Holes which are designed larger may come out closer to their target than smaller designed holes.

Overall, the second iteration of the 1D PhCC sample was vastly superior to the first due to improved fabrication. Having analysed the experimental results the optimal experimental cavity design was chosen to be:

$$n_m = 10$$

$$n_t = 5$$

$$a_0 = 220nm$$

$$a_{min} = 188nm$$

These parameters were chosen as they gave the lowest wavelength spread for like devices and thus the most consistent fabrication. These cavity parameters were chosen as the basis for the cavity design for the full cantilever tunable cavity devices along with a small range of r_0, w_c and w_b

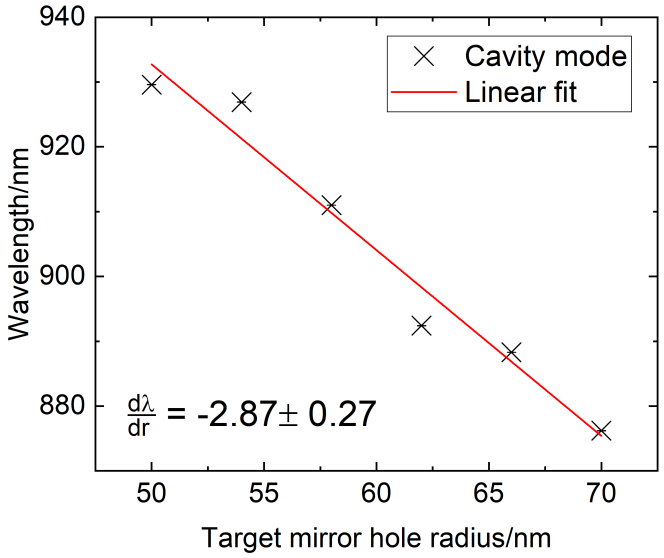

Figure 76: Graph showing the experimental results for increasing the design radius of 1D PhCCs on the wavelength of the cavity mode. A linear fit to the data shows the rate of change of mode wavelength with respect to designed hole radius to be $\frac{d\lambda}{dr} = -2.87 \pm 0.27$. The error bars on the mode wavelength are too small to be visible at this scale.

5.7 Experimental measurements of cantilever devices

With an optimal experimental set of parameters for the 1D PhCCs chosen after analysis of the two test samples, a full tunable cavity device design was fabricated. This sample contained a small range of cavity and perturbing beam parameters. However, the number of devices was limited by the need to facilitate the electromechanical actuation of the cantilevers via the use of diodes. The structure of the diodes on this sample was somewhat unconventional. Both the membrane containing the QDs and the substrate below the sacrificial AlGaAs layer are doped, with the membrane being a p-i-n diode and the top of the substrate being n-doped. To reduce the dimensions and complexity of the diode, only two of the three doped layers could be contacted. The diodes on the sample were contacted from the n-doped layer in the substrate to the n-doped layer in the membrane. This was done to reduce the voltage required to actuate the cantilevers. The p-doped layer in the membrane was then intentionally shorted to the n-doped layer in the membrane to avoid the QDs experiencing an unknown floating bias. This diode scheme is depicted in Figure 77.

In addition to the small cavity parameter range, a small range of perturbing beam parameters were included. The radii of the air holes and the gap between the cavity and perturbing beams were varied slightly. An additional 2D perturbing area design was also included on the sample. This design is designed to reduce the etch areas near to the cavity to improve the uniformity of the

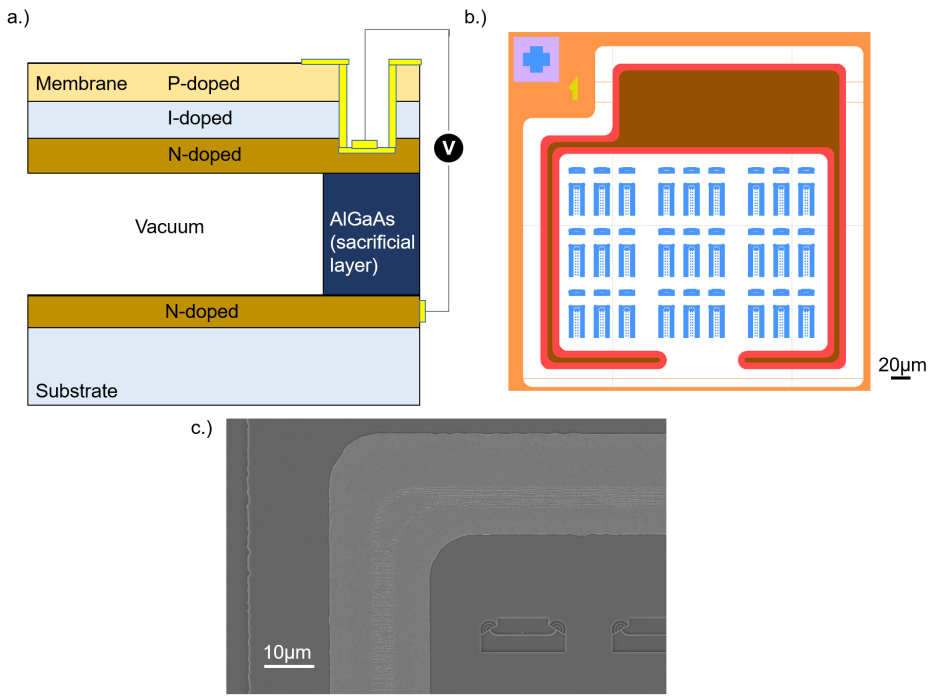

Figure 77: a.) Cross sectional schematic view of the diode structure used on the cantilever sample. The diode is contacted between the n-doped layers, with the p-doped layer on the membrane being shorted to the n-doped layer to prevent the QDs experiencing an unknown floating bias. b.) Image of the diode design, the brown areas show the etch down to the n-layer of the membrane where the diode top contact is made. The red area is the p-doped layer where the gold is deposited to intentionally short the p-i-n membrane. c.) SEM image showing the successful shorting of the p-i-n membrane.

holes, moreover, the 2D area should be less likely to fuse with the cavity beam at small separations when a bias is applied.

Due to an unknown error during the metallisation of the diodes on the sample, the gold initially did not strongly adhere to the surface of the membrane. This caused the contacts to de-laminate when wire bonding was attempted. As a result, the optimal dose copy of the sample could not be electrically contacted. The remaining copies underwent rapid thermal annealing which successfully re-adhered the gold contacts to the sample. Figure 78 shows some SEM images from the successfully fabricated sample. Figure 78 a.) and b.) Show the two different perturbing beam types. The 1D perturbing beam designs were very well fabricated with very small gaps between the beams which have remained parallel. The 2D perturbing area designs showed similarly narrow separations, however, the weight of the beams caused the cantilevers to droop. This can be clearly seen in Figure 78 b.). The drooping causes the perturbing areas to be displaced from their zero displacement position, thus reducing the tuning range of the devices. To verify that the diode

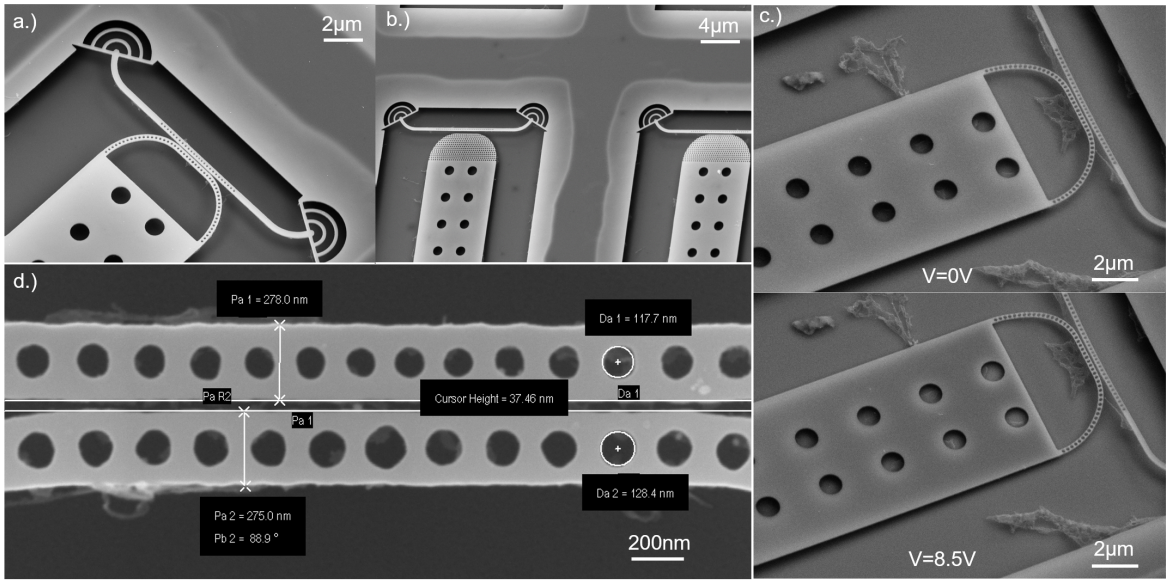

Figure 78: Series of SEM images of the completed cantilever sample. a.) Tilted image of cavity beam and perturbing beam. b.) Two cavity beam and 2D perturbing area devices. A small out-of-plane offset can be seen between the cavity and 2D areas due to a droop in the cantilever. c.) Images showing a device actuating due to the electrostatic force between the cantilever and the substrate at room temperature. The centres of the two beams appear to remain level despite the rest of the device clearly being deflected. d.) Close-up image on the cavity centre next to a perturbing beam. The separation between the beams is $d_0 = 37.46nm$ which is the smallest recorded on the sample.

configuration was successfully fabricated and that the devices actuated as expected, a custom built electrical contacting mount was used to allow for a bias to be applied to the diodes whilst in the SEM. This allowed for the devices to be imaged live as the bias was applied to the diodes. Figure 78 c.) Shows SEMs of a cantilever device at $V = 0V$ and $V = 8.5V$. Between the two images it is clear that the cantilever has been actuated at $V = 8.5V$. This confirms that the devices work as expected. It can also be seen in Figure 78 c.) that the centre of the perturbing beam appears to remain parallel to the cavity beam even at $V = 8.5V$ whilst the rest of the cantilever and perturbing beam have clearly been deflected. This may be caused by the fibrous residue that can be seen in the images supporting the centre of the beams from below. Alternatively this could be caused by electrostatic attraction between the beams, however, the beams do not appear to have fused in the images so this is unlikely. Finally, in Figure 78 d.) a close-up of the cavity centre and perturbing beam from the device which exhibited the smallest separation between the beams is shown. The separation between the beams is $d_0^{min} = 37.46nm$ which would correspond to a maximum tuning range of $\Delta\lambda \approx 5.5nm$. This is an exceptionally small separation and indicates the high quality of the fabrication of the sample. Of all the devices measured on the sample, the mean separation between beams is $d_0^{mean} = 58.87nm$ giving a tuning range of $\Delta\lambda \approx 2nm$. The largest separation

between the beams was $d_0^{max} = 80.4nm$ giving a tuning range of $\Delta\lambda \approx 1nm$ which is well above the standard deviation of the mode wavelength distribution measured for the cavity design parameters on the sample.

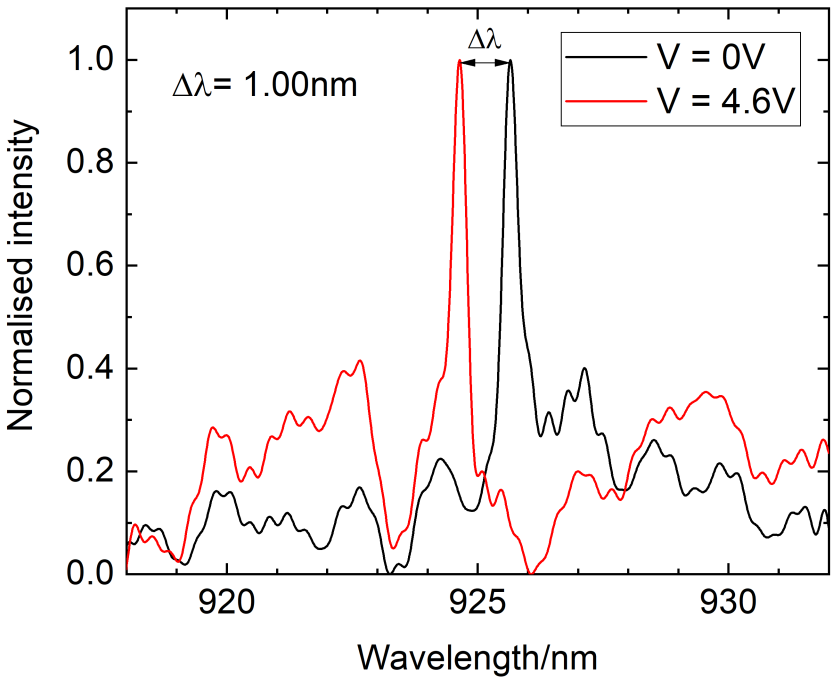

Figure 79: White light reflectivity spectra of the cavity mode in a cantilever device at $V = 0V$ and $V = 4.6V$ showing tuning of the cavity mode of up to $1nm$. The spectra have been filtered using a FFT to remove etaloning fringes.

Unfortunately, the devices on the sample did not exhibit any PL emission from QDs despite PL being visible in the bulk regions of the sample. The wafer chosen for this sample contained thin AlAs quantum well layers acting as barriers to improve the electrical tuning range of the QDs. The sacrificial layer is made from AlGaAs and was etched away using HF acid which attacks the Al content of the alloy. This HF etch may also have etched the AlAs barriers away in the membrane, preventing the QD from emitting PL. As a result, white light reflectivity measurements had to be used to investigate the cavities.

Figure 79 shows the first experimental demonstration of electro-mechanical cantilever cavity tuning on a GaAs QD wafer. A maximum tuning of $\Delta\lambda = 1.00nm$ was observed from the device. Figure 80 shows the effect on the cavity mode Q-factor and wavelength of fine incremental increases in the applied bias across the device. The Q-factor of the cavity mode reduces slightly at medium to high

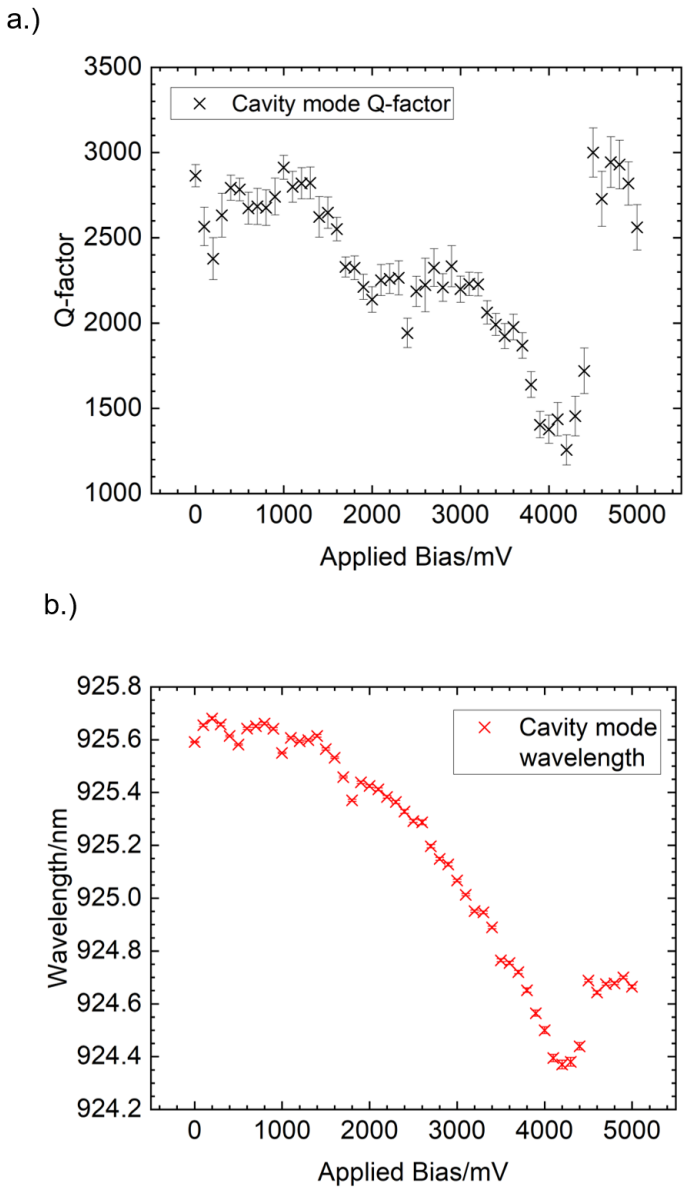

Figure 80: Effect of fine increases to the applied voltage across the tunable cavity on a.) The Q-factor and b.) The wavelength of the cavity mode.

applied bias. At the highest applied bias the Q-factor begins to increase again as seen in Figure 80 a.). This agrees with the simulation in the case where the perturbing beam parameters are not optimal. From Figure 63 it can be seen that for all cases away from the optimal parameter set the Q-factor is reduced between values of 0-250nm for out-of-plane displacement. This is the region where the majority of the cavity mode tuning occurs. After this, the Q-factor begins to recover. Experimentally, a similar trend is seen. Between 1000-4000mV of applied bias, the Q-factor of the mode trends to lower values before beginning to recover at values of applied bias >4000mV. From Figure 80 b.) it is clear that this region coincides with the region where the majority of the cavity mode tuning occurs. Figure 80 b.) also shows the high degree of control over the mode wavelength the device exhibits. The experimentally observed tuning curve in Figure 80 b.) also agrees with the simulated tuning curves from Section 5.4. By making fine adjustments to the applied bias, the mode wavelength can be precisely tuned over the entire tuning range. Moreover, the experimentally observed tuning range of the device is much greater than the standard deviation of the wavelength spread for the cavity design ($\Delta\lambda = 0.6nm$). A Python script is used to calculate the likelihood of any two random cavities whose cavity mode wavelength is taken from a normal distribution with $\sigma_\lambda = 0.6nm$ centred at $\lambda_0 = 925nm$ will be within the maximum device tuning range, $\Delta\lambda = 1nm$ of each other. 10^6 iterations of the script were run to ensure a highly accurate result was obtained. From this, the likelihood of any two cavities being within the tuning range of each other given these parameters is $P_{succ} = 76.2\%$. If the tuning range is increased to $\Delta\lambda = 2nm$ to represent the expected range from the mean beam separation measured then the likelihood rises to 98.2%.

5.8 Conclusions

The first demonstration of an electro-mechanically actuated cantilever tunable cavity in a GaAs semiconductor based system is presented with highly controllable tuning of up to 1nm exhibited. The cavity was designed from the ground up via extensive simulation studies of the entire parameter space. The final design exhibits world-leading figures of merit for both strong and weak coupling regimes. The robustness of the design was tested in simulation by emulating fabrication errors in the structure using Monte Carlo simulation methods and elliptical air holes. The fabrication process was streamlined and the cavity parameters optimised for fabrication to achieve a highly repeatable cavity design with a mode wavelength standard deviation of $\sigma_\lambda = 0.6nm$. This, combined with the tuning range of the device leads to the probability of any two cavities being within tuning range of each other being $P_{succ} = 76.2\%$.

Further work to be done on these devices includes fabricating a sample in which the QDs show PL emission in the cavity devices so that tuning a QD on and off resonance with the cavity can be demonstrated. Moreover, to improve the Q-factor of the devices which is likely limited by surface absorption effects, passivation of the sample surface directly after fabrication will be attempted as this has been shown to improve not only the Q-factor but also to reduce the wavelength spread of

like cavities in GaAs structures [120]. Going forward, a design that allows for both actuation of the cantilevers and electrical control over the QDs is required to improve the success rate P_{succ}. This could be achieved by fabricating separate diodes in the membrane and across the sacrificial layer as shown in this work. Moreover, an additional design consideration would be to introduce a third nanobeam in order to side-couple light into the cavity. This method has been shown to allow highly efficient injection of light into the cavity [182].

This page intentionally left blank.

6 Strong directionality and light-matter interaction enhancement for a QD in a waveguide coupled micro-cavity

6.1 Introduction

As stated in Chapter 5, QDs in nano-photonic structures can exhibit extremely strong light-matter interactions which are essential for the realisation of both QIP and quantum networking with photons. Another desirable trait exhibited by QDs in certain photonic structures is the directionality of their emitted light (see Section 2.7). Independently, these two phenomena have been shown to have many crucial applications in QIP, such as a fast deterministic single photon source [43] and improvement of single photon indistinguishability [183] for light-matter interaction. While for chirality, spin-path entanglement [85] and entanglement generation between multiple emitters [184, 185] have been demonstrated. A vast number of different systems exist which provide the conditions for strong light-matter interactions, very few of them also provide the conditions for strong directionality. In waveguide systems where strong directionality is easier to achieve such as in a glide-plane waveguide [103] or topological waveguide [88, 186], the light-matter interaction enhancement comes from the slow-light effect. This only allows for a modest Purcell factor be be achieved. In a glide-plane waveguide the highest demonstrated Purcell factor for a chiral QD is $F_P = 8$ [187]. Directionality of emission has also been shown for a single atom coupled to a whispering gallery mode resonator, giving a low Purcell factor of $F_P = 2.2$ for a chiral emitter [188].

The device proposed here is a waveguide coupled PhCC cavity system consisting of an H1 PhCC coupled to two modified W1 waveguides as first proposed by Hallett et al. [189]. In PhCC systems, the asymmetry normally required to facilitate the directionality of light in PhCs severely reduces the confinement of light in the cavity. As a result, the achievable Purcell factor becomes extremely low. In the device presented here, the chirality is not derived from asymmetry in the cavity design. Instead, it is derived from the careful engineering of the waveguide position and geometry. This maintains the symmetry of the cavity and so, the achievable Purcell factor remains high whilst simultaneously enabling directional emission. The device is capable of exhibiting near unity directionality and a Purcell factor of $F_P = 70$ simultaneously. Moreover, the design is robust to the position of the emitter within the cavity, with the maximum chiral contrast of the device being achievable for an emitter within $\pm 60nm$ of the cavity centre. This robustness is far superior to competing waveguide schemes [189].

In this chapter, the device design is first outlined. The origin of the directionality in the design will then be explained in detail. The expected transmission dynamics of the system will be considered using a theoretical model and in simulation so that comparison to experimental measurements can be made. After outlining the device design and theory, the experimental results will be shown and discussed. An overview of the sample design and fabrication process will be

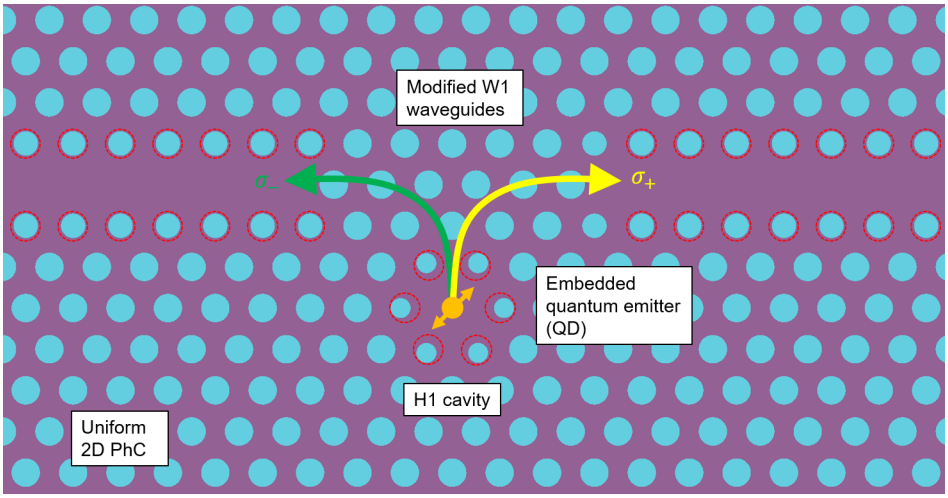

Figure 81: Schematic of the waveguide coupled H1 cavity system studied in this chapter. The band structure of the waveguides is tailored by reducing the size of the holes either side of the waveguide itself. A circularly polarised emitter located in the cavity will emit only into a single waveguide. The waveguide it will emit into depends on the handedness of the polarisation.

presented before analysing the results from the measurements conducted on the sample. Firstly, characterisation measurements of the different types of devices will be presented. Following this, magnetic field dependence measurements for a QD in a device will be presented.

6.2 Theory

6.2.1 Origin of directionality in a waveguide coupled H1 photonic crystal cavity

As stated in Section 6.1, the origin of the directionality of light in the waveguide coupled H1 cavity derives from the careful design and positioning of the two modified W1 waveguides that couple light out from the cavity. As shown in Section 2.4.4, Figure 18, an H1 cavity contains two orthogonal fundamental modes. Normally these modes are degenerate. However, by introducing the two waveguides the degeneracy is lifted. H1 cavities are extremely sensitive to the symmetry of the surrounding PhC. By introducing the waveguides either side of the cavity in one axis, the effective cavity length of that axis is increased due to the alteration of the PhC in that direction. This causes the two orthogonal modes to become non-degenerate. A schematic of the waveguide coupled cavity is shown in Figure 81. In reality, disorder in the fabrication of the H1 cavity also leads to lifting of the degeneracy, even for uncoupled cavities.

The now non-degenerate cavity modes couple to the waveguides differently from one another. This can be seen by examining the electrical field profiles for the two modes. The two orthogonal modes are defined as the χ and Ψ modes, a convention set by Thijssen et al. [190]. From Figure 82, the spatial electric field modes in the x and y directions (E_x and E_y respectively) can be seen for

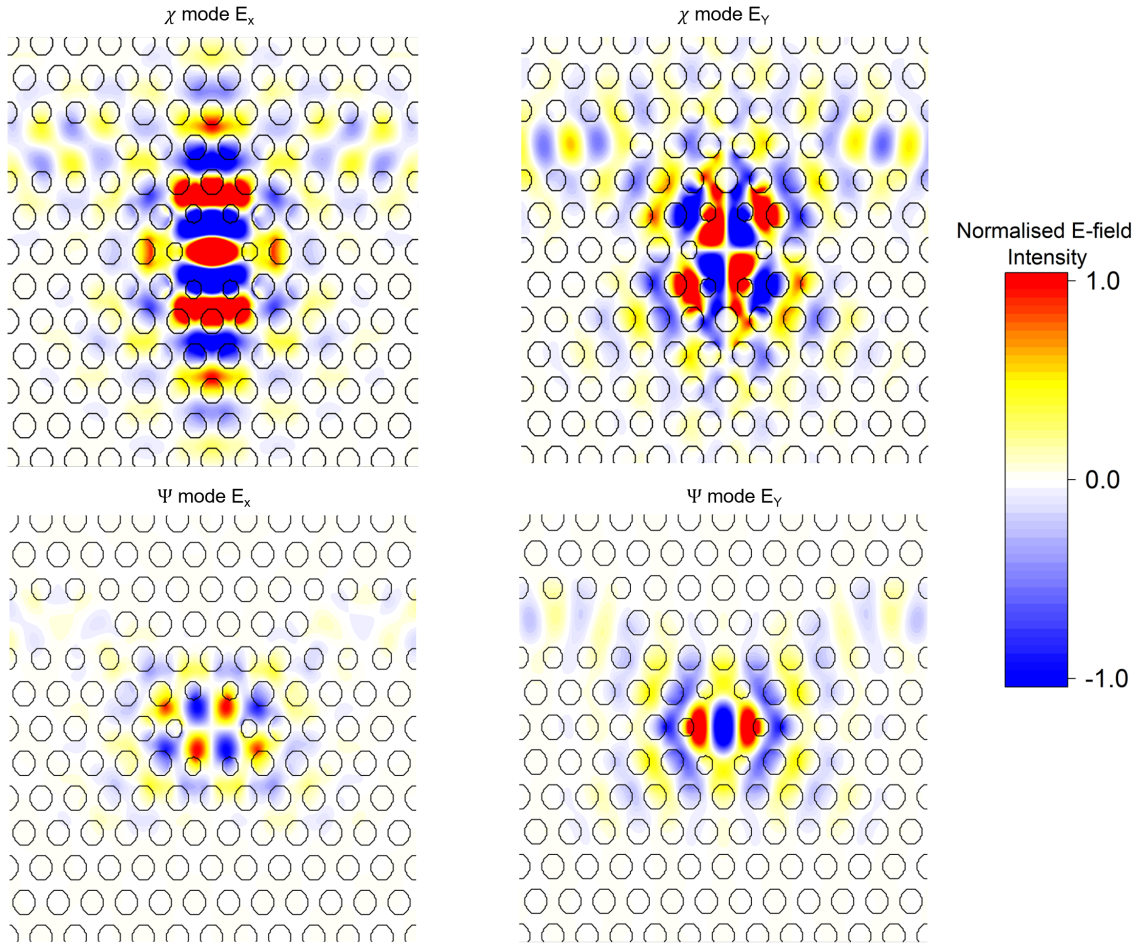

Figure 82: Electric field profiles for the orthogonal cavity modes in the waveguide coupled H1 cavity. The x and y polarisation components of each mode are plotted individually. The field profiles were obtained by exciting each mode individually using x and y linearly polarised dipole sources at the cavity centre to excite only the χ and Ψ modes respectively.

each of the two modes. If the E_x components of the χ and Ψ modes are considered, it can be seen that the χ mode exhibits even parity between the waveguides in E_x. Conversely, the Ψ mode is shown to exhibit odd parity between the waveguides in E_x. The opposite case is true for the E_y components of the χ and Ψ modes. In the E_y case the χ mode exhibits odd parity between the waveguides whereas the Ψ mode exhibits even parity between the waveguides. As a result, the phase relationship between the modes in the left and right waveguides are different. In the left waveguide the field profiles of the χ and Ψ modes are in phase while the opposite is true for the right hand waveguide where the modes are in anti-phase with each other [189]. This condition allows for the interference between the modes to be different in each waveguide. This interference between the modes in the waveguides is only possible as both modes couple to the W1 modes in the waveguides exactly, leading to a spatial overlap of the χ and Ψ modes in the waveguides.

Chirality in photonic systems requires the emission of circularly polarised light into the system. If a circularly polarised dipole emitter embedded at the cavity centre emits photons into the cavity, both cavity modes will be excited simultaneously creating a superposition between them [190]. The cavity modes in the superposition will have a well-defined phase difference between them, either $+\frac{\pi}{2}$ or $-\frac{\pi}{2}$ depending on the handedness of the circularly polarised excitation. Moreover, an additional phase factor between the cavity modes derives from the detuning of the emitter from the individual cavity modes. If this additional detuning-related phase difference equals $\pm\frac{\pi}{2}$ then it is possible to achieve perfectly constructive/destructive interference in opposite waveguides (assuming the intensity of the modes are equal). If these conditions are met then the emission from the embedded emitter will be perfectly chiral.

Hallett et al. present an analytical model which describes the effect of the detuning of the cavity modes on the performance of the device [189]. The model treats the non-degenerate cavity modes as Lorenzian functions with amplitudes given by:

$$E_j = \frac{\sqrt{\Gamma_j}}{\Gamma_j/2 + i\left(\lambda - \lambda_0^j\right)} \tag{51}$$

where λ_0^j is the cavity mode wavelength, $\Gamma_j = \lambda_0^j/Q$ is the decay rate of the cavity mode and $j = \chi, \Psi$. The phase of each cavity mode is given by:

$$\theta_j = \arctan\left(\frac{\Gamma_j \lambda}{\lambda^2 - \lambda_0^{j^2}}\right) \tag{52}$$

As the modes are non-degenerate, a wavelength dependent phase difference arises:

$$\Delta\theta = \theta_\chi - \theta_\Psi \tag{53}$$

From this model, a QD emitting at a wavelength of $\lambda_{QD} = \frac{\lambda_\chi - \lambda_\Psi}{2}$ will exhibit purely directional emission as at this wavelength the cavity modes have equal intensity and a phase difference of $\frac{\pi}{2}$. In Section 2.7, the '*Degree of Circular Polarisation*' (DCP) in terms of the Stokes parameters was defined in Equation 32 as a measure of the chiral contrast of a system. Applying this equation to the waveguide coupled H1 allows for differences in the amplitude of the two cavity modes, as well as the phase difference between them to be accounted for. Hallett et al. demonstrate that this model closely matches simulations of the system [189]. Figure 83 shows the key results from the analytical model. From Figure 83 a.) the expected wavelength dependent DCP for a waveguide coupled cavity system with: $\lambda_\chi = 931.0nm, Q_\chi = 500$ and $\lambda_\Psi = 932.5nm, Q_\Psi = 1000$ can be seen. These values are chosen as they represent the expected parameters for a fabricated device. The maximum value for the DCP from these parameters is ≈ 1 and occurs at the crossing point between the cavity mode traces at $\lambda = 931.8nm$. The device exhibits a near unity DCP at the optimal wavelength, moreover, the DCP remains > 0.9 over a bandwidth of 0.63nm. Figure 83

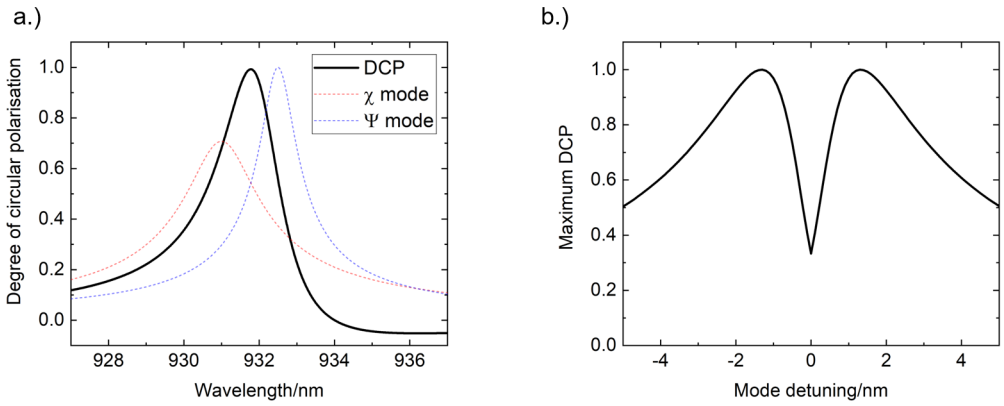

Figure 83: Results from the analytical model proposed by Hallett et al. [189]. a.) Shows the expected wavelength dependent degree of circular polarisation for a device with: $\lambda_\chi = 931.0nm, Q_\chi = 500$ and $\lambda_\Psi = 932.5nm, Q_\Psi = 1000$. The maximum expected DCP for an emitter in this device occurs at $\lambda = 931.8nm$ where DCP ≈ 1. b.) Shows the relationship between the maximum DCP achievable in a device and the detuning between the two cavity modes in a.). The maximum DCP is obtained for a detuning of $\Delta\lambda = \pm 1.3nm$. A sharp drop-off in the maximum DCP occurs at very small values of detuning where the modes become degenerate.

b.) shows the dependence of the maximum DCP exhibited by a device on the detuning between the two cavity modes. When the detuning between the modes is very small, the maximum DCP is also very low as the modes start to become degenerate at low detuning. The maximum DCP is seen at $\Delta\lambda = \pm 1.3nm$, at larger magnitudes of detuning the maximum DCP slowly decreases. The maximum achievable DCP remains > 0.9 over a bandwidth of 1.4nm at both positive and negative detuning. These results are extremely useful when considering the design of the system for fabrication. It is clear that obtaining the optimal detuning of the modes is essential to the success of the device. It has been shown that the detuning of the modes in an H1 PhCC can be adjusted by stretching the PhC lattice in one direction both in design by adjusting the pitch of the PhC [117], by applying uniaxial strain to the cavity [118] and by local oxidation [191]. Such methods can be utilised to optimise the cavity detuning to ensure a high DCP is achievable. Moreover, any QD in the cavity could have its emission energy tuned to the optimal wavelength via a multitude of tuning methods (see Section 2.3).

6.2.2 Waveguide to waveguide transmission dynamics

Understanding the theoretical waveguide to waveguide transmission dynamics of the system will provide a valuable insight into the operation of the device, allowing for experimental measurements to be better understood and compared to the theory.

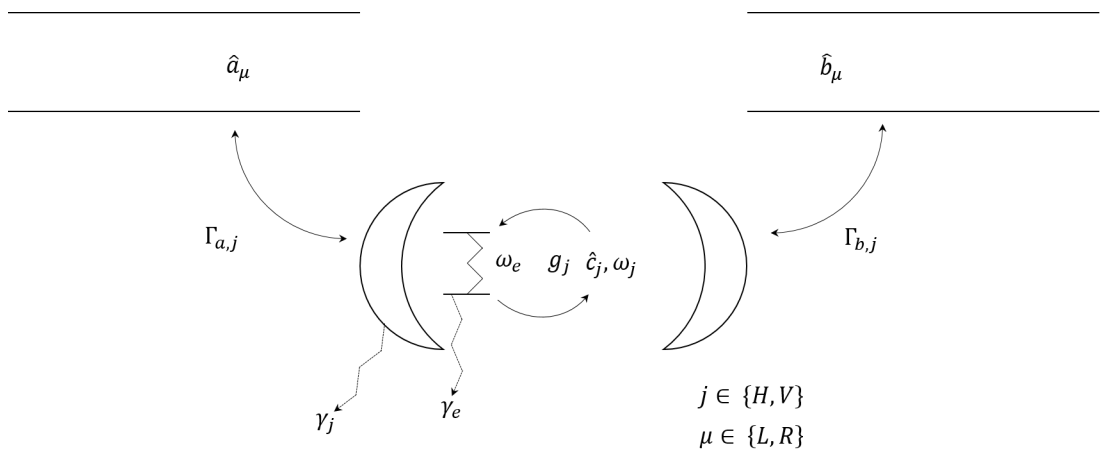

Figure 84: Diagram showing the numerical model used for the waveguide to waveguide transmission for the waveguide coupled H1 cavity structures studied in this chapter. $\hat{a}_\mu$ and $\hat{b}_\mu$ are the waveguide modes propagating in the μ direction. $\Gamma_{a,j}$ and $\Gamma_{b,j}$ are the coupling rates between the waveguides and the cavity emitter system where $j \in \{H, V\}$ are the two orthogonal cavity modes. ω_e is the transition frequency of the emitter which couples to the cavity modes c_j with constant g_j. γ_j and γ_e are loss rates from the cavity to non-guided modes and non-radiative losses from the emitter, respectively.

A theoretical model for transmission developed by Pieter Kok and Elena Callus of the University of Sheffield is presented here with their permission. The model is based on input-output formalism in cQED [192] and considers two feeding waveguides which couple solely to the cavity-emitter system. Figure 84 shows a diagram of the numerical model used to investigate the device transmission. The model considers a system of two waveguides with modes $\hat{a}_\mu$ and $\hat{b}_\mu$, where μ is the direction of propagation of the mode. The only source of coupling between the modes is via the cavity-emitter system. The coupling rate between the waveguide and the cavity modes is given by $\sqrt{\frac{\Gamma}{2}}$ and is assumed to be independent of frequency (this is true if the linewidth of the optical state is sufficiently narrow). In the cavity, the emitter has a transition frequency of ω_e and couples with constants g_j to the cavity modes $\hat{c}_j$ where $j \in \{H, V\}$ are the two orthogonal cavity modes. Loss channels $\gamma_j = \kappa^2$ and $\gamma_e = \gamma^2$ are included to account for losses from the cavity coupling to non-guided modes and non-radiative losses from the emitter, respectively. The initial state of the system consists of a state propagating along $\hat{a}$ in the right hand direction. This state either couples to the cavity or is reflected back along the waveguide. [193–195]

Using this model, if a single photon with frequency k is considered propagating towards the right

in $\hat{a}$ then the amplitude of the scattering into the right propagating mode in $\hat{b}$ is given by:

$$S_{p,k;b,a} = \frac{1}{C} \sum_{j,k=H,V\, j\neq k} \Gamma^*_{b,j} \left[\left(\frac{\Lambda(j,k)}{2} + \frac{g^*_j g_k}{i\omega_e - ip + \frac{\gamma_e}{2}} \right) \Gamma_{a,k} - \left(i\omega_k - ip + \frac{\gamma_k}{2} + \frac{\Lambda(k,k)}{2} + \frac{|g_k|^2}{i\omega_e - ip + \frac{\gamma_e}{2}} \right) \Gamma_{a,j} \right] \delta(k-p) \quad (54)$$

where

$$\Lambda(j,k) = \Gamma_{a,j}\Gamma^*_{a,k} + \Gamma_{b,j}\Gamma^*_{b,k} \quad (55)$$

and

$$C = \left(i\omega_H - ip + \frac{\gamma_H}{2} + \frac{\Lambda(H,H)}{2} + \frac{|g_H|^2}{i\omega_e - ip + \frac{\gamma_e}{2}} \right) \left(i\omega_V - ip + \frac{\gamma_V}{2} + \frac{\Lambda(V,V)}{2} + \frac{|g_V|^2}{i\omega_e - ip + \frac{\gamma_e}{2}} \right) - \left(\frac{\Lambda(H,V)}{2} + \frac{g^*_H g_V}{i\omega_e - ip + \frac{\gamma_e}{2}} \right) \left(\frac{\Lambda(V,H)}{2} + \frac{g^*_H g_V}{i\omega_e - ip + \frac{\gamma_e}{2}} \right) \quad (56)$$

The amplitude for a back-scattering event into the left propagating mode ($\hat{a}_L$) is given by:

$$S_{p,k;b,a} = 1 + \frac{1}{C} \sum_{j,k=H,V\, j\neq k} \Gamma^*_{a,j} \left[\left(\frac{\Lambda(j,k)}{2} + \frac{g^*_j g_k}{i\omega_e - ip + \frac{\gamma_e}{2}} \right) \Gamma_{a,k} - \left(i\omega_k - ip + \frac{\gamma_k}{2} + \frac{\Lambda(k,k)}{2} + \frac{|g_k|^2}{i\omega_e - ip + \frac{\gamma_e}{2}} \right) \Gamma_{a,j} \right] \delta(k-p) \quad (57)$$

With the model defined, the expected transmission behaviour of the system can be studied.

The effect of the detuning of the cavity modes on the transmission of the device was both calculated using the above model, and simulated in FDTD in order to compare the two and verify the accuracy of the model. The detuning of the modes in simulation was controlled by stretching the period of the PhC lattice in one direction while the other remained constant. This allows the wavelength of the modes to be tuned independently of one another as mentioned in Section 6.2.1. The y-direction lattice period a_y was varied relative to the x-direction lattice period a_x in regular steps and the transmission behaviour recorded. The transmission through the device was acquired in simulation by embedding a broadband mode source into the left waveguide. The source injected light directly into the W1 waveguide propagating in the right hand direction. A transmission monitor was positioned in the right hand waveguide sufficiently far from the cavity waveguide interface as not to pick up any extra light that was not truly scattered into the waveguide. By detuning the emitter far from the cavity modes, the transmission model can then be used to consider a bare cavity. By individually exciting the orthogonal cavity modes in simulation with linearly polarised dipoles positioned at the centre of the cavity, The Q-factors and wavelengths (and therefore the detuning) of the modes could be obtained. These parameters obtained from the simulations were

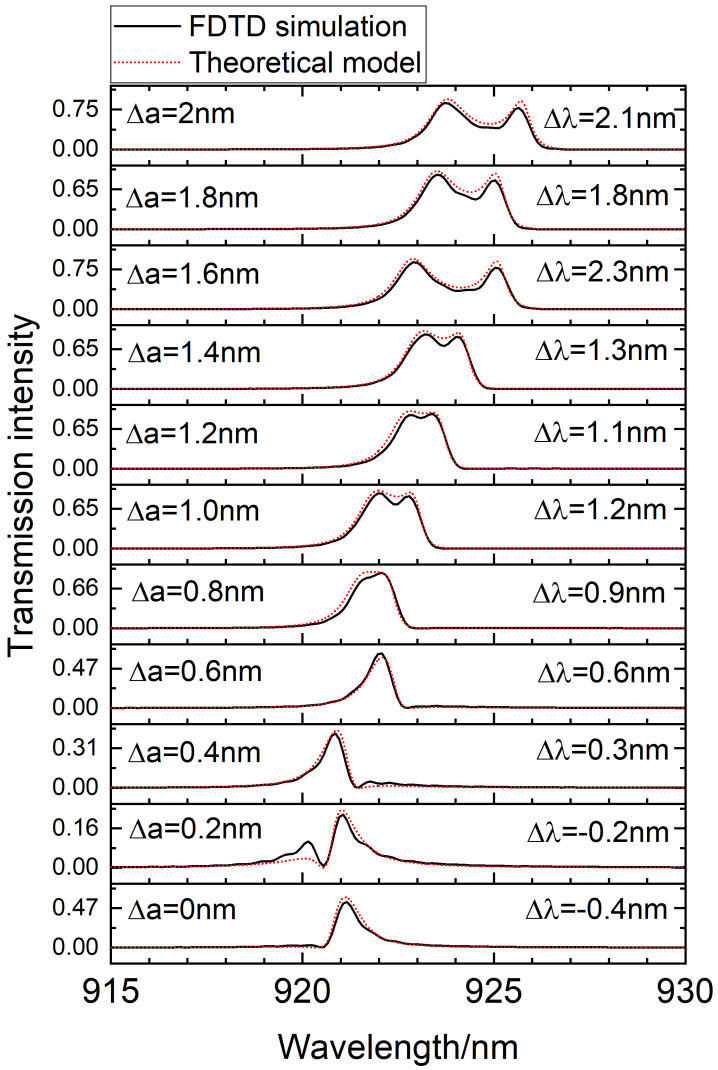

Figure 85: Comparison between the simulated and theoretical transmission for a waveguide coupled H1 cavity. The mode spacing is altered in simulation by adjusting the difference between the a_x and a_y lattice periods of the PhC where $\Delta a = a_y - a_x$. The detuning of the modes is found in simulation by exciting the modes individually with linearly polarised dipole sources at the cavity centre. The mode detuning and cavity mode Q-factors measured in simulation $\Delta\lambda = \lambda_V - \lambda_H$ are then used to calculate the theoretical transmission according to the model presented in Equation 54. It can be seen that the theoretical model agrees strongly with the simulated transmission results. The maximum transmission is seen to decrease at very small mode detuning.

input into the theoretical model to obtain the theoretical transmission behaviour. A comparison between the simulated and numerically-acquired transmission behaviour can be seen in Figure 85.

It is clear from Figure 85 that the theoretical model agrees well with the simulations of the sys-

tem. In both the simulations and from the model, at large mode detuning, the transmission signal shows two distinct mode peaks. As the detuning reduces, the two modes begin to overlap, and subsequently interfere with each other. From Figure 83 the maximum achievable DCP occurs at a mode detuning of $\Delta\lambda = 1.3nm$. From the simulations this detuning occurs for a lattice difference of $\Delta a = 1.4nm$. The modes at this point overlap significantly. However, a small drop in transmission between the individual modes remains. At this value for detuning, the overall transmission remains high with a maximum value of $T_{max} = 0.89/0.95$ in simulation / theory, respectively. At a detuning of $\Delta\lambda = 1.1nm$ the modes overlap to a degree that there is very little drop in the transmission between them. At lower values of mode detuning, the modes begin to interfere with each other. For $|\Delta\lambda| \geq 0.3nm$ a single asymmetric transmission peak is observed. Destructive interference between the modes causes a transmission dip to appear on the long wavelength side of the transmission peak. At very small values of detuning the interference is extremely strong and the transmission of the system is strongly repressed. The transmission dip becomes a prominent feature in the transmission signal. Moreover, the point where $\Delta\lambda = 0nm$ occurs at a non-zero lattice mismatch. This is due to the presence of the waveguides lifting the degeneracy of the modes prior to the lattice mismatch. An overall red-shifting of the cavity modes is seen with increasing Δa. The results from these simulations aided in the device design process as the relationship between the Δa and $\Delta\lambda$ was understood. Moreover, by analysing experimental transition measurements, the mode detuning was estimated from the shape of the transmission signal by comparing it to the theoretical results.

If the wavelength of the cavity coupled emitter in the transmission model is positioned between the cavity modes, the transmission dynamics of the system are altered significantly. Figure 86 shows results from the theoretical model for three linearly-polarised QDs of different wavelengths in a waveguide coupled cavity. The QD is set to only couple to the shorter wavelength χ mode. This is analogous to the emission from the QD being linearly-polarised in-phase with the χ mode. In all three cases, the inclusion of the QD produces a large effect on the transmission. At wavelengths shorter than the peak of the cavity modes, a Fano-like lineshape is seen at the QD wavelength. This implies that an interference effect between cavity mode and the QD occurs. When the QD wavelength is between the two cavity modes, a sharp transmission dip is seen at the QD wavelength. At wavelengths longer than both cavity modes, a sharp transmission peak is seen at the QD wavelength. As the QD does not couple to the longer wavelength Ψ cavity mode, no interference effect is seen. In all three cases the QD related features exhibit a large effect on the transmission of the system.

6.3 Sample and device design

An initial test sample of various cavity designs and parameter ranges was fabricated to identify an optimised approach for the experimental realisation of the waveguide coupled H1 cavity with an embedded QD. Figure 87 shows the three different waveguide arrangements which were fabricated

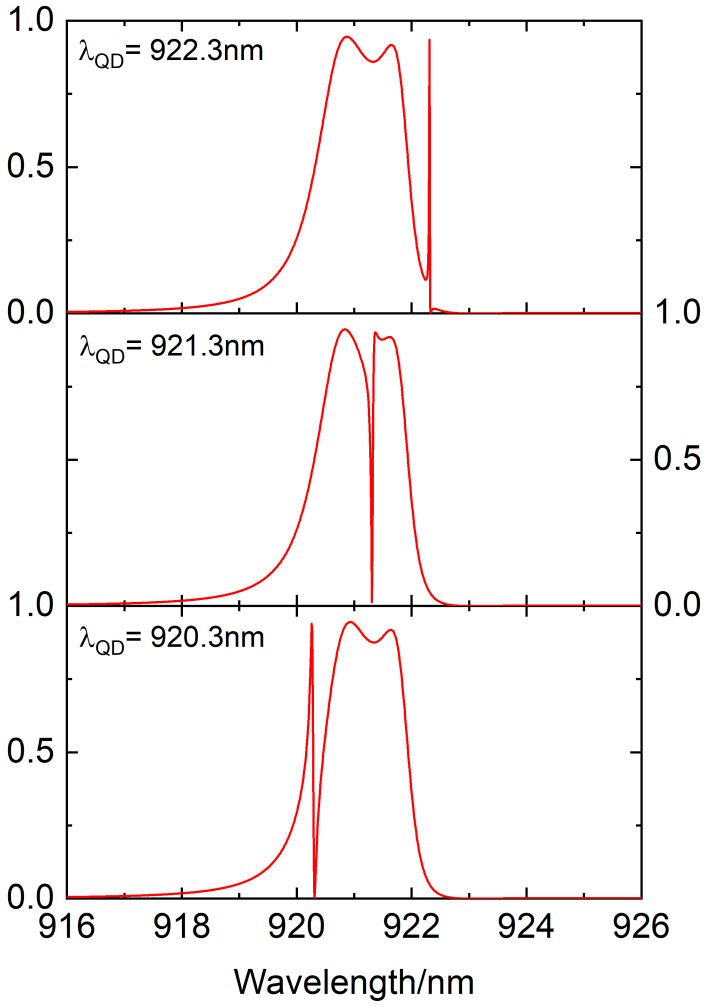

Figure 86: Theoretical transmission behaviour for a waveguide coupled H1 cavity with a linearly-polarised embedded emitter at different wavelengths. The cavity mode parameter are; $\lambda_\chi = 920.7nm$, $Q_\chi = 790$ and $\lambda_\Psi = 921.85nm$, $Q_\Psi = 1535$. The QD couples to the χ mode with coupling strength $g_\chi = 0.1$ and does not couple to the Ψ mode.

on the sample. Figure 87 a.) shows the regular waveguide orientation which is used throughout the numerical methods and simulations from Section 6.2. b.) and c.) show an alternative waveguide orientation in which both waveguides are on the same side of the H1 cavity. This orientation still enables the chiral effects of the waveguide coupled cavity system to occur due to the symmetry of the H1 system. By positioning the waveguides on the same side of the cavity the amount of light scattered between the waveguides that has not interacted with the cavity should be reduced. Moreover, as the outcouplers are far from the cavity-waveguide interface the effect of back reflections should be reduced compared to the regular design in Figure 87 a.). The W1 waveguides are

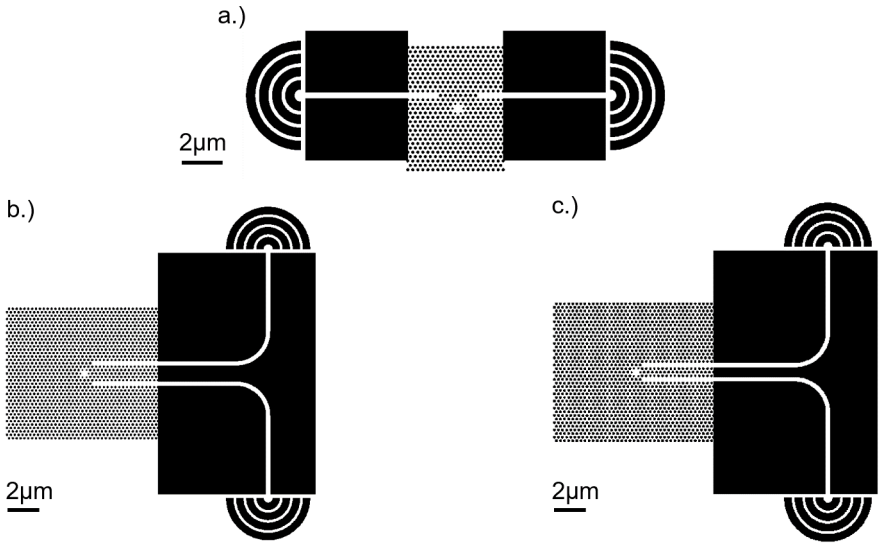

Figure 87: Schematics of the designs of the three waveguide configurations included on the sample. a.) Shows the standard design with the waveguides on either side of the cavity. b.) & c.) Show an alternative design where the waveguides are on the same side of the cavity. This design was created to try and reduce unwanted transmission through the waveguides and reduce back reflections into the cavity from the outcouplers. The lateral spacing between the waveguides differs between b.) and c.).

separated by 5 or 3 rows of air holes in Figure 87 b.) and c.) respectively. The increased separation between the waveguides in b.) will reduce coupling between the two waveguide modes but will also reduce the coupling from the waveguides into and out of the cavity. For each waveguide configuration, devices with a range of PhC parameters were fabricated. This was done in order to identify the parameter combination that results in devices with the desired mode detuning, wavelength and Q-factor. For all designs, the radius of the air holes and the difference between the PhC lattice periods Δa were varied to optimise the cavity mode wavelengths and the detuning between them. Additionally, for the regular design, the number of air holes between the two waveguides was altered. By changing the number of air holes between the waveguides, the strength of the coupling between the waveguides and the cavity is altered. By increasing the number of air holes between the waveguides, the Q-factor of the cavity will increase as it couples less strongly to the waveguides. Moreover, the coupling between the two waveguides will be reduced, improving the purity of the transmission signal between the outcouplers. Figure 88 shows the difference between the maximum and minimum number of holes between the waveguides/ between the waveguides and the cavity for the regular and alternate designs. On the sample, devices are fabricated in a range between these two values to investigate the effect of changing the coupling strength on the device performance.

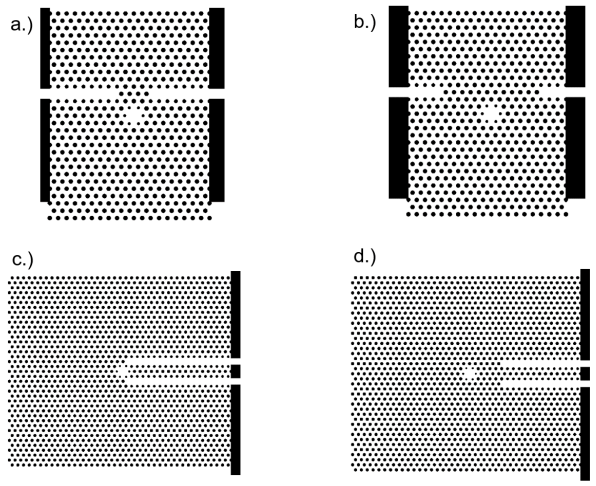

Figure 88: Schematics of the minimum (left) and maximum (right) numbers of holes between the waveguides and cavity for both the regular design, a.) and b.), and the alternate design, c.) and d.).

On the sample the air hole radii are varied from 50-70nm. The period of the PhC in the x direction is always given by $a_x = 0.3r$. The period in the y direction, a_y is varied relative to a_x over the range of: $5nm \leq \Delta a \leq -5nm$. The spacing between the waveguides in the regular design was varied from 4 - 12 holes in increments of 2 holes. Finally, in the alternate design, the number of holes between the waveguides and the cavity was varied from 0 - 5 holes.

6.4 Results

The cavity parameter test sample was fabricated on a GaAs semiconductor wafer with embedded InAs QDs in an 170nm thick free-standing membrane. The wafer was not electrically contacted to increase the space available for devices on the chip and reduce the complexity of the fabrication. Measurements to characterise the devices and identify the optimal design for an electrically contacted sample were conducted on the remaining devices. In addition to the parameter variations mentioned in Section 6.3, the sample contained H1 cavities with no coupling waveguides and all three waveguide arrangements without H1 cavities. These structures were included to provide references to compare the coupled cavity devices to. Figure 89 shows SEM images of each of the cavity designs fabricated on the sample.

6.4.1 Uncoupled H1 cavity results

To characterise the devices, PL from the QDs in the cavities was excited using an above band (633nm) HeNe laser at high power (150μW). The PL emission was collected via a μPL set up and recorded on a CCD spectrometer. Firstly, the uncoupled H1 cavities were measured. The median Q-factor of the cavity modes was $Q_{med} \approx 3500$ and an increase in the air hole radius of 2nm in

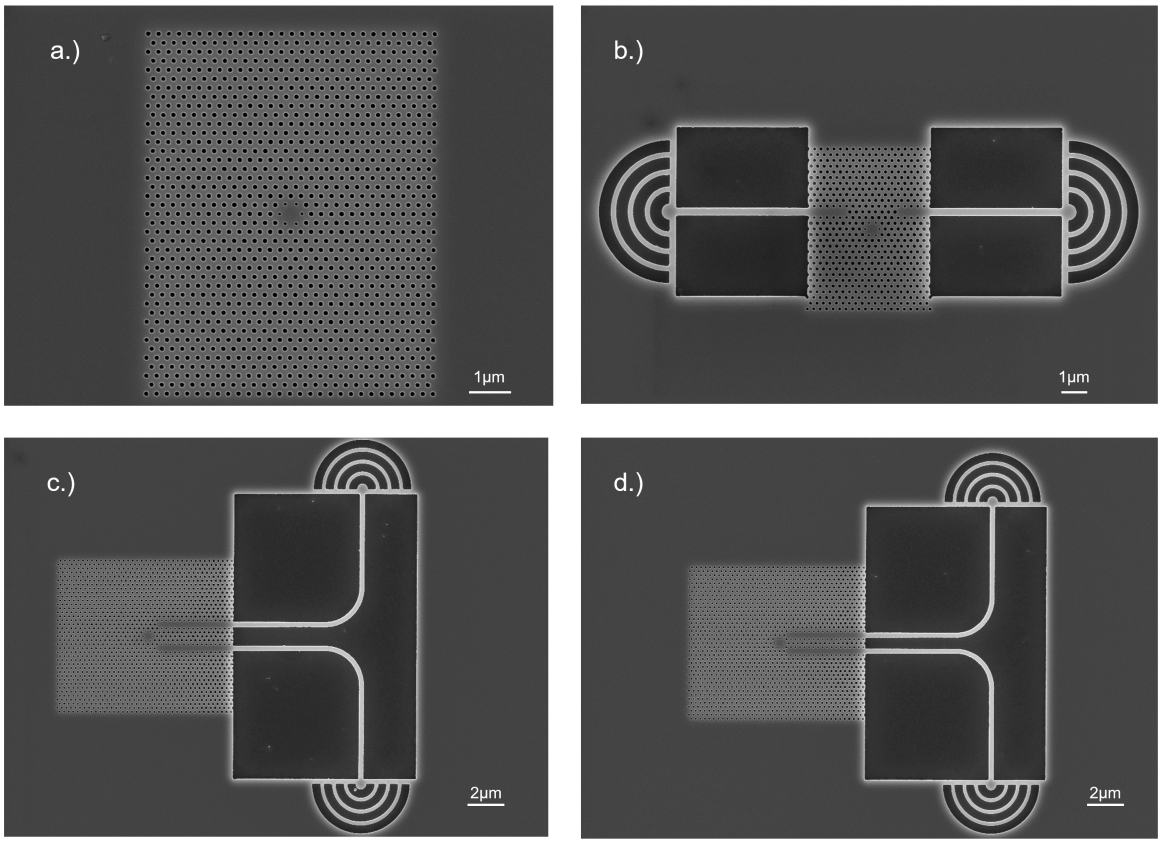

Figure 89: SEM images from the cavity test sample. a.) Uncoupled H1 cavity. b.) Regular design waveguide coupled H1 cavity. c.) & d.) The two alternate waveguide coupled cavity designs.

the design resulted in a red-shift of the cavity modes of approximately 10nm. This Q-factor can be taken as the intrinsic Q-factor of the cavities as no coupling losses into the waveguides are possible. Figure 90 shows the initial characterisation results for the uncoupled H1 cavities. In these experiments the cavity modes of the H1 cavities were measured by exciting and collecting PL from directly above the cavity. The Q-factor and mean mode wavelength for the device with zero lattice shift ($a_x = a_y$) are presented. From Figure 90 a.) the Q-factor can be seen to remain roughly constant at $Q_{med} \approx 3500$ for $60nm \leq r \leq 68nm$. This indicates that there is not a single optimal radius for the H1 cavity design on the sample. Instead, the devices maintain their optimal performance over a wide range of cavity mode wavelengths. Figure 90 b.) shows how altering the hole radii of the devices effects the wavelength of the cavity modes for the $\Delta a = 0nm$ device. A strong linear dependence is observed. By applying a linear fit to the data, the rate of change of cavity mode wavelength with respect to hole radii is found to be $\frac{d\lambda}{dr} = -4.078 \pm 0.120$. As the median Q-factor is roughly constant over a range of an $8nm$ change in hole radius, this allows for the devices to operate optimally over a wavelength bandwidth of $\approx 32nm$.

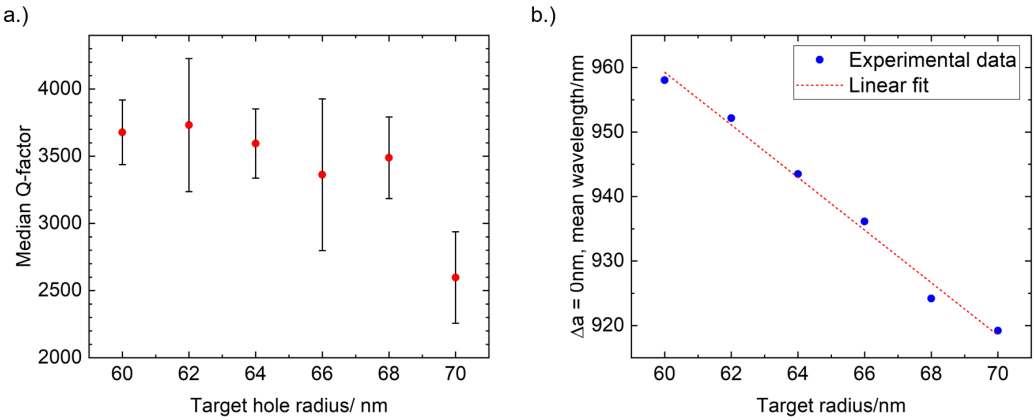

Figure 90: Results of the characterisation of the uncoupled H1 cavities. a.) Median Q-factor for H1 cavity sets of different hole radii. b.) Mean mode wavelength of the $\Delta a = 0nm$ device for each radius. A linear relationship is seen with a gradient of $\frac{d\lambda}{dr} = -4.078 \pm 0.120$ obtained from a linear fit to the data.

After collecting the basic cavity performance statistics, the effect of altering the lattice mismatch Δa in uncoupled H1 cavities was investigated.

From Figure 91 a.) the experimental effect of altering Δa on the mode detuning $\Delta\lambda$ can be seen. A strongly linear dependence is seen from the data, this is true for all four of the device sets with differing radii. A linear fit of the data shows that the rate of change of detuning with respect to PhC lattice mismatch is $\frac{d(\Delta\lambda)}{d(\Delta a)} = 1.357 \pm 0.147$ for uncoupled H1 cavities. The simulated detuning data from Figure 85 is also included on the graph for comparison. By fitting the simulated data with a linear fit the rate of change of detuning with respect to PhC lattice mismatch is $\frac{d(\Delta\lambda)}{d(\Delta a)} = 1.277 \pm 0.119$. The values for the gradient of the experimental and simulated results are both within the error tolerance of each other. Therefore, strong agreement between theory, simulation and experiment is seen for the rate of change of detuning with respect to PhC lattice mismatch. What does differ between the results is the offset. The simulated devices show a much lower offset than the experimental results. This may be caused by the differences in hole radii between simulated and experimentally measured devices. Moreover, the simulated devices included coupling waveguides which could affect the offset whereas the experimentally measured cavities were uncoupled. Figure 91 b.) shows a set of PL spectra from the $r = 68nm$ devices from which the detuning values for graph a.) were calculated. The change in detuning between spectra can be clearly seen. Furthermore, a systematic red-shifting of the cavity modes is seen with increasing Δa. This occurs due to the stretching of the lattice altering the band structure of the PhC and therefore altering the supported modes of the PhC. By increasing the period of the PhC the bands

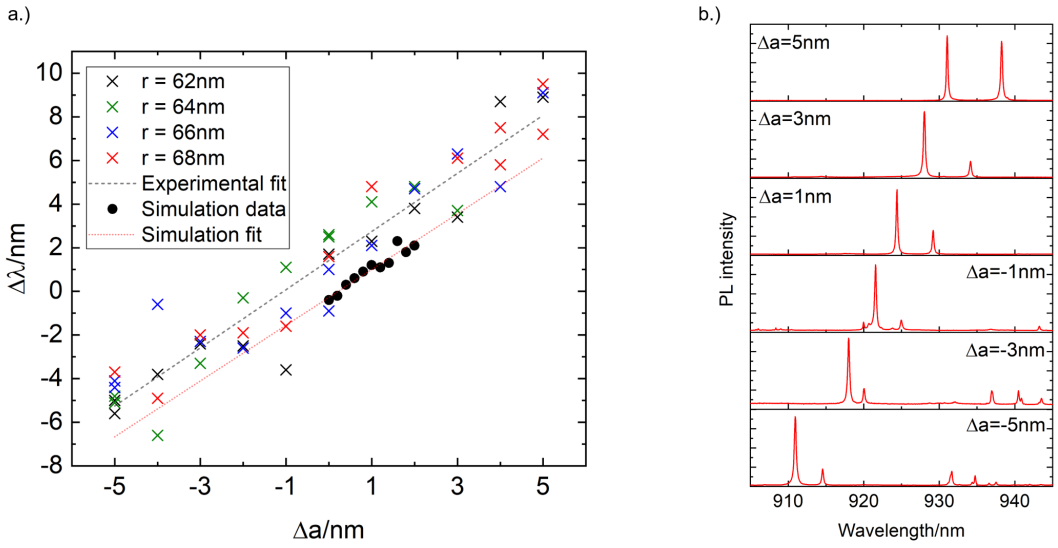

Figure 91: Results from characterisation measurements of the uncoupled H1 cavities. a.) Graph showing the relationship between the PhC lattice period mismatch Δa and the detuning of the cavity modes $\Delta\lambda$. Four different target hole radii structures were measured and all show the same strongly linear dependence. A linear fit of the data is shown which yields a gradient of $\frac{d(\Delta\lambda)}{d(\Delta a)} = 1.357 \pm 0.147$. The results from the simulations in Figure 85 are included for comparison and are fitted like the experimental data. The gradient of the fit on the simulated data is $\frac{d(\Delta\lambda)}{d(\Delta a)} = 1.277 \pm 0.119$ b.) PL spectra of the cavity modes from the $r = 68nm$ devices. The detuning change can be clearly seen. Moreover, the modes are seen to red-shift with increasing Δa

are shifted towards longer wavelengths, this causes the modes of the H1 cavity to shift accordingly.

Having obtained experimental results for the uncoupled H1 cavities, the measurements on the waveguide coupled devices can be compared to the uncoupled case as a reference to infer if any effects come solely from the waveguide coupling.

6.4.2 Regular waveguide coupled H1 device results

The next set of devices measured were the regular waveguide coupled cavities from Figure 89 a.). The results of the measurements from these devices are presented in Figure 92. The measurements for Figure 92 a.) and b.) were obtained by exciting PL from the QDs in the cavity. An above band (633nm) HeNe laser was incident on the cavity centre at high power (100μW). The resultant PL from the QD coupled to the cavity mode and was collected from above the cavity for Figure 92 a.) and from one of the device outcouplers for Figure 92 b.).

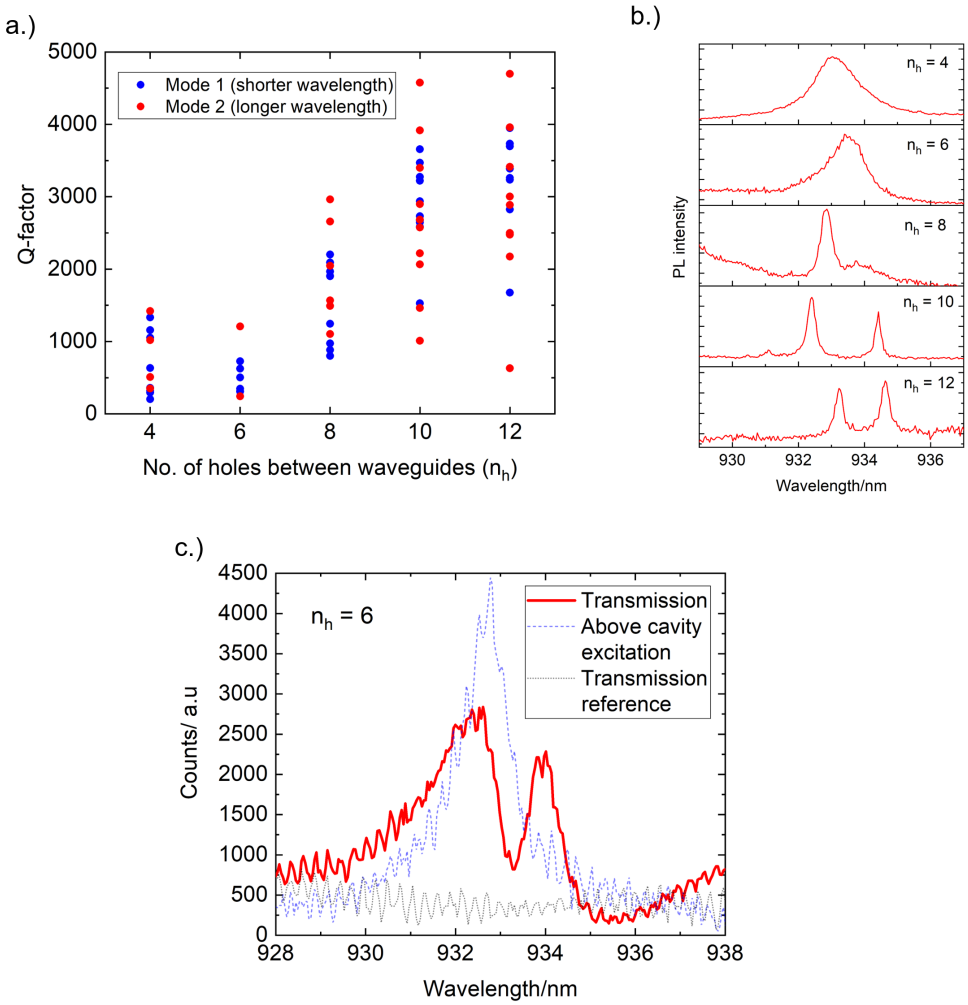

Figure 92: Results from the measurements of the regular design waveguide coupled H1 cavities. a.) The measured Q-factors of the cavities in relation to how many air holes were between the waveguides on each device (n_h). As the number of holes between the waveguides increases so does the mean measured Q-factor. b.) PL spectra of the cavity modes for devices with equal air hole radii and different values of n_h. The Q-factor of the modes can clearly be seen to reduce as n_h reduces. The wavelength of the cavity modes remains roughly constant. At low values of n_h the two cavity modes appear to overlap. c.) White-light measurements of the cavity modes from the $n_h = 6$ device shown in b.). When the cavity is excited via transmission through the waveguide, light collected from the other waveguide exhibits a transmission dip. This phenomena is predicted by the theoretical model for very low mode detuning values.

In Figure 92 a.) the effect of altering the number of holes between the two waveguides n_h on the experimentally obtained cavity mode Q-factor is seen. As is expected, reducing the number

of holes between the waveguides also reduces the measured Q-factor of the cavity modes. This is due to the increased coupling between the cavity and the waveguides. When n_h is low the cavity is in much closer proximity to the waveguides. Therefore, the cavity mode overlaps more with the waveguides increasing the coupling strength compared to when the waveguides are far away. For $n_h \geq 10$ the mean measured Q-factor saturates at a value of $Q_{mean} \approx 3050$. This implies that at values of $n_h \geq 10$ the Q-factor of the cavity is not limited by coupling losses into the waveguides. It is likely that the Q-factor is instead limited by scattering losses due to fabrication imperfections and surface absorption. At values of $n_h < 10$ the mean measured Q-factor decreases with decreasing n_h. Moreover, the detuning between the modes appears to decrease rapidly. This is where the coupling losses to the waveguide begin to dominate the Q-factor. The lowest mean Q-factor appears to occur at a value of $n_h = 6$, not the lowest value of $n_h = 4$. This may be due to the modes beginning to overlap at $n_h = 6$ and so appearing as one broad mode on the spectrum as the two individual modes cannot be resolved. As the coupling is further increased at $n_h = 4$ the modes may be even more overlapped leading to a narrower peak than for $n_h = 6$ where the detuning of the modes is larger. Furthermore, at lower values of n_h the signal to background ratio of above-cavity collection schemes is severely reduced. This makes extracting the Q-factor accurately extremely difficult and therefore will likely increase the error on the Q-factor measurements significantly. As fairly low Q-factors are required to obtain the highest device transmission, the optimal value for the number of holes between the waveguides is $8 > n_h > 4$.

Figure 92 b.) shows a set of the PL spectra from a.). The spectra for devices with equal hole radii and differing n_h are presented together for comparison. As also seen in Figure 92 a.) the Q-factor of the cavity modes can be seen to reduce for $n_h > 10$. Moreover, the detuning of the modes is also observed to reduce. While the detuning of the modes changes, the absolute position of the modes remains roughly constant, with the modes being centred around $\lambda = 933.5nm$. This shows that although the detuning of the modes is affected by n_h, the modes themselves are not shifted. As mentioned above, for $n_h > 8$ the PL peaks broaden significantly and only a single peak is visible. This could indicate that not only is the Q-factor reduced, but that the modes are overlapping.

From the theoretical model for transmission through the devices, at very low detuning, a dip in the transmission spectrum is expected at the overlap of the modes due to interference between them. This result is also reflected in the simulations of the system. To test if the modes were indeed overlapping significantly in Figure 92 b.), the $n_h = 6$ mode was measured in transmission using a broadband white light source incident on the left hand OC. The light was scattered into the waveguide and through the cavity before being collected at the right hand OC. The broadband white light source was chosen over the standard above band PL measurement to remove any QD background from the signal, specifically any single QD lines. Moreover, the white light is much

more powerful than the PL laser, allowing for the modes to be more strongly excited. The results of this transmission measurement are presented in Figure 92 c.). The white light transmission signal between the OCs (red) is plotted alongside an un-polarised white light reflectivity measurement, exciting and collecting above the cavity (blue) and the transmission through a reference waveguide - the device with the H1 cavity omitted - (grey). The device transmission clearly shows a strong dip in the signal corresponding to the wavelength of the peak of the above cavity reflectivity measurement. This confirms that the modes must be strongly overlapped. By comparing the device transmission signal shape to the results from Figure 85, the magnitude of the detuning can be estimated to be $|\Delta\lambda| \leq 0.2nm$ as the strong dip between two peaks is only seen in the $\Delta\lambda = -0.2nm$ case. Below $\Delta\lambda = -0.2nm$ the model predicts the depth of the dip to increase relative to the height of the peaks and at a detuning of $\Delta\lambda = 0nm$ the transmission dip is expected to be seen exactly between two symmetrical peaks. This is close to what is observed in Figure 92 c.). Therefore it can be concluded that the mode separation is extremely small and that reducing the value of n_h strongly affects the cavity mode detuning. Moreover, for the $n_h \geq 10$ the coupling between the cavity and waveguide no longer limits the Q-factor of the cavity. Therefore, to obtain sufficient coupling, the number of holes between the waveguides should be: $n_h \leq 8$.

6.4.3 Alternative waveguide orientation device results

The alternative waveguide configuration design was investigated next. The hope of this design was to increase the amount of background transmission rejected between the OCs, increasing the signal to background ratio whilst not affecting the operation of the devices. The effect of changing the PhC lattice mismatch on the mode detuning was first investigated. This was done to observe any differences in the device behaviour with this new waveguide orientation. Figure 93 shows the results from this study for both the devices with 5 air holes separating the waveguide(a.) and b.)) and the devices with 3 air holes separating the waveguides (c.) and d.)). Figure 93 a.) shows the relationship between the PhC lattice mismatch Δa and the mode detuning $\Delta\lambda$ for the 5 hole separated waveguide devices. A linear fit of the experimental data obtains a value for the gradient of: $\frac{d\Delta\lambda}{d\Delta a} = 1.191 \pm 0.116$. This value is comparable with the values obtained for the simulations of the regular waveguide orientation devices and the experimental result from the uncoupled H1 cavities as all three of the values fall within the error range of each other. However, the intercept of the linear fit in Figure 93 a.) is lower than the intercept of the uncoupled H1 fit, -6.728 compared to -5.405. Moreover, the intercept is extremely similar to the intercept acquired from the fit to the simulation data for the regular waveguide orientation devices, -6.664. This indicates that the introduction of any waveguide coupling shifts the offset of the detuning relationship down by a consistent amount. Figure 93 b.) shows some of the spectra used in a.) from the $r = 64nm$ devices. It is clear that these spectra are much more difficult to understand than spectra from both the uncoupled H1 cavities and the regular waveguide orientation devices. This is due to the many additional mode-like features present in the PL spectra. These are likely caused by localised

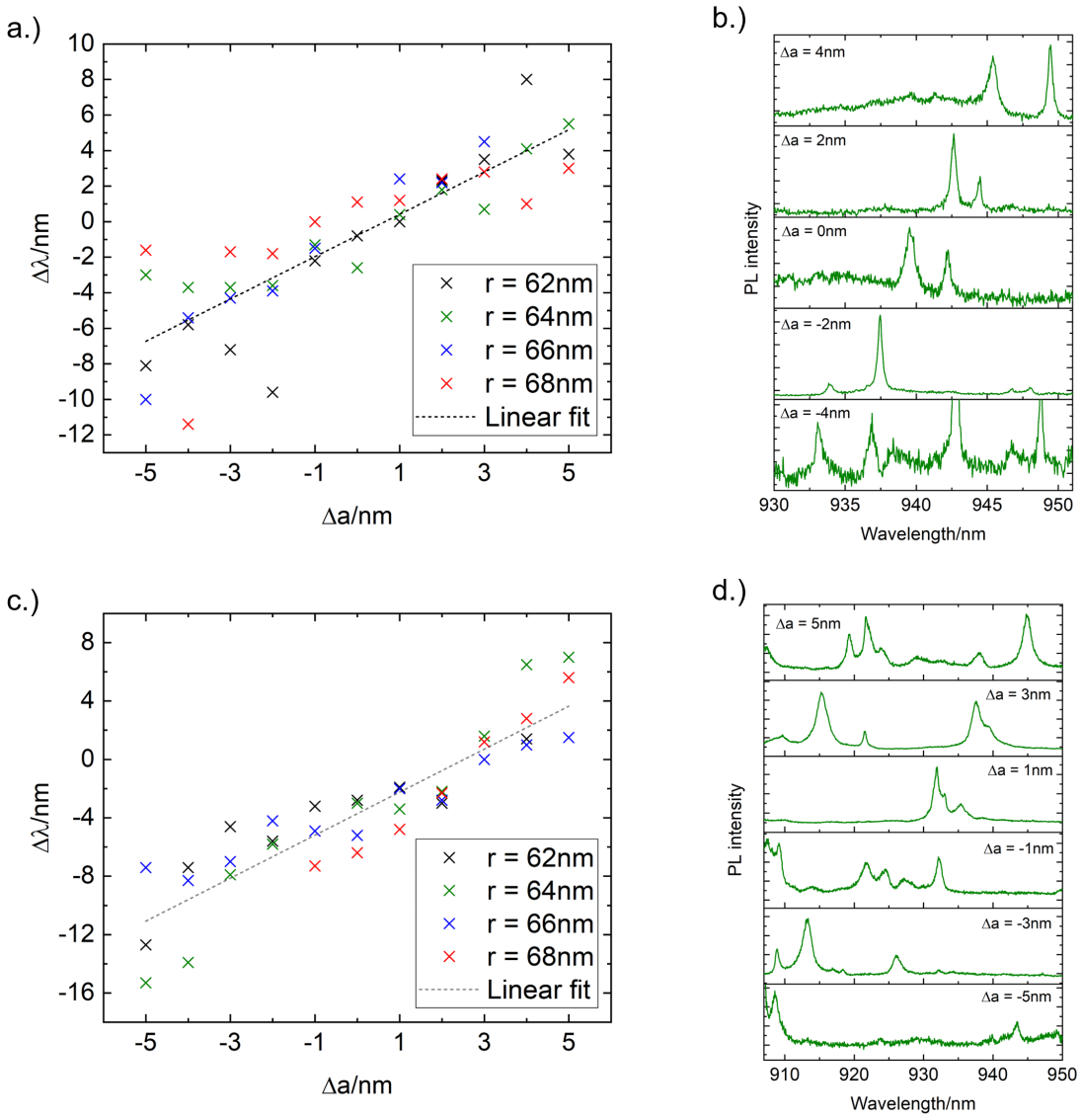

Figure 93: Results from the investigation on the alternate waveguide orientation devices. The effect of changing Δa on the detuning $\Delta\lambda$ was studied. a.) & b.) Show results from the devices with 5 air holes between the waveguides and c.) & d.) Show the results for devices with 3 holes between the waveguides. a.) & c.) Show the dependence of the detuning on the PhC lattice mismatch. b.) and d.) Show some of the $r = 64nm$ spectra from each of the dependences.

modes in the PhC. As these are largely not present in the regular waveguide orientation devices, it would suggest that the alternate waveguide arrangement increases the likelihood of these extra features appearing in the spectra. This may be due to modes forming in the small gap between the waveguides as they run parallel for a large number of unit cells.

Figure 93 c.) shows the relationship between the PhC lattice mismatch Δa and the mode detuning $\Delta\lambda$ for the 3 hole separated waveguide devices. From a linear fit to the data, the rate of change of detuning with respect to lattice mismatch is $\frac{d\Delta\lambda}{d\Delta a} = 1.473 \pm 0.111$ with an intercept of -11.080. This gradient is the steepest of any device set and does not overlap within the error of the 5 hole alternate waveguide orientation devices, despite overlapping within the error of the other two devices. This suggests that reducing the spacing between the waveguides in this orientation alters the rate of detuning change when shifting the PhC lattice orthogonal to the waveguide. Moreover, the intercept for the 3 hole alternate waveguide orientation device is nearly two times lower than the next lowest device set. From Figure 93 d.) some examples of the PL spectra used to calculate the mode detuning for c.) are presented. As with the spectra shown in b.), many additional peaks exist alongside the cavity mode peaks. This makes reading the graph and identifying the cavity modes extremely challenging. Only by following the trend across several graphs is it possible to identify with confidence which features are the cavity modes. Figure 94 shows results from measurements

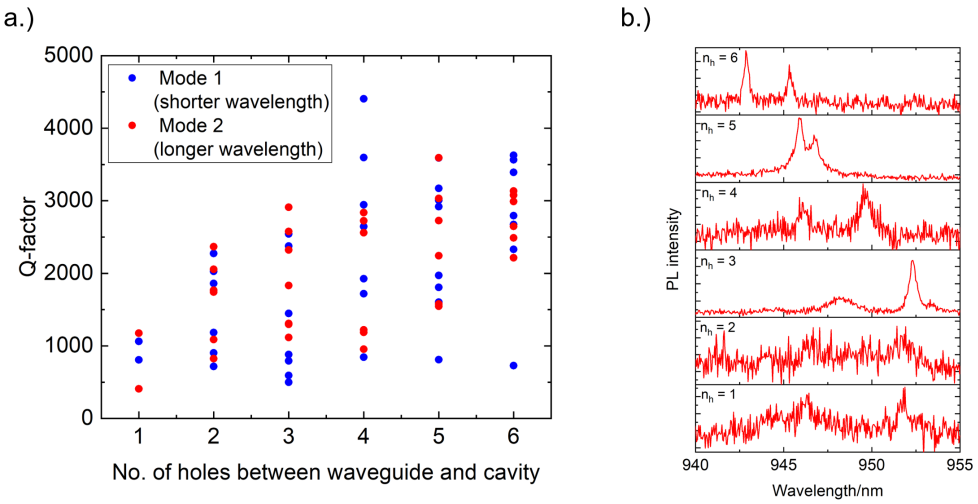

Figure 94: Graphs showing the results from alternate waveguide orientation devices with 3 rows of holes between the waveguides and varied numbers of holes between the cavity and the waveguides. a.) Shows the effect of increasing the number of holes between the cavity and the waveguides on the Q-factor of the cavity modes. b.) Shows some PL spectra from a.) for each number of holes between the cavity and waveguide.

of alternate waveguide orientation devices with varying numbers of holes between the end of the waveguides and the cavity. In these devices, the number of rows of holes between the waveguides is kept constant at 3 rows. From Figure 94 a.) a similar trend to the results from the equivalent regular waveguide orientation devices in Figure 92 is observed. The Q-factor of the devices reduces as

the number of holes between the waveguides and the cavity is reduced. This is due to the increased coupling strength of the cavity to the waveguides caused by an increase in the mode overlap. At one hole between the cavity and waveguides, very few cavity modes were measured. Figure 94 b.) shows the spectra of one of the modes measured for the lowest separation. The modes are barely visible above the background. As the Q-factor of the modes is likely extremely low, the strength of the signal when collecting from above the cavity will be weak, as most of the light will couple into the waveguides and not be scattered up. Therefore, it is highly likely that the measured Q-factors for the devices with one hole between the waveguides and cavities are much lower than what is shown in Figure 94 a.). Figure 94 b.) shows that the modes blue-shift slightly as the number of holes between the waveguides and the cavity increases. This trend is not seen in Figure 92 and therefore is likely an effect unique to this waveguide orientation. The spread of cavity Q-factors is much broader for the alternate waveguide orientation devices than for the regular waveguide orientation devices. This is likely due to the lower signal to background ratio and larger number of non-cavity related peaks in the spectra for the alternate designs when compared to the regular design. Overall, the designs behave similarly although the regular design is easier to measure at higher coupling strengths.

6.4.4 Transmission comparison between waveguide orientation designs

As the alternate waveguide orientation devices were designed to reduce unwanted scatter in the transmission spectra, the transmission through these devices should be compared to that of the regular design. Unfortunately, due to the critical point drying error, most of the alternative design structures either have one or both nanobeams collapsed. This makes it impossible to measure the transmission through these structures. As only a very small number of devices survived, comparisons of individual devices must be drawn rather than the entire ensemble of devices. Figure 95 a.) shows the extent of the damage to the alternate waveguide orientation devices caused by the critical point drying failure. Nearly all of the devices have at least one of the nanobeam waveguides broken. Because of this, transmission measurements cannot be completed on these structures. This severely limits the scope of the comparison that can be made between these devices and the regular waveguide orientation devices in transmission. Figure 95 b.) and c.) show typical transmission spectra of the regular and alternate waveguide orientations. Both graphs show the transmission through the structure when using the white light laser to directly probe the structure using a broadband source, and when using a high power HeNe laser to excite PL from QDs in the outcouplers to probe the devices. When comparing b.) and c.) it is clear that not only is the intensity of the transmission higher for both the white light and HeNe excitation in the regular device, but also the spectra are much clearer with fewer non-cavity features. It is practically impossible to discern which peaks are related to the cavity in Figure 95 b.) whereas in c.) the cavity modes are clearly the only bright, broad features in the spectrum. Therefore, although the alternate waveguide orientation design reduces the overall transmission between the waveguides, the regular waveguide transmission design

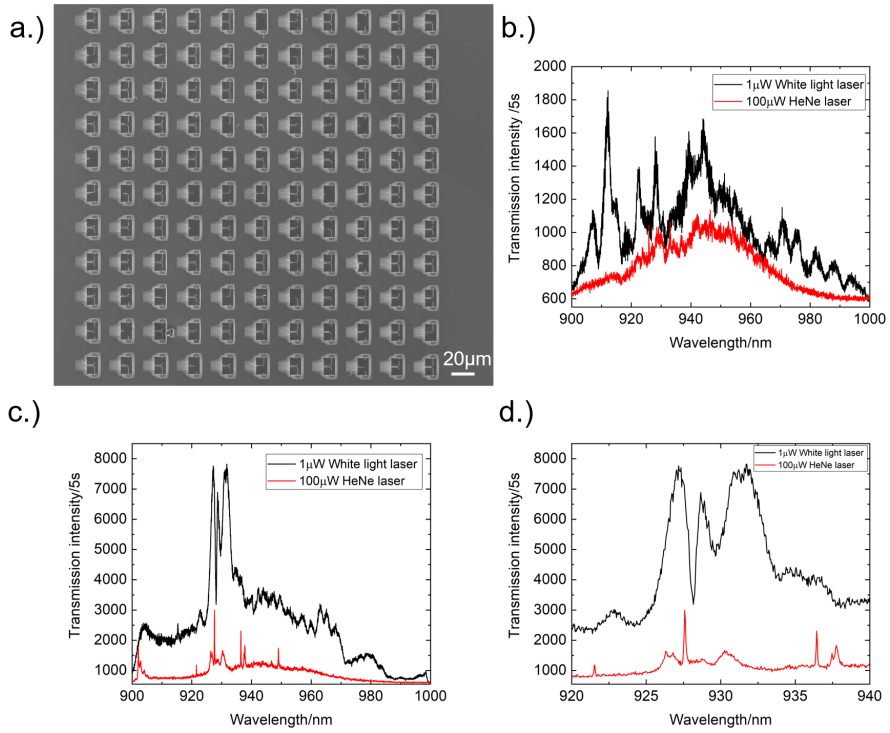

Figure 95: a.) SEM image of an array of alternate waveguide orientation devices. Most of the devices have either one or both nanobeam waveguides collapsed, making it impossible to conduct transmission measurements on them. b.) Graph comparing the transmission spectra when exciting with a white light laser and a HeNe laser for an alternate waveguide orientation device. c.) Graph comparing the transmission spectra when exciting with a white light laser and a HeNe laser for a regular waveguide orientation device. d.) Zoom-in on the cavity modes in graph c.) to more clearly see the sharp transmission dip in the cavity modes which coincides with the spectral location of a QD.

still exhibits the highest visibility of the cavity modes in transmission.

Studying Figure 95 c.) in more detail, a sharp transmission dip can be seen between the two cavity modes in the white light measurement. This dip cannot be related to interference between the modes as seen in Figure 85 and Figure 92 as the mode detuning is large. Both modes can be seen independently of each other with the sharp dip coming on the long wavelength side of the shorter wavelength mode. This can be more clearly seen in Figure 95 d.). The dip seen in the white light measurement signal appears to coincide with the wavelength of a QD line in the HeNe measurement signal. This suggests that it is the presence of the QD that causes the white light transmission to be strongly modulated at this wavelength. This dip is similar to the results from

the transmission model shown in Figure 86. This further suggests that this transmission dip is caused by the presence of the QD in the cavity. However, the fact that the transmission dip only occurs for the white light measurement and not for the HeNe measurement could indicate the effect is more complicated, as a dip in both measurements would likely be expected. Further investigation on this phenomenon is required, as the cause of this transmission dip is not sufficiently understood.

6.4.5 Magnetic field dependence of QD in a waveguide coupled H1 cavity

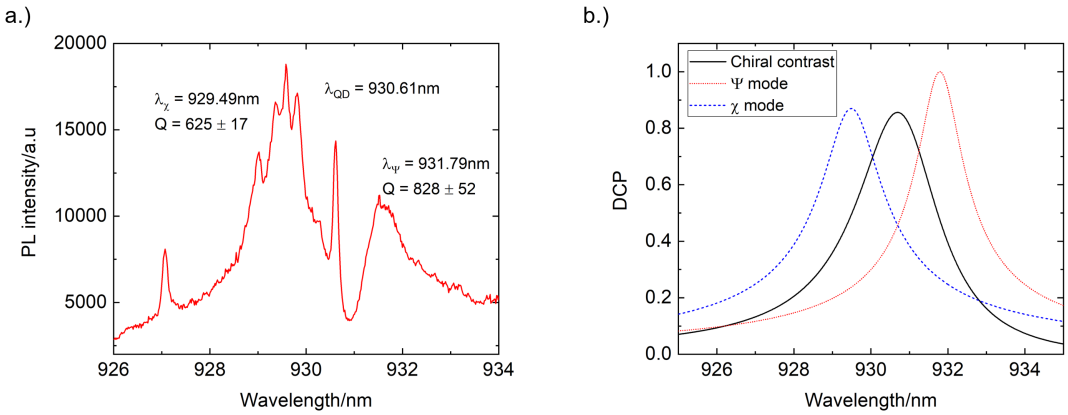

Figure 96: a.) PL spectrum of a regular waveguide orientation device with a QD in the cavity. The spectrum was obtained by exciting and collecting from above the cavity with a 350μW quasi-resonant TiS laser at 880nm. The two cavity modes have wavelengths of $\lambda_\chi = 929.49nm$ and $\lambda_\Psi = 931.79nm$. A QD located in the cavity region of the device has a wavelength of $\lambda_{QD} = 930.61nm$ between the two cavity modes. b.) Shows the expected wavelength dependence of the chiral contrast from the experimentally measured cavity parameters. At the QD wavelength a maximum chiral contrast of 0.852 is expected. The maximum chiral contrast of the device is 0.856 at $\lambda = 930.70nm$

After all the devices were characterised, the regular waveguide orientation devices were decided upon as the superior design. The sample was loaded into a bath cryostat with a superconducting magnet. When a magnetic field is applied to QD the degeneracy of the fine structure states is lifted and the transitions become circularly polarised (see Section 2.3.2). This produces two circularly polarised transitions with opposite handedness which are separated by the magnitude of the fine structure splitting. By increasing the magnitude of the applied magnetic field the splitting of the two transitions is increased. These circularly polarised transitions will couple asymmetrically to the two waveguides if the wavelength of the transition is between the modes.

Low power (3μW) PL measurements with a HeNe laser were used to characterise the cavities

and see which had QDs at wavelengths between the cavity mode wavelengths in the cavity centre. For any candidate devices, the maximum chiral contrast of the QD was calculated from the theory. If a QD had a potential chiral contrast > 0.8 then it was selected for a magnetic field dependence measurement. One such device was identified, the high power (350μW) mode spectrum of which is shown in Figure 96 a.). As can be seen from the figure, the QD at $\lambda_{QD} = 930.61nm$ is situated between the two cavity modes. Whilst the polarisation of the modes is not known, the χ mode is denoted as the shorter wavelength mode. The χ mode has a central wavelength of $\lambda_\chi = 929.49nm$ and a Q-factor of $Q_\chi = 625 \pm 17$. The longer wavelength Ψ mode has a central wavelength of $\lambda_\Psi = 931.79nm$ and a Q-factor of $Q_\Psi = 828 \pm 52$. These cavity mode parameters were obtained by fitting the spectrum in Figure 96 a.) with two simultaneous Lorentzian peaks. These parameters were input into the equation used in Figure 83 a.) to obtain the theoretical wavelength-dependant maximal chiral contrast for these modes which is plotted in Figure 96 b.). At the QD wavelength ($\lambda_{QD} = 930.61nm$ the maximum chiral contrast is 0.852 which is very close to the maximum of the entire distribution, 0.856 at $\lambda = 930.70nm$. From this the chiral contrast observed from the device has the potential to be extremely high. As the QD is located between the modes, the Purcell factor that the QD experiences will not be the maximum of the device. However, it should still experience a small Purcell factor from the tails of both modes.

A magnetic field dependence measurement was conducted on the candidate QD. This measurement aimed to observe chiral behaviour of the QD emission. To measure the chirality of the QD the emission into both waveguides must be measured and compared. If the QD had a chirality of 1.0 then each of the circularly polarised transitions would couple to only one of the waveguides each. Therefore, the signals from opposite OCs would be asymmetric. If no chirality is present then the output of the two OCs should be identical. The QD was directly excited from above with a quasi-resonant TiS laser operating at 862nm. This excites the QDs through the wetting layer. The laser power was adjusted to maximise the brightness of the QD over the background, a power of 18μW was chosen. The magnetic field that was applied to the sample was varied to alter the splitting between the two QD transitions. The signal from the OCs was recorded at 1T intervals over a range of $-5T \leq B \leq 5T$. The signals from both the left and right OCs are plotted together in Figure 97 b.) for comparison.

From Figure 97 b.) the splitting of the QD fine structure states can be seen. At a magnetic field of B = -5T, the signal from both OCs is extremely similar. This indicates that no or very little chirality is present in the system. From Equation 33 the chiral contrast in experiment is calculated by:

$$C = \frac{I_R - I_L}{I_R + I_L}$$

At B = -5T, the chiral contrast of the QD transitions is found to be $C_S = -0.21$ and $C_L = 0.09$ for the short ($\lambda_s = 930.22nm$) and long ($\lambda_l = 930.89nm$) wavelength transitions, respectively. How-

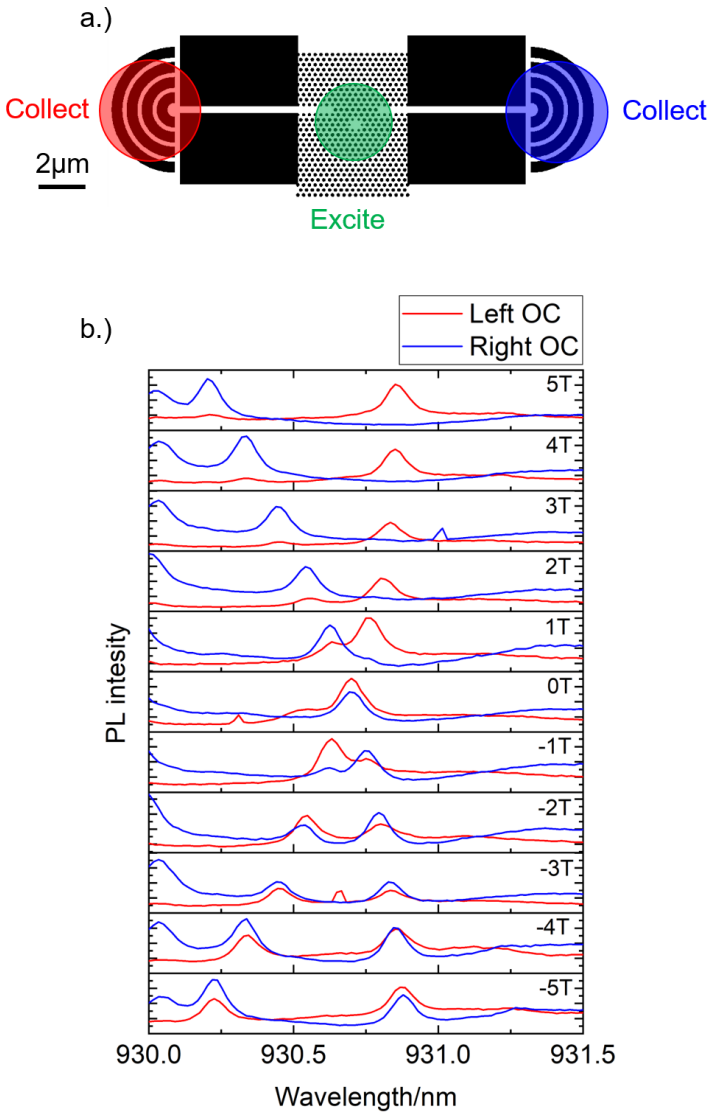

Figure 97: a.) Schematic of the measurement scheme for the magnetic field dependence measurement in b.). The QD in the cavity was excited via quasi-resonant excitation at 862nm. The resulting light scattered out of each OC was collected separately. b.) Shows a comparison between the spectra obtained from the left (red) OC and the right (blue) OC for different values of the magnetic field strength. The QD splits into two circularly polarised transitions at non-zero magnetic field. At B = -5T the chiral contrast of the two QD transitions is extremely low. However, as the strength of the magnetic field increases, the chiral contrast between the left and right OCs appears to increase. At B = 5T, extremely strong chirality is observed as each transition can only be seen from opposite OCs.

ever, when the magnetic field is increased through to 5T the chiral contrast increases dramatically. At B = 5T, the chiral contrast of the QD transitions is found to be $C_S = -0.53$ and $C_L = 0.77$. This is vastly different to the case at -5T despite the transitions having the same wavelengths at 5 and -5T. As the chiral contrast is wavelength-dependent, there should therefore be no difference in the chiral contrast between 5T and -5T. From the dependence in Figure 96 b.) the expected chiral contrast for the two transitions at ± 5T is $C_S = 0.76$ and $C_L = 0.84$ for the short ($\lambda_s = 930.22nm$) and long ($\lambda_l = 930.89nm$) wavelength transitions, respectively. The theoretical maximum chiral contrast for the transitions is much higher than the measured values for the -5T case, however, the 5T case is much closer to these values. This indicates 5T, the device behaves as expected whereas

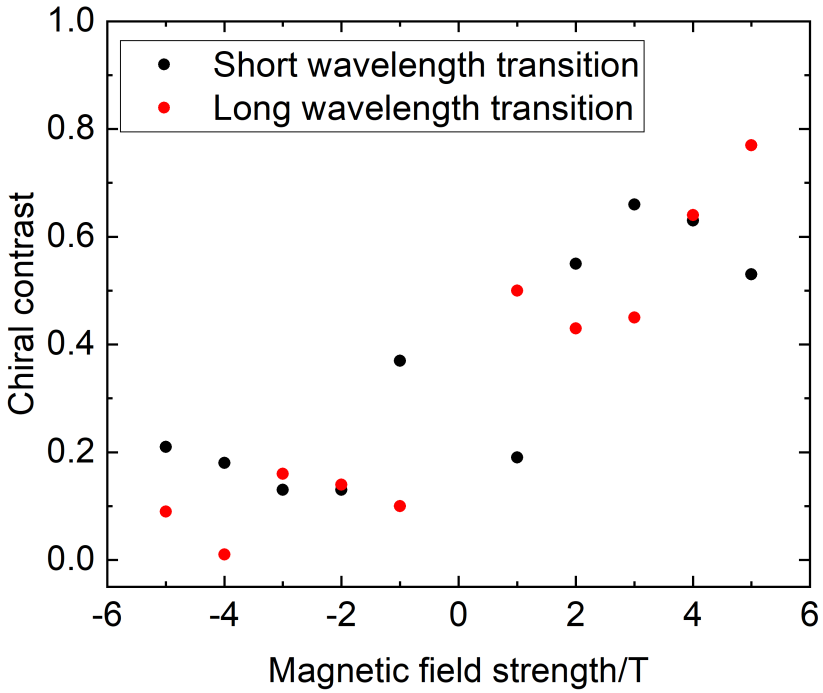

Figure 98: Graph showing the relationship between the experimentally measured chiral contrast and the magnetic field strength for the QD measured in Figure 97.

at -5T an unexpected effect is observed.

Figure 98 shows the magnetic field dependence on the chiral contrast of the two QD transitions from Figure 97 b.). A discontinuity between positive and negative magnetic fields is seen. At negative fields the observed chiral contrast is consistently below 0.25 for all but one data point. Conversely, for positive magnetic fields all but one of the data points are above 0.4. Moreover, at positive field values the chiral contrast appears to increase with increasing field strength. This asymmetry in the magnetic field dependence of the chiral contrast is not explained by the theory or

the wavelength dependence of the chiral contrast. One possible explanation could be an apparent increase/ decrease in chiral contrast due to the changing Purcell factor experienced by the QD transitions as they shift in wavelength. If one transition experiences an increase in Purcell factor while the other experiences a reduction, the relative intensities of the transitions will change. This could be mistaken for a change in chiral contrast. This effect however, will be small for the device measured as both the Q-factors of the cavity modes and the tuning of the QD transitions are low. As such there will be a minimal change in the relative Purcell factors of the transitions although there will be a small effect due to this. Moreover, if the wavelength dependence of the chiral coupling in Figure 96 b.) is considered, the difference in maximum chiral contrast between the two QD states at the largest splitting is very small. Therefore, this effect cannot be explained by the chiral coupling wavelength dependence. Between positive and negative fields, the only change in the operation of the device is which spin transition couples to which waveguide. This is seen from Equation 9 where the magnitude of the splitting between the states is dependent on the strength of the magnetic field. It is possible therefore, that the waveguides do not couple both transitions equally as they should. Fabrication errors could cause one or more of the field components of the two modes to couple weakly to the waveguide. If this is the case, the interference between the cavity modes in the waveguide region would be minimal and so only a very weak chiral effect would be observed. As all four mode profiles (as shown in Figure 82) have different distributions in the waveguide regions, it is highly likely that any fabrication imperfections would not affect the coupling of each mode's polarisation states equally. Therefore, it is possible that the interference between the mode components is only seen for one of the circular polarisations and not the other. The results from Figure 98 seem to suggest that there is no correlation of the chiral contrast and magnetic field at negative magnetic fields, whereas at positive field, a linear correlation is seen. This suggests that there is no effect present at negative fields, instead, any chirality measured is a result of intensity mismatch from background light or Purcell enhancement. Ultimately, this effect is not well understood and will require further investigation.

Despite the unexpected asymmetry of the chiral contrast at negative field values, the device did indeed exhibit a high chiral contrast of a QD embedded in the cavity of $C = 0.77$ at B = 5T. State-of-the-art values for the chiral contrast can be as high as $C \sim 0.9$ in both NBW [85] and PhC waveguide devices [103] with the latter giving the potential for light-matter enhancement.

6.4.6 Lifetime measurements of QD in a waveguide coupled H1 cavity

Having measured a strongly chiral QD in a waveguide coupled H1 device, the next step was to quantify the Purcell enhancement experienced by the QD. When a QD is Purcell enhanced, the lifetime of the excitonic state in the QD is decreased due to the increase in light-matter interaction enhancing the rate of emission into the cavity. Therefore, if the lifetime of the QD is measured to be significantly shorter than comparable QDs on the sample, the QD is likely Purcell enhanced.

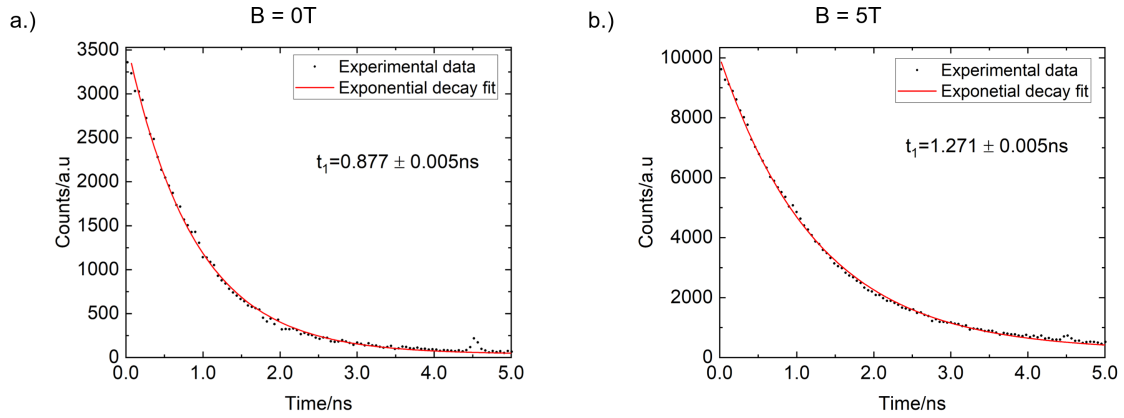

Figure 99: Lifetime measurements for the QD studied in Section 6.4.5 at a.) B = 0T and b.) B = 5T. The lifetime is calculated to be $t_1 = 0.877 \pm 0.005ns$ at B = 0T and $t_1 = 1.271 \pm 0.005ns$ at B = 5T.

The ratio between the enhanced QD and a known un-enhanced QD can be used to estimate the magnitude of the Purcell factor. Figure 99 shows measurements of the lifetime of the QD at both B = 0T and B = 5T where the QD was most chiral. The measurement was conducted by exciting the QD using a fast, tunable, pulsed laser source operating at 862nm. The pulsed source excites charge carriers to an excited state in the QD. These charge carriers then relax after some random time and emit a photon. By measuring a time-dependant intensity spectrum of the QD emission, an exponential curve can be fitted to the data to obtain a value of t_1. The spectrum from the QD was passed through a very narrow optical filter to remove as much background as possible. The light was incident on a set of superconducting nanowire detectors which recorded the time of arrival of each photon within a 15ps response time. Figure 99 a.) shows the result of the lifetime measurement at B = 0T. A value of $t_1 = 0.877 \pm 0.005ns$ is obtained. At B = 5T, the value of $t_1 = 1.271 \pm 0.005ns$. This value is significantly larger than at B = 0T showing a change in the Purcell factor of the QD has occurred. This is expected as the wavelengths of the QD in the two lifetime measurements is different ($\lambda = 930.61nm$ at B =0T and $\lambda = 930.85nm$ at B = 5T).

The lifetimes, although different, do not look fast enough to indicate a Purcell enhanced QD. Therefore, before any Purcell factor is calculated, the ensemble lifetime must be measured so the lifetimes calculated for the QD in Figure 99 can be compared to the lifetime expected from an un-enhanced QD on the sample. Figure 100 shows the measured QD ensemble lifetime. The data for the lifetime were obtained using an avalanche photodiode with a response time of $\approx 400ps$. This was done as the precision of the nanowire detectors was superfluous for the long lifetimes expected from this measurement. A value of $t_1 = 1.104 \pm 0.008ns$ is obtained for the QD ensemble lifetime.

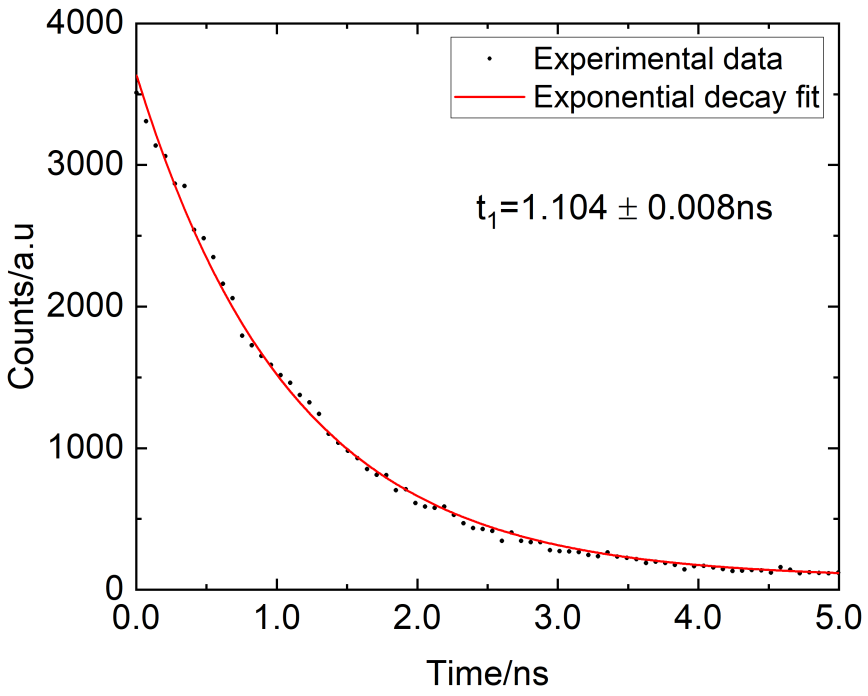

Figure 100: Lifetime measurement for the QD ensemble in the bulk GaAs crystal at B = 0T. The ensemble lifetime is calculated to be $t_1 = 1.104 \pm 0.008ns$.

This lifetime measurement is shorter than the measured lifetime of the QD in the cavity from Figure 99 b.), where the QD was held at B = 5T. This suggests that the QD does not experience any Purcell enhancement at B = 5T, and only a very small enhancement at B = 0T. The QD therefore, must be located in an area of the cavity which does not provide a large Purcell enhancement. The Purcell enhancement of the QD measured in Figure 99 can now be estimated. By taking the ratio between the QD and ensemble lifetimes, the Purcell factor is calculated to be $F_P = 1.259 \pm 0.012$ at B = 0T. The difference in Purcell factor between the B = 0T and B = 5T case can be understood by considering the wavelength dependence of the Purcell factor. At B = 5T the QD transition has a wavelength of $\lambda = 930.85nm$, this is closer to the crossing point between the modes than at B = 0T where $\lambda = 930.61nm$. Therefore, the QD should experience less of an enhancement from the cavity as the transition is less overlapped with the cavity mode. The measured Purcell factor of the QD is very low. However, as this is a test sample, and the devices are not optimised, this is to be expected. Furthermore, the position of the QD in the cavity has a large impact on the Purcell factor, if the QD is not positioned near the centre of the cavity then the expected Purcell factor drops off rapidly. This result shows the potential of waveguide coupled H1 cavities as a system where both strong chirality and Purcell enhancement can be achieved.

6.5 Conclusions and future work

The experimental observation of strong chiral contrast and Purcell enhancement of a QD in a waveguide coupled H1 cavity system is presented here. A QD with a strong chiral contrast $C = 0.77$ and small Purcell enhancement of $F_P = 1.259 \pm 0.012$ at B = 0T is observed. The QD exhibits asymmetrical chiral contrast between positive and negative magnetic fields, a phenomenon which is unexplained by the theory. The origin of this phenomenon is still unknown currently, however, it may be caused by asymmetric coupling of the two QD transitions to each waveguide. Strong agreement between experiment, simulation and theory was observed for the rate of mode shift with lattice stretching for all of the different device designs. A characteristic transmission dip was observed in a device with very small mode detuning, an effect predicted in both simulations and the theoretical transmission model. Between the characterisation of the devices and calculated optimal mode splitting, the designs of the devices for the next sample were decided upon.

The next steps for this work are for a new sample to be fabricated with a focus on the most successful devices measured in this work. Regular waveguide orientation devices will be fabricated with 6 or 8 holes between the waveguides. Moreover, the sample will be fabricated with electrical diodes to allow tuning of the QD energies. This will allow QDs to be tuned to a wavelength which will show a higher chiral contrast and the optimisation of the wavelengths of the Zeeman split QD transitions at non-zero magnetic field. This will also allow for the investigation of the wavelength dependence of chirality more thoroughly as the QD magnetic field tuning can be reversed by the electrical tuning, eliminating wavelength dependence as a variable. Furthermore, to adjust the detuning of the cavity modes, the sample will be mounted in a uni-axial strain tuning mount. Such a mount will allow a small strain field to be applied in one PhC axis. As has been previously demonstrated [118] this allows for the detuning between the cavity modes to be adjusted by altering the PhC lattice constant in one direction. As seen in Figure 91 this strain field will also shift the wavelength of the cavity modes. The combination of electrical and strain tuning in the system will lead to a much higher order of control over the system parameters. Combined with an optimised design, these tuning methods will allow for the devices to exhibit near unity chiral contrast with QDs that can be easily tuned to the wavelength which gives the maximal Purcell enhancement and chirality.

This page intentionally left blank.

7 Summary and outlook

7.1 Summary

The conclusions from each experimental chapter will be summarised here. Overall, the work in this thesis has shown the potential of III-V semiconductor-based nano-photonic systems as an architecture for a quantum network.

In Chapter 1, a general introduction to the field of QIP and the role of III-V semiconductors within that field was presented. The concept of a quantum network is outlined as the long-term goal of these systems.

Chapter 2 gave a detailed overview of the relevant background physics pertaining to the work in this thesis. This included the properties of SKQDs and nano-photonic structures which were studied extensively in this work.

The experimental and computational methods use in this thesis were presented in Chapter 3. The process by which the samples measured in this thesis were fabricated was also discussed.

7.1.1 Chapter 4

In Chapter 4, the growth of SCQDs was investigated. The length of the growth interrupt was altered between 15 - 300s. It was found that longer growth interrupt times improved the single QD nanohole occupancy rate and shifted the ensemble mean emission wavelength towards longer wavelengths. It was also found that larger nanohole array pitches provided superior single QD nanohole occupancy. Following this, an *in-situ* local QD emission energy strain tuning method was tested. The technique had only recently been demonstrated by J. Grim et al. [81], therefore, the tuning mechanism was not well understood. The effect of altering the heating laser power and cumulative exposure time on the magnitude of the QD energy shift was investigated. Long range tuning of a QD of up to 5.06nm in a NBW, and 3.59nm in a PhC waveguide were seen. This tuning method was used to tune two pairs of QDs into resonance over a short ($\Delta\lambda = 0.14$nm) and long ($\Delta\lambda = 0.72$nm) spectral range. This chapter demonstrated the potential of combining SCQDs with the powerful local strain tuning method for scale-up of resonant QDs in a nano-photonic device.

7.1.2 Chapter 5

In Chapter 5 a scheme for an electro-mechanically tunable 1D PhCC was presented. The design featured a 1D PhCC perturbed by a 1D PhC in a NBW attached to the end of a cantilever device. By actuating the cantilever via a capacitive effect between the membrane and the substrate of the device, the cavity mode wavelength of the 1D PhCC could be controllably tuned. The design of the

1D PhCC was optimised in FDTD simulations through rigorous and extensive parameter sweeps, covering the entire parameter space. The robustness of the design against fabrication imperfections was also tested in simulation using a Monte Carlo method approach. This process was repeated for optimisations of the perturbing beam. Two 1D PhCC test samples were fabricated to determine the optimal experimental parameter set. A cavity design was chosen that exhibited a very small cavity mode wavelength distribution for like devices ($\sigma_\lambda = 0.6$nm). Finally, the full structures were fabricated and a controllable cavity tuning of up to 1nm was demonstrated. The experimental measurements agreed well with the results from the simulations. From the results, an estimated 76% of like cavities could be brought into resonance. This chapter demonstrated the potential of this tunable cavity scheme for scale-up of the number of resonant cavities on-chip.

7.1.3 Chapter 6

In Chapter 6 a design for a waveguide coupled H1 PhCC was presented. The design, first proposed by D. Hallett et al. [189], is capable of enabling an embedded emitter to experience both a high Purcell factor and near unity directionality, simultaneously. The design is highly robust to emitter position within the cavity, a key advantage over competing systems. A model of the transmission properties of the system was presented and compared to FDTD simulations. Characterisation results from a test sample of the proposed structures were presented and analysed to determine the optimal experimental design. These results were compared to the results from the theoretical model and the simulations. Finally, a magnetic field dependence measurement on a QD in a waveguide coupled H1 cavity was conducted. The QD exhibited a maximum chiral contrast of $C = 0.77$ at B = 5T. The QD did not exhibit any Purcell enhancement at B = 5T. At B = 0T the QD exhibited a small Purcell enhancement of $F_P = 1.40$. This chapter demonstrated the potential of waveguide coupled H1 cavities for the realisation of simultaneous high Purcell factor and strongly directional emission from a QD.

7.2 Outlook

This section will detail any future work which is planned to follow-on from the results obtained in this work. As much of the work in this thesis was conducted on test samples, improvements to the samples and device design will be a key part of this section.

7.2.1 Chapter 4 further work

The aim of the work in Chapter 4 was to build towards a combination of the SCQD work and the strain tuning work as a joint system. For this overarching goal to be achieved, more work is required on each individual system before combining the two.

Integration of SCQDs into waveguide compatible wafers is the main focus of the SCQD side of

this work. Free-standing nano-photonic structures are the standard for device design in III-V semiconductor systems. Moreover, the strain tuning method presented in Chapter 4 requires the QDs to be located in a free-standing waveguide. While there is no fundamental reason preventing the growth of SCQD in waveguide-ready semiconductor wafers, the difficulty lies in keeping the thickness of the membrane low, while obtaining narrow linewidth QDs [196, 197]. The problem lies in reducing the effect of charge noise from the regrowth interface on the QDs. This could be reduced without increasing the buffer by further improving the cleaning process between the nanohole etch and buffer growth. Moreover, this would lead to an improvement in the optical properties of the QDs by reducing the mean linewidth of the distribution.

For the strain tuning work, fabrication of a new sample with electrical control would be the next step in the process. This would allow for the stabilisation of the QD charge states during the tuning process. Moreover, electrical tuning of the QDs could be used to make fine adjustments to the tuning process. The addition of electrical control requires the fabrication of diodes. A standard diode structure, where the contact pads are located close to the devices, is not suitable for use with ALD coated samples. When the samples are coated via ALD, the contact pads would also be covered, rendering them unusable. To avoid this, the contact pads must be moved away from the devices so that the can be covered during the ALD process, without effecting the devices. Figure 101 shows

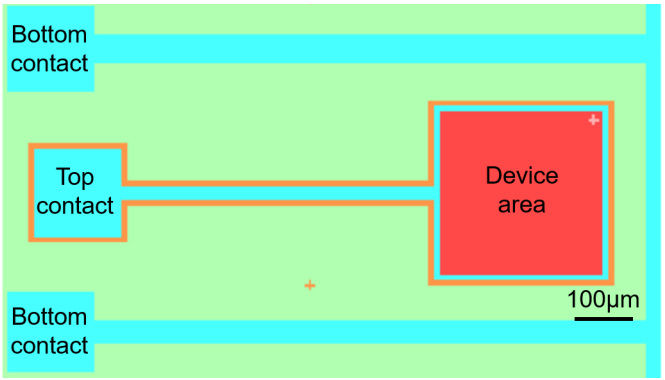

Figure 101: Schematic of a proposed diode design to be used for the next ALD deposition strain tuning sample. The red area is where the devices are to be fabricated. The orange area defines the diode mesa. The blue area defines the metallised contacts.

a schematic of a proposed design for an ALD compatible diode structure. The contact pads are located over 500μm from the device area. This separation provides ample room for the contacts to be shielded from the ALD process, while not affecting the devices. In addition to electrical tuning, the next sample will include more complex nano-photonic devices. '*Multi-mode interferometers*' (MMIs) with SEG OCs, and topological waveguides will be included. By tuning two QDs into resonance in the inputs of a MMI, an on-chip Hong-Ou-Mandel measurement could be conducted.

7.2.2 Chapter 5 further work

The work conducted in Chapter 5 clearly paves the way for the scale-up of the number of resonant cavities on-chip. For the cavities to interact with each other, they must be coupled to a shared waveguide. It has been shown that a chain of three resonant coupled cavities can produce

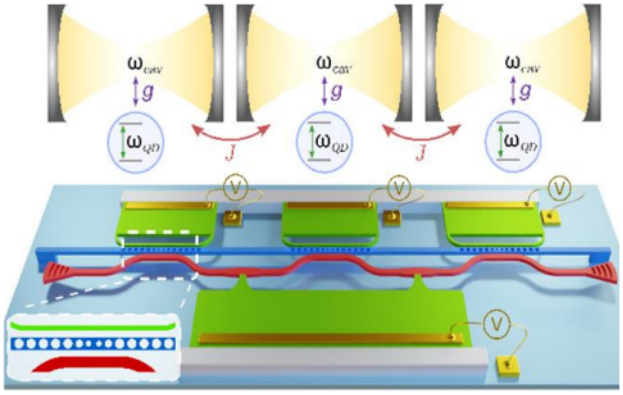

Figure 102: Schematic showing the proposed design for three tunable cavities connected by a waveguide which can be actuated to alter the coupling strength. Three tunable 1D PhCCs are connected via a bus waveguide, which can be actuated to alter the coupling strength between the cavities.

many-photon entangled states [165]. Figure 102 shows a schematic of a proposed design to achieve this entanglement generation. Three cantilever tunable cavities are connected via a side-coupled NBW terminated by SEG OCs. The cavities can be tuned independently of each other. Moreover, the waveguide can be actuated to adjust the coupling strength. By controlling the spatial and momentum-space overlap of the cavity and waveguide modes, side-coupling of a NBW to a 1D PhCC has been shown to provide highly efficient coupling with minimal Q-factor degradation [182].

In addition to the cavity-cavity coupling potential of this tunable cavity scheme, these devices could also be used to tune a QD and a cavity into resonance. The sample measured in this work did not exhibit any QD emission in the free-standing membranes. Therefore, a new sample must be fabricated in which the QDs emit in the free-standing membranes. The sample measured in this work contained AlAs barriers. These barriers were potentially etched away by the extended HF etch required to fully under-etch the large cantilever structures. By choosing a wafer without aluminium based barriers, the membranes should contain QDs which show emission. Therefore, attempts to tune QDs into resonance with cavities can be made. The ultimate goal of this device is to tune multiple sets of cavities and QDs into resonance. The Q-factor of the cavities measured in Chapter 5 were much lower than in simulation. This Q-factor drop cannot entirely be down to fabrication imperfections, as from the Monte Carlo simulations, the minimum Q-factor was more than an order of magnitude higher than the highest experimentally measured Q-factor. The limiting

factor on the Q-factor of the cavities is likely surface absorptions. Passivation of the sample surface has been shown to improve the mean Q-factor of cavities compared to an unpassivated sample [120]. Moreover, the wavelength distribution of cavities is reduced. Any new sample fabricated will also be surface-passivated to improve the cavity performance.

7.2.3 Chapter 6 further work

The results from Chapter 6 show the potential of the waveguide coupled H1 cavity design as a system where a QD can experience both a high Purcell enhancement and strong directionality. As the sample measured in this work was a test sample, the number of optimal devices on the sample is low. The sample also lacked electrical control. The next step in this work would be to fabricate a new sample with electrical contact, and a more optimised cavity design. This would increase the chance of cavities which contain QDs close to the cavity mode wavelength being measurable, as the QDs could be electrically tuned to a wavelength where a higher chiral contrast and Purcell factor are expected. Moreover, by mounting the sample on a piezoelectric strain mount, the detuning of the cavity modes could be controlled [118]. This would allow for a further degree of control over the sample, increasing the chance of measuring a QD with high Purcell enhancement and strong directionality. The sample would also be passivated to improve the uniformity of the cavities.

This page intentionally left blank.

Acronyms

AFM	Atomic Force Microscopy
AlAs	Aluminium Arsenide
ALD	Atomic Layer Deposition
AlGaAs	Aluminium Gallium Arsenide
APD	Avalanche Photodiode
CAD	Computer-Aided Design
CCD	Charge-Coupled Device
cQED	Cavity Quantum Electrodynamics
DCP	Degree of Circular Polarisation
EBL	Electron-Beam Lithography
FDTD	Finite Difference Time Domain
FFT	Fast-Fourier-Transform
FSS	Fine-Structure Splitting
GaAs	Gallium Arsenide
GPW	Glide Plane Waveguide
HeNe	Helium-Neon
HF	Hydrofluoric Acid
HfO_2	Hafnium Oxide
HWP	Half-Wave Plate
ICP	Inductively-Coupled Plasma
InAs	Indium Arsenide
LAO	Local Anodic Oxidation
LED	Light-Emitting Diode
LP	Linear Polariser
MBE	Molecular Beam Epitaxy
MPB	MIT Photonic Bands
μPL	Micro Photoluminescence
NBW	Nanobeam Waveguide
ND	Neutral-Density
OC	Output Coupler
PhC	Photonic Crystal
PhCC	Photonic Crystal Cavity
QCSE	Quantum-Confined Stark Effect
QD	Quantum Dot
Q-factor	Quality-Factor
QIP	Quantum Information Processing
RHEED	Reflection High Energy Electron Diffraction

SCND	Superconducting Nanowire Detectors
SCQD	Site-Controlled Quantum Dot
SEG	Shallow-Etched Grating
SEM	Scanning Electron Microscope
SK	Stranski-Krastanow
TE	Transverse-Electric
Ti:S	Titanium:Sapphire
TIR	Total Internal Reflection
TM	Transverse-Magnetic
WL	Wetting Layer

This page intentionally left blank.

References

[1]G.Moore, "Cramming more components onto integrated circuits", Electronics **38**, 114 (1965) (cit. on p. 1).

[2]N. Gisin, G. Ribordy, W. Tittel, and H. Zbinden, "Quantum cryptography", Rev. Mod. Phys **74**, 145–195 (2002) (cit. on p. 1).

[3]V. Giovannetti, S. Lloyd, and L. Maccone, "Advances in quantum metrology", Nature Photonics **5**, 222–229 (2011) (cit. on p. 1).

[4]F. Arute, K. Arya, and R. B. et. al., "Quantum supremacy using a programmable superconducting processor", Nature **574**, 505–510 (2019) (cit. on p. 1).

[5]H. J. Kimble, "The quantum internet", Nature **453**, 1023–1030 (2008) (cit. on pp. 2, 4).

[6]D. Copsey, M. Oskin, F. Impens, T. Metodiev, A. Cross, S. IEEE, F. T. Chong, I. L. Chuang, and J. Kubiatowicz, "Toward a scalable, silicon-based quantum computing architecture", IEEE Journal of Selected Topics in Quantum Electronics **9**, 1552–1569 (2003) (cit. on p. 2).

[7]L.K.Grover, ed., *A fast quantum mechanical algorithm for database search*, STOC '96: Proceedings of the Twenty-Eighth Annual ACM Symposium on Theory of Computing,Association for Computing Machinery (USA, 1996) (cit. on p. 2).

[8]P.W.Shor, "Polynomial-time algorithms for prime factorization and discrete logarithms on a quantum computer", SIAM J.Comput **26**, 1484–1509 (1997) (cit. on p. 2).

[9]A. Lenstra, H. L. Jr., M. Manasse, and J. Pollard, eds., *The number field sieve*, Proceedings of the twenty-second annual ACM symposium on Theory of computing (1990), pp. 564–572 (cit. on p. 2).

[10]R.P.Fenynman, "Simulating physics with computers", International Journal of Theoretical Physics **21**, 467–488 (1982) (cit. on p. 3).

[11]D. DiVincenzo, "The physical implementation of quantum computation", Fortschr. Phys. **48**, 771–783 (2000) (cit. on pp. 3, 64).

[12]A.F.Kockum and F.Nori, "Quantum bits with Josephson Junctions", in F.Tafuri, *Fundamentals and frontiers of the josephson effect*, Vol. 286 (Springer International Publishing, 2019) (cit. on p. 4).

[13]S.Prawer and A.D.Greentree, "Diamond for quantum computing", Science **320**, 1601–1602 (2008) (cit. on pp. 4, 38).

[14]J.I.Cirac and P.Zoller, "Quantum computations with cold trapped ions", Phys. Rev. Lett **74**, 4091–4094 (1995) (cit. on pp. 4, 38).

[15]P. Kok, W. J. Munro, K. Nemoto, T. C. Ralph, J. P. Dowling, and G. J. Milburn., "Linear optical quantum computing with photonic qubits", Rev. Mod. Phys **79**, 135–174 (2007) (cit. on p. 4).

[16]L. M. K. Vandersypen and I. L. Chuang., "NMR techniques for quantum control and computation", Rev. Mod. Phys **76**, 1037–1069 (2005) (cit. on p. 4).

[17]D.Loss and D.P.DiVincenzo, "Quantum computation with quantum dots", Phys. Rev. A **57**, 120–126 (1998) (cit. on p. 4).

[18]A. Cho and J. Arthur, "Molecular beam epitaxy", Progress in Solid State Chemistry **10**, 157–191 (1975) (cit. on pp. 4, 14).

[19]I. Garcia, B. Galiana, I. Rey-Stolle, and C. Algora, "MOVPE technology for the growth of III-V semiconductor structures", in 2007 Spanish Conference on Electron Devices (2007), pp. 17–20 (cit. on p. 4).

[20]P.Senellart, G.Solomon, and A. White, "High performance semiconductor quantum dot single photon sources", Nature Nanotechnology **12**, 1026–1039 (2017) (cit. on pp. 4, 25, 38).

[21]Y. Chen, "Nanofabrication by electron beam lithography and its applications: a review", Microelectronic Engineering **135**, 57–72 (2015) (cit. on p. 4).

[22]S. J. Pearton, U. K. Chakrabarti, W. S. Hobson, and A. P. Kinsella, "Reactive ion etching of GaAs, AlGaAs, and GaSb in Cl_2 and $SiCl_4$", Journal of Vacuum Science and Technology B: Microelectronics Processing and Phenomena **8**, 607–617 (1990) (cit. on p. 4).

[23]W. Qiu and J. Wang, "Highly controllable ICP etching of GaAs based materials for grating fabrication", Journal of Semiconductors **33**, 026001 (2012) (cit. on p. 4).

[24]P. Lodahl, S. Mahmoodian, and S. Stobbe, "Interfacing single photons and single quantum dots with photonic nanostructures", Rev. Mod. Phys. **87**, 347–400 (2015) (cit. on pp. 4, 25, 38).

[25]X. Zhou, I. Kulkova, T. Lund-Hansen, S. L. Hansen, P. Lodahl, and L. Midolo, "High-efficiency shallow-etched grating on GaAs membranes for quantum photonic applications", Appl. Phys. Lett. **113**, 2511–3 (2018) (cit. on pp. 4, 25, 28).

[26]T. Yoshie, A. Scherer, J. Hendrickson, and et al., "Vacuum rabi splitting with a single quantum dot in a photonic crystal nanocavity", Nature **432**, 200–203 (2004) (cit. on pp. 4, 25).

[27]W. Langbein, P. Borri, U. Woggon, V. Stavarache, D. Reuter, and A. D. Wieck, "Radiatively limited dephasing in inas quantum dots", Phys. Rev. B **70**, 033301 (2004) (cit. on p. 5).

[28]A. J. Brash, L. M. P. P. Martins, F. Liu, J. H. Quilter, A. J. Ramsay, M. S. Skolnick, and A. M. Fox, "High-fidelity initialization of long-lived quantum dot hole spin qubits by reduced fine-structure splitting", Phys. Rev. B **92**, 121–301 (2015) (cit. on pp. 5, 13).

[29]D. Press, K. D. Greve, P. L. McMahon, T. D. Ladd, B. Friess, C. Schneider, M. Kamp, S. Höfling, A. Forchel, and Y. Yamamoto, "Ultrafast optical spin echo in a single quantum dot", Nature Photonics **4**, 367–370 (2010) (cit. on p. 5).

[30]R. J. Warburton, "Single spins in self-assembled quantum dots", Nature Materials **12**, 483–493 (2013) (cit. on p. 5).

[31]C. Emary, X. Xu, D. G. Steel, S. Saikin, and L. J. Sham, "Fast initialization of the spin state of an electron in a quantum dot in the voigt configuration", Phys. Rev. Lett. **98**, 047401 (2007) (cit. on p. 5).

[32]P.Lodahl, "Quantum-dot based photonic quantum networks", Quantum Sci. Technol **3**, 013001 (2018) (cit. on pp. 5, 6).

[33]D. Press, T. D. Ladd, B. Zhang, and Y. Yamamoto, "Complete quantum control of a single quantum dot spin using ultrafast optical pulses", Nature **456**, 218–221 (2008) (cit. on p. 5).

[34]G. Burkard, D. Loss, and D. P. DiVincenzo, "Coupled quantum dots as quantum gates", Phys. Rev. B **59**, 2070 (1999) (cit. on p. 5).

[35]J. R. Schaibley, A. P. Burgers, G. A. McCracken, L.-M. Duan, P. R. Berman, D. G. Steel, A. S. Bracker, D. Gammon, and L. J. Sham, "Demonstration of quantum entanglement between a single electron spin confined to an inas quantum dot and a photon", Phys. Rev. Lett. **110**, 167401 (2013) (cit. on p. 5).

[36]M. Anderson, T. Müller, J. Huwer, and et al., "Quantum teleportation using highly coherent emission from telecom C-band quantum dots.", npj Quantum Inf **6** (2020) (cit. on pp. 5, 13).

[37]J. Huwer, R. M. Stevenson, J. Skiba-Szymanska, M. B. Ward, A. J. Shields, M. Felle, I. Farrer, D. A. Ritchie, and R. V. Penty, "Quantum-dot-based telecommunication-wavelength quantum relay", Phys. Rev. Applied **8**, 24–7 (2017) (cit. on p. 5).

[38]A. Barenco, C. H. Bennett, R. Cleve, D. P. DiVincenzo, N. Margolus, P. Shor, T. Sleator, J. A. Smolin, and H. Weinfurter, "Elementary gates for quantum computation", Phys. Rev. A **52**, 3457–3467 (1995) (cit. on pp. 6, 64).

[39]H. Kim, R. Bose, T. C. Shen, G. S. Solomon, and E. Waks, "A quantum logic gate between a solid-state quantum bit and a photon", Nature Photonics **7**, 373–377 (2013) (cit. on pp. 6, 25).

[40]S. M. Thon, M. T. Rakher, H. Kim, J. Gudat, W. T. M. Irvine, P. M. Petroff, and D. Bouwmeester, "Strong coupling through optical positioning of a quantum dot in a photonic crystal cavity", Appl. Phys. Lett. **94** (2009) (cit. on pp. 6, 24, 36).

[41]J. P. Reithmaier, G. Sek, A. Löffler, C. Hofmann, S. Kuhn, S. Reitzenstein, L. V. Keldysh, V. D. Kulakovskii, T. L. Reinecke, and A. Forchel, "Strong coupling in a single quantum dot–semiconductor microcavity system", Nature **432**, 197–200 (2004) (cit. on pp. 6, 31, 36).

[42]R. Ohta, Y. Ota, M. Nomura, N. Kumagai, S. Ishida, S. Iwamoto, and Y. Arakawa, "Strong coupling between a photonic crystal nanobeam cavity and a single quantum dot", Appl. Phys. Lett. **98**, 173104 (2011) (cit. on pp. 6, 32, 36).

[43]F. Liu, A. J. Brash, J. O'Hara, L. M. P. P. Martins, C. L. Phillips, R. J. Coles, B. Royall, E. Clarke, C. Bentham, N. Prtljaga, I. E. Itskevich, L. R. Wilson, M. S. Skolnick, and A. M. Fox, "High Purcell factor generation of indistinguishable on-chip single photons", Nature Nanotechnology **13**, 835–841 (2018) (cit. on pp. 6, 33, 36, 38, 93, 143).

[44]N.Tomm, A.Javadi, N.O.Antoniadis, D.Najer, M.C.Löbl, A.R.Korsch, R.Schott, S.R.Valentin, A.D.Wieck, A.Ludwig, and R.J.Warburton, "A bright and fast source of coherent single photons", Nature Nanotechnology **16**, 399–403 (2021) (cit. on pp. 6, 31, 36, 38).

[45]A. Laucht, T. Gunthner, S. Putz, R. Saive, S. Frederick, N. Hauke, M. Bichler, M.-C. Amann, A. W. Holleitner, M. Kaniber, and J. J. Finley, "Broadband Purcell enhanced emission dynamics of quantum dots in linear photonic crystal waveguides", Journal of Applied Physics **112** (2012) (cit. on pp. 6, 29, 36).

[46]X. Ding, Y. He, Z.-C. Duan, N. Gregersen, M.-C. Chen, S. Unsleber, S. Maier, C. Schneider, M. Kamp, S. Höfling, C.-Y. Lu, and J.-W. Pan, "On-demand single photons with high extraction efficiency and near-unity indistinguishability from a resonantly driven quantum dot in a micropillar", Phys. Rev. Lett. **116**, 020401 (2016) (cit. on p. 6).

[47]A. V. Kuhlmann, J. H. Prechtel, J. Houel, A. Ludwig, D. Reuter, A. D. Wieck, and R. J. Warburton, "Transform-limited single photons from a single quantum dot", Nature Communications **6** (2015) (cit. on pp. 6, 17, 38).

[48]M. Arcari, I. Söllner, A. Javadi, S. L. Hansen, S. Mahmoodian, J. Liu, H. Thyrrestrup, E. H. Lee, J. D. Song, S. Stobbe, and P. Lodahl, "Near-unity coupling efficiency of a quantum emitter to a photonic crystal waveguide", Phys. Rev. Lett **113**, 093603 (2014) (cit. on pp. 6, 27, 29).

[49]A. Faraon, I. Fushman, D. Englund, N. Stoltz, P. Petroff, and J. Vučković, "Coherent generation of non-classical light on a chip via photon-induced tunnelling and blockade", Nature Physics **4**, 859–863 (2008) (cit. on p. 6).

[50]A. Javadi, I. Söllner, M. Arcari, S. L. Hansen, L. Midolo, S. Mahmoodian, G. Kiršanskė, T. Pregnolato, E. H. Lee, J. D. Song, S. Stobbe, and P. Lodahl, "Single-photon nonlinear optics with a quantum dot in a waveguide", Nature Communications **6**, 8655 (2015) (cit. on p. 6).

[51]I. Schwartz, D. Cogan, E. R. Schmidgall, Y. D. Gantz, O. Kenneth, N. H. Lindner, and D. Gershoni, "Deterministic generation of a cluster state of entangled photons", Science **354**, 434–437 (2016) (cit. on p. 6).

[52]C. H. H. Schulte, J. Hansom, A. E. Jones, C. Matthiesen, C. L. Gall, and M. Atatüre, "Quadrature squeezed photons from a two-level system", Nature **522**, 222–225 (2015) (cit. on p. 6).

[53]H. Wang, Y. He, Y.-H. Li, Z.-E. Su, B. Li, H.-L. Huang, X. Ding, M.-C. Chen, C. Liu, J. Qin, J.-P. Li, Y.-M. He, C. Schneider, M. Kamp, C.-Z. Peng, S. Höfling, C.-Y. Lu, and J.-W. Pan, "High-efficiency multiphoton boson sampling", Nature Photonics **11**, 361–365 (2017) (cit. on p. 6).

[54]H.-S. Zhong, H. Wang, Y.-H. Deng, L.-C. P. Ming-Cheng Chen and, Y.-H. Luo, J. Qin, D. Wu, X. Ding, Y. Hu, P. Hu, X.-Y. Yang, W.-J. Zhang, H. Li, Y. Li, X. Jiang, L. Gan, G. Yang, L. You, Z. Wang, L. Li, N.-L. Liu, C.-Y. Lu, and J.-W. Pan, "Quantum computational advantage using photons", Science **370**, 1460–1463 (2020) (cit. on p. 6).

[55]R.M.Feenstra and J. A.Stroscio, "5.3. Gallium Arsenide", in *Methods in experimental physics*, Vol. 27 (Academic Press, 1993), pp. 251–276 (cit. on p. 10).

[56]M.Fox, "Semiconductor p-i-n diodes", in *Optical properties of solids*, Vol. 3, 2nd (Oxford University Press, 2010) (cit. on p. 12).

[57]N. Somaschi, V. Giesz, J. C. L. L. De Santis, M. P. Almeida, G. Hornecker, S. L. Portalupi, T. Grange, C. Antón, J. Demory, C. Gómez, I. Sagnes, N. D. Lanzillotti-Kimura, A. Lemaítre, A. Auffeves, A. G. White, L. Lanco, and P. Senellart, "Near-optimal single-photon sources in the solid state", Nature Photonics **10**, 340–345 (2016) (cit. on pp. 13, 25, 38).

[58]A.Rastelli, S.Kiravittaya, and O.G.Schmidt, "Growth and control of optically active quantum dots", in *Single semiconductor quantum dots* (2009) (cit. on p. 14).

[59]J. Skiba-Szymanska, A. Jamil, I. Farrer, M. B. Ward, C. A. Nicoll, D. J. P. Ellis, J. P. Griffiths, D. Anderson, G. A. C. Jones, D. A. Ritchie, and A. J. Shields, "Narrow emission linewidths of positioned InAs quantum dots grown on pre-patterned GaAs(100) substrates", Nanotechnology **22** (2011) (cit. on pp. 14, 17, 67).

[60]J. Herranz, L. Wewior, B. Alén, D. Fuster, L. González, and Y. González, "Role of re-growth interface preparation process for spectral line-width reduction of single InAs site-controlled quantum dots", Nanotechnology **26**, 195301 (2015) (cit. on p. 14).

[61]W.Que, "Excitons in quantum dots with parabolic confinement", Phys. Rev. B **45** (1992) (cit. on p. 14).

[62]S. Tarucha, D. G. Austing, T. Honda, R. J. van der Hage, and L. P. Kouwenhoven, "Shell filling and spin effects in a few electron quantum dot", Phys .Rev. Lett **77** (1996) (cit. on p. 14).

[63]M.I.Dyakonov, "Basics of semiconductor and spin physics", in *Springer series in solid-state sciences* (Springer Berlin Heidelberg, 2008), pp. 1–28 (cit. on p. 15).

[64]P. Hawrylak and M. Korkusiński, "Electronic properties of self-assembled quantum dots", in *Single quantum dots: fundamentals, applications and new concepts*, Vol. 90, edited by P.Michler, Topics in Applied Physics (Springer, Berlin, 2003), pp. 25–91 (cit. on p. 16).

[65]K. Peng, S. Wu, J. Tang, and et al., "Probing the dark-exciton states of a single quantum dot using photocurrent spectroscopy in a magnetic field", Phys. Rev. Applied (2017) (cit. on p. 16).

[66]R.Seguin, A.Schliwa, S.Rodt, K.P.U.W.Pohl, and D.Bimberg, "Size-dependent fine-structure splitting in self-organized InAs/GaAs quantum dots", Phys. Rev. Lett **95** (2005) (cit. on pp. 16, 87).

[67]E.Poem, Y.Kodriano, C.Tradonsky, N.H.Lindner, B.D.Gerardot, P.M.Petroff, and D.Gershoni, "Accessing the dark exciton with light", Nature Physics **6**, 993 (2010) (cit. on p. 16).

[68]A. J. Bennett, R. B. Patel, J. Skiba-Szymanska, C. A. Nicoll, I. Farrer, D. A. Ritchie, and A. J. Shields, "Giant stark effect in the emission of single semi-conductor quantum dots", Appl. Phys. Lett. **97**, 031104 (2010) (cit. on p. 19).

[69]B. Alén, F. Bickel, K. Karrai, R. J. Warburton, and P. M. Petroff, "Stark-shift modulation absorption spectroscopy of single quantum dots", Appl. Phys. Lett. **83**, 2235–2237 (2003) (cit. on p. 19).

[70]J. J.Finley, M. Sabathil, P.Vogl, G.Abstreiter, R.Oulton, A.I.Tartakovskii, D.J.Mowbray, M.S.Skolnick, S.L.Liew, A. Cullis, and M.Hopkinson, "Quantum-confined stark shifts of charged exciton complexes in quantum dots", Phys. Rev. B **70**, 201308 (2004) (cit. on p. 19).

[71]M. Winger, T. D. Blasius, T. P. M. Alegre, A. H. Safavi-Naeini, S. M. J. Cohen, S. Stobbe, and O. Painter, "A chip-scale integrated cavity-electro-optomechanics platform", Optics Express **19**, 24905–24921 (2011) (cit. on p. 20).

[72]R. M. Stevenson, R. J. Young, P. Atkinson, K. Cooper, D. A. Ritchie, and A. J. Shields, "A semiconductor source of triggered entangled photon pairs", Nature **439**, 179–182 (2006) (cit. on p. 20).

[73]M. Bayer, G. Ortner, O. Stern, A. Kuther, A. A. Gorbunov, A. Forchel, P. Hawrylak, S. Fafard, K. Hinzer, T. L. Reinecke, S. N. Walck, J. P. Reithmaier, F. Klopf, and F. Schäfer, "Fine structure of neutral and charged excitons in self-assembled In(Ga)As/(Al)GaAs quantum dots", Phys. Rev. B **65**, 195315 (2002) (cit. on p. 20).

[74]T. M. Godden, S. J. Boyle, A. J. Ramsay, A. M. Fox, and M. S. Skolnick., "Fast high fidelity hole spin initialization in a single InGaAs quantum dot", Appl. Phys. Lett. **97**, 061113 (2010) (cit. on p. 20).

[75]J. Berezovsky, M. H. Mikkelsen, N. G. Stoltz, L. A. Coldren, and D. D. Awschalom, "Picosecond coherent optical manipulation of a single electron spin in a quantum dot", Science **320**, 349–352 (2008) (cit. on p. 20).

[76]C. Bonato, E. van Nieuwenburg, J. Gudat, S. Thon, H. Kim, M. P. van Exter, and D. Bouwmeester, "Strain tuning of quantum dot optical transitions via laser-induced surface defects", Phys. Rev. B **84**, 075306 (2011) (cit. on pp. 20, 22).

[77]F. Ding, R. Singh, J. D. Plumhof, T. Zander, V. Křápek, Y. H. Chen, M. Benyoucef, V. Zwiller, K. Dörr, G. Bester, A. Rastelli, and O. G. Schmidt, "Tuning the exciton binding energies in single self-assembled InGaAs GaAs quantum dots by piezoelectric-induced biaxial stress", Phys. Rev. Lett **104**, 067405 (2010) (cit. on pp. 20, 22).

[78]S.Seidl, M.Kroner, A.Högele, K.Karrai, R.J.Warburton, A.Badolato, and P.M.Petroff, "Effect of uniaxial stress on excitons in a self-assembled quantum dot", Appl. Phys. Lett. **88**, 203113 (2006) (cit. on pp. 21, 22).

[79]J. Beetz, T. Braun, C. Schneider, S. Höfling, and M. Kamp, "Anisotropic strain-tuning of quantum dots inside a photonic crystal cavity", Semiconductor Science and Technology **28**, 122002 (2013) (cit. on p. 22).

[80]A. W. Elshaari, E. Büyüközer, I. E. Zadeh, T. Lettner, P. Zhao, E. Schöll, S. Gyger, M. E. Reimer, D. Dalacu, P. J. Poole, K. D. Jöns, and V. Zwiller, "Strain-tunable quantum integrated photonics", Nano Letters **18**, 7969–7976 (2018) (cit. on p. 22).

[81]J. Grim, A. Bracker, M. Zalalutdinov, S. G. Carter, A. C. Kozen, M. Kim, C. S. Kim, J. T. Mlack, M. Yakes, B. Lee, and D. Gammon, "Scalable in operando strain tuning in nanophotonic waveguides enabling three-quantum-dot superradiance.", Nature Materials **18**, 963–969 (2019) (cit. on pp. 22, 65, 74, 76, 82, 83, 174).

[82]D. Englund, A. Faraon, I. Fushman, N. Stoltz, P. Petroff, and J. Vučković, "Controlling cavity reflectivity with a single quantum dot.", Nature **450**, 857–861 (2007) (cit. on p. 23).

[83]J.-H. Kim, S. Aghaeimeibodi, C. J. K. Richardson, R. P. Leavitt, and E. Waks, "Super-radiant emission from quantum dots in a nanophotonic waveguide", Nano Letters **18**, 4734–4740 (2018) (cit. on p. 23).

[84]K. H. Lee, A. M. Green, R. A. Taylor, D. N. Sharp, J. Scrimgeour, O. M. Roche, J. H. Na, A. F. Jarjour, A. J. Turberfield, F. S. Brossard, D. A. Williams, G. Andrew, and D. Briggs, "Registration of single quantum dots using cryogenic laser photolithography", Appl. Phys. Lett. **88**, 1–4 (2006) (cit. on p. 23).

[85]R. J. Coles, D. M. Price, J. E. Dixon, B. Royall, E. Clarke, P. Kok, M. S. Skolnick, A. M. Fox, and M. N. Makhonin, "Chirality of nanophotonic waveguide with embedded quantum emitter for unidirectional spin transfer", Nature Communications **7** (2016) (cit. on pp. 24, 25, 27, 41, 143, 169).

[86]L. Sapienza, M. Davanço, A. Badolato, and K. Srinivasan, "Nanoscale optical positioning of single quantum dots for bright and pure single-photon emission", Nature Communications **6**, 7833 (2015) (cit. on p. 25).

[87]T. Pregnolato, X. Chu, T. Schröder, R. Schott, A. D. Wieck, A. Ludwig, P. Lodahl, and N. Rotenberg, "Deterministic positioning of nanophotonic waveguides around single self-assembled quantum dots", APL Photonics **5** (2020) (cit. on p. 25).

[88]T. Yamaguchi, Y. Ota, R. Katsumi, K. Watanabe, S. Ishida, A. Osada, Y. Arakawa, and S. Iwamoto, "GaAs valley photonic crystal waveguide with light emitting InAs quantum dots", Appl. Phys. Express **12**, 062005 (2019) (cit. on pp. 25, 30, 143).

[89]M. Sieger, F. Balluff, X. Wang, S.-S. Kim, L. Leidner, G. Gauglitz, and B. Mizaikoff, "On-chip integrated mid-infrared GaAs/AlGaAs mach–zehnder interferometer", Anal. Chem. **85**, 3050–3052 (2013) (cit. on p. 25).

[90]L. Midolo, S. L. Hansen, W. Zhang, C. Papon, R. Schott, A. Ludwig, A. D. Wieck, P. Lodahl, and S. Stobbe, "Electro-optic routing of photons from a single quantum dot in photonic integrated circuits", Opt. Express **25**, 33514–33526 (2017) (cit. on pp. 25, 95).

[91]M. J. Mehrabad, A. P. Foster, R. Dost, E. Clarke, P. K. Patil, I. Farrer, J. Heffernan, M. S. Skolnick, and L. R. Wilson, "A semiconductor topological photonic ring resonator", Appl. Phys. Lett **116**, 061102 (2020) (cit. on pp. 25, 30, 41).

[92]J. Haas, P. Artmann, and B. Mizaikof, "Mid-infrared GaAs/AlGaAs micro-ring resonators characterized via thermal tuning", RSC Adv. **9**, 8594–8599 (2019) (cit. on p. 25).

[93]H. Thyrrestrup, L. Sapienza, and P. Lodahl, "Extraction of the β factor for single quantum dots coupled to a photonic crystal waveguide", Appl. Phys. Lett **96**, 231106 (2010) (cit. on p. 26).

[94]R. Uppu, H. T. Eriksen, H. Thyrrestrup, A. D. Uğurlu, Y. Wang, S. Scholz, A. D. Wieck, A. Ludwig, M. C. Löbl, R. J. Warburton, P. Lodahl, and L. Midolo, "On-chip deterministic operation of quantum dots in dual-mode waveguides for a plug-and-play single-photon source", Nature Communications **11**, 3782 (2020) (cit. on p. 26).

[95]H. Thyrrestrup, G. Kiršanskė, H. L. Jeannic, T. Pregnolato, L. Zhai, L. Raahauge, L. Midolo, N. Rotenberg, A. Javadi, R. Schott, A. D. Wieck, A. Ludwig, M. C. Löbl, I. Söllner, R. J. Warburton, and P. Lodahl, "Quantum optics with near-lifetime-limited quantum-dot transitions in a nanophotonic waveguide", Nano Letters **18** (2018) (cit. on p. 26).

[96]A. Faraon, I. Fushman, D. Englund, N. Stoltz, P. Petroff, and J. Vučković, "Dipole induced transparency in waveguide coupled photonic crystal cavities", Opt. Express **16**, 12154–12162 (2008) (cit. on p. 27).

[97]J. D. Joannopoulos, S. G. Johnson, J. N. Winn, and R. D. Meade, *Photonic crystals: molding the flow of light*, 2nd (Princeton University Press, 2008) (cit. on p. 28).

[98]M. Notomi, K. Yamada, A. Shinya, J. Takahashi, C. Takahashi, and I. Yokohama, "Extremely large group-velocity dispersion of line-defect waveguides in photonic crystal slabs", Phys. Rev. Lett **87** (2001) (cit. on p. 29).

[99]L. Sapienza, H. Thyrrestrup, S. Stobbe, P. D. Garcia, S. Smolka, and P. Lodahl, "Cavity quantum electrodynamics with anderson-localized modes", Science **327**, 1352–1356 (2010) (cit. on p. 29).

[100]M. Lončar, D. Nedeljković, T. Doll, J. Vučković, A. Scherer, and T. P. Pearsall, "Waveguiding in planar photonic crystals", Appl. Phys. Lett **77** (2000) (cit. on p. 30).

[101]M. Tokushima, H. Kosaka, A. Tomita, and H. Yamada, "Lightwave propagation through a 120° sharply bent single-line-defect photonic crystal waveguide", Appl. Phys. Lett **76** (1999) (cit. on p. 30).

[102]B. Miao, C. Chen, S. Shi, J. Murakowski, and D. W. Prather, "High-efficiency broad-band transmission through a double-60° bend in a planar photonic crystal single-line defect waveguide", IEEE Photonics Technology Letters **16** (2004) (cit. on p. 30).

[103]I. Söllner, S. Mahmoodian, S. L. Hansen, L. Midolo, A. Javadi, G. Kiršanskė, T. Pregnolato, H. El-Ella, E. H. Lee, J. D. Song, S. Stobbe, and P. Lodahl, "Deterministic photon–emitter coupling in chiral photonic circuits", Nature Nanotechnology **10** (2015) (cit. on pp. 30, 41, 143, 169).

[104]B. Gayral, J. M. Gérard, A. Lemaître, C. Dupuis, L. Manin, and J. L. Pelouard, "High-Q wet-etched GaAs microdisks containing InAs quantum boxes", Appl. Phys. Lett. **75**, 1908–1910 (1999) (cit. on p. 31).

[105]C. Sauvan, G. Lecamp, P. Lalanne, and J. Hugonin, "Modal-reflectivity enhancement by geometry tuning in photonic crystal microcavities", Optics Express **13**, 245–255 (2005) (cit. on p. 32).

[106]A. R. M. Zain, N. P. Johnson, M. Sorel, and R. M. D. L. Rue, "Ultra high quality factor one dimensional photonic crystal/photonic wire micro-cavities in silicon-on-insulator (SOI)", Optics Express **16**, 12084–12089 (2008) (cit. on p. 32).

[107]P. Lalanne and J. P. Hugonin, "Bloch-wave engineering for High-Q, Small-V microcavities", IEEE Journal of Quantum Electronics **39**, 1430–1438 (2003) (cit. on p. 32).

[108]S. I. Halimi, Z. Fu, F. O. Afzal, J. A. Allen, S. Hu, and S. M. Weiss, "Controlling the mode profile of photonic crystal nanobeam cavities with mix-and-match unit cells", Journal of the Optical Society of America B **37**, 3401–3406 (2020) (cit. on p. 32).

[109]Y. Zhang, M. Khan, Y. Huang, J. Ryou, P. Deotare, R. Dupuis, and M. Lončar, "Photonic crystal nanobeam lasers", Appl. Phys. Lett **97**, 95–98 (2010) (cit. on p. 32).

[110]Y. Gong, B. Ellis, G. Shambat, T. Sarmiento, J. S. Harris, and J. Vučković, "Nanobeam photonic crystal cavity quantum dot laser", Optics Express **18**, 8781–8789 (2010) (cit. on pp. 32, 36).

[111]S. Buckley, M. Radulaski, J. L. Zhang, J. Petykiewicz, K. Biermann, and J. Vučković, "Nonlinear frequency conversion using high-quality modes in GaAs nanobeam cavities", Optics Letters **39**, 5673–5676 (2014) (cit. on p. 32).

[112]X. Zhou, R. Uppu, Z. Liu, C. Papon, R. Schott, A. D. Wieck, A. Ludwig, P. Lodahl, and L. Midolo, "On-chip nanomechanical filtering of quantum-dot single-photon sources", Laser and Photonics Reviews **14**, 1900404 (2020) (cit. on pp. 32, 93, 94).

[113]X. Chew, *Student Member*, IEEE, G. Zhou, F. S. Chau, and J. Deng, "Nanomechanically tunable photonic crystal resonators utilizing triple-beam coupled nanocavities", IEEE Photonics Technology Letters **23**, 1310–1312 (2011) (cit. on pp. 32, 93–95).

[114]Z. Han, C. Wang, Y. Liu, and H. Tian, "Simultaneous detection of complex refractive index and temperature using a compact side-coupled photonic crystal nanobeam cavity", Journal of the Optical Society of America B **38**, 2765–2774 (2021) (cit. on p. 32).

[115]M. Shirane, S. Kono, J. Ushida, and S. Ohkouchi, "Mode identification of high-quality-factor single-defect nanocavities in quantum dot-embedded photonic crystals", Journal of Applied Physics **101**, 073107 (2007) (cit. on p. 32).

[116]Y. Akahane, T. Asano, B.-S. Song, and S. Noda, "High-Q photonic nanocavity in a two-dimensional photonic crystal", Nature **425**, 944–947 (2003) (cit. on p. 32).

[117]I. J. Luxmoore, E. D. Ahmadi, A. M. Fox, M. Hugues, and M. S. Skolnick, "Unpolarized H1 photonic crystal nanocavities fabricated by stretched lattice design", Appl. Phys. Lett. **98**, 041101 (2011) (cit. on pp. 33, 93, 147).

[118]I. J. Luxmoore, E. D. Ahmadi, B. J. Luxmoore, N. A. Wasley, A. I. Tartakovskii, M. Hugues, M. S. Skolnick, and A. M. Fox, "Restoring mode degeneracy in H1 photonic crystal cavities by uniaxial strain tuning", Appl. Phys. Lett. **100**, 12116 (2012) (cit. on pp. 33, 93, 147, 172, 178).

[119]Y. Ota, M. Shirane, M. Nomura, N. Kumagai, S. Ishida, S. Iwamoto, S. Yorozu, and Y. Arakawa, "Vacuum rabi splitting with a single quantum dot embedded in a H1 photonic crystal nanocavity", Appl. Phys. Lett **94**, 033102 (2009) (cit. on pp. 33, 36).

[120]K. Kuruma, Y. Ota, M. Kakuda, S. Iwamoto, and Y. Arakawa, "Surface-passivated high-Q GaAs photonic crystal nanocavity with quantum dots", APL Photonics **5**, 046106 (2020) (cit. on pp. 34, 124, 141, 178).

[121]E. Jaynes and F. Cummings, "Comparison of quantum and semiclassical radiation theories with application to the beam maser", Proceedings of the IEEE **51**, 89–109 (1963) (cit. on p. 35).

[122]E. Purcell, "Spontaneous emission probabilities at radio frequencies", Phys. Rev **69**, 681 (1946) (cit. on p. 36).

[123]M. Fox, "Photon statistics", in *Quantum optics: an introduction* (Oxford University Press, Oxford, 2006) (cit. on pp. 37, 39).

[124]F. A. Haight, *Handbook of the poisson distribution* (Wiley, New York USA, 1967) (cit. on p. 37).

[125]M. Dagenais and L. Mandel, "Investigation of two-time correlations in photon emissions from a single atom", Phys. Rev. A **18**, 2217–2228 (1978) (cit. on p. 38).

[126]F. Diedrich and H. Walther, "Nonclassical radiation of a single stored ion", Phys. Rev. Lett. **58**, 203–207 (1987) (cit. on p. 38).

[127]P. A. Barton, C. J. S. Donald, D. M. Lucas, D. A. Stevens, A. M. Steane, and D. N. Stacey, "Measurement of the lifetime of the $3d^2D_{\frac{5}{2}}$ state in $^{40}Ca^{+}$", Phys. Rev. A **62**, 032503 (2000) (cit. on p. 38).

[128]C. Kurtsiefer, S. Mayer, P. Zarda, and H. Weinfurter, "Stable solid-state source of single photons", Phys. Rev. Lett. **85**, 290–293 (2000) (cit. on p. 38).

[129]R. Brouri, A. Beveratos, J.-P. Poizat, and P. Grangier, "Photon antibunching in the fluorescence of individual color centers in diamond", Optics Letters **25**, 1294–1296 (2000) (cit. on p. 38).

[130]A. Beveratos, R. Brouri, T. Gacoin, J.-P. Poizat, and P. Grangier, "Nonclassical radiation from diamond nanocrystals", Phys. Rev. A **64**, 061802 (2001) (cit. on p. 38).

[131]M.Beck, *Quantum mechanics : theory and experiment* (OUP, USA, 2012) (cit. on p. 39).

[132]H. J. Carmichael, "Quantum trajectory theory for cascaded open systems", Phys. Rev. Lett. **70**, 2273–2276 (1993) (cit. on p. 40).

[133]C. W. Gardiner, "Driving a quantum system with the output field from another driven quantum system", Phys. Rev. Lett **70**, 2269–2272 (1993) (cit. on p. 40).

[134]M. Lax, W. H. Louisell, and W. B. McKnight, "From Maxwell to paraxial wave optics", Phys. Rev. A **11**, 1365–1370 (1975) (cit. on p. 40).

[135]T. V. Mechelen and Z. Jacob, "Universal spin-momentum locking of evanescent waves", Optica **3**, 118–126 (2016) (cit. on p. 40).

[136]F. L. Kien, J. Liang, K. Hakuta, and V. Balykin, "Field intensity distributions and polarization orientations in a vacuum-clad subwavelength-diameter optical fiber", Optics Communications **242**, 445–455 (2004) (cit. on p. 41).

[137]P. Lodahl, S. Mahmoodian, S. Stobbe, P. S. Arno Rauschenbeutel, J. Volz, H. Pichler, and P. Zoller, "Chiral quantum optics", Nature **541**, 473–480 (2017) (cit. on p. 41).

[138]E.Collett, *Field guide to polarisation* (SPIE Press, Bellimgham WA USA, 2005) (cit. on p. 41).

[139]I. J. Luxmoore, N. A. Wasley, A. J. Ramsay, A. C. T. Thijssen, R. Oulton, M. Hugues, S. Kasture, V. G. Achanta, A. M. Fox, and M. S. Skolnick, "Interfacing spins in an InGaAs quantum dot to a semiconductor waveguide circuit using emitted photons", Phys. Rev. Lett **110**, 037402 (2013) (cit. on p. 41).

[140]I. J. Luxmoore, N. A. Wasley, A. J. Ramsay, A. C. T. Thijssen, R. Oulton, M. Hugues, A. M. Fox, and M. S. Skolnick, "Optical control of the emission direction of a quantum dot", Appl. Phys. Lett. **103**, 241102 (2013) (cit. on p. 41).

[141]B. le Feber, N. Rotenberg, and L. Kuipers, "Nanophotonic control of circular dipole emission", Nature Communications **6**, 6695 (2015) (cit. on p. 41).

[142]P. J. Dobson, "An introduction to reflection high energy electron diffraction", in *Surface and interface characterization by electron optical methods* (Springer, 1998) (cit. on p. 43).

[143]K. Yee, "Numerical solution of initial boundary value problems involving Maxwell's equations in isotropic media", IEEE Transactions on Antennas and Propagation **14**, 302–307 (1966) (cit. on p. 57).

[144]A. Taflove and S. C. Hagness, *Computational electrodynamics: the finite difference time domain method*, 2nd Edition (Artech House, Norwood, 2000) (cit. on p. 59).

[145]S. G. Johnson and J. D. Joannopoulos, "Block-iterative frequency-domain methods for Maxwell's equations in a planewave basis", Optics Express **8**, 173–190 (2001) (cit. on p. 60).

[146]R. D. Richtmyer and J. von Neumann, "Statistical methods in neutron diffusion", LAMS **551**, 751–764 (1947) (cit. on p. 60).

[147]B. Yang, F. Liu, and M. G. Lagally, "Local strain-mediated chemical potential control of quantum dot self-organization in heteroepitaxy", Phys. Rev. Lett **92**, 025520 (2004) (cit. on p. 66).

[148]D.J.Srolovitz, "On the stability of surfaces of stressed solids", Acta Metallurgica **37**, 621–625 (1989) (cit. on p. 66).

[149]J. Wu and P. Jin, "Self-assembly of InAs quantum dots on GaAs(001) by molecular beam epitaxy", Front. Phys. **10**, 7–58 (2015) (cit. on p. 66).

[150]C. J. Mayer, M. F. Helfrich, and D. M. Schaadt, "Influence of hole shape/size on the growth of site-selective quantum dots", Nanoscale Research Letters **8**, 504 (2013) (cit. on pp. 66, 69).

[151]M. K. Yakes, L. Yang, A. S. Bracker, T. M. Sweeney, P. G. Brereton, M. Kim, C. S. Kim, P. M. Vora, D. Park, S. G. Carter, and D. Gammon, "Leveraging crystal anisotropy for deterministic growth of InAs quantum dots with narrow optical linewidths", Nano Letters **13**, 4870–4875 (2013) (cit. on p. 66).

[152]P. Atkinson, S. Kiravittaya, M. Benyoucef, A. Rastelli, and O. G. Schmidt, "Site-controlled growth and luminescence of InAs quantum dots using in situ Ga-assisted deoxidation of patterned substrates", Appl. Phys. Lett. **93**, 101908 (2008) (cit. on p. 67).

[153]V. Cambela) and J. Šoltýs, "The influence of sample conductivity on local anodic oxidation by the tip of atomic force microscope", Journal of Applied Physics **102**, 074315 (2007) (cit. on p. 68).

[154]J.Martín-Sánchez, Y.González, L.González, M.Tello, R.García, D.Granados, J.M.García, and F.Briones, "Ordered InAs quantum dots on pre-patterned GaAs (001) by local oxidation nanolithography", Journal of Crystal Growth **284**, 313–318 (2005) (cit. on p. 68).

[155]E.Tranvouez, M.Gendry, P.Regreny, and G.Bremond, "InP patterning using contact mode and non-contact AFM lithography for quantum dot localization", Superlattices and Microstructures **36**, 325–333 (2004) (cit. on p. 68).

[156]P. Atkinson, O. G.Schmidt, S. P.Bremner, and D. A.Ritchie, "Formation and ordering of epitaxial quantum dots", Comptes Rendus Physique **9**, 788–803 (2008) (cit. on p. 69).

[157]S. Kiravittaya, A. Rastelli, and O. G. Schmidt, "Photoluminescence from seeded three-dimensional InAs/GaAs quantum-dot crystal", Appl. Phys. Lett. **88**, 043112 (2006) (cit. on p. 69).

[158]L. N. McCabe, Y. Wang, M. F. Doty, and J. M. O. Zidea, "Low-density patterned InAs quantum dot arrays", Journal of Vacuum Science and Technology **38**, 022803 (2020) (cit. on pp. 69, 70).

[159]K. M. Cha, I. Horiuchi, K. Shibata, and K. Hirakawa, "Size-limiting effect of site-controlled InAs quantum dots grown at high temperatures by molecular beam epitaxy", Appl. Phys. Express **5**, 085501 (2012) (cit. on p. 69).

[160]J. Herranz, L. González, L. Wewior, B. Alén, D. Fuster, and Y. González, "Study of growth parameters for single InAs qd formation on GaAs(001) patterned substrates by local oxidation lithography", Cryst. Growth Des. **15**, 666–672 (2014) (cit. on p. 69).

[161]M. Berdova, X. Liu, C. Wiemer, A. Lamperti, G. Tallarida, E. Cianci, M. Fanciulli, and S. Franssila, "Hardness, elastic modulus, and wear resistance of hafnium oxide-based films grown by atomic layer deposition", Journal of Vacuum Science & Technology A **34**, 051510 (2016) (cit. on p. 74).

[162]D. K. Venkatachalam, J. E. Bradby, M. N. Saleh, S. Ruffell, and R. G. Elliman, "Nanomechanical properties of sputter-deposited HfO_2 and $Hf_xSi_{1-x}O_2$ thin films", Journal of Applied Physics **110**, 043527 (2011) (cit. on p. 76).

[163]D. M.Hausmann and R. G.Gordon, "Surface morphology and crystallinity control in the atomic layer deposition (ald) of hafnium and zirconium oxide thin films", Journal of Crystal Growth **249**, 251–261 (2003) (cit. on p. 76).

[164]J. D. Mar, J. J. Baumberg, X. L. Xu, A. C. Irvine, and D. A. Williams, "Precise measurements of the dipole moment and polarizability of the neutral exciton and positive trion in a single quantum dot", Phys. Rev. B **95**, 201304 (2017) (cit. on p. 88).

[165]T. C. H. Liew and V. Savona, "Multimode entanglement in coupled cavity arrays", New Journal of Physics **15**, 025015 (2013) (cit. on pp. 93, 177).

[166]S. L. Mouradian and D. Englund, "A tunable waveguide-coupled cavity design for scalable interfaces to solid-state quantum emitters", APL Photonics **2**, 046103 (2017) (cit. on p. 93).

[167]X. Chew, G. Zhou, H. Yu, F. S. Chau, J. Deng, Y. C. Loke, and X. Tang, "An in-plane nanomechanics approach to achieve reversible resonance control of photonic crystal nanocavities", Optics Express **18**, 22232–22244 (2010) (cit. on pp. 93, 95).

[168]M. Petruzzella, T. Xia, F. Pagliano, S. Birindelli, L. Midolo, Z. Zobenica, L. H. Li, E. H. Linfield, and A. Fiore, "Fully tuneable, Purcell-enhanced solid-state quantum emitters", Appl. Phys. Lett **107**, 141109 (2015) (cit. on p. 94).

[169]Z. Xu, C. Qiu, Y. Yang, Q. Zhu, X. Jiang, Y. Zhang, W. Gao, and Y. Su, "Ultra-compact tunable silicon nanobeam cavity with an energy-efficient graphene micro-heater", Optics Express **25**, 19479–19486 (2017) (cit. on p. 95).

[170]J. Pan, Y. Huo, K. Yamanaka, S. Sandhu, L. Scaccabarozzi, R. Timp, M. L. Povinelli, S. Fan, M. M. Fejer, and J. S. Harris, "Aligning microcavity resonances in silicon photonic-crystal slabs using laser-pumped thermal tuning", Appl. Phys. Lett. **92**, 103114 (2008) (cit. on p. 95).

[171]S. A. Tadesse and M. Li, "Sub-optical wavelength acoustic wave modulation of integrated photonic resonators at microwave frequencies", Nature Communications **5**, 5402 (2014) (cit. on p. 95).

[172]A. F. Koenderink, M. Kafesaki, B. C. Buchler, and V. Sandoghdar, "Controlling the resonance of a photonic crystal microcavity by a near-field probe", Phys. Rev. Lett **95**, 153904 (2005) (cit. on p. 95).

[173]S. Han, T. J. Seok, N. Quack, B.-W. Yoo, and M. C. Wu, "Large-scale silicon photonic switches with movable directional couplers", Optica **2**, 370–375 (2015) (cit. on p. 96).

[174]Z. K. Bishop, A. P. Foster, B. Royall, C. Bentham, E. Clarke, and L. R. Wilson, "Electromechanical control of an on-chip optical beam splitter containing an embedded quantum emitter", Optics Letters **43**, 2142–2145 (2018) (cit. on pp. 96, 99).

[175]S. D. Senturia, "Bending of beams", in *Microsystem design* (Springer, Boston MA, 2001) Chap. 9, pp. 207–217 (cit. on p. 98).

[176]Q. Quan, P. B. Deotare, and M. Loncar, "Photonic crystal nanobeam cavity strongly coupled to the feeding waveguide", Appl. Phys. Lett. **96**, 17–20 (2010) (cit. on p. 100).

[177]Z. Huang, K. Cui, Y. Li, X. Feng, F. Liu, W. Zhang, and Y. Huang, "Strong optomechanical coupling in nanobeam cavities based on hetero optomechanical crystals", Scientific Reports **5**, 15964 (2015) (cit. on p. 100).

[178]F.T.Pedersen, Y.Wang, C.T.Olesen, S.Scholz, A.D.Wieck, A.Ludwig, M.C.Löbl, R.J.Warburton, L.Midolo, R.Uppu, and P.Lodahl, "Near transform-limited quantum dot linewidths in a broadband photonic crystal waveguide", ACS Photonics **7**, 2343–2349 (2020) (cit. on p. 100).

[179]Y. Zhang, M. W. McCutcheon, I. B. Burgess, and M. Loncar, "Ultra-high-Q TE/TM dual-polarized photonic crystal nanocavities", Optics Letters **34**, 2694–2696 (2009) (cit. on p. 110).

[180]D. O. Bracher, X. Zhang, and E. L. Hu, "Selective Purcell enhancement of two closely linked zero-phonon transitions of a silicon carbide color center", PNAS **114**, 4060–4065 (2017) (cit. on pp. 110, 124).

[181]M. Minkov and V. Savona, "Automated optimisation of photonic crystal slab cavities", Scientific Reports **4**, 5124 (2014) (cit. on pp. 115, 116, 123).

[182]F. O. Afzal, S. I. Halimi, and S. M. Weiss, "Efficient side-coupling to photonic crystal nanobeam cavities via state-space overlap", Journal of the Optical Society of America B **36**, 585–595 (2019) (cit. on pp. 118, 141, 177).

[183]C. P. Dietrich, A. Fiore, M. G. Thompson, M. Kamp, and S. Höfling, "GaAs integrated quantum photonics: towards compact andmulti-functional quantum photonic integrated circuits", Laser Photonics Rev **10**, 870–894 (2016) (cit. on p. 143).

[184]G. Buonaiuto, R. Jones, B. Olmos, and I. Lesanovsky, "Dynamical creation and detection of entangled many-body states in a chiral atom chain", New J. Phys **21**, 113021 (2019) (cit. on p. 143).

[185]D. F. Kornovan, M. I. Petrov, and I. V. Iorsh, "Transport and collective radiance in a basic quantum chiral optical model", Phys. Rev. B **96**, 115162 (2017) (cit. on p. 143).

[186]S. Barik, A. Karasahin, C. Flower, T. Cai, H. Miyake, W. DeGottardi, M. Hafezi, and E. Waks, "A topological quantum optics interface", Science **359**, 666–668 (2018) (cit. on p. 143).

[187]S. Mahmoodian, K. Prindal-Nielsen, I. Söllner, S. Stobbe, and P. Lodahl, "Engineering chiral light–matter interaction in photonic crystal waveguides with slow light", Optical Materials Express **7**, 43–51 (2017) (cit. on p. 143).

[188]I. Shomroni, S. Rosenblum, Y. Lovsky, O. Bechler, G. Guendelm, and B. Dayan, "All-optical routing of single photonsby a one-atom switch controlledby a single photon", Science **345**, 903–905 (2014) (cit. on p. 143).

[189]D. Hallett, A. P. Foster, D. Whittaker, M. S. Skolnick, and L. R. Wilson, "Engineering chiral light–matter interactions in a waveguide- coupled nanocavity", ACS Photonics **9**, 706–713 (2022) (cit. on pp. 143, 145–147, 175).

[190]A. C. T. Thijssen, M. J. Cryan, J. G. Rarity, and R. Oulton, "Transfer of arbitrary quantum emitter states to near-field photon superpositions in nanocavities", Optics Express **20**, 22412–22428 (2012) (cit. on pp. 144, 146).

[191]K. Hennessy, C. Högerle, and E. Hu, "Tuning photonic nanocavities by atomic force microscope nano-oxidation", Appl. Phys. Lett **89**, 041118 (2006) (cit. on p. 147).

[192]D. Walls and G. J. Milburn, "Input–output formulation of optical cavities", in *Quantum optics* (Springer, Berlin, Heidelberg, 2008) (cit. on p. 148).

[193]C. W. Gardiner and M. J. Collett, "Input and output in damped quantum systems: quantum stochastic differential equations and the master equation", Phys. Rev. A **31**, 3761–3774 (1985) (cit. on p. 148).

[194]S. Fan, Ş. E. Kocabaş, and J.-T. Shen, "Input-output formalism for few-photon transport in one-dimensional nanophotonic waveguides coupled to a qubit", Phys. Rev. A **82**, 063821 (2010) (cit. on p. 148).

[195]E. Rephaeli, S. Fan, and F. IEEE, "Few-photon single-atom cavity QED with input-output formalism in fock space", IEEE Journal of selected Topics in Quantum Electronics **18**, 1754–1762 (2012) (cit. on p. 148).

[196]M. Felici, G. Pettinari, F. Biccari, A. Boschetti, S. Younis, S. Birindelli, M. Gurioli, A. Vinattieri, A. Gerardino, L. Businaro, M. Hopkinson, S. Rubini, M. Capizzi, and A. Polimeni, "Broadband enhancement of light-matter interaction in photonic crystal cavities integrating site-controlled quantum dots", Phys. Rev. B **101**, 205403 (2020) (cit. on p. 176).

[197]B. Rigal, B. Dwir, A. Rudra, I. Kulkova, A. Lyasota, and E. Kapon, "Single photon extraction and propagation in photonic crystal waveguides incorporating site-controlled quantum dots", Appl. Phys. Lett. **112**, 051105 (2018) (cit. on p. 176).